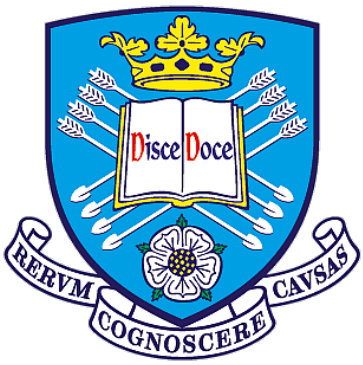

The University Of Sheffield.

Large-area Fabrication of Plasmonic Nanostructures by Interferometric Lithography

by

Ibrahim Saleem S. Alatawi

A thesis submitted in partial fulfilment of the requirements for the degree of Doctor of Philosophy

The University of Sheffield

Faculty of Science

Department of Chemistry

November 2022

Declaration

The work described in the thesis was undertaken between October 2018 and October 2022 under the supervision of Professor Graham J. Leggett. Unless otherwise stated, it is the work of the author and has not been submitted in whole or in part for any other degree at this or any other institution.

November 2022

Signed…….…….

Ibrahim Saleem S. Alatawi
Department of Chemistry,
Dainton Building,
University of Sheffield,
Brook Hill,
Sheffield,
United Kingdom
S3 7HF

Acknowledgments

First of all, I would like to express my gratitude and appreciation to Professor Graham Leggett for giving me the opportunity to work under his supervision, and for all the helpful discussions and his advice during the fourth years I spend in his group. I really want to say that thank you Professor Graham for always being patient with me.

I would like to thank Doctor Anna Tsargorodska for sharing her deep knowledge with me and giving me valuable suggestions during my Ph.D. studies. She has taught me more than I thought I could learn.

I would like to thank Doctor Deborah Hammond for her kind assistance with XPS technique.

I would also like to thank Doctor Benjamin Bower for his collaboration in making Rhodamine B available in our laboratory.

I would like to thank my labmates, past and present, for their assistance and cooperation.

My sincere appreciation to the University of Tabuk for its financial support throughout my studies. All this would not have been possible without you.

My sincere appreciation to my family and friends for their support and encouragement during my studies.

Table of Content

List of Figures

List of Tables

Abbreviation

SPRs	Surface plasmon resonances
SPPs	Surface plasmon polaritons
LSPRs	Localised surface plasmon resonances
AuNPs	Gold nanoparticles
NPs	Nanoparticles
SAMs	Self-assembled monolayers
ODT	1-octadecanethiol
PHDA	16-phosphonohexadecanioc acid
AUT	11-amino-1-undecanethiol
$RBON_3$	Rhodamine B azidopropyl ester
BIBB-APTES	2-bromoisobutyryl bromide + 3-aminopropyltriethoxysilane
BIBB	2-bromoisobutyryl bromide
APTES	3-aminopropyltriethoxysilane
SIP	Surface-initiated polymerisation
ATRP	Atomic transfer radical polymerisation
SI-ATRP	Surface-initiated atom transfer radical polymerisation
ARGET	Activator regenerated by electron transfer
ARGET-ATRP	Activator regenerated by electron transfer-atom transfer radical
NIL	Nanoimprint lithography
EBL	Electron-beam lithography
FIBL	Focused ion beam lithography
SEM	Scanning electron microscope
NSL	Nanosphere lithography
IL	Interferometric lithography
AFM	Atomic force microscope
SPM	Scanning probe microscope
XPS	X-ray photoelectron microscopy
SE	Spectroscopic ellipsometry
CA	Contact angle
UV	Ultraviolet

XRD	X-ray diffraction
DLS	Dynamic light scatterning
QCM	Quartz Crystal microbalance
UHV	Ultra-high vaccum
RI	Refractive index
FWHM	Full width at half maximum
DBS	Diffractive beam splitter
Min	Minute/minutes
h	Hour/hours
DMF	Dimethylformamide
AT	Annealing temperature
ϕ	Represnts the angle of rotation
θ	Represents the angle of incidence

Abstract

Plasmon resonances have attracted a great deal of research interest in recent years for their potential applications, including biosensing, subwavelength optics, negative refractive index metamaterials, as well as their ability to generate enhanced electromagnetic fields. Localised surface plasmon resonance (LSPR) in metallic nanostructures is able to provide large electromagnetic field enhancements, and nanometre-scale localisation of electric fields. Their resonance wavelengths and properties can be tuned by varying the nanostructure geometry and are very sensitive to the environmental refractive index. The coupling of LSPR can lead to new hybrid states that cannot be supported by individual metallic nanostructures, overcome certain limitations of single localised surface plasmon resonances, and open up possibilities for new applications as well as active control of plasmon resonances. The use of interferometric lithography (IL) to develop a variety of nanostructures has been and continues to be essential for mask production and biosensor application, and relies on its high resolution, flexibility, and compatibility with other conventional fabrication processes.

This study presents results from samples fabricated by IL under various fabrication conditions including sample surfaces, exposure doses, and etching solutions to establish novel resonance modes that may make them suitable for important applications. Initially, results are presented from samples fabricated by exposing self-assembled monolayers of 1-octadecanethiols on gold surfaces to UV light at a wavelength of 244 nm in a Lloyd's mirror interferometer system. The fabricated structures are analysed based on variations in their geometries, periods and heights; details of the fabrication of square, hexagonal and elongated arrays are described. Results are also presented from samples designed to evaluate the effect of chromium thicknesses and annealing temperatures on nanostructure geometries and plasmon resonances. Evidence for the existence of plasmon-exciton coupling is also presented from an array of gold nanostructures immobilised with rhodamine B.

Next, results are presented from samples of polymer brushes patterned by IL with nanoscale features. Polymer brushes were grown from surface-linked initiator sites using atom transfer radical polymerisation. The polymerisation of cysteine methacrylate was primarily chosen for its ease of preparation and the ability to control its thickness on solid surfaces. Moreover, the direct patterning method significantly reduces the risk of surface contamination and enables the fabrication of polymeric nanostructures with fewer steps. By exploiting the advantage that the polymer chains are only bound to the surface in the unexposed regions, gold nanoparticles

were successfully assembled into specific architectural arrangements; thus, enhancing their unique properties. Finally, results are presented from samples fabricated by exposing self-assembled monolayers of 16-phosphonodecanoic acid on aluminium surfaces to 244 nm UV light. Aluminium is becoming increasingly popular due to its plasmonic response that reaches beyond visible to ultraviolet range, contrary to gold and silver. Moreover, it is non-toxic, cheap and abundant. Hitherto, aluminium nanoparticles have proven to be beneficial in a number of applications, such as enhanced fluorescence and photocatalysis. However, it is still challenging to produce aluminuim nanostructures with perfectly defined dimensions and good structural and surface quality. Consequently, in the third chapter, an attempt to fabricate controllable and reproducible aluminium nanostructures using IL is presented. As a consequence, IL together with Lloyd's mirror interferometer system has shown to be a promising approach to create uniform aluminium nanostructures.

Keywords: *plasmonic, localised surface plasmon resonance, interferometric lithography, nanofabrication, periodic nanostructure, arrays, surface topography, nanoparticles, polymer brushes, polymerisation, splitting, self-assembled monolayers, patterning, Au nanostructures, polymer nanostructures, aluminium nanostructures,*

Chapter 1

1 Introduction

Advances in nanofabrication over the past few decades, along with a better understanding of the interaction of light with matter, have paved the way for a wide range of technologies that trap or control light on surfaces. Of these technologies, the most successful developments have been made in the field of plasmonics. In response to the external and oscillating electric field, some materials (e.g. metals) exhibit a collective oscillation in their Fermi electrons, known as surface plasmons. The external electric field pulls the mobile electron plasma away from its parent nuclei, creating a Coulombic restoring force between them. At a certain frequency, this causes the electron plasma to resonate, which results in strong absorption of light at that frequency, and generates a strong electric near-field close to the surface. Accordingly, light can act as an incident electric field, and surface plasmons thus provide a mechanism for coupling light to material surfaces. Surface effects such as these, however, only occur in structures with high surface area-to-volume ratios, including nanoparticles. [1, 2]

Silver and gold colloids have been known to generate vibrant colours when mixed with glass since Roman times nearly 2000 years ago. Moreover, this property has been widely exploited for centuries to decorate church windows (i.e. stained glass). Subsequently, in the 19th century, Faraday performed the first scientific study of the colours of gold particles. [3] However, the secret behind the stained glass was not understood until Mie presented a theory explaining the optical properties of spheres in 1908. [4] According to the Mie theory, the sphere size, its dielectric function, and the refractive index of the surrounding medium are responsible for the colour of the metal nanoparticles. Despite this physical description, plasmons were only viewed as a minor feature of the metal for decades. Indeed, without the nanofabrication techniques that exist nowadays, it would be difficult to control the properties of surface plasmons. In addition, the development of metallic nanoparticle synthesis and lithographic tools in recent decades has revitalised research in plasmonics. The field now includes advances in: biosensing [5]; surface-enhanced Raman spectroscopy [6]; nanoantenna [7]; and medical diagnostics [8]; among many others exciting techniques.

1.1 Thesis Outline

This thesis consists of a literature review chapter, one chapter for experimental procedures, three chapters to present the research results, and a final chapter presenting the conclusions and recommendations of this study.

Chapter One provides an overview of the fundamental theory of surface plasmons, as well as the principle of coupling of plasmons to excitons, and the use of plasmonic nanostructures as a biosensing platform. The various approaches used to fabricate metallic nanostructures and nanoparticles with interesting properties are also reviewed. Particularly, IL is explained in more detail as the primary technique used for patterning thin metal films in this study. Chapter One also includes a discussion on the formation of self-assembled monolayers from solid surfaces, as well as the growth of polymer brushes. Chapter Two describes the experimental procedures in detail, and provides an overview of the most commonly used characterisation techniques for studying and analysing the samples. These techniques are summarised with basic working principles that provide a more detailed explanation of their importance and advantages in analysing the samples. Chapter Three then explores the role of various parameters, including Cr/ Au layer thicknesses, exposure doses, mirror angles, annealing temperatures, and others in controlling the plasmonic properties of Au nanostructures. It also provides a proof-of-concept for strong plasmon-exciton coupling using Au nanostructures. Chapter Four aims to combine nanopatterning approaches with studies of surface-grafting polymers functionalised with dyes. It also explores a new strategy to control the immobilisation of colloidal gold nanoparticles. Chapter Five explores the feasibility of replacing gold with aluminium, which also has strong plasmon absorptions, and is desirable because aluminium is cheap and abundant. Chapter Six summarises the conclusion that is able to be drawn at this stage, together with a short summary of future work.

1.2 Surface Plasmon Resonances

Surface plasmon resonances (SPRs) are evident in two forms [9]: surface plasmon polaritons (SPPs) and localised surface plasmon resonances (LSPRs); depending on the surface structure (see Figure 1.1). SPPs are electromagnetic waves that propagate along the interface between a metal and a dielectric medium. These waves are generated by the coupling of electromagnetic field to oscillations of the conduction electrons. [10] Historically, SPPs were recognised in the early 20th century in the context of radio wave propagation. In 1902, Wood discovered a pattern of dark and light bands "anomalous" in the reflected light, when he focused polarised light onto a mirror with a diffraction grating on its surface. [11] Nevertheless, the first physical explanation for this discovery was proposed by Rayleigh in 1907 [10]; and further refined by Fano in 1941 [12], which led to the conclusion that these anomalies were related to surface waves supported by the network. A detailed explanation of the phenomenon, however, did not become available until 1968, when Otto and Kretschmann reported the excitation of surface plasmons. [13]

LSPRs similar to SPPs are electromagnetic waves that originate at the interface between a dielectric and a finite-size conductor, including nanoparticles, nanoholes and other structures. In particular, the resonance frequency can be modulated by particle size, shape, composition, and local optical conditions [14], which mostly occurs in the visible and near-infrared region of the spectrum for nanostructures of noble metal, such as gold and silver. Overall, LSPRs have become an attractive alternative to SPPs in many applications, mainly because momentum matching is not required to excite LSPRs, due to their lack of translational symmetry. Further, they benefit from simple preparation methods for: metal nanoparticles (i.e. colloidal chemistry involving metal salt reduction) [15]; nanoparticle arrays (e.g. nanosphere lithography) [16]; along with their unique features and functionalities (i.e. the possibility to manipulate and transform light at the nanoscale level) [17]; subwavelength imaging [18], and improved photovoltaic devices. [19] Moreover, LSPRs have a less turbulent history, as the mathematical foundation was also established in the early 20th century by Mie (1908).

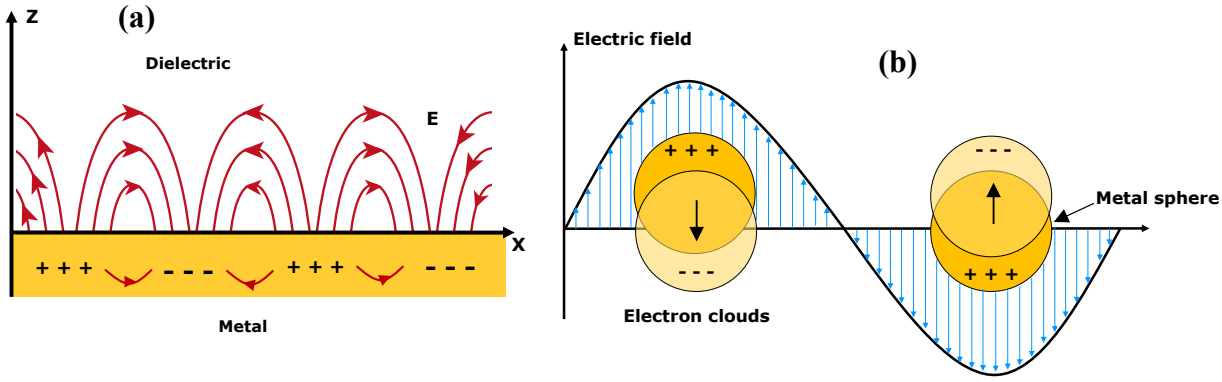

Figure 1.1. Schematic depicting: (a) propagating surface plasmons of a metal surface and (b) localised surface plasmons of a metal nanosphere.

1.3 Fundamentals of Plasmonic Metal Nanostructures

Surface plasmons, which are coherent oscillations of free electrons in a metal, have an intrinsic wave nature. This in turn requires that light be defined as an electromagnetic wave and surface plasmons be its response. In order to describe the electromagnetic wave equations and surface plasmons , Maxwell's equations must first be considered [20]:

$$\nabla \cdot \mathbf{D} = \rho \tag{1.1}$$

$$\nabla \cdot \mathbf{B} = 0 \tag{1.2}$$

$$\nabla \times \mathbf{E} = -\frac{\partial \mathbf{B}}{\partial t} \tag{1.3}$$

$$\nabla \times \mathbf{H} = \frac{\partial \mathbf{D}}{\partial t} + \boldsymbol{J} \tag{1.4}$$

The above equations connect the four macroscopic fields: **D** - the electric displacement field; **B** - the magnetic induction or magnetic flux density; **E**- the electric field; **H**- the magnetic field; ρ - the charge density; and $\boldsymbol{J}$ - the current density. The macroscopic fields **D**, **B**, **E**, and **H** are further linked via the polarisation (**P**) and the magnetisation (**M**) by:

$$\mathbf{D} = \epsilon_0 \mathbf{E} + \mathbf{P} \tag{1.5}$$

$$\mathbf{H} = \frac{1}{\mu_0} + \mathbf{B} - \mathbf{M} \tag{1.6}$$

where ϵ_0 and μ_0 are the electric permittivity and the magnetic permeability of vacuum, respectively. In case of isotropic and linear media, equations (1.5) and (2.6) could be restated as

$$\boldsymbol{D} = \epsilon_0(\,1 - x_e\,)\,\mathbf{E} = \epsilon\mathbf{E} \tag{1.7}$$

$$\mathbf{B} = \mu_0(1 - x_m)\,\mathbf{E} = \mu\mathbf{H} \tag{1.8}$$

where ϵ and μ represent the permittivity and permeability of the medium, respectively. Moreover, x_e and x_m are the electric and magnetic susceptibility of the medium where $\mathbf{P} = \epsilon_0 x_e \mathbf{E}$ and $\mathbf{M} = x_m \mathbf{H}$. Then, Maxwell equations take the form of

$$\boldsymbol{\nabla}.\mathbf{E} = \frac{\rho_{ext}}{\epsilon} \tag{1.9}$$

$$\boldsymbol{\nabla}.\mathbf{B} = 0 \tag{1.10}$$

$$\boldsymbol{\nabla} \times \mathbf{E} = -\frac{\partial \mathbf{B}}{\partial t} \tag{1.11}$$

$$\boldsymbol{\nabla} \times \mathbf{B} = \mu \boldsymbol{J_{ext}} + \mu\epsilon \frac{\partial \mathbf{E}}{\partial t} \tag{1.12}$$

In the absence of external current and charge, by solving equation 1.10 and then introducing equation 1.11 into it, we can obtain

$$\boldsymbol{\nabla} \times \boldsymbol{\nabla} \times \mathbf{E} = -\mu_0 \frac{\partial^2 \mathbf{E}}{\partial t^2} \tag{1.13}$$

Using vector identity $\boldsymbol{\nabla} \times \boldsymbol{\nabla} \times \mathbf{E} = \boldsymbol{\nabla}(\boldsymbol{\nabla}.\mathbf{E}) - \boldsymbol{\nabla^2}\mathbf{E}$ and recognising this condition ($\boldsymbol{\nabla}.\mathbf{E} = \mathbf{0}$), an electromagnetic wave equation can be formed

$$\boldsymbol{\nabla^2}.\mathbf{E} = \mu\sigma \frac{\partial^2 \mathbf{E}}{\partial t} + \mu\epsilon \frac{\partial^2 \mathbf{E}}{\partial t^2} \tag{1.14}$$

where σ is the conductivity of the metal which comes from the ohms law $\boldsymbol{J_{ext}} = \sigma\mathbf{E}$.

By assuming a harmonic form for E-field, $\mathbf{E}\,(t) = \mathbf{E}(\mathbf{r})\boldsymbol{e}^{-i\omega t}$, Helmholtz wave equation can be achieved.

$$\nabla^2.\mathbf{E} = \omega^2\mu\epsilon\mathbf{E}(\mathbf{r}) = 0 \quad (1.15)$$

in which ϵ is referred to as complex permittivity in the form of

$$\epsilon = \epsilon + \frac{i\sigma}{\omega} = 0 \quad (1.16)$$

Conductivity (σ) here is also complex, and to understand this complex behavior one must be familiar with the Drude–Sommerfeld model. In a metal, valence electrons behave like a gas of free electrons and oscillate with respect to immobile ion cores. Electron-electron and electron-ion interactions caused by collisions are ignored and collisions are considered instantaneous in the Drude-Sommerfeld model. It describes how electrons respond to an applied external field, providing information about the optical properties of metals.

Ignoring the magnetic field, we begin by taking into account the external incident light on a metal surface. The spatial variation of the field is also not considered. This is possible unless the field changes much over distances comparable with the electrons mean free path. According to the Drude mode, the equation governing the motion of an electron is [21]

$$m^* \frac{d\mathbf{v}(\mathrm{t})}{dt} = -\frac{m^*}{\tau}\,\mathrm{v}(\mathrm{t}) - \mathrm{e}\mathbf{E}(\mathrm{t}) \quad (1.17)$$

Where e and m^* denote to the charge and effective mass of electrons in a crystal, respectively. In addition, τ is the relaxation time. Assuming that the driving E-field has harmonic time dependence, $E(t) = E_0 e^{-i\omega t}$, and by substituting $\mathbf{E}(t)$ into equation (2.17), it will give the mean velocity as,

$$\mathbf{v}(t) = -\frac{e\tau}{m^*(1 - i\omega t)}\,\mathbf{E}(t) \quad (1.18)$$

which is in the form of $\mathbf{v}(t) = \mathrm{v}_0 e^{-i\omega t}$. By substituting $\mathbf{v}(t)$ into the current density equation, $\boldsymbol{J}_{ext} = -ne\mathrm{v}$, it can be obtained as:

$$\boldsymbol{J}_{ext} = \frac{ne^2\tau}{m^*(1 - i\omega t)}\,\mathbf{E}(t) \quad (1.19)$$

where n is the number of conduction electrons per unit volume. By comparing equation 1.19 with ohms law $\boldsymbol{J}_{ext} = \sigma\mathbf{E}$, conductivity is expressed as:

$$\sigma = \frac{ne^2\tau}{m^*(1 - i\omega t)} \tag{1.20}$$

By utilising the complex permittivity equation ($\epsilon = \epsilon + \frac{i\sigma}{\omega}$) derived from the Helmholtz wave equations, an expression for the complex permittivity can be given as:

$$\epsilon = \epsilon - \frac{{\omega_p}^2\epsilon_0}{\omega^2 + i\omega/\tau} \tag{1.21}$$

where ω_p is known as the plasma frequency:

$${\omega_p}^2 = \frac{ne^2}{\epsilon_0 m^*} \tag{1.22}$$

In equation 1.21, the first term is the result of the bound charges in metal and the second is the result of the free electrons. By dividing both sides of the equation, the relative complex permittivity ($\epsilon_r = \epsilon/\epsilon_0$) is obtained in the form of

$$\epsilon_r = 1 - \frac{{\omega_p}^2}{\omega^2 + i\omega/\tau} \tag{1.23}$$

For better understanding, equation 1.23 is divided into two parts, its real and imaginary parts on the form of $\epsilon_r = \epsilon_r' + i\epsilon_r''$, that gives the results,

$$\epsilon_r' = 1 - \frac{{\omega_p}^2\tau^2}{1 + \omega^2\tau^2} \tag{1.24}$$

$$\epsilon_r'' = \frac{{\omega_p}^2\tau^2}{\omega(1 + \omega^2\tau^2)} \tag{1.25}$$

For visible or shorter wavelengths $\omega\tau \gg 1$and $\tau \approx 10^{-15}s$ at room temperature [21], so ϵ_r' (real part) can be estimated as:

$$\epsilon_r' \approx 1 - \frac{{\omega_p}^2}{\omega^2} \tag{1.26}$$

For $\omega < \omega_p$, equation 1.26 becomes negative. Negative real relative permittivity makes metals highly reactive. Conversely, $\omega > \omega_p$ condition makes ϵ_r' positive and Helmholtz wave equation (1.15) give oscillatory solutions and the metal becomes transparent. Hence, the plasma frequency is the frequency at which metal becomes transparent to incoming light. The coupling of plasma to the incoming light is the simplest explanation of the generation of SPPs. The main requirement in this coupling is the resonance with plasma frequency.

The Drude-Sommerfeld model provides very accurate predictions for the optical properties of metals in the infrared regime. Nevertheless, it requires to be extended in the visible range by taking into account the response of bound electrons as well. For instance, in the case of gold, at wavelengths below 550 nm, the imaginary part of the observed dielectric function increases more significantly as stated by the Drude-Sommerfeld theory [22]. This is due to the fact that photons with higher energy can elevate electrons from lower energy bands to the conduction band. Excitation of the oscillation of bound electrons may describe such transitions, in a classical picture. The equation governing the motion of the bound electron is as follows

$$m\ddot{\boldsymbol{x}} + m\gamma\dot{\boldsymbol{x}} + m\omega_0^2\,\boldsymbol{x} = -e\boldsymbol{E} \tag{1.27}$$

here, m represents the effective mass of the bound electron, which generally differs from the effective mass of a free electron within a periodic potential, γ is the damping constant, and ω_0 is bound electron resonance frequency. By solving the equation 1.27 to model $\varepsilon_r\,(\omega)$ for metals, we arrive at the term of

$$\varepsilon_r\,(\omega) = 1 + \frac{{\omega_p}^2}{\omega_0^2 - \omega^2 - i\gamma\omega} \tag{1.28}$$

Equation 1.28 can be simplified by separating it into real and imaginary parts, leading to the following equations

$$\epsilon_r' = 1 + \frac{({\omega_0}^2 - \omega^2)\,{\omega_p}^2}{({\omega_0}^2 - \omega^2)^2 + \gamma^2\,\omega^2} \tag{1.29}$$

and

$$\epsilon_r'' = \frac{\gamma\omega{\omega_p}^2}{({\omega_0}^2 - \omega^2)^2 + \gamma^2\,\omega^2} \tag{1.30}$$

The real part of the equation shows dispersion-like behaviour, while the imaginary part shows resonant behaviour.

1.3.1 Dispersion Relation

To understand the correlation between the plasma frequency and its wavevector, we begin by deriving Helmholtz wave equations from Maxwell's equations. By solving these equations under appropriate boundary conditions, we can derive the dispersion relation. Helmholtz wave equation in the absence of external charge and current is

$$\boldsymbol{\nabla}^2.\mathbf{E} + k_0^2\,\epsilon\mathbf{E}(\boldsymbol{r}) = 0 \tag{1.31}$$

where $k_0 = \frac{\omega}{c}$ is the propagating wave vector.

Assuming a linear interface of two homogenous, non-magnetic ($(\mu = 1)$ and optically isotropic medium and with the upper material as the dielectric with dielectric constant ϵ_1 and a metal with frequency dependent complex permittivity, $\epsilon_1(\omega) = \epsilon'(\omega) + i\epsilon''(\omega)$, for the other half of the space.

Regarding the illustrated interface geometry shown in Figure 1.2, we can describe propagating waves as $\mathbf{E}(x, y, z) = \mathbf{E}(y)e^{i\beta x}$, where β refers to the wave vector in the direction of propagating and is known as the propagation constant ($\beta = k_x$). By introducing this expression into equation (2.31), it yields

$$\frac{\partial^2\mathbf{E}(\mathbf{z})}{\partial y^2} + (k_0^2\,\epsilon - \beta^2)\mathbf{E} \tag{1.32}$$

From the equation (1.18),

$$\frac{\partial \mathrm{E_z}}{\partial y} - \frac{\partial \mathrm{E}_y}{\partial z} = i\omega\mu_0 H_x \tag{1.33}$$

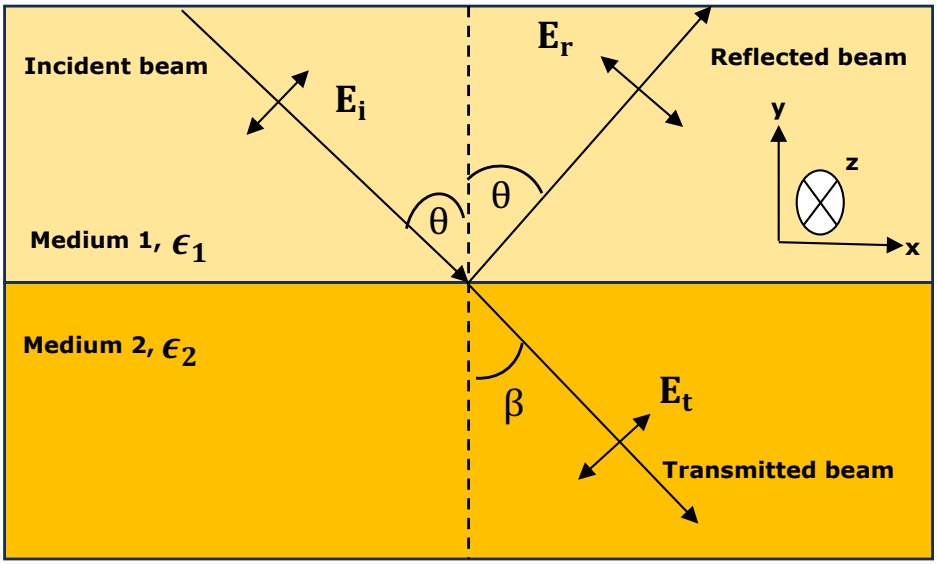

Figure 1.2. Planar interface geometry. Z-direction is into the page and propagating is in x-direction. Incident radiation is p-polarised ($\epsilon_2 > \epsilon_1$).

$$\frac{\partial \mathrm{E}_x}{\partial z} - \frac{\partial \mathrm{E}_z}{\partial x} = i\omega\mu_0 H_y \qquad 1.34$$

$$\frac{\partial \mathrm{E}_y}{\partial x} - \frac{\partial \mathrm{E}_x}{\partial y} = i\omega\mu_0 H_z \qquad 1.35$$

From the equation (1.19),

$$\frac{\partial H_z}{\partial y} - \frac{\partial \mathrm{H}_y}{\partial z} = i\omega\mu_0 E_x \qquad 1.36$$

$$\frac{\partial H_x}{\partial z} - \frac{\partial \mathrm{H}_z}{\partial x} = i\omega\mu_0 E_y \qquad 1.37$$

$$\frac{\partial H_y}{\partial z} - \frac{\partial \mathrm{H}_x}{\partial y} = i\omega\mu_0 E_z \qquad 1.38$$

Because of propagation in x-direction ($\frac{\partial}{\partial x} = i\beta$) and homogeneity in z-direction, equations (1.33) and (1.36) can be simplified to the following set of equations.

$$\frac{\partial E_z}{\partial y} = i\omega\mu_0 H_x \; and \; \frac{\partial H_z}{\partial y} = i\omega\mu_0 E_x \tag{1.39}$$

$$i\beta E_z = -i\omega\mu_0 H_y \; and \; H_z = -i\omega\mu_0 E_y \tag{1.40}$$

$$i\beta E_y - \frac{\partial E_x}{\partial y} = i\omega\mu_0 H_z \; and \; i\beta H_y - \frac{\partial H_x}{\partial y} = i\omega\mu_0 E_z \tag{1.41}$$

The equations mentioned above can be solved for both s and p polarised modes in the case of propagating waves. However, for the SPP wave, only TM modes are permissible. Thus, we will proceed with only the p-polarised equations, which means there are $E_x, E_y, and\ H_z$ components. This brings us to a similar set of equations

$$E_x = \frac{1}{\omega\epsilon_0\epsilon}\frac{\partial H_z}{\partial y} \; and \; E_z = -\frac{\mathbf{1}}{\omega\epsilon_0\epsilon} H_y \tag{1.42}$$

and the TM mode wave equation is given as,

$$\frac{\partial^2 H_z}{\partial y^2} + (k_0^2\epsilon - \beta^2)H_z = 0 \tag{1.43}$$

Once the general sets of equations for TM modes are derived, they can be solved separately for both the upper and lower regions as depicted in Figure 2.1.

TM solutions to equation set of (1.42) and (1.43) for $y < 0$ are

$$H_z(y) = A_1 e^{ik_1 y} e^{i\beta x} \tag{1.44}$$

$$E_x(y) = \frac{-A_1 k_1}{\omega\epsilon_0\epsilon_1}\, e^{ik_1 y} e^{i\beta x} \tag{1.45}$$

$$E_y(y) = \frac{-A_1 \beta_1}{\omega\epsilon_0\epsilon_1}\, e^{ik_1 y} e^{i\beta x} \tag{1.46}$$

and for y $>$ 0 are

$$H_z(y) = A_2 e^{-k_2 y} e^{i\beta x} \quad 1.47$$

$$E_x(y) = \frac{iA_2 k_2}{\omega \epsilon_0 \epsilon_2} e^{-k_2 y} e^{i\beta x} \quad 1.48$$

$$E_y(y) = \frac{-A_2 \beta}{\omega \epsilon_0 \epsilon_2} e^{-k_2 y} e^{i\beta x} \quad 1.49$$

k_1 and k_2 represent the perpendicular components of the wave vector in the y-direction at the interface of the two media. The boundary conditions and continuity at the interface lead to equations (1.44) and (1.47), resulting in $A_1 = A_1$

$$\frac{k_2}{k_1} = \frac{\epsilon_2}{\epsilon_1} \quad 1.50$$

and

$$k_1^2 = \beta^2 - k_0^2 \epsilon_1 \quad 1.51$$

$$k_2^2 = \beta^2 - k_0^2 \epsilon_2 \quad 1.52$$

Combining equation (1.50) and (1.51) yields the SPP condition.

$$\beta = k_x = k_0 \sqrt{\frac{\epsilon_1 \epsilon_2}{\epsilon_1 + \epsilon_2}} \quad 1.53$$

For Drude model in vacuum ($\epsilon_2 = 1$) equation 2.42 gives

$$k_x = \frac{\omega}{c} \sqrt{\frac{\omega^2 - \omega_p^2}{2\omega^2 - \omega_p^2}} \quad 1.54$$

To derive the dispersion relation for surface plasmons, we extract ω from equation 1.54;

$$\omega^2(k_x) = \frac{\omega_p^2}{2} + c^2k_x^2 - \sqrt{\frac{\omega_p^4}{4} + c^4k_x^4} \qquad 1.55$$

By normalising equation 1.55 with respect to ω_p, we can visualise the dispersion behaviour of SPPs (see Figure 1.3).

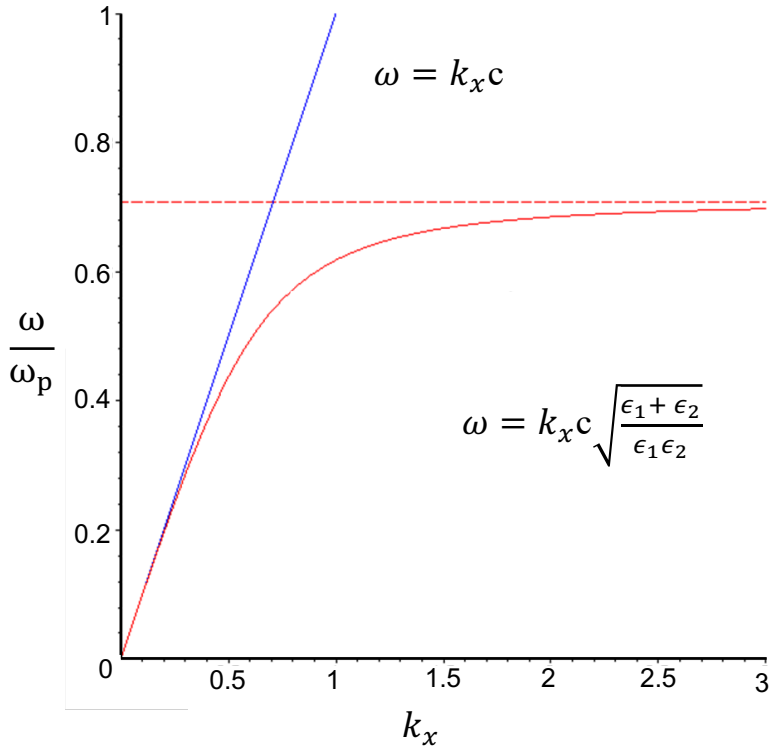

Figure 1.3. Dispersion relation of SPP.

1.4 Exciton-Plasmon Coupling Interaction

The concept of excitons was first proposed by Frenkel in 1931. [23] An exciton is a bound state of an electron and an electron hole (an empty energy state in the valence band) in a solid-state material. These electron-hole pairs are attracted to each other by electrostatic Coulomb forces, creating a quasi-particle with properties different from those of isolated electrons and holes. Excitons plays a crucial role in various phenomena, including the absorption and emission of light in semiconductor, and are essential for understanding the optical and electrical properties of these materials. [23−25] When excitons and plasmons are brought into close proximity, they can interact with each other through the electric field generated by the plasmon. [25] This interaction has a number of effects on the properties of the material. For example, the coupling leads to changes in the emission spectrum of the material, as the plasmons can modify the way that excitons emit light. Additionally, it can lead to changes in the absorption spectrum, as the plasmons can modify the way excitons absorb light. One way to describe the exciton-plasmon coupling is to consider the exciton-plasmon hybridisation, which results from the overlap of the wave functions of the excitons and plasmons. [23] This hybridisation leads to the formation of new states, which can have different energy levels and decay rates than the original exciton and plasmon states.

In general, the exciton-plasmon coupling occurs in different regimes depending on the strength of the interaction between the excitons and plasmons. When the coupling strength is weak, the system is said to be in the weak coupling regime. In this regime, the coupling strength is much smaller than the energy of the individual exciton or plasmon modes. [26] Therefore, the exciton and plasmon modes do not hybridise significantly, and the interaction between them can be described using perturbation theory. [27] In the strong coupling regime, the interaction between excitons and plasmons is strong enough to lead to the formation of new hybrid states. [26] The energy splitting between the upper and lower polariton branches can be significantly larger than the linewidth of the individual modes (also known as Rabi oscillation), indicating the strong coupling regime. [27] The strong coupling regime is of particular interest in the study of optoelectronic, as it can lead to a number of interesting phenomena, such as modifying the optical properties, enhancing the light-matter interactions, and forming new quasiparticles with unique properties. [28] Moreover, the strong regime coupling has potential applications in areas such quantum information processing, where the strong coupling can be used to generate and manipulate quantum states of light and matter. [29] In semi-conductor nanostructures, the interaction between LSPRs and excitons can lead to complementary benefits upon optical

performance, such as extending the lifetime of excitons within these materials and greatly increasing the quantum yield. [30] In addition to producing localised electromagnetic fields, metal nanostructures are able to enhance electric field intensity [31], and nonlinear effects. [32] The strong coupling can be determined by considering three parameters [27]: the rate of energy transfer between light and matter (g); the rate at which the light escapes from the system (k); and the rate at which the matter loses its polarisation (γ). When the rate of energy transfer, g, is much greater than the other two rates, ($g \gg k, \gamma$) then a strong coupling between light and matter can be achieved. The opposite order exists, where $g \ll k, \gamma$, is known as the weak coupling limit, as the light and matter trapped in the resonator do not interact more strongly with each other than with light or matter outside the system. [33] Indeed, the energy exchange between light and matter will be periodical (with a period of $2\pi/g$), for a number of periods before the energy escapes the system. The physical process involved in the transfer of energy between light and matter initially orders a coupling between dipole and the electric field. The energy, E, associated with this coupling can be calculated as follows: $E = \vec{\mu}.\vec{E}$, where $\vec{\mu}$ is the dipole moment of the matter component, and $\vec{E}$ is the vacuum electric field; the transfer rate, g, is proportional to E, where $g = E/\hbar$.

1.5 Localised Surface Plasmon Resonance as Biosensing Platform

Much of the research to date has mainly focused on fabricating nanostructures and evaluating their properties. As a result, biosensing with the LSPR platform has remained at the proof-of-concept stage. Nevertheless, a number of studies have demonstrated the potential of LSPR technology in the field of medicine. In biosensing, LSPR is used to detect small molecules. As bioreceptors (i.e., enzymes and antibodies) have dimensions less than 20 nm, which are similar to those of nanostructures, the two can be considered as structurally compatible. Therefore, it is possible to achieve highly miniaturised signal transducers by combining nanostructure characteristics, a wide range of available bioreceptors, and the rapid development of surface biofunctionalisation techniques. [34]

The initial phase in the LSPR biosensor is to form nanostructure-biomolecule conjugates. Specifically, metal nanostructures have distinct photonic, electronic, and catalytic properties. By integrating these nanostructures with biomolecules (i.e. proteins or DNA), novel platforms are able to be designed for use in a variety of biomedical applications, such as diagnosis and therapy, as well as sensing and imaging. [35] For example, significant progress has been made through the use of LSPR to detect DNA hybridisation [36]; while peptide nucleic acid-DNA

hybridisation was observed through the use of a substrate with a gold-coated nanostructure layer. [7] The optical properties of the substrate were obtained via transmission measurements, which enabled the detection of DNA at concentrations below 1 fM. In addition, ultrasensitive detection of influenza has been successfully demonstrated by LSPR analysis through antigen-antibody interaction on an Au surface. [37] In that particular study, an active immobilisation system was developed to improve the biosensing of avian influenza virus. The gold binding polypeptide (GBP)-fusion protein was attached to the gold surface by a specific interaction. Using the GBP-fusion method, proteins are able to be immobilised on the surface in bioactive forms without surface modification. Correspondingly, this method can be developed to enable the detection of clinical diseases and further protein-protein interactions.

A highly sensitive LSPR immunosensor has been proposed to recognise the presence of human immunodeficiency virus (HIV-1). [38] The surface of gold nanostructure was functionalised with HIV-1 antibody fragments to measure different concentrations of HIV-1 particles with a detection limit of 200 fg/mL detection limit. What is more, as this immunosensor produces the advantages of short preparation time, high sensitivity, and high selectivity, it has the potential to screen other viral particles. Furthermore, LSPR-based biosensors can be utilised to diagnose pregnancy-related conditions, including preeclampsia [39]; and can be also applied to detect insulin levels for diabetes. [40]. In 2020, the World Health Organization listed COVID-19 as a pandemic, as the outbreak of this deadly disease, which first appeared in China in December 2019 due to the SARS-CoV-2 virus, spread rapidly across the world, causing unpredictable and devastating health, social, and economic consequences. [41] This, in turn, created an active research atmosphere in its associated diagnostics and medical treatments. For instance, the plasmonic biosensor platform, which provides highly sensitive devices, played a significant role in the detection of SARS-CoV2. As a consequence, a number of studies have been published. Funari et al. [42] developed an opto-microfluidic system using gold nanoparticles and based on LSPR for the detection of antibodies specific to SARS-CoV2 S-protein. In this study, diluted blood plasma samples taken from patients were used to test the feasibility of the sensor. The efficiency of the proposed sensor was subsequently compared with the current conventional serological assays. The comparison showed that the proposed sensor is able to quantitatively detect SARS-CoV2 antibodies in less than 30 minutes, which is faster than most conventional detection methods that use only 1μL of plasma.

Another group has developed a low-cost plasmon nanoarray SPR chip that is integrated into a generic microplate reader without requiring a prism or other optical coupling to excite SPPs. [43] The functionalisation of the gold nanoparticles was achieved by immobilising the ACE2

receptors to specifically bind to the SARS-CoV2 S-protein. Consequently, the portable sensor is capable of detecting a quantity as low as 30 virus particles in less than 15 min. The authors stated that based on the characteristic spectral changes that were found, it became possible to detect the virus using SPR with high sensitivity. [43] In another study, a detection technique based on the plasmonic photothermal effect (PPT) and LSPR phenomenon was also fabricated to recognise viral sequences of SARS-CoV2. [44] Additionally, the gold nanoislands sensing layer is integrated with complementary DNA receptors, which provide sensitive detection by nucleic acid hybridisation. LSPR sensing is affected by the absence of the PPT unit; thus, PPT improves the hybridisation kinetics of viral DNA.

1.6 Plasmonic Metals

1.6.1 Silver

Silver is the most straightforward plasmonic material to understand, as it is perfectly modelled by the Drude model. Of all the metals, silver is the most electrically conductive, and there are no strong inter-band transitions in the visible electron ($\sigma = 6.30 \times 10^7$ S/m). As a result, silver has the lowest damping for plasmonic applications. The downside of silver is that it tends to oxidise, which leads to a gradual decay in resonance quality and limits its applications in ambient environments. [45, 46]

1.6.2 Gold

Gold has a high conductivity and exceptional inertness which makes it highly valuable ($\sigma = 4.11 \times 10^7$ S/m). For some applications, gold is also preferred, due to its surface chemistry and biocompatibility. However, as can be predicated from its colour, gold has an inter-band transition in the visible region of the spectrum, at approximately 470 nm, and more so in the ultraviolet, at around 325 nm. [45, 47] This results in an increase in damping near these wavelengths when compared to silver, which increases the imaginary component of the dielectric function. Correspondingly, gold is used for plasmonic resonances with wavelengths > 600 nm because of these interband transitions. In this region the damping is smaller, and gold becomes close to a 'perfect' metal. [47]

1.6.3 Copper

The plasmonic properties of copper are similar to those of gold, and its colour also indicates that it has inter-band transitions towards the blue end of the visible spectrum. The conductivity of copper is greater than that of gold ($\sigma = 5.96 \times 10^7$ S/m), and it is also cheaper than gold and silver. However, copper suffers from rapid oxidation when exposed to air, which limits its effectiveness in plasmonic applications. Nevertheless, it can be protected from oxidation by coating with a layer of graphene, which maintains its plasmonic properties. [48, 49]

1.6.4 Aluminium

Compared to conventional metals, aluminium is an interesting candidate for use as a plasmonic material, as it has some advantages over gold and silver. It is much less expensive and more readily available than those two particular metals, which greatly reduces the potential cost of any future plasmonic devices. Moreover, aluminium is more widely used in complementary

metal-oxide semiconductor (CMOS) technology, and thus, integrating aluminium plasmonic devices into such a form of technology is likely to be easier and more efficient. Aluminium's ability to support surface plasmons at a wide range of frequencies is one of its major advantages for plasmonics. [50]

Silver and gold are limited in the maximum energy of the plasmon they support, as both are limited by the beginning of their inter-band transition energies, which physically leads to a sharp increase in the value of the imaginary component of the complex dielectric function, away from the low values required to support resonances. The energy put into gold and silver following their inter-band transition is utilised to excite electrons between band states. For aluminium, the inter-band transition occurs within a narrow range, between 750 nm and 850 nm, which makes it capable of supporting LSPRs across most of the visible spectrum and, importantly, in the ultraviolet regions. Nevertheless, in the visible region, aluminium suffers from greater optical losses than noble metals, and this is due to the greater scattering of free electrons in the material, which limits its application range; Its conductivity is $(\sigma) = 3.77 \times 10^7$ S/m. [51−53]

1.6.5 Other Plasmonic Metals

There are many other metals that support surface plasmon resonances, including alkali metals, such as potassium, sodium and lithium, as well as platinum, nickel and palladium. [54] These metals mainly suffer from high losses and are therefore used only in cases where they provide some other useful properties, such as catalysis. [52]

1.7 Metallic Nanoparticles: Top-down and Bottom-up Approaches

For the synthesis of metallic nanoparticles, two distinct methods are used. The first is referred to as the top-down approach, while the second method is the bottom-up approach (see Figure 1.4). [55] The top-down approach involves the synthesis of nanoparticles starting with a large piece of material, which is scaled down to nanometres after a series of operations. [56] The most common examples of the top-down approach are etching through the mask, ball milling, and lithographic techniques such as electron beam lithography, etc. The process of lithography, for example, involves patterning a surface by exposing it to light, ions, or electrons, followed by etching and depositing the material onto that surface to achieve the desired structure. [57] Specifically, One of the main features of the top-down approach to the fabrication of metallic nanostructures is the fact that all of their parts are fabricated in such an orderly fashion that no additional assembly is required. Comparatively, the main disadvantages of these techniques are that they require large installations and huge capital to build their setups, which makes them very expensive.

In contrast, the bottom-up approach involves the assembly of small units (atoms or molecules) until the desired nanostructures are formed. [58] Typical examples of this approach include the formation of nanoparticles from colloidal dispersion, as well as physical and chemical vapour deposition, etc. [58] The formation of nanoparticles includes two main steps [56]: firstly, the metal precursor, which is usually an aqueous solution, is reduced to nanoparticles via a specific reducing agent such as citrate; while, secondly, the nanoparticles are stabilised by a capping agent, which in turn prevents the agglomeration of the particles. [58] Overall, the bottom-up methods are much cheaper than top-down methods. In this section, lithographic techniques and the formation of gold nanoparticles from colloidal dispersion are discussed.

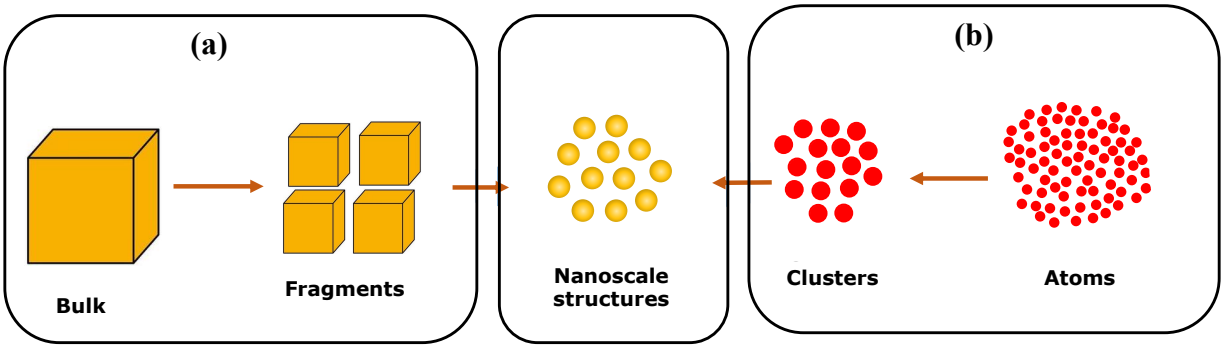

Figure 1.4. (a) Top-down and (b) bottom-up methods for synthesising metallic nanoparticles.

1.7.1 Lithographic Fabrication of Plasmonic Nanostructures

The origins of the use of lithography can be traced back to the 17th century, when Senefelder succeeded in transferring a pattern from a stone to a piece of paper. [59] Nowadays, lithography techniques and applications have been diversified, although the original concept is still valid. lithographic techniques can be classified into different categories from varied perspectives; the most common strategy is to separate them as a function of the interface utilised to define the features. Therefore, surface patterning can be achieved through masked lithography, maskless lithography (i.e. direct writing) and mold processing. [60] Other classifications focus on the use (or not) of resist: resist-based versus resistless processes.

Masked lithography is a lithographic process in which a photosensitive layer is exposed to light through a mask, leaving mask geometries on the exposed surface. Examples of this type are nanoimprint lithography [61], soft lithography [62], and photolithography. [63] Comparatively, maskless lithography is a lithographic process in which no mask is required to create the final pattern, such as focused ion beam lithography [64], electron beam lithography [65], and scanning probe lithography. [66] These techniques enable ultra-high-resolution patterning of arbitrary shapes with minimum feature dimensions of a few nanometres, while they have also been used to fabricate masks for masked lithography techniques. In this section, some of the most commonly used techniques are reviewed.

1.7.1.1 Electron Beam Lithography

Electron-beam lithography (e-beam lithography or EBL) is one of the most flexible techniques that can undertake the realisation of submicronic devices, and thus, is suited to nanofabrication and the production of masks for other lithographic techniques. EBL uses a modified scanning electron microscope (SEM) to draw a custom nanoscale pattern by means of a focused electron beam on an electron-sensitive resist. [67] It was first developed in 1967 and has continued to undergo technical developments to achieve higher spatial resolution. [67] Nowadays, EBL enables users to create high-resolution patterns at 10 nm, as well as even lower. [68] EBL is similar in principle to conventional lithography, which consists of three steps: exposing the sample surface; developing the exposed area; and finally transferring the pattern. Within the EBL system, there are two basic processes included: projection printing and direct writing (see Figure 1.5). [65] The main difference between these schemes is that projection printing utilises a relatively larger-sized electron beam projected in parallel through a mask onto a resist-coated substrate by using a high-resolution lens system; while comparatively, in direct writing, a small

spot of the electron beam is utilised to draw the shape of the patterns directly onto resist coated substrate, eliminating the high cost and time involved in producing masks. Direct EBL writing can also be classified, depending on the beam utilised, into two subcategories: the Gaussian electron-beam system, which is commonly utilised for its flexibility and fine spatial resolution; and the shaped electron-beam system. [69] In the direct EBL writing system, a fine electron beam is projected onto a surface that is covered with an electron-sensitive resist. The electron beam is directed either by raster scanning or vector scanning, which is controlled with a blanker to switch the beam on and off. Once the patterns are transferred on to the resist (depending on the form of resist - positive or negative) the exposed region of the resist is etched using a developer. Overall, EBL provides higher patterning resolution due to the shorter wavelength associated with the 10 –100 keV electrons involved. [70] EBL requires a long processing time to complete the transfer of patterns to the resist, as the electron beam is focused on a single point of the patterns at one time. This, along with the high operating costs of the technique, limits its use for commercial purposes. [67, 71]

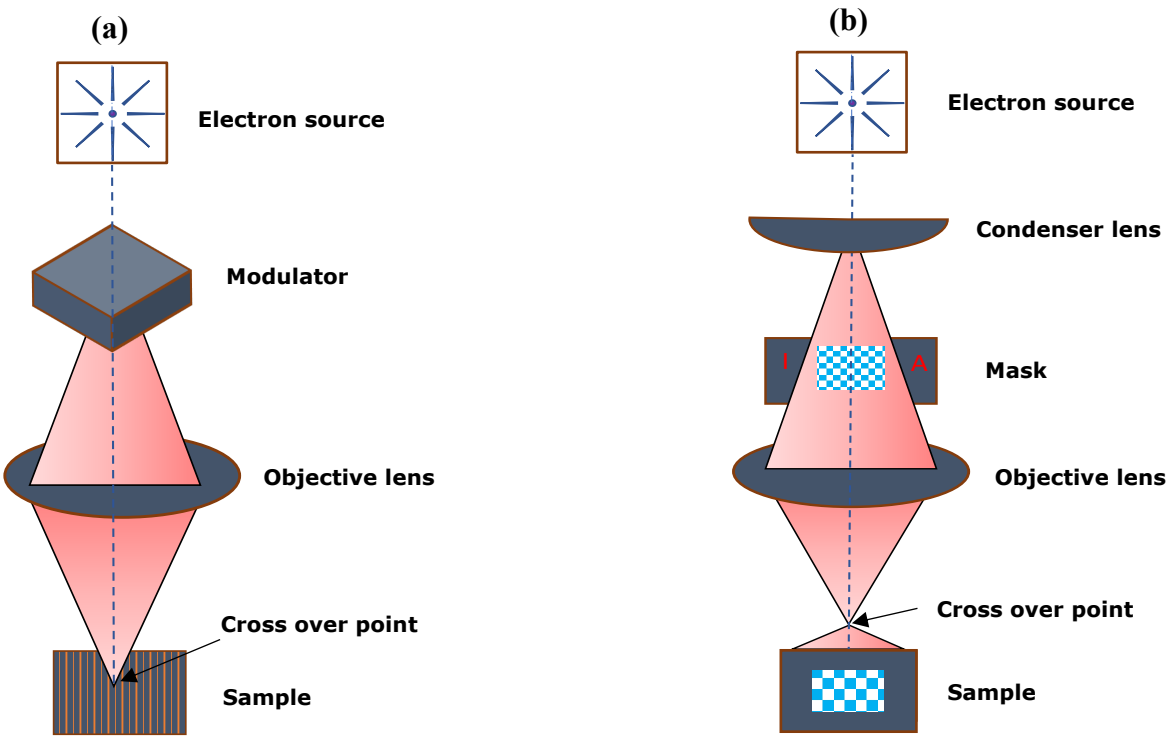

Figure 1.5. A schematic diagram illustrating the process of (a) direct writing and (b) projection printing.

1.7.1.2 Focused Ion Beam Lithography

Focused ion beam lithography (FIBL) is another nanofabrication technique that is similar to EBL lithography, however, an accelerated ion beam is used to achieve lithography, instead of an electron beam. FIBL provides higher resolution patterning than EBL, as the ions used are heavier than electrons, which provides the ion beam with a smaller wavelength. [72] The FIBL system creates a stream of high-energy ionised atoms of a relatively large element and focuses them onto the sample surface for the purpose of milling, imaging, etching, or deposition of the materials. [73] FIBL relies on heavy ions, such as gallium (Ga^+) and helium (He^+) for direct nanopatterns, enabling a stable and fine beam [74]; while FIBL columns are combined with scanning electron microscope (SEM) to ensure vision and writing simultaneously. Electrons used in EBL have larger Debroglie wavelengths and enlarged beam sizes due to scattering, while the heavy ions in FIBL have a lower penetration depth, which reduces the aspect ratio of the nanostructures. [75] FIBL utilises higher energies of about 100−200 keV to direct the ion beam and increase the energy deposition rates on the resist, resulting in a higher exposure sensitivity. [73] Similar to the EBL, throughput and large-area fabrication remain a challenge for the FIBL system.

1.7.1.3 Nanosphere Lithography

Nanosphere lithography (NSL), also known as colloidal lithography, is a flexible, inexpensive microfabrication technique for a large variety of 2D nanostructures. In NSL, spherical colloids are deposited on a substrate and dried to form a hexagonally closed pack (HCP) monolayer [67], which can be transferred to the substrate using various methods, including spin coating [76]; dip coating [77]; and Langmuir-Blodgett coating. [78] This HCP monolayer is utilised as a mask and post-processing steps are performed to fabricate different nanostructure arrays. [79] The material is deposited through organised gaps in the mask created by the layer of spheres before the mask is removed leaving an ordered array of nanostructures on the substrate surface. The size and geometry of the nanostructures can be controlled by changing the bead size. The NSL system is a hybrid of two approaches (top-down and bottom-up), which enables flexible fabrication. [80] A potential drawback of this technique is that, as the HCP monolayer is used as a mask for the lithography process, the shape and size of the angstrom scale nanostructure features are limited; thus, it is difficult to produce nanostructures with versatile geometries and features.

1.7.1.4 Photolithography

Photolithography (PL), also known as optical lithography, is a microfabrication process that uses ultraviolet light to pattern a photosensitive layer deposited on the surface of a substrate. In this process, an optical mask is positioned above the photoresist to block exposure to specific areas, in order for only unmasked areas to be exposed to ultraviolet light. [81] Subsequently, the geometric pattern in the photoresist is revealed when the unprocessed areas are removed with an appropriate organic or aqueous solvent. In general, the PL process requires three basic materials: the light source; the photo mask; and the photosensitive material (photoresist). [82] Thus, the patterns are formed by exposing the photosensitive material to light, which results in a chemical change in the solubility, allowing some of the photoresist to be removed by a special solution known as the "developer". The photosensitive material is either positive or negative (see Figure 1.6). [83] The positive resist is a photoresist in which the exposed region is soluble in the developer, while the unexposed region remains on the surface. Conversely, with negative photoresist, the unexposed region is soluble in the developer, while the exposed region remains insoluble. The remaining resist is often baked, and the pattern is transferred onto the substrate using either wet or dry etching methods. [84] PL has been a practical technique for fabricating microstructures, as it is capable of producing patterns as small as a few tens of nanometres in size. The main challenge with this technique, nonetheless, is to reduce the minimum feature sizes and increase the aspect ratio of the features that can be fabricated. In addition, it is not effective in producing non-flat shapes, and it requires very clean operating conditions.

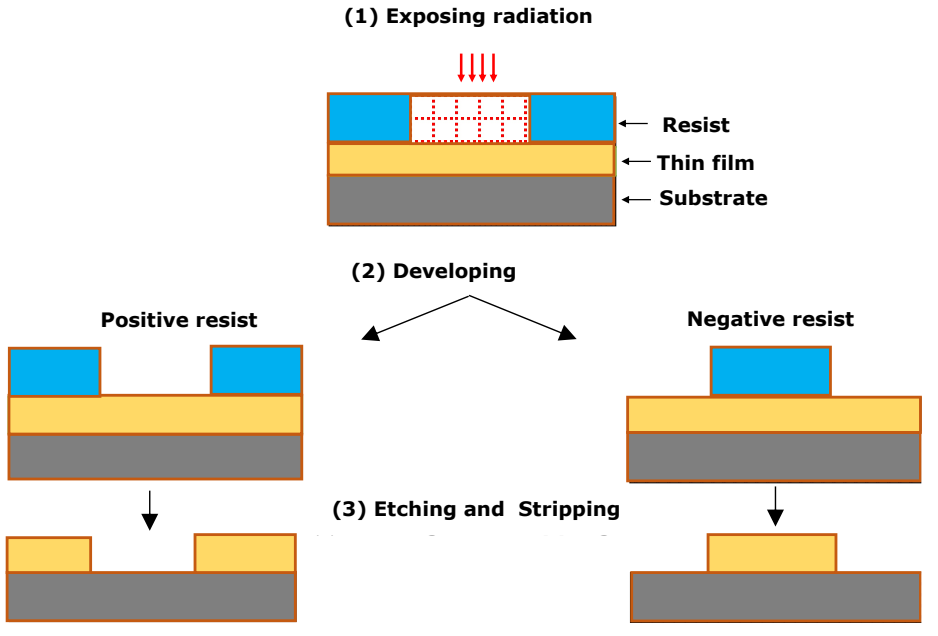

Figure 1.6. Sequential steps in transferring a pattern to the surface.

1.7.1.5 Interferometric Lithography

Interferometric or interference lithography (IL) is a powerful technique used in nanofabrication to create periodic patterns or structures with submicron or nanoscale resolution. It is a form of photolithography that uses the interference patterns of light waves to generate high-resolution patterns on a photosensitive material. When two waves meet, they superimpose, resulting in a phenomenon called interference. Interference occurs due to the superposition of the electric and magnetic fields of the two waves. In interference, two important concepts come into play: constructive and destructive interference (see Figure 1.7). Constructive interference occurs when two waves combine to reinforce each other, resulting in a wave with a larger amplitude. In contrast, destructive interference occurs when the waves out of phase, cancelling each other out and resulting in a wave with reduced or zero amplitude. Therefore, the phase difference is a critical factor in determining whether constructive or destructive interference will occur. The phase difference represents the relative shift between the crests and troughs of the waves. When the phase difference is zero or an integer multiple of 2π (complete cycles), the waves are said to be in phase and experience constructive interference, whereas if the phase difference is an odd multiple of π, the waves are out of phase and undergo destructive interference. [85−87]
IL has the advantage that it does not require a photomask to draw a pattern on the photoresist as in conventional lithography, allowing patterns of different sizes and shapes to be created. Meanwhile, the resolution of the feature size is not limited to the diffraction of light typically seen with mask lithography. It is only limited by the wavelength of light used. [88] As a result, its resolution is much higher than that of photolithography, and a period of 150 nm can be easily achieved. [89] Indeed, IL is often used to fabricate masks for other techniques, such as micro-contact printing. [90]

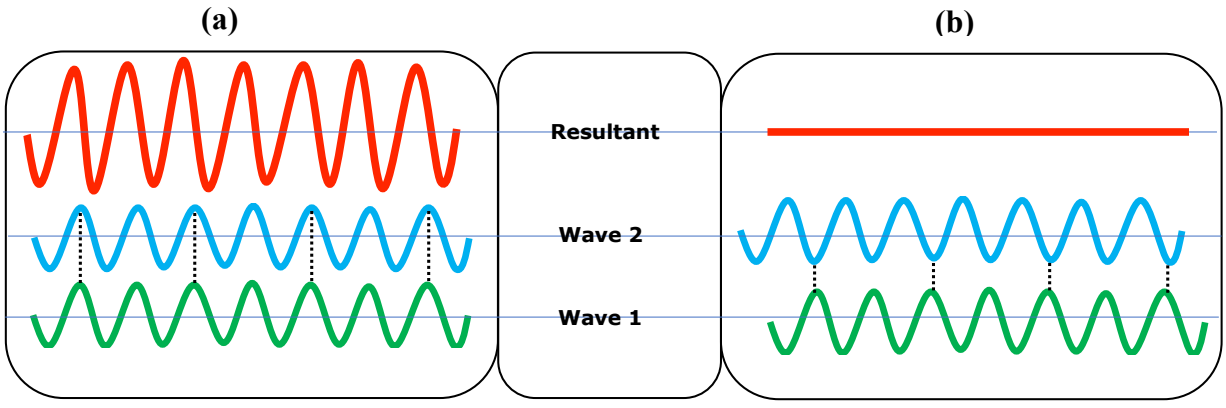

Figure 1.7. Wave interference: (a) constructive and (b) destructive.

There are certain limitations associated with this technique, however, as not all shapes can be fabricated, and the minimum period of nanostructures is limited to half the wavelength of light. This in turn necessitates the use of deep ultraviolet light for smaller features [67], which makes it expensive. While for a large exposure area, IL requires a laser source with long coherence length. [88] Generally, two optical configurations are utilised for IL: two-beam and multi-beam interferometry.

1.7.1.5.1 Two-beam Interference

In the two-beam interference, two plane wavefronts overlap to generate line interference fringe patterns on a substrate surface supported by a thin photoresist layer (see Figure 1.8). In a simple two beam IL system, the main laser beam is split into two sub-beams. The resulting periodicity of the interference fringes can be expressed as follows [85]:

$$p = \frac{\lambda}{2\sin(\theta)} \qquad 1.56$$

where p is the periodicity (or pitch), λ is the wavelength of the laser, and θ is the angle of the incident beam on the surface.

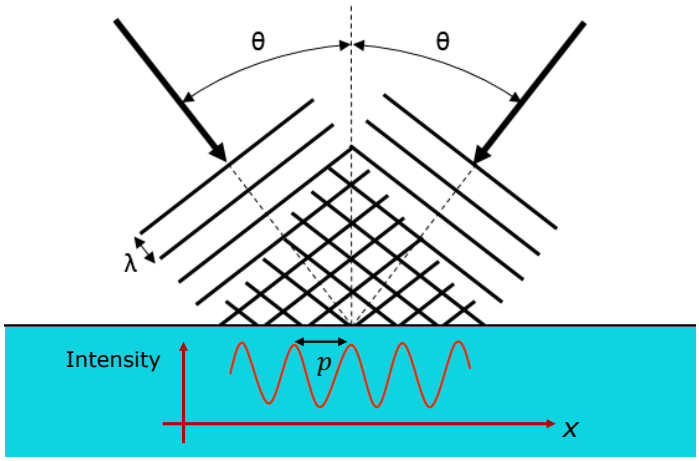

Figure 1.8. Interference of two linearly polarised waves with an angle θ and periodicity traveling along the x direction.

Splitting the main laser beam into two sub-beams can be achieved using two common methods: division of amplitude and division of wavefront. [91−94] In the division of amplitude, a beam splitter is utilised to split the incoming laser beam into two sub-beams based on the principle of partial reflection and transmission. The beam splitter is typically a partially reflective mirror that allows a portion of the incident laser beam to pass through while reflecting the remaining portion. Consequently, the transmitted beam and the reflected beam form the two sub-beams. Figure 1.9a demonstrates an example of this type, where the main laser beam is divided into two sub-beams by a beam splitter, and the sub-beams are controlled by mirrors to generate interference fringes on the surface of the substrate. One advantage of this configuration is its flexibility in optical arrangement; a large-scale diffraction grating can be easily fabricated by expanding the two sub-beams using a beam expander. This configuration, nevertheless, is weak against external perturbations, as the optical paths of the two sub-beams are long. This issue can be addressed through the use of active control techniques for optical phase-stabilisation [95]; however, this makes the overall setup more complicated.

In the division of wavefront, the laser beam is split into two sub-beams based on the wavefront characteristics; the wavefront splitter uses the principle of interference to split the wavefront into two components. This can be achieved through techniques such as the use of Fresnel biprism, Fresnel mirrors, and Lloyd's mirror. [96] Figure 1.9b shows an example of the optical configuration based on the division of wavefront method, which is referred to as Lloyd's mirror interferometer. [97]

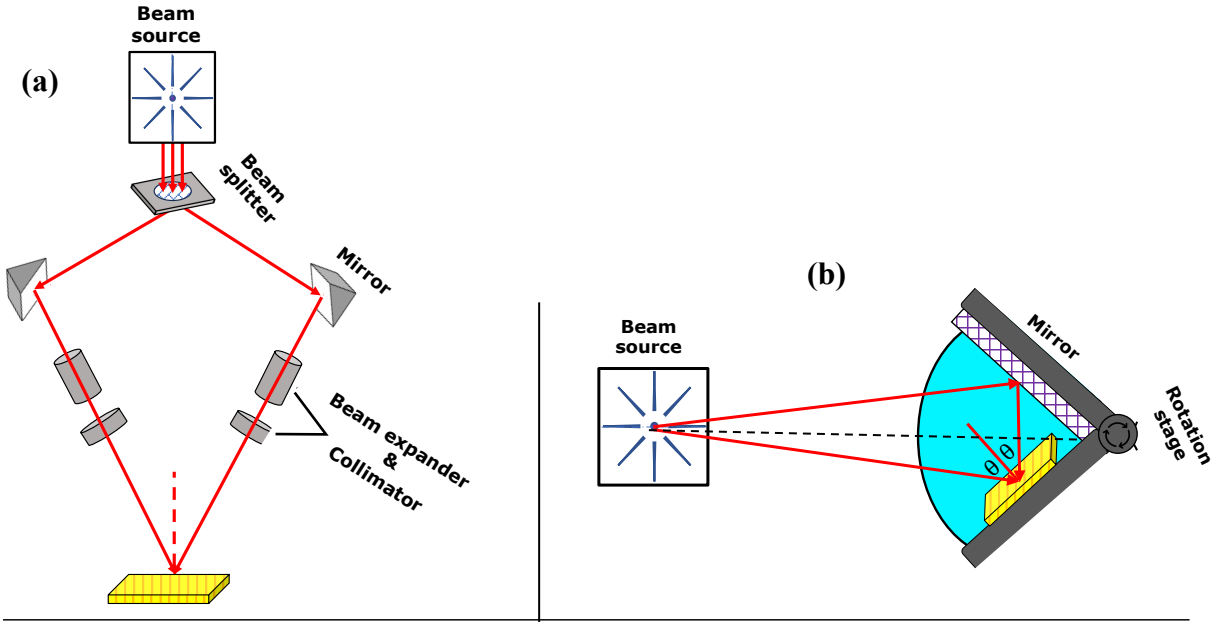

Figure 1.9. Optical configurations of IL: (a) with a beam splitter and (b) with a Lloyd's mirror.

The Lloyd's mirror is composed of a laser with a long coherent gaussian, a lens, a pinhole, and a mirror. The mirror is placed perpendicular to the sample stage to reflect the incident beam. The lens and pinhole are placed into the beam path to create a diverging beam. In this setup, as shown in Figure 1.9b, half of the laser beam is focused directly on the sample surface, while simultaneously, the other half of the laser beam is focused on the mirror, which is reflected and interfered with the other half of the beam on the sample surface. This results in a sinusoidal interference pattern and is caused by the constructive and destructive interference between the direct incident beam and the beam reflected from the mirror. The main feature of the Lloyd's mirror setup is that the sample and the mirror are fixed on the same rigid fixture. As a result, it is less susceptible to vibrations than a traditional setup with a beam splitter and separate optical components. The final pitch of the resulting pattern can also be changed very easily by rotating the sample stage and changing the angle θ. For example, using a range of incidence angles from 5° to 85° with a laser wavelength of 532 nm yields patterns with pitches from 3 μm to 270 nm. [98] On the other hand, the sample size can be determined by the overlapping area; for instance, in the case of small incidence angles, the total overlapping area is reduced in the horizontal direction, as the size of the beam reflected from the mirror is proportional to sin (θ) [99]

1.7.1.5.2 Multi-beam Interference

In the case of multi-beam interference, most of the sub-beams are generated from a single main laser beam. Both methods, the division of amplitude and the division of wavefront, can be used to generate multi-beam interference. Figure 1.10a shows an optical setup based on the division of the amplitude method, where a diffractive beam splitter (DBS) is used to split the main beam into multiple diffracted beams, and some of which are selected as sub-beams by an aperture to form interference patterns on the surface. [100] Figure 1.10b presents an example of an optical configuration based on the division of the wavefront method, which is referred to as two-axis Lloyd's mirror interferometer. In this setup, a second mirror is added to the conventional one-axis Lloyd's mirror interferometer, whilst both mirrors are positioned perpendicular to the sample stage with the angle between the mirror is adjusted to be 120°. The direct beam and the two sub-beams reflected from the mirrors interfere with each other on the sample surface to produce hexagonal interference patterns. [97, 101]

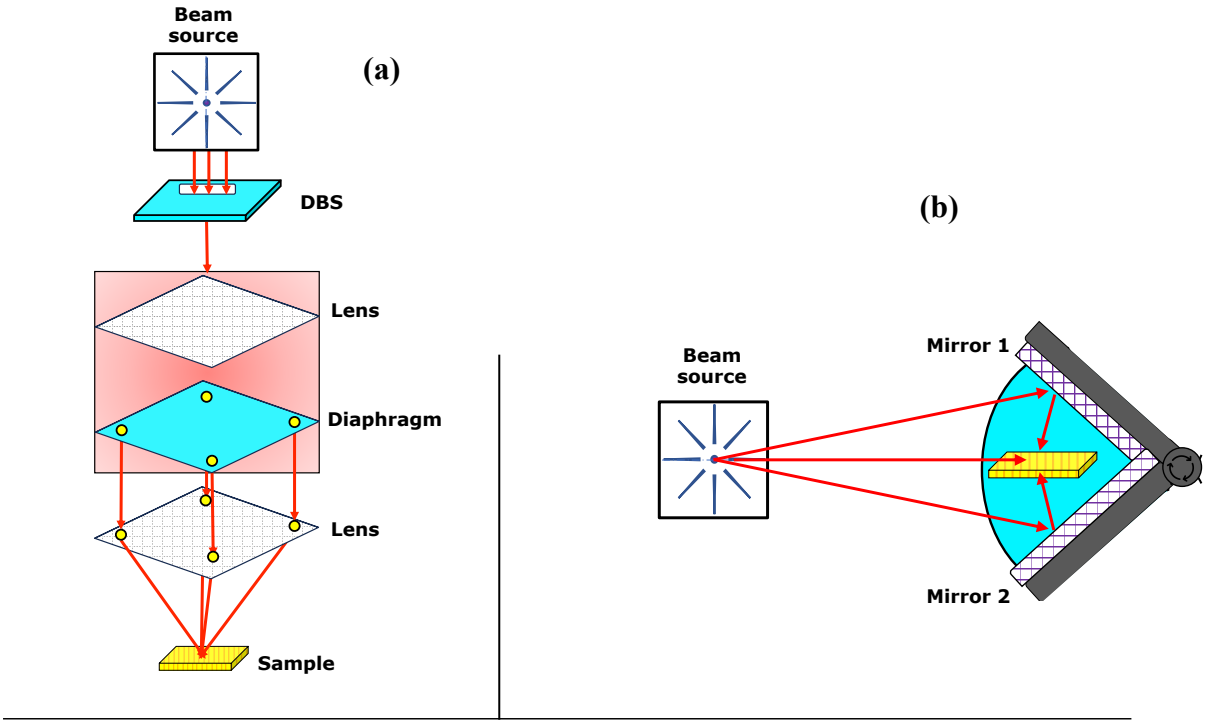

Figure 1.10. Multi-beam configuration: (a) with a DBS splitter and (b) with a Lloyd's mirror.

1.7.2 Synthetic Methods for Gold Nanoparticles

1.7.2.1 Turkevich Method

This method was initially introduced by Turkevich in 1951 [102] and is one of the most widely used methods for synthesising spherical gold nanoparticles (AuNPs) in the size range between 10 and 20 nm. The basic principle of Turkevich's method is based on the reduction of gold ions (Au^{3+}) to gold atoms (Au^{0}) using reducing agents, such as citrate [103], amino acids [104], or UV light. [105] In 1973, Frens [106] reported that by controlling the ratio of the reducing / stabilising agent (trisodium citrate/ gold), AuNPs with diameters ranging from 116 to 147 nm could be obtained. It was also reported that a higher citrate concentration stabilises small-sized AuNPs more quickly, while a lower concentration of citrate causes small particles to aggregate into larger particles. Recently, the role of pH, temperature, and trisodium citrate concentration in controlling the size of the nanoparticles has been better understood by a theoretical model and experimental results. [107−109]

1.7.2.2 Brust Method

Another Method that has also been reported for the synthesis of AuNPs is the Brust method, which was initially reported by Brust in 1994 [110] and involves a two-phase reaction to prepare AuNPs with diameters ranging from 1.5 to 5.2 nm using organic solvents. The Brust method is based on transferring a gold salt from an aqueous solution to an organic solvent (i.e., toluene) via a phase transfer agent, such as tetraoctylammonium bromide (TOAB). The gold is then reduced with sodium borohydride ($NaBH_4$) in presence of an alkanethiol, which stabilised the AuNPs [111], resulting in a colour change from orange to deep brown.

1.7.2.3 Seeded Growth Method

The two methods mentioned above are only capable of producing spherical-shaped AuNPs; however, AuNPs can be formed into different shapes, such as rods [112], cubes [113], tubes [114], etc. One of the most widely used methods for generating AuNPs in other forms is seed-mediated growth. [115] The main concept behind this method is to prepare the seed particles by reducing the gold salts with a strong reducing agent, such as $NaBH_4$. The prepared seed particles are then added to the metal salt solution in presence of a weak reducing agent, such as ascorbic acid, which prevents further nucleation and accelerates the synthesis of rod-shaped AuNPs. Thus, the particle size of AuNPs can be controlled by changing the seed concentration, reducing agents and structure directing agents.

1.8 Self-Assembled Monolayers

Self-assembled monolayers (SAMs) are referred to as well-organised molecular assemblies; they are formed spontaneously on a solid surface by the adsorption of molecules from solutions or from the gas phase. [116] Molecules that make SAMs typically consist of three main parts. Firstly, there is a headgroup that links to the substrate surface, where the molecules bind to the surface through an interaction between the headgroup and the substrate to form a chemical bond. There are a variety of headgroups that bind to specific surfaces, such as metallic surfaces, metal oxides, and semiconductors. For example, thiols bind to gold surface via a S−Au bond, carboxylic acids bind to silver surfaces via an ionic COO^{-} Ag^{+} bond, and organosilanes bind to hydroxylated surfaces via a Si−O bond. Secondly, a backbone connects the headgroup and the tailgroup, and this part controls the intermolecular interaction and molecular orientation. The backbone can provide a well-defined thickness, which can affect the electronic conduction. Thirdly, there is a tailgroup that forms the outer surface of the film (see Figure 1.11).

Understanding the self-assembly process is essential in the process to building well-ordered SAMs. The self-assembled process has been studied extensively for SAMs of alkanethiols on gold. In general, there are two distinct stages to the process. In the first stage, the headgroup of the molecules binds to the surface within a few minutes of adsorption. As a consequence, approximately 80% of the gold's surface is covered with alkanethiols; although it is very difficult to determine the assembly process in the solution. Specifically, Yamada [117] and Sylvain [118] observed an organised assembly of alkanethiol molecules on a flat surface using in-situ scanning probe microscopy. With increasing surface coverage, islands are formed along the domain boundary of the striped structure, as a result of the transformation of molecules into a standing configuration, due to the lateral pressure.

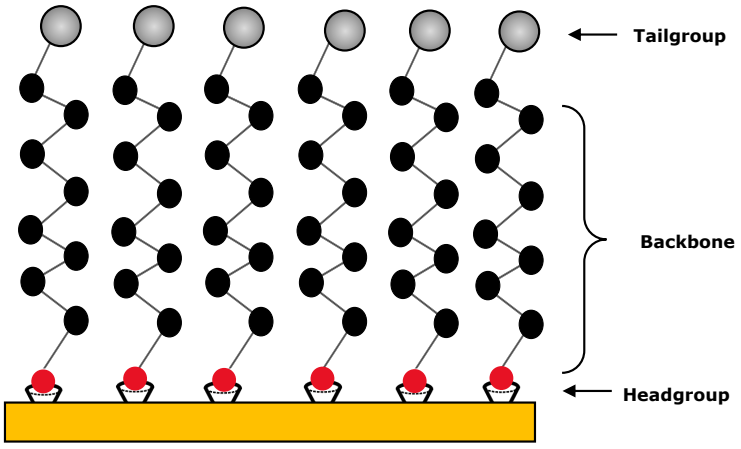

Figure 1.11. Schematic diagram depicting a monolayer structure.

In the second stage, which lasts a few hours, the islands continue to grow until the substrate surface reaches a saturation point. At this stage, the molecules arrange themselves to achieve equilibrium, resulting in an ordered film. The arrangement of the molecules on the substrate surface arises from the enhancement of the lateral interaction between the molecular moieties (i.e. intermolecular van der Waals interaction). However, the final structure involves the balance between the headgroup-surface interaction that arises in the initial stage and the intermolecular interaction that arises in the final stage. The interaction between the headgroup and the surface is the strongest interactions [119]; this strong interaction causes molecules to bind at a specific site on the substrate surface. For alkanethiol SAMs on gold substrates, the energy involved in the S−Au interaction is approximately 190 kJ/mol. [120] Consequently, as a result of this strong interaction, the molecules will occupy every available surface area. The self-assembly approach allows the possibility to achieve well-defined molecular films with tailored properties. Originally, the first SAMs of organosilicon (octadecyltrichlorosilane) on hydroxylated surface were reported by Sagiv. [121] For these SAMs, the Si headgroup releases all the Cl atoms upon interaction with the OH groups on the substrate and forms as a Si−O bond to the surface and a network of Si−O−Si bonds between the molecules. This enables the molecules to bind to the surface as well as to each other (see Figure 1.12a). This type of system can be used to build multiple layers. By modifying the tailgroups of the SAM components to hydroxyl groups that form a hydroxylated surface, another layer of OTS can be obtained (see Figure 1. 12b).

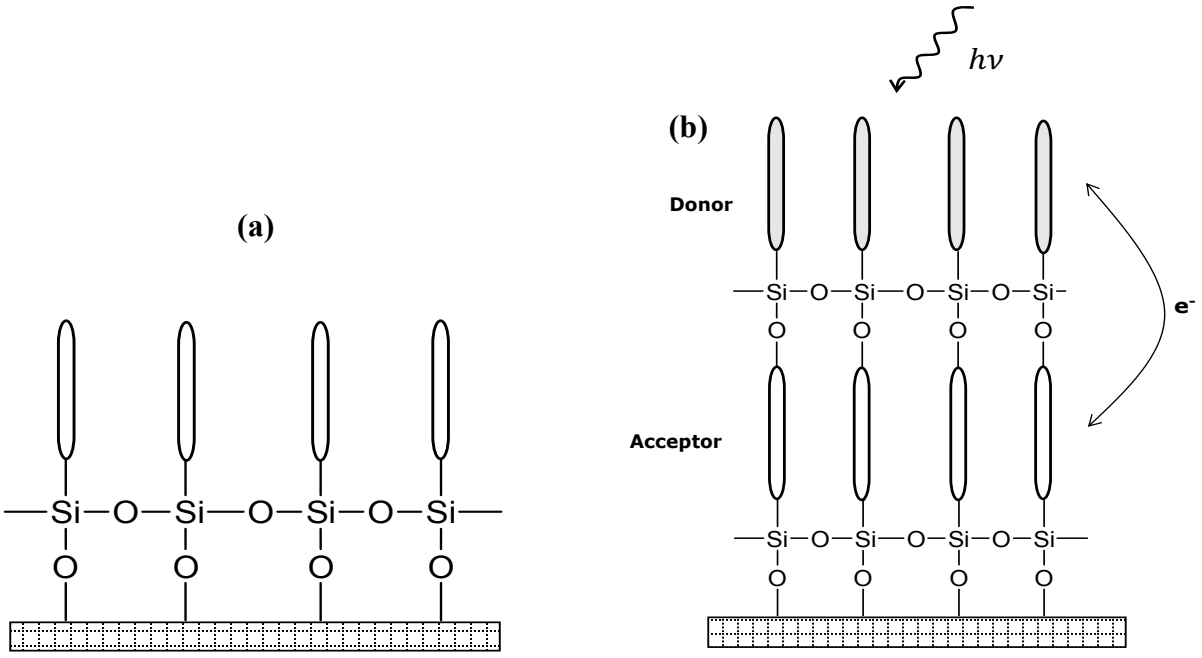

Figure 1.12. (a) SAMs of organochlrosilane and (b) Multilayer of organochlorosilane.

It can be observed that the multilayer consisting of electron donor and acceptor groups that are spaced at a well-defined distance from each other can enable the charge transfer. Nevertheless, this type of SAMs is very sensitive to preparation conditions, including immersion time and temperature. [122, 123]

The most studied type of SAMs is based on the adsorption of thiol (−SH) molecules onto metal surfaces. The thiol headgroup is a functional group that forms a strong interaction with noble metals. [124, 125] Therefore, it is possible to use thiol molecules to create well-ordered SAMs on gold and silver surfaces. Apart from thiols, selenol (−SeH) is another headgroup that is able to be used as a substitute for thiols, as it has the same chemical properties as thiols. It has been reported that selenol compounds create SAMs on silver and gold substrates. [126, 127] It was observed that the packing density and molecular orientation of the alkaneselonate SAMs on Au(111) were similar to those of alkanethiols, but alkaneselonates possess high toxicity [128]. Other systems, such as phosphonic acids, are somewhat less well-characterised compared to thiol and silane, but have become of great practical interest due to their ability to form SAMs on a range of metal oxide surfaces. [129] Additionally, the lack of a hydrolysable P−O−C link allows phosphonates to be more stable in aqueous solution and easier to generate SAMs with organophosphates; phosphonates and phosphonic acids create SAMs on titanium (Ti) surfaces by forming Ti−O−P bonds. The deposition procedure is based on SAMs formed from aqueous alkyl phosphate solutions, which do not require the use of organic solvents. In comparison to silanes, these SAMs have a higher hydrolytic stability under physiological conditions, and no surface conditioning is required to obtain high coverage.

The 3-Aminopropylalkoxysilane (APTES) SAMs are used to form amine-terminated surfaces via a siloxane (Si−O−Si) bond, which are ideal for further derivatisation. Various methods have been applied to prepare APTES films; for example, Petrie et al. [130] reported that APTES films can be deposited on planar surfaces by immersing clean Si wafers in a 1% solution of APTES in toluene at 60 ℃ for 4 minutes. Zhang et al. [131] reported that APTES films were prepared by dipping clean glass slides into an APTES solution diluted in methanol for 24 hours at room temperature. Heid et al. [132] analysed the assembly behaviour in self assembled films and found that aminosilanes assemble into disordered multilayer films.

1.9 Polymer Brushes

Polymer brushes are long-chain molecules that are grafted or tethered to a solid surface via one end. The tethering density is relatively high so that the polymer chains are crowded and forced to stretch away from the surface to avoid overlapping. [133] Once the polymer chains are stretched, they provide different properties from the original polymer chains in the solution. This has resulted in them becoming popular surface modifications in the development of bioinspired lubricants and antimicrobial surfaces. [134, 135] They can be widely applied, from biomedical materials to membrane technologies. [136, 137] The properties of polymers can be affected by small changes in their environment, such as changes in temperature, pH, or solvent composition. [138] As a result, they have been applied to control adhesion and friction, as well as drug release. [139−141] The stretched polymer chains are similar to the bristles in a brush; thus, the term "polymer brush" is used. [133]

The grafting density is an important parameter for polymer brushes, as tethered polymer chains can adopt different conformations, depending on the density of the attachment. As illustrated in Figure 1.13, if the grafting density is too low, the polymer chains will be far away from each other; therefore, the distance between the grafting points will be greater than the radius of gyration of the polymer chains in a good solvent in an unperturbed state. The grafted chains will, thus, adopt the so-called "mushroom" conformation. [142] As the grafting density increases to the point where the radius of gyration of the tethered polymer chains approaches the distance between the grafting points, the grafted chains start to experience sterical repulsion and, thus, tend to stretch away from the surface to avoid this unfavourable interaction. This is the transition point between the mushroom regime and the brush regime. [139]

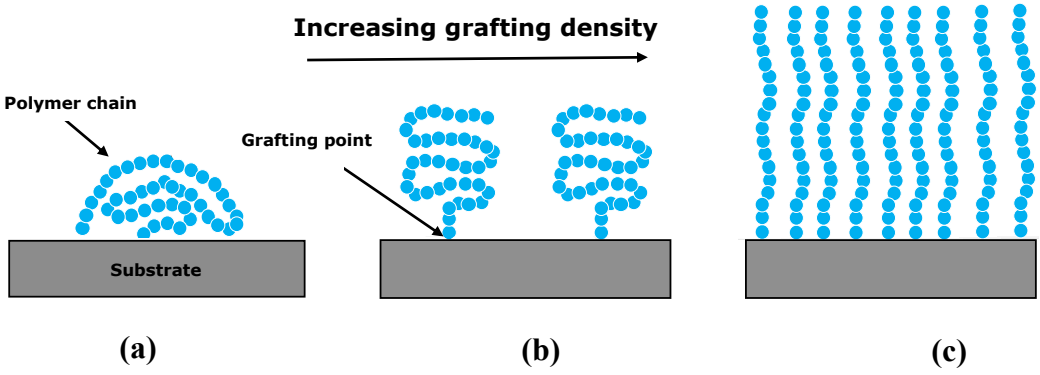

Figure 1.13. Schematic illustration of the conformation changes of grafted polymer chains on surfaces with grafting density: (a) Mushroom regime, (b) Transition regime, (c) Brush regime.

The transition from isolated chains to a brush is often described in terms of the reduced tethered density, as follows [138]:

$$\Sigma = \rho_g \pi r_{gyr}^{\ 2} \qquad 1.57$$

where ρ_g represents the number of chains per unit area, r_{gyr} represents the radius of gyration of each grafted chain under specified conditions of solvent and temperature, and therefore, Σ represents the number of chains occupying the surface area covered by an individual chain under ideal conditions. Even though $\Sigma < 1$ results in non-overlapping mushrooms or pancakes by this definition, $\Sigma > 1$ does not necessarily mean a fully elongated polymer brush. The point at which the grafted polymer layer begins to exhibit the characteristic scaling of the brush appears to vary from system to system, but occurs most often for $\Sigma > 5$. [142] An interesting intermediate system for brushes occurs in the approximate range $1 < \Sigma < 5$ under poor solvent conditions. In this case, the brushes may separate into inhomogeneous aggregates on the surface, which is sometimes referred to as "octopus micelles" [143] and reduces the free energy of unfavourable solvent interactions at the expense of chain stretching. Interestingly, these octopus micelles can only form when the grafted polymers break down rapidly. Comparatively, for the slow decrease in solvent quality, the polymers individually collapse into mushrooms, which cannot aggregate once the solvent quality has decreased sufficiently to make this favourable. [144]

1.9.1 Synthesis of Polymer Brushes

The methods of preparing polymer brushes fall into two broad categories [145]: grafting-to and grafting-from (see Figure 1.14). In grafting-to, preformed polymer chains are chemically or physically attached to the surface. [146] The first possibility to implement the "grafting-to" method is the physisorption process, in which polymer chains are anchored to the surface by dispersing diblock copolymers in selective solvents, which result in selective solvation. One block of the diblock copolymer reacts vigorously with the surface to form an anchor layer, while the other block stretches away from the surface resulting in a polymer film. The grafting density and thickness of the resulting polymer brush films are controlled by thermodynamic equilibrium in this procedure. [147] Indeed, tethered polymer films are not easy to fabricate by physisorption, as is required to prepare a suitable diblock copolymer prior to the adsorption process. Furthermore, polymer films prepared with this strategy show poor thermal and solvent stability, due to the weak interaction between the block copolymer and the surface. Particularly,

a van der Waals interaction or hydrogen bonding is most often involved in these interactions. Moreover, desorption may occur when the polymer films are introduced into good solvents. Hence, the covalent attachment method is often preferred.

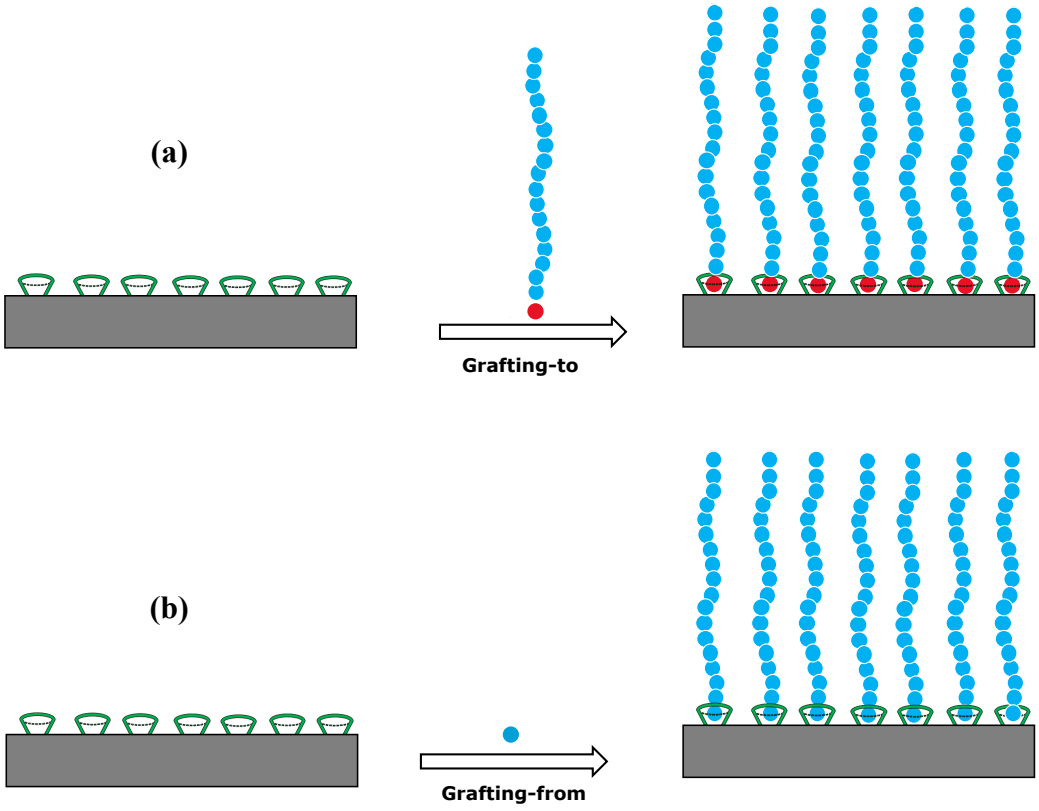

Figure 1.14. Schematic illustration of the two broad strategies for polymer brush preparation: (a) in grafting-to, polymer chains with reactive end groups are attached to anchoring groups at a surface. (b) In grafting-from, polymerization occurs in situ from surface-bound initiators.

Another strategy to implement the "grafting-to" process involves the interaction of preformed, end-functionalised polymer chains with a suitable substrate surface (i.e., with functional groups embedded on the surface that can readily interact with the end-groups of the preformed polymer chains) to form polymer films. [148] As a result of the covalent bond present between polymer chains and the surface, the polymer films that are formed demonstrate good thermal and solvent stability. The grafting density, however, that can be achieved is limited by the concentration gradient generated by the already-grafted polymer chains. [149] The already-grafted polymer chains kinetically impede the attachment of new chains to the substrate surface, resulting in a low grafting density. Meanwhile, the tethered polymer chains with low grafting density will adopt the mushroom conformation, which may limit their uses. The thickness of polymer films that can be achieved by this process is also limited and is not proportional to the polymerisation degree of the chains. [143]

The “grafting-from” method is considered the most promising process for preparing polymer brushes with a high grafting density. In the “grafting-from” procedure, two steps are involved: firstly, the substrate is functionalised with a specific initiator; and secondly, the functionalised substrate is immersed in a suitable polymerisation solution, where the brush is grown on the surface by a process called surface-initiated polymerisation (SIP). In the SIP approach, the initiator can be covalently attached to the substrate surface with a high density, forming a self-assembled monolayer. [150] The already-grafted polymer chains do not severely hinder the addition of monomers to the initiator radicals, or the chain ends, as the grafted layer is swollen by the monomer solution that feeds the growing chains. As a result, polymer films in the true brush regime (i.e., $\Sigma > 5$) are able to be obtained. Overall, the thickness of the polymer can be affected by several factors, such as: initiator surface coverage, monomer type, polymerisation time, solvent, catalyst type, amongst others. [151] In general, the polymer brushes that are formed with this procedure are thicker than those formed by the “grafting-to” approach, when the same degree of polymerisation is used.

1.9.2 Surface-initiated Polymerisation

Most of the polymerisation techniques used in the preparation of bulk polymers can be applied to the surface-initiated polymerisation of polymer brushes on various surfaces. Free radical polymerisation is one of the most widely used methods, as it has the advantage that it does not require high purity of the reactants. [152] Using this method, Hyun and Chilkoti were able to produce polystyrene films with a thickness of 10−20 nm on a gold surface. [153] Despite this, the free radical polymerisation method exhibits poor control over the molecular weights and polydispersity of the resulting polymer. The high concentration of reactive free radicals results in side reactions, including termination and chain transfer, to a large extent. More controlled polymerisation methods are required for polymers with higher demands on well-defined structures; while reactions in which termination does not occur and the polymerisation proceeds in a controlled manner until all the monomers consumed are referred to as living. Among these techniques are living cationic, and group-transfer polymerisations. These reactions, however, are industrially demanding, requiring high purity of the reactants, along with the absence of water and oxygen, which limits their use in industry. This has led to the development of more controlled radical polymerisation techniques, such as atom transfer radical polymerisation (ATRP), nitroxide-mediated free radical polymerisation (NMP), and reversible addition-fragmentation chain-transfer polymerisation (RAFT).

1.9.2.1 Atom Transfer Radical Polymerisation

Among the most widely researched radical polymerisation techniques is ATRP, which was developed by Wang in 1995, and has been routinely adopted in the preparation of well-defined polymers due to its good control over molecular parameters and structures, as well as easy access to the reagents involved. The ATRP system consists of a monomer, an initiator with a transferable halogen atom, often bromine or chlorine, a suitable solvent, and a catalyst. The most important component is the catalyst, which is a key factor for the 'living'/controlled characteristics of polymerisation. Hitherto, multiple forms of transition metal complexes have been successfully used as catalysts in ATRP systems, such as Cu, Mo, Ni, and Co coordination compounds. [154]

The normal ATRP mechanism is catalysed by the transition metal complex, i.e., $M_t^n - Y/Ligand$ (see Figure 1.15). Initially, the transition metal catalyst extracts the halogen atom X from the organic halide, $R - X$, resulting in the formation of the organic radical R•, as well as the higher oxidation-state transition metal complex, $X - M_t^{n+1} - Y/Ligand$. [155] This organic radical can then undergo monomer addition, as in conventional free radical polymerisation, adding a number of monomers with a rate constant of propagation, k_p, before being deactivated by the $X - M_t^{n+1} - Y/Ligand$ with the halogen atom being transferred back, which 'caps' the chain end of the active growing chain. A dynamic equilibrium is subsequently established for this redox process, in which the halogen atoms are reversibly abstracted from the ends of the grown chains, causing them to go from a dormant to an active state, and vice-versa. The reversible halogen atom transfer process occurs at a constant rate of activation, k_a, and deactivation, k_d. This equilibrium is situated on the side of the dormant chain ends (i.e., $k_a << k_d$) to maintain a sufficiently low concentration of active growing chain radicals, and thus, termination reactions are reduced. Furthermore, as the active and dormant states of the growing chains exchange very rapidly, all living chains would have a relatively equal chance of growth, resulting in low polydispersity and good control of the molecular weight of the resulting polymers. [156, 157]

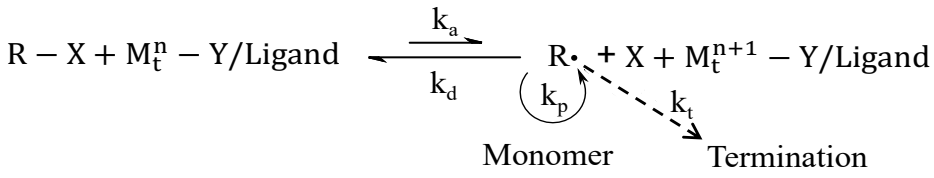

Figure 1.15. Mechanism of ATRP, where R-X is dormant organic halide species, X is halogen (Br or Cl), where Y is counterion, and R• is growing active radical.

Considering Cu-mediated ATRP as an example, the ATRP rate law of ATRP can be modelled using the following equation, when the termination step is neglected and a fast equilibrium approximation is used (K_a and K_d are large enough to enable rapid exchange between the dormant state and the active state of the growing chains, which is necessary to obtain low polydispersity). [155, 156]

$$R_p = k_p[R\bullet][M] = k_p \frac{k_a}{k_d}[RX]\frac{[Cu^+]}{[Cu^{2+}]}[M] \quad 1.58$$

where R_p is the polymerisation rate; k_p is the propagation rate constant; [R•] represents the concentration of active growing chain radicals; [M] is the monomer concentration; k_a and k_d are the activation and deactivation rate constants, respectively; [RX] is the concentration of dormant species; while $[Cu^+]$ and $[Cu^{2+}]$ are the concentrations of Cu^+ and Cu^{2+} catalyst, respectively.

As in free radical polymerisation, termination reactions occur in ATRP, especially in the early stages of polymerisation. The active radical produced by the halogen abstraction through the transition metal complex catalyst is able to undergo coupling and disproportionation reactions, which may lead to the accumulation of an oxidised metal complex, $X - M_t^{n+1} - Y/Ligand$, as persistent radicals in the polymerisation solution. This accumulation lowers the equilibrium concentration of active radicals, which is able to reduce further termination reactions. [144] In the ATRP solution, the rate of polymerisation depends on each of its components, as shown in equation 1.27. It is proportional to the concentrations of the monomer, initiator, Cu^+ compound, and inversely proportional to the concentration of Cu^{2+}. Each monomer has its own propagation rate constant and atom transfer equilibrium constant ($K_{eq}= k_a/k_d$) for its active and dormant species. Under certain reaction conditions, the yield of kp and the equilibrium constant Keq (which also controls the polymerisation rate) can be very low, preventing ATRP from occurring or causing it to occur too slowly. [155] Surface-initiated ATRP adheres to the same procedure as ATRP in the solution, except that the ATRP-initiating functional groups are immobilised on the solid surfaces, instead of in the solution. The functionalised surface is immersed in a mixture of monomer, catalyst, and ligand to initiate polymer growth from the initiating sites on the surface. Once the growth time is complete, the substrate is removed from the solution to stop polymerisation. [158] Ultimately, the mechanism of surface-initiated ATRP is the same as that of non-surface-initiated ATRP; hence, the rate of polymerisation will be similar. [159]

1.10 Scope of This Thesis

Plasmonic devices are attracting a lot of interest. However, to mass-produce chip-based sensors at low cost, we need techniques that can enable us to fabricate dense arrays with well-defined properties over macroscopic areas. Interferometric lithography provides a means to achieve this, in a way that neither electron beam lithography (expensive) nor colloidal lithography (lacking in precision and flexibility) do. I will explore the fabrication of gold nanostructures on solid surfaces using self-assembled monolayers as resists. I will investigate coupling to dye molecules to see whether strong coupling can be observed in these systems. To extend the capability of IL for fabricating structures based on metal nanostructures, I will also explore whether it is possible to pattern surface grafted brushes and use the resulting structures to organise gold nanoparticles. Finally, the cost of gold nanostructures and the scarcity of gold are a problem for many potential applications (e.g. sensors and photovoltaics). In contrast, Aluminium is cheap and abundant. I will test the feasibility of using IL to produce chip-based Al arrays.

Chapter 2

2 Experimental

2.1 Materials and Reagents

All chemicals used in the present study were of analytical grade purity and were used without any further purification. Glass microscope coverslips (22 × 60 mm, 1.5 mm thickness) were obtained from VWR. Gold wire (99%) and chromium chips (99%) were obtained from Sigma-Aldrich. Aluminium wire (99%) and tungsten boats were purchased by Testbourne. Deionised water (resistance >15.0 MΩ cm), used in all experiments, was obtained from the ultrapure water system in the laboratory. Other chemicals and solvents used in this study are listed below in Table 2.1.

Table 2.1. List of chemicals and solvents that used in the present work.

Chemicals / Solvent	Purity	Supplier
1-Octadecanethiol	98 %	Sigma- Aldrich
Cysteamine	98 %	Sigma- Aldrich
16-Phosphonohexadecanoic acid	98 %	Sigma- Aldrich
L-Cysteine	98 %	Sigma- Aldrich
2,2'-Bipyridyl	99 %	Sigma- Aldrich
Copper (II) chloride	99 %	Sigma- Aldrich
3-Aminopropyltriethoxysilane	98 %	Sigma- Aldrich
2- bromoisobutyryl bromide	98 %	Sigma- Aldrich
Triethylamine	99 %	Sigma- Aldrich
L-Ascorbic acid	98 %	Sigma- Aldrich
3-(Acryloyloxy)-2-Hydroxypropyl methacrylate	99 %	Sigma- Aldrich
Tetrachloroauric (III) acid trihydrate	99 %	Sigma- Aldrich
Trisodium citrate dihydrate	98 %	Sigma- Aldrich
Dimethylphenyl phosphine	99 %	Sigma- Aldrich
Ethanol	HPLC	Fisher Scientific
Sulfuric acid	95 %	Fisher Scientific
Ammonia Solution	32 %	Sigma-Aldrich
Hydrogen peroxide	30 %	Fisher Scientific

2.2 Pre-treatment of Glassware and Tools

Prior to any treatment, all glass microscope slides and glass tubes were cleaned with piranha solution. In a typical procedure, glass microscope slides were initially placed into glass tubes (70 mm × 25 mm), followed by the placement of the glass tubes into a large Pyrex glass beaker. The glass beaker and glass tubes were washed several times with soapy tap water before being placed inside a chemical fume hood. Three parts of 95% sulfuric acid (H_2SO_4) was initially added, followed by one part of 30% hydrogen peroxide (H_2O_2) to the glass tubes and beaker, in order for the level of the mixture to be approximately 1 cm above the tubes. The glass tubes were immersed until the solution stopped bubbling and cooled to room temperature. Following the piranha treatment, the cold solution was poured into a dilution tank, and the glass beaker was removed from the fume hood. The glass tubes containing glass microscope slides were rinsed thoroughly with deionised water and placed into the oven (ca. 90 °C) to dry. All slides were used within two days of cleaning. **Caution:** the reaction of H_2O_2 with concentrated H_2SO_4 produces highly reactive peroxymonosulfuric acid (H_2SO_5), which is known to detonate spontaneously upon contact with organic solvents.

All tweezers and spatulas used in chemical handling and treated surfaces were cleaned before use by sonication in acetone for 10 min, followed by sonication in deionised water for 10 min, and then blown dry with nitrogen.

2.3 Fabrication of Metallic Nanostructures

2.3.1 Thermal Evaporation of Metals

A thermal evaporator, an Edwards Auto 306 bell jar vacuum coating system (see Figure 2.1), was used to evaporate metal films on glass substrates. In a typical procedure, clean glass slides were first placed on a stage above a current-driven evaporation source. The metal source to be evaporated, usually chromium, gold or aluminium was placed in a suitable filament or crucible, within a high-vacuum chamber. The evaporation chamber was then roughed out via a rotary pump to a pressure of 10^{-1} mbar, before engaging the diffusion pump to obtain a high vacuum. Once a pressure of at least 10^{-6} mbar was reached, the current supplied to the crucible was increased until a deposition rate of 0.1 nm s^{-1} was reached. Layer thicknesses and deposition rates were recorded using a quartz crystal microbalance (QCM) thickness monitor placed near the substrate stage. After the desired thickness was achieved, the current was slowly lowered, and the coated glass substrates were left to cool for at least 30 min. The chamber was ventilated with air with the slides removed and placed in glass tubes.

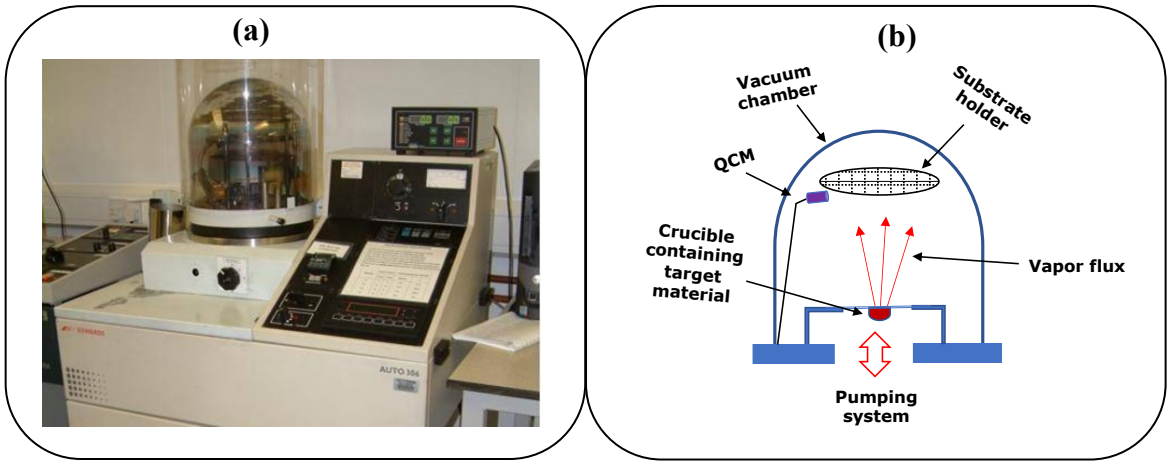

Figure 2.1. (a) photograph of Edwards auto 306 bell jar vacuum coating system; and (b) a schematic illustration showing the evaporation process.

2.3.2 Preparation of Self-assembled Monolayers on Gold Surfaces

Gold was used as a substrate for self-assembled monolayers (SAMs). It was chosen because it has a strong affinity for thiols, which were utilised as a head group in most of the molecules in this work. Furthermore, gold is a largely inert metal compared to other metals, including silver and/or copper. This feature makes it a useful option for handling and manipulating samples in ambient air, rather than ultra-high vacuum (UHV). SAMs can be formed on surface substrates, either by adsorption from solution or evaporation. In the current work, SAMs were prepared by the solution method due to its convenience. Therefore, a 1 mM solution of 1-octadecanethiol (ODT) in ethanol was first prepared in a volumetric flask and then added to freshly coated gold substrates (Au /Cr /glass) in 33 mL glass tubes. The tubes were then sealed and placed in a drawer for at least 24 h to allow the closely packed SAMs to form.

2.3.3 Photopatterning of Self-assembled Monolayers

Prior to IL photopatterning, the gold substrates were removed from the ODT solution, and the residual solution on the slides was removed by rinsing with ethanol and drying with nitrogen. The gold substrates were cut into small samples (0.5 × 1.0 cm) using a diamond-tipped scribe, and then sonicated in ethanol for approximately 3 min. Interferometric lithography was then used to draw patterns on ODT SAMs on the gold surface. The output laser power was measured at 70 mW. The laser power on a sample was 20−24 mW. The first exposure was carried out at a dose of 38.4 J cm^{-2} and the second exposure was carried out at a dose of 27.3 J cm^{-2}. Exposure times were calculated as follows: $t = \frac{\text{Exposed area} \times \text{Exposure Dose}}{\text{laser power on sample}}$.

2.3.4 Etching Procedure

After photopatterning, an etching step was employed to remove the gold film from the exposed region. The sample designated for etching was initially rinsed with ethanol, dried with nitrogen, and then immersed in the etching solution. This solution consisted of 2 mM cysteamine and 8% ammonia in HPLC-grade ethanol. The photopatterned sample was remained in the solution for a specific duration without excitation or solution stirring. Once the etching process was finished, the sample was taken out of the solution, rinsed with ethanol and dried with nitrogen.

2.3.5 Annealing Process

In response to the absence of plasmon resonances in the fabricated samples, a thermal annealing process was employed to enhance the crystallinity of the gold and reduce its granularity. In this study, freshly fabricated samples of gold nanostructures were annealed by placing them inside a chamber furnace (see Figure 2.2). The annealing temperature ranged between 450 and 600 °C, and the annealing time was set for 2 h at a heating rate of 7 °C min^{-1}. Following annealing, the samples were allowed to cool in a laboratory atmosphere. The annealed samples were then characterised using atomic force microscopy and absorption spectroscopy.

Figure 2.2. Photo of the carbolite chamber Furnace; and (b) the gold nanostructure samples inside the chamber furnace.

2.4 Pattering of Poly(Cysteine Methacrylate) Brushes

2.4.1 Preparation of BiBB-APTES Initiator on Glass Slides

The clean substrates were immersed initially in freshly prepared 3-aminopropyltriethoxysilane (APTES) solution in ethanol at the APTES concentration of 2% by volume at room temperature for 30 min. The substrates were then removed from the solution, rinsed with ethanol, dried with nitrogen, and then annealed at 120 °C for 30 min by a hot plate. The APTES coated substrates were then immersed in a solution of dichloromethane (60 mL) containing 2-bromoisobutyryl bromide (BIBB) (0.37 mL, 3 mmol) and triethylamine (0.41 mL, 3 mmol) for 30 min at room temperature. After completion of the reaction, the BIBB-APTES functionalised substrates were sequentially washed with ethanol and dichloromethane and dried with nitrogen gas. These steps result in a highly reproducible and uniform BIBB-APTES film.

2.4.2 Synthesis of Cysteine Methacrylate Monomer

Cysteine methacrylate monomer (CysMA) was synthesised following the procedure outlined in a previous study published by Alswieleh et al. [160] Initially, L-Cysteine powder (7.54 g, 62.23 mmol) was dissolved in 100 mL of deionised water and then transferred into a round-bottomed flask containing a magnetic stir bar. Subsequently, 3-(acryloyloxy)-2-hydroxypropyl methacrylate (14.86 g, 69.36 mmol) and dimethylphenyl phosphine (20 μL, 1.41×10^{-8} mol) were added to the flask, and the mixture was stirred at a speed of 300 r/min at room temperature for approximately 2 h, until the end of the reaction. The product was washed with ethyl acetate (2 ×100 mL) and dichloromethane (3 ×100 mL) extracted in a separatory funnel. The final monomer product was isolated from water as a pure white solid by freeze drying, which was then dried under reduced pressure for at least 48 h. The resulting product, weighing around 15 g, was stored in a desiccator at room temperature until needed.

2.4.3 Polymerisation of Cysteine Methacrylate Monomer

In one of the early stages of monomer polymerisation (PCysMA), four different solutions were prepared as follows: CysMA monomer (750 mg, 2.231 mmol, 4 mL H_2O); 1-ascorbic acid (100 mg, 0.568 mmol, 10 mL H_2O); copper (II) chloride ($CuCl_2$) (14.6 mg, 0.109 mmol, 5 mL H_2O), and 2,2'-Bipyridyl (38.8 mg, 0.248 mmol, 5 mL ethanol). The 2,2'-Bipyridyl solution was then mixed with the $CuCl_2$ solution, resulting in a blue mixture [$Cu(bipy)_2Cl_2$]. Then, the 1-ascorbic acid (0.18 mL, 1.02×10^{-5} mol) was added to the CysMA monomer solution, after which the Cu $(bipy)_2$ Cl_2 solution (0.35 mL, 3.82×10^{-6} mol) was added. The monomer/catalyst mixture was mixed and left for approximately 30 min until the mixture turned to brown (see Figure 2.3), indicating the formation of active Cu (II) complexes.

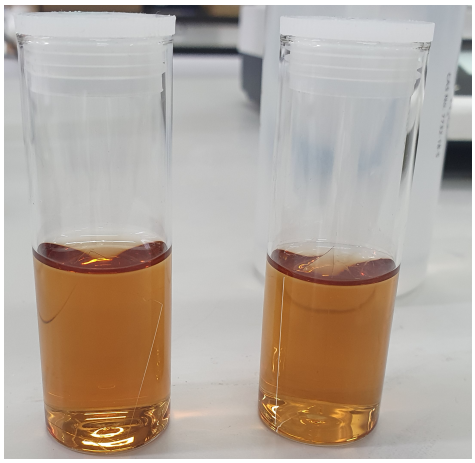

Figure 2.3. Brown solution confirming the formation of Active Cu (II) complexes.

2.4.4 Poly(cysteine methacrylate) Brushes Grafted on BIBB-APTES

BiBB-APTES film functionalised substrates were cut into small samples (0.5 × 1.0 cm), and then placed in clean glass tubes. The PCysMA solution (1mL) was syringed into each tube, and surface polymerisation was allowed to continue for the desired time. Each polymerisation was stopped by removing the sample from its tube, followed by washing with deionised water and ethanol to remove excess PCysMA. After polymerisation, the samples were stored in ethanol at 5 °C until used.

2.5 Interference Lithography

Every stage of my work involved the use of samples fabricated by IL utilising a Lloyd's mirror two-beam interferometer in conjunction with the frequency-doubled argon ion laser emitted at 244 nm with a power of 70 mW (Innova FredD 300C, Coherent, UK).The schematic setup of this technique is illustrated in Figure 2.4. The UV laser beam was passed through a lens-pinhole system equipped with objective lens, and a 5 µm pinhole, before falling onto a Lloyd's mirror interferometer, which consisted of a UV-reflecting mirror glued at 90° on a vacuum plate, generating a semicircular laser spot with a radius of 1 cm. The Lloyd's mirror and sample was positioned on a two-axis stage (X and θ) in such a way that the common corner of the mirror and the sample was positioned on the optical axis.

A time-controlled shutter was installed between the laser beam source and the objective lens to control the exposure time during the experiment. The pinhole was used to remove unwanted components of the laser beam. The distance between the pinhole and the sample along the direction of the optical axis was 20 cm. In this configuration, half of the beam was directly focused onto the sample surface, while the other half of the beam was focused onto the mirror, which was reflected from the mirror to the sample. These two beams were overlapped with each other so that the sinusoidal interference patterns were exposed on the photoresist layer on the sample surface. A single exposure was used to create periodic arrays of line patterns, under optimised dose conditions. Double exposures, with sample rotation in-between, were used to create arrays of squares, hexagonal or rows, depending on the angle of rotation used (see Figure 2.5).

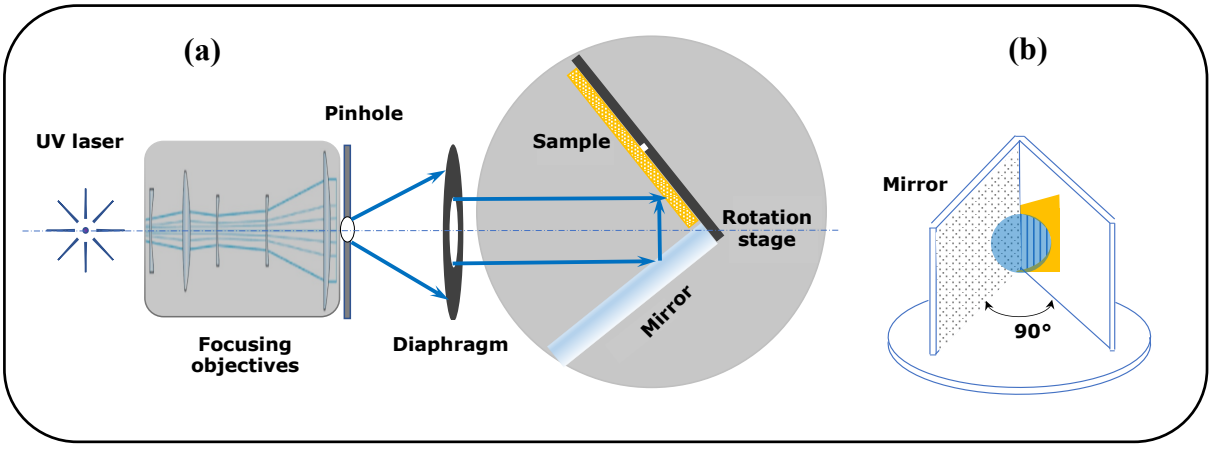

Figure 2.4. (a) A Schematic diagram showing the configuration of the IL; and (b) the Lloyd's mirror interferometer System.

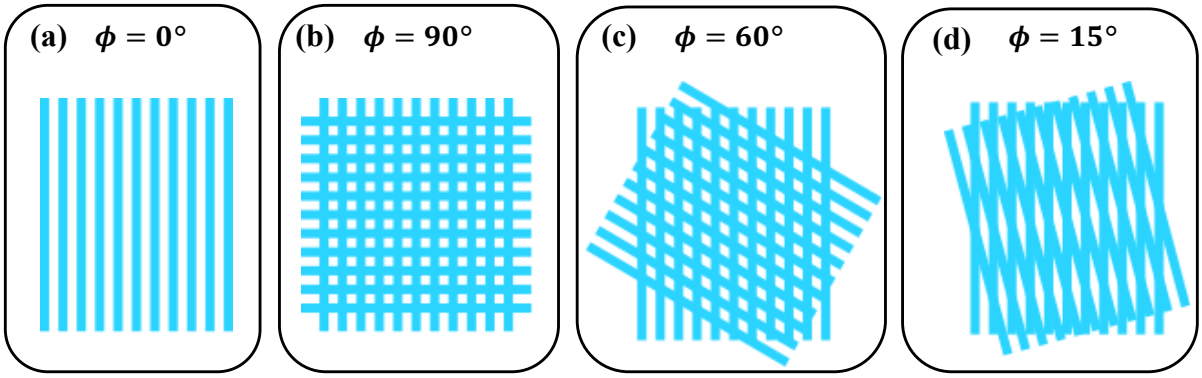

Figure 2.5. Schematic diagram showing IL patterns: (a) line structures generated by applying a single exposure; while (b) square arrays, (c) hexagonal arrays, and (d) elongated arrays generated by applying double exposure with different rotation angles.

2.6 Characterisation Techniques

Advanced analytical tools and techniques are essential for characterisation and monitoring thin film structures and properties. Among the techniques used in the current study is AFM, which provides direct images of nanostructure arrays at high resolution. Another powerful technique is XPS, which is used to provide information regarding the presence of specific molecular bonding within the film. This section therefore will discuss some of the techniques used during the current study in more detail.

2.6.1 Contact Angle Measurement

2.6.1.1 Background

When a drop of liquid is placed on a flat solid surface, the liquid spreads until it reaches a state of equilibrium. The spreading behaviour depends on the thermodynamics of the liquid-solid interaction, as well as external factors, such as temperature. This field is broadly classified as 'wetting'. The spreading phenomenon, inferred from observations of how a liquid behaves on a solid surface, can be used to characterise the thermodynamics of a liquid-solid interface if the liquid is well characterised by the properties of the solid. [161]

The contact angle is the angle resulting from the intersection of the liquid-solid interface and the vapour-liquid interface (obtained geometrically by applying a tangent line from the point of contact along the vapour-liquid interface in the droplet profile). [162] Furthermore, contact angle measurements can be applied to detect the presence of molecular layers and to estimate the density of molecular adsorption on a solid surface. [163, 164] Figure 2.6 illustrates that the contact angle of the surface becomes smaller when the liquid spreads over it, while it becomes larger when the liquid beads on the surface. Therefore, if the contact angle is less than 90°, the

surface is considered to be 'wettable' (i.e. hydrophilic if the liquid is water) and the liquid will spread over a large area on the surface. In contrast, if the contact angle is greater than 90°, the surface is considered 'non-wettable' (i.e. hydrophobic), and the liquid will minimise its contact with the surface to form a packed liquid droplet. [165] For example, in the case of complete wetting, the contact angle reaches 0°, and the droplet turns into a flat puddle. However, in case of ultra-hydrophobic, the contact angle exceeds 150°, resulting in almost no contact between the droplet and the surface. [166] The shape of the droplet is controlled by the surface tension of the liquid. [167]

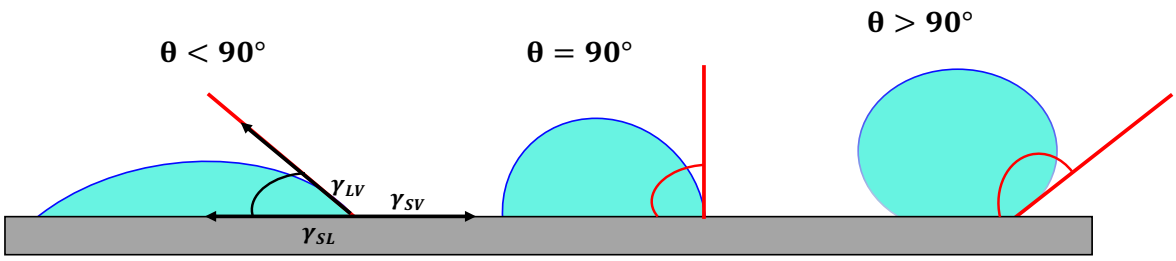

Figure 2.6. Schematic illustration of contact angle formed by sessile liquid drops on a flat solid surface.

In liquids, molecules are pulled evenly in all directions by the neighbouring liquid molecules, resulting in a net force of zero. [168] Liquid molecules along the top surface, however, do not have neighbouring molecules in all directions to form a balanced net force and, thus, are pulled inward by the neighbouring molecules, creating an internal pressure. Consequently, the liquid will contract in its surface region to attain its lowest surface free energy, while external factors, such as gravity, may deform the droplet. As a result, the value of the contact angle will depend on the surface tension of the liquid, the surface energy of the substrate, and external conditions. [169] As first explained by Young in 1805, the contact angle is determined by the mechanical equilibrium of the droplet under the action of three interfacial tensions [170]:

$$\gamma_{SV} = \gamma_{SL} + \gamma_{LV} \cos\theta_Y \qquad 2.1$$

where θ_Y represents the contact angle (Young's contact angle) between the liquid and solid surface (see Figure 2.6). γ_{LV} , γ_{SV} and γ_{SL} refer to the interfacial tensions of the liquid-vapour, solid-vapour, and solid-liquid interfaces, respectively. The most common method utilised to measure the contact angle is the sessile drop technique, in which a liquid droplet is placed on a solid surface by a syringe. The resulting contact angle is measured by means of a goniometer attached to an optical microscope; while the contact angles due to the expansion and retraction of the liquid droplet are defined as the advancing contact angle (θa) and the receding contact

angle (θr), respectively. The difference between these two angles (i.e. θa and r) is referred to as the surface hysteresis, which can be used to provide information regarding the homogeneity of the surface. [165] Metals and glass are examples of high-energy surfaces on which most liquids spread spontaneously, where the angle tends to zero. In contrast, plastic materials are an example of low-energy surfaces, in which the liquid applied to their surfaces remains as droplets with limited contact angles. This is because the surface energy of the substrate is less than the surface tension of the liquid. Thus, the interpretation of the contact angle is based on comparisons of values obtained from different systems. By comparing the contact angle of the treated substrate with that of a clean substrate, the difference in values can indicate the layer composition. Moreover, the contact angle is affected by the terminal groups of molecules; for example, smooth surfaces composed of methyl (CH_3) end groups exhibit higher contact angles for deionised water than those composed of methylene (CH_2) groups. [171]

2.6.1.2 Experimental Procedure

The contact angle measurement was conducted on a Rame-Hart goniometer using the sessile drop method (see Figure 2.7). The contact angle goniometer consists of a sample stage to hold the substrate, a syringe to apply a droplet of liquid, and a light source to illuminate the droplet, Which was observed with a magnifying microscope, and the resulting contact angle was measured by a goniometer installed in the eyepiece. In detail, a drop of deionised water with a fixed size was suspended from a microliter syringe positioned above the sample. The syringe was gently lowered towards the sample surface so that the drop of water came into contact with the surface. The syringe was then withdrawn, leaving the drop on the surface.

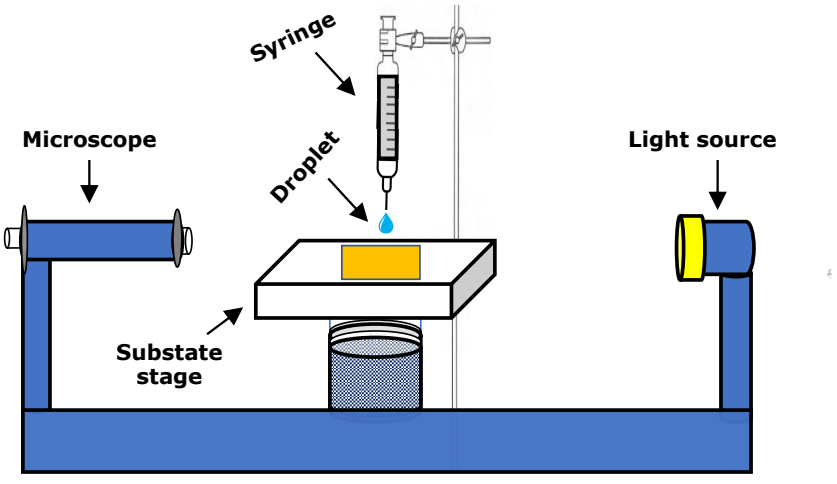

Figure 2.7. A schematic illustration of the Rame-Hart goniometer.

2.6.2 Atomic Force Microscope

2.6.2.1 Background

Atomic force microscopy (AFM) was initially introduced by Gerd Binnig and Heinrich Rohrer in 1986, and it has since developed into a powerful measurement tool for surface analysis. [172] The AFM belongs to the group of scanning probe microscopy (SPM), in which a fine tip is moved across the sample to obtain information regarding its surface structure by measuring the interaction between the tip and the surface. The tip can be either in direct contact or a few nanometres away from the surface. In contrast to scanning tunnelling microscopy, AFM is able to measure, not only conducting, but also non-conducting samples, which makes it a useful tool in physics, chemistry, and biological applications. The interaction between the tip and sample surface can be explained by considering van der Waals interactions and Pauli repulsion [173], which occur between two atoms or molecules and are mainly affected by their distance. The van der Waals attractive force is made up of three components: dipole-dipole force, dipole-induced dipole interactions and the dispersion interaction that is caused by induced dipoles in atoms or molecules. The repulsive interaction is attributed to the Pauli principles, which states that two or more fermions (e.g. electrons) cannot have the same quantum numbers; when two atoms or molecules are close to each other, the wavefunctions begin to overlap as they begin to occupy the same volume of space, which results in repulsion. The sum of these interactions is described by the Lennard-Jones potential, which is a mathematical model used to describe the interaction between two neutral atoms or molecules in close proximity. It is named after the physicists John Lennard-Jones, who first proposed the model in 1924. The Lennard-Jones potential is expressed as [174]:

$$V\,(r) = 4\epsilon\left[\left(\frac{\sigma}{r}\right)^{12} - \left(\frac{\sigma}{r}\right)^{6}\right] \qquad 2.2$$

where r is the distance between the two particles, ϵ is the depth of the potential well, and σ is the distance at which the potential energy is zero. The first term in the equation represents the repulsive interaction between the two particles due to their electron clouds, while the second term represents the attractive interaction due to van der Waals forces. A typical Lennard-Jones potential curve is shown in Figure 2.8.

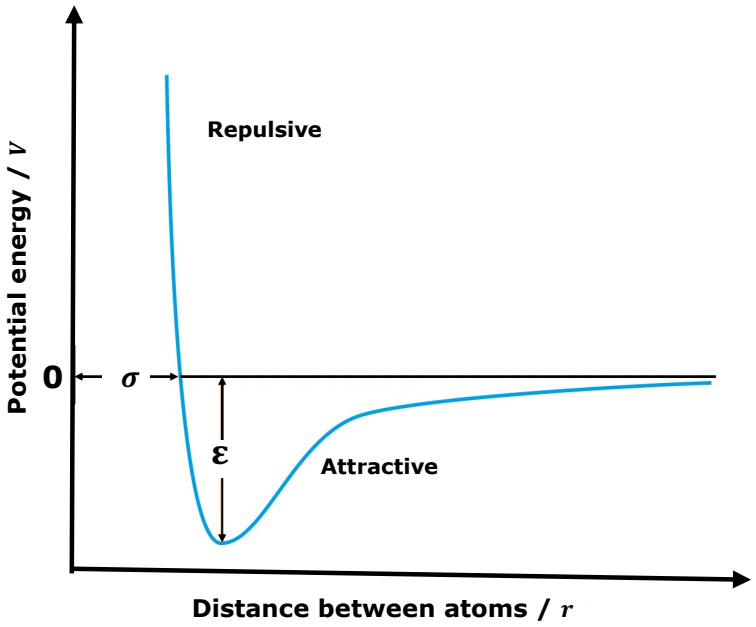

Figure 2.8. Schematic illustration of the Lennard-Jones potential

Relative to atomic dimensions, the AFM probe is effectively a macroscopic object. Thus, the pairwise interactions between atoms in the AFM probe and the sample surface have to be integrated. The following expression is obtained for the interaction energy W as a function of separation D between a sphere of radius R and a planar counter-surface, a reasonable mode for the tip-sample interaction:

$$W = -\frac{AR}{6D} \qquad 2.3$$

where A is the Hamaker constant.

AFM is a type of SPM that uses a small probe to scan a surface and create a three-dimensional image with atomic resolution. Figure 2.9 shows schematically the basic components of an AFM instrument; it consists of a cantilever with a sharp probe, a laser source, a piezoelectric scanner, a photodetector, a feedback system, and a computer. Therefore, AFM works by using a small, sharp tip, which is attached to a cantilever. The probe is brought into close proximity with the surface of the sample, and as the cantilever moves up and down in response to the atomic forces between the probe and the surface, its deflection is measured using a laser. The deflection data is then used to generate a topographical map of the surface. Accordingly, cantilevers and tips are essential parts of the AFM system, as they control the final lateral resolution of the system and the force applied to the surface. The interaction between the tip and the surface is often measured using a flexible cantilever. The cantilever is a thin, elongated beam that is attached

to the tip. When a force is applied to the tip, the cantilever bends, and this bending can be measured by Hooke's Law, which can be expressed mathematically as follows [175]:

$$F = -\Delta x.k \qquad 2.4$$

where F is the force applied to the tip, Δx is the displacement or bending of the cantilever, and k is the spring constant. The spring constant represents its stiffness, and determines how much the cantilever deflects when a force is applied to it. Specifically, a cantilever with a lower spring constant is more sensitive to small forces because it deflects more easily.

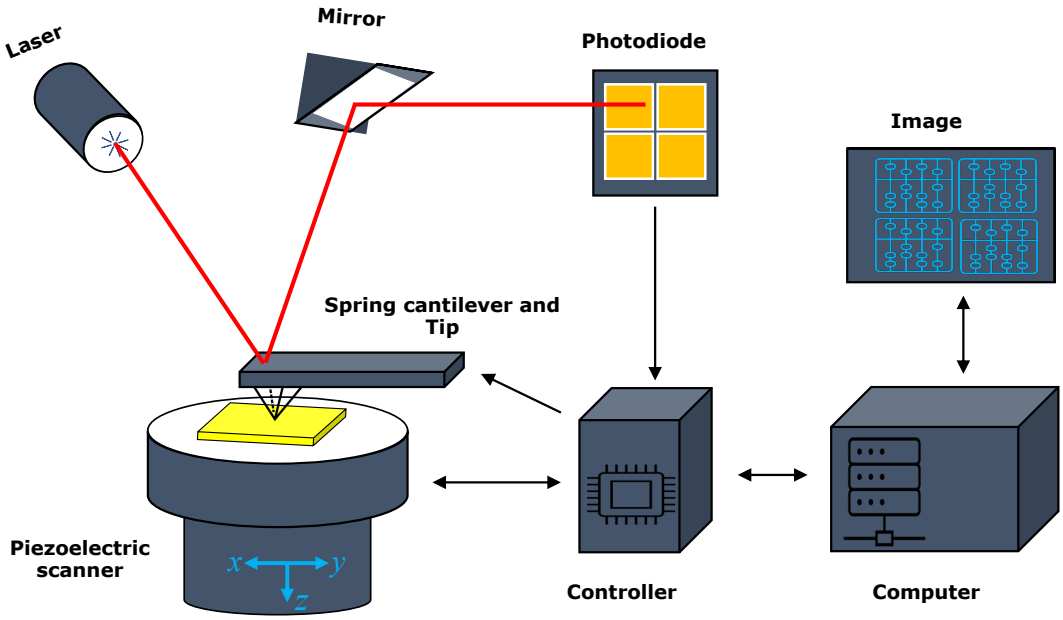

Figure 2.9. Schematic illustration of the basic components of an atomic force microscopy.

AFM tips are typically made of either silicon or silicon nitride, both of which offer unique properties and advantages for different applications. Silicon tips are relatively soft and can be fabricated with a variety of shapes and sizes, making them suitable for various imaging modes in AFM. They are also compatible with many sample surfaces, making them versatile for different experimental conditions. However, due to their relatively low mechanical strength, they may deteriorate quickly or break during use. In contrast, silicon nitride tips are generally harder and more durable than silicon tips, with better resistance to wear or fracture. This makes them suitable for high-resolution imaging of hard samples, such as ceramics or metals, and for use in contact and tapping mode imaging. However, they may be less suitable for delicate or soft samples, as they can cause more damage than silicon tips. [176]

A piezoelectric scanner is used to control the movement of the probe. It can move the probe in the X, Y, and Z directions, allowing scanning of the entire region of interest on the sample surface. The piezoelectric scanner typically consists of a piezoelectric material, such as lead zirconate titanate (PZT), sandwiched between two electrodes. When a voltage is applied to the electrodes, the piezoelectric material undergoes a controlled deformation, which results in the movement of the scanning probe. In order to detect the deflection of the cantilever, a laser beam is directed onto the back of the cantilever; the reflected beam is collected by a position-sensitive photodiode (PSD). The position of the reflected beam on the PSD is directly related to the deflection of the cantilever. By measuring this position, the deflection can be quantified, which is then used to reconstruct the surface topography. In addition, the feedback system (i.e. control electronics) uses the information from the PSD to adjust the position of the scanner and keep the cantilever in constant contact with the sample surface, as well as maintain a constant force between the tip and the surface. The final component of the AFM is a computer with software that controls the instrument and analyses the data collected during the scan. The software is able to create high-resolution images of the sample surface, measure the height and shape of features on the surface, and provide other types of data about the sample. [177]

AFM can be operated in a number of modes, depending on the application required. In general, imaging modes can be classified into static (i.e. contact) and dynamic (i.e. tapping or non-contact) modes, in which the cantilever oscillates or vibrates at certain frequencies. During the contact mode, the tip is in constant contact with the surface (< 0.5 nm tip-surface separation), which allows for high-resolution images of the sample topography. The contact mode is often utilised for roughness and hardness measurements due to its simplicity of operation and high level of accuracy. However, the constant contact of the tip with the sample surface is able to cause the tip to wear out quickly or may cause damage to the surface. It is also not suitable for imaging soft or delicate samples that can become deformed under the applied force (see Figure 2.10a).

During the tapping mode, the tip oscillates perpendicular to the sample surface at a frequency close to the resonance frequency of the cantilever (0.5−2 nm tip-surface separation). This oscillation causes the tip to intermittently come into contact with the sample surface, tapping the surface and providing a high-resolution image of the sample topography. The energy released by the tip is sufficient to avoid the tip sticking to the sample surface; whereas in each oscillation when the tip approaches the surface, it experiences an attractive and repulsive force that leads to a change in the amplitude. When compared to the contact mode, the tapping mode is superior, as the lateral forces on the sample surface are mainly removed. This is due to the

fact that the tip is in contact with the surface for a short period of time and is not dragged along the surface during imaging (see Figure 2.10b). The tapping mode is useful for imaging soft or fragile samples, as it minimises the damage that could be caused by the tip pressing onto the sample surface. [178, 179] During the non-contact mode, the tip is brought very close to the sample surface (5−15 nm tip-surface separation), but it does not make physical contact with the sample surface. Instead, the tip interacts with the surface through long-range forces, such as Van der Waals forces. It is used for imaging delicate specimens or specimens that are easily damaged during contact. The resolution in the non-contact mode, nevertheless, is not as high as in the contact mode or tapping mode, but it allows for a non-invasive measurement of the sample topography (see Figure 2.10c). [179]

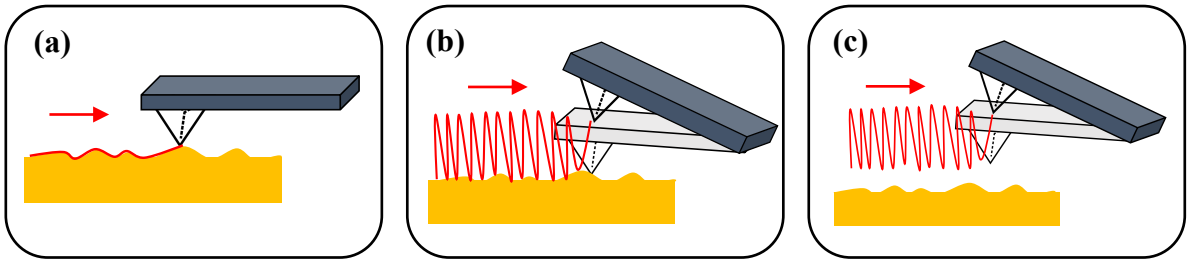

Figure 2.10. Schematic depiction of the AFM modes: (a) contact, (b) tapping, and (c) non-contact.

2.6.2.2 Experimental Procedure

As-fabricated or annealed (gold, aluminium) nanostructures and patterned PCysMA brushes were imaged by AFM using a Nanoscope Multimode 5 atomic force microscope operating in tapping mode. A standard cantilever with tapping conical shaped tips made of silicon nitride (OTESPA-R3 model, Bruker) was used. The cantilever oscillation frequency was in the range of 300 kHz, with a spring constant of 17.5 N/m. AFM images were recorded with 512 lines per image, and a scan rate of 0.996 Hz. AFM imaging was repeated at various scales from 20 × 20 μm^2 to 500 × 500 nm^2 of the sample surface. All images were obtained by standard procedures without any optimisation; and all AFM experiments were performed under ambient laboratory conditions about 20 °C. NanoScope Analysis (v.1.5) software was used for data analysis; and information, such as surface roughness and surface morphology, were obtained.

2.6.3 X-ray Photoelectron Spectroscopy

2.6.3.1 Background

X-ray photoelectron spectroscopy (XPS) is a surface analysis technique commonly applied to reveal the elemental composition, chemical and electronic state of atoms within a material on a given surface. [180] The origin of XPS is linked with the discovery of the photoelectric effect by Hertz in 1887 and extended to surface analysis by Siegbahn in the 1960s. [181] The main process is based on the photoelectric effect, which is the ejection of electrons from a material, due to the absorption of radiation with a very short wavelength. The photoelectric effect occurs when an X-ray photon interacts with an electron at a core level. Subsequently, this leads to the transfer of photon energy, which causes electron emissions (see Figure 2.11). Specifically, the emitted photoelectrons have specific kinetic energy, which is determined by a detector. Meanwhile, soft X-rays, Mg Kα (1253.6 eV) and Al Kα (1486.6 eV), are often used as the exciting photon source. [180] The energy and line width of the X-rays are selected to maximise photoemissions and improve the level of spectral resolution. The kinetic energy of the photoelectron is known to be the difference between the X-ray photon energy hυ (h is the Planck's constant and υ is the X-ray frequency) and the binding energy of the core-level electron. As the energy of the X-ray is known and the kinetic energy of the photoelectrons can be obtained experimentally, the binding energy of an electron can be easily calculated based on the following equation [181, 182]:

$$\mathrm{KE} = hv - E_b - \phi \qquad 2.5$$

where hv is the energy of the incident radiation, KE is the kinetic energy of the electron, E_b is the binding energy of the core electron, and ϕ is the spectrometer work function.

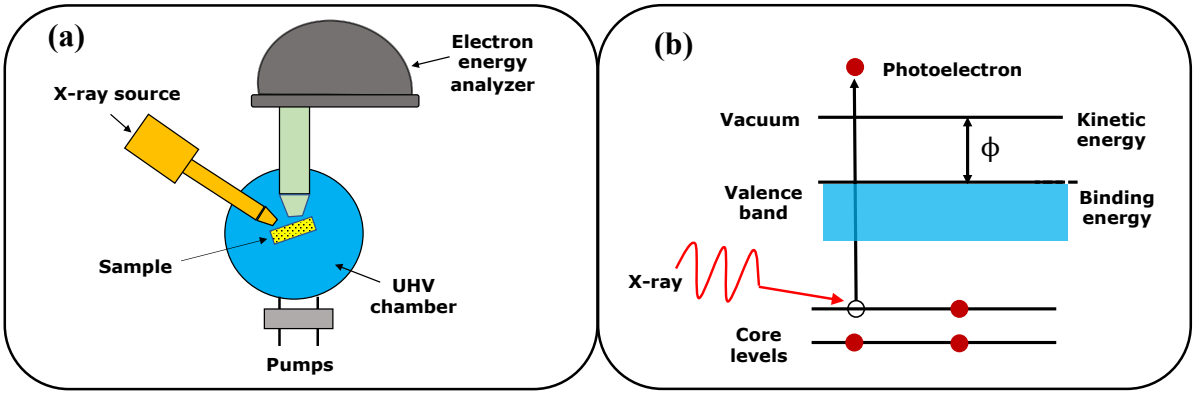

Figure 2.11. Schematic of (a) the XPS configuration and (b) the electronic transitions during the XPS process.

All elements on the sample surface can be detected, except for Hydrogen and Helium, which have very small photoelectron cross-sections and hardly share their electrons to form other compounds. [183] Every other element has a characteristic binding energy associated with its core atomic orbital, such that every element will exhibit a set of peaks in their photoelectron spectra through kinetic energies determined by the photon energy and the related binding energies. Separately, XPS is a surface-sensitive technique, as only electrons that are generated near the surface escape and are identified. The analytical depth is defined by the distance that a photoelectron is able to penetrate without losing energy (10 nm from the top of the surface). Moreover, as a result of a photoelectric process, relaxation of the excited ion may occur. When an electron from a core level is emitted, another electron from an upper-level falls into the hole left by the emitted electron, which causes a third electron emission, known as an auger electron, to retain the energy previously released. [181, 182] Due to the high surface sensitivity and to avoid the energy loss of electrons in the analyser region, XPS measurements require UHV conditions often in the range 10^{-9} mbar. [181] XPS can be performed on almost all flat samples with a maximum resolution of a few micrometres, and is particularly suitable for analysing metallic and inorganic materials; however, it can be used for insulating materials, including polymers. Whenever polymers or other materials are analysed, the C 1s, O 1s, and N 1s peaks are of primary interest. The majority of information about the material can be obtained through careful analysis of the peak profile of C 1s, which informs about the chemical environments of the different carbon atoms present in the sample.

2.6.3.2 Experimental Procedure

XPS measurements were performed using a Kratos Axis Ultra and Supra DLD spectrometer (Kratos Analytical, UK) equipped with a monochromatic Al Kα X-ray source (1486.6 eV). The X-ray source was operated at a power of 150 W with a current of 8 mA and the pressure in the analysis chamber was maintained at around 1×10^{-9} mbar. Wide-scanning spectra were acquired at pass energy of 160 eV and high-resolution spectra (C 1s, O 1s, N 1s, Au 4f and Br 3d) were obtained by narrow scanning at the pass energy of 20 V. All XPS spectra were analysed and curve-fitted using Casa XPS software (v.2.3.15) and all binding energies were calibrated by setting the main C1s component at 285.0 eV. The elemental compositions of the samples were calculated by the region of the respective photoelectron peaks after subtracting a Shirley-type background.

2.6.4 Ultraviolet–Visible Spectroscopy

2.6.4.1 Background

Ultraviolet-visible (UV-Vis) spectroscopy is an analytical technique used to investigate how a sample responds to light. [184] When a beam of light travels through a substance or solution, it is likely that some of the light will be absorbed, and the remainder will be transmitted through the sample. The ratio of the intensity of light entering the sample (I_0) to that leaving the sample (I_t) at a given wavelength is known as the transmittance (T). This is described as the percentage transmittance ($\%\,T$), which is the transmittance multiplied by 100 as illustrated in equation 2.6:

$$\%\,T = \frac{I_0}{I_t} \times 100 \qquad 2.6$$

The absorbance (A) of a sample is the negative logarithm of the transmittance (equation 2.7):

$$A = -\log T \qquad 2.7$$

The UV-Vis spectroscopy offers maximum flexibility and is suitable for applications ranging from 190 to 1100 nm in wavelength. The fundamental principle in absorption analysis is the Beer-Lambert Law, which indicates that for an ideal solution, concentration and absorbance are linearly related, provided that the path length remains constant. [185] The absorptivity (e) is a constant for each molecule for each wavelength (equation 2.8):

$$A = \varepsilon c l \qquad 2.8$$

where ε is the absorptivity of the sample, c is the concentration of the absorbing sample and l is the path length through the sample. Provided that ε and l remain constant for a given set of measurements, the plot of sample absorbance against the concentration of the absorbing sample should provide a straight line. In general, calibration curves are derived by plotting the absorbance a series of standard samples against as a function their concentration. Another aspect of the Beer-Lambert Law is that the path length can be changed in order to affect the absorbance, which can be beneficial if lower detection limits are required, as the path length can be increased or if the absorption is too high to be measured, then the path length can be reduced. Figure 2.12 shows the optical setup of a UV/Vis spectrophotometer, in which a beam of light from the source passes through a monochromator consisting of diffraction gratings or a prism and a wavelength limiter (slit). The resulting monochromatic wavelength can be tuned

and scanned to the desired range of the electromagnetic spectrum. The detector collects the light that passes through the sample; the reference spectrum (the spectrum without a sample for calibration) must initially be collected in order to measure the absorption caused by the samples.

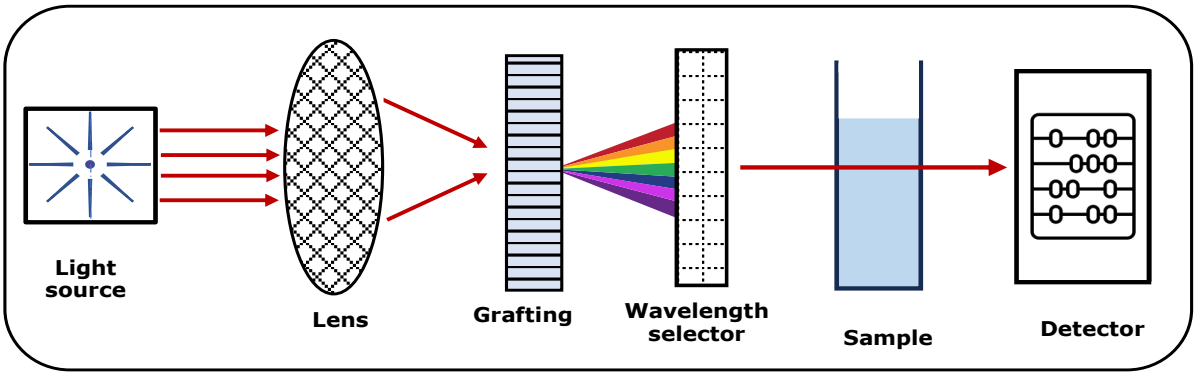

Figure 2.12. Schematic illustration of a monochromator UV/Vis spectrophotometer setup.

2.6.4.2 Experimental Procedure

Ultraviolet visible (UV-Vis) absorption measurements in both air and liquid were conducted using a Cary 50 spectrophotometer (Agilent Technologies, USA). The spectral range was set between 450 nm and 900 nm. A PTFE sample holder was designed to hold dry ($1cm^2$) samples upright within a cuvette cell for both measurements, and this enabled the UV laser beam to pass through the same spot of the sample during all stages of the experiment (see Figure 2.13). The baseline correction was performed without any sample in the spectrometer sample holder and an empty cuvette cell was utilised as the reference sample. For liquid measurements, the cuvette cell was rinsed with deionised water and then rinsed with the actual sample to be measured. Therefore, 3 mL of the liquid sample was often injected into the cuvette cell using a syringe pipette.

Figure 2.13. A PTFE sample holder.

2.6.5 Spectroscopic Ellipsometry

2.6.5.1 Background

Spectroscopic ellipsometry (SE) is a powerful and versatile analytical tool used to characterise the optical properties of materials in a thin film. The SE process involves the measurement of changes in the polarisation state of light when it is reflected from the sample surface and is, therefore, insensitive to changes in the absolute intensity of the measurement beam. [186] This makes the SE measurement accurate and reproducible; as it is a non-invasive technique, it requires only a low-powered light source and, thus, does not affect most operations, which makes it a suitable tool for in situ studies. [187] The foundation of SE goes back to the 19th century, when Drude utilised polarised light in a reflection configuration to study the optical properties and thickness of thin metallic films. [188] Since then, many studies and applications have emerged, which are based either on the ellipsometry or profit directly from its sensitivity; the main idea of ellipsometry is shown in Figure 2.14. When a monochromatic plane light wave is focused on a flat surface at an oblique incidence, the plane of incidence is described as the plane perpendicular to the surface, which includes the vector that indicates the direction of propagation of the light wave (the wavevector, $\mathbf{k}_{in}$). There are two mutually perpendicular vectors of the magnetic field B and the electric field E of a light wave that are perpendicular to $\mathbf{k}_{in}$. The E-vector is designated as the vector, which defines the polarisation of the light wave, as it is decomposed into two components: mutually perpendicular and perpendicular to $\mathbf{k}_{in}$, where they are parallel and perpendicular, respectively, to the plane of incidence. [186].

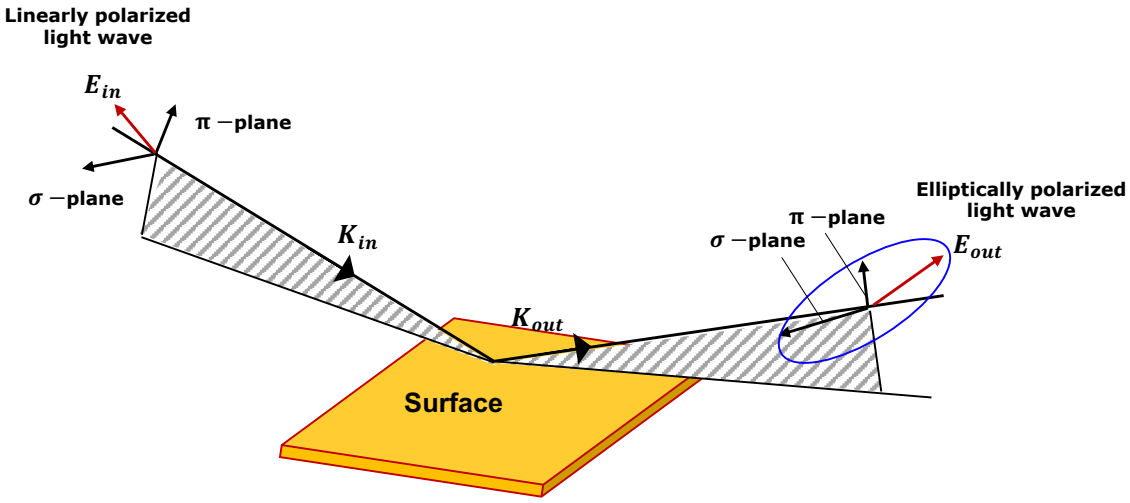

Figure 2.14. Schematic illustration of the general principle in ellipsometry.

The vectors are named based on their German names, Parallel and Senkrecht, and correspond to the Greek letters π and σ, respectively. The components π and σ of **E** can be thought of as oscillating with an amplitude and mutual phase making the endpoint of **E** to move in a straight line along the plane of the two components. As the light wave is reflected from the surface, the polarisation changes to elliptical polarisation, which suggests that the amplitude and mutual phase of the π and σ of **E** have changed; thus, causing the endpoint of **E** to move in an ellipse. The configuration of the ellipse can be detected by a detector and can theoretically be linked to the ellipsometric parameters ψ and Δ. The SE parameters are able to be linked to the reflection coefficients of the light polarised parallel and perpendicular to the plane of incidence ρ_π and ρ_σ, respectively. This relationship is the fundamental equation in ellipsometry and is provided by the complex ratio ρ of the two reflection coefficients. [189].

$$\rho = \frac{\rho_\pi}{\rho_\sigma} = tan(\psi)e^{i\Delta} \tag{2.9}$$

The ellipsometric parameters ψ and Δ are obtained by an ellipsometer and the two reflection coefficients are functions of the complex refractive index of the material. To extract sample parameters, such as film thickness from the measured SE data, an optical model must be built to fit the data. In accordance, CompleteEASE software provides a graphical user interface for designing models, displaying measured data, and fitting models. One such model is Cauchy, which is often used to fit ellipsometric data for dielectrics and semiconductors. The Cauchy model enables the possibility to determine the optical parameters (complex refractive index) and the thickness of analysed layers of a given structure. Specifically, the Cauchy model can be formulated with the following equation [190]:

$$n(\lambda) = A + \frac{B}{\lambda^2} + \frac{C}{\lambda^4} + \cdots, \tag{2.10}$$

2.6.5.2 Experimental Procedure

SE experiments were performed either on thin metal films functionalised with ODT SAMs or on glass /silicon slides functionalised with BIBB-APTES SAMs. All measurements were taken at an angle of incidence of 75° using an Alpha-SE ellipsometer (J.A Woollam CO., Inc., USA) equipped with a He-Ne laser (λ = 633 nm). The ellipsometric Ψ(λ) and Δ(λ) spectra were collected in the range of 370 nm to 1000 nm, and all data were acquired in air and each sample was measured at two different locations to obtain an average. Modelling was performed by

CompleteEASE (v.6.6) software. The thickness of ODT film on the continuous gold surface was obtained by fitting the data to a three-layer model (see Table 2.2). Values of optical constants n and k for BK7 glass, chromium, and gold were obtained by the standard materials library.

Table 2.2. The model used for spectroscopic ellipsometry data fitting.

Layer	Material	Fitted parameters	Comments
Layer #3	Cauchy	*d, A*	*d* is the thickness of the adsorbed layer in nm. The parameters $B_n = 0.01$ and $C_n = 0$ were modified during the fitting.
Layer #2	Gold	*d*	Thickness of the deposited gold film in nm
Layer #1	Chromium	*d*	Thickness of the deposited chromium layer in nm
Substrate	BK7 glass	-	$n = 1.515$

Chapter 3

3 Strong Coupling of Dyes to Plasmon Modes

3.1 Introduction

The development of integrated circuits and their associated lithographic techniques in recent years has enabled tremendous advances to be made in controlling the interaction of light with metallic nanoparticles or nanostructured film. The interaction of light with metal nanostructure is often referred to as plasmonics. [191] Plasmonic nanostructures are characterised by their strong interaction with incident light and free electrons, while metallic nanostructures serve as a platform for localising light in subwavelength regions of space, known as LSPR. [192] The resonance condition of a metallic nanostructure is a function of its size, shape, interparticle distance, composition, and the surrounding medium. [193−195] Several studies have shown that these properties are able to be used for a variety of purposes. [196−199] For instance, Surface-enhanced Raman scattering (SERS) is one of the most common applications of LSPR in biosensing.

Using lithography techniques, arbitrarily shaped nanostructures can be fabricated with rational arrangements. Wesheng et al. [200] reported two EBL-based processes for fabricating gold nanostructures. One process involved making use of metal lift-off and the other involved the use of the plasma etching. As a result, EBL demonstrated the ability to fabricate and control the geometry of gold nanostructure, and both processes were used successfully to produce gold nanoarrays with different periodic arrangements. Comparatively, Ryosuke et al. [201] took a different approach, using nanoimprint lithography to fabricate gold nanostructures on quartz crystal microbalance surfaces; thus, creating a device that could simultaneously measure the mass and the refractive index of the analyte. Other nanofabrication techniques such as colloidal lithography and FIBL have also been used to fabricate Au nanostructures. [202, 203] Although most lithographic techniques have been developed to fabricate complex 2D and 3D structures, some of them show significant limitations, including low fabrication speed, complex fabrication procedures, low flexibility, high costs, and some require templates. To overcome these limitations, a technique, such as IL offers attractive characterisations, and is considered an ideal method for fabricating nanostructures. It is versatile and allows for high resolution and precise control over the geometry and separation of nanostructures, resulting in fabrication reproducibility and precision down to the nanoscale. Moreover, IL does not require a high-cost

infrastructure nor need a photomask to draw patterns, and can form patterns over large areas (up to mm in diameter). Hedberg-Dirk et al. [204] showed that by using IL, it is possible to create large-scale protein arrays, where IL was used to fabricate arrays of channels with a depth of 33 nm in the gold surface over a large area (4 cm^2). The Lloyd's interferometer provides a flexible IL setup with the ability to generate nanostructures at different periodicities without additional modifications to the optical alignment. [103, 104]

To control solid surface properties, SAMs are often used as model systems due to their ability to form highly ordered thin molecular films with tailored chemical properties. One of the most extensively studied platforms are SAMs formed by adsorption of alkanethiols on gold surfaces. Thiol groups have a strong affinity for noble metals, which makes it possible to form uniform and well-packed monolayers on their surfaces. [205−208] Accordingly, SAMs are well suited for use in the field of nanoscience, as they are easy to prepare, that is, they do not need UHV or specialised equipment in their preparation. They are formed on objects of different sizes and are essential components for stabilising and adding function to preformed nanoscale objects, such as thin films. [209] Furthermore, SAMs can be applied to couple the external environment with optical properties of metallic nanostructures (e.g. local refractive index), and to link molecular-level structures with macroscopic interfacial phenomena, such as wetting, adhesion, and friction. [210] Moreover, SAMs can be photopatterned on flat solid substrates, and it was found that by exposing the alkanethiol SAMs on the gold surface to a UV laser beam, the thiol head groups photooxidised to sulfoxide species. [211] This can be explained by the following equation:

$$\mathrm{Au-SR}+\frac{3}{2}\,\mathrm{O_2}+\mathrm{e^-}\rightarrow \mathrm{Au^+}+\mathrm{RSO_3^-} \qquad 3.1$$

As a result, the photooxidation of SAMs enables clean, well-defined surfaces. Tsargorodska et al. [89] fabricated SAMs of alkylthiolates on gold surfaces by IL, and used a Lloyd's mirror interferometer in conjunction with a frequency-doubled argon ion laser emitted at 244 nm, with double exposures. The resulting nanostructures covered macroscopic areas (cm^2), with various morphologies, and had a pitch ranging from 149 nm to 536 nm.

The LSPR of metallic nanoparticles are highly sensitive to refractive index changes that occur when a target analyte binds to the metal film, and they have, therefore, been used for chemical and biological sensing. The interaction between plasmonic nanoparticles and molecular dyes has gained much attention recently due to a wide range of applications including SERS [212], plasmon-enhanced fluorescence [213] and nonlinear optical applications. [214] The interaction

between plasmon and molecule may lead to strong coupling; thus, forming hybrid plasmon-molecule states. These new states (i.e. plexcitons) manifest distinct properties that differ from those of the original states. Therefore, accurate modelling of nanostructure, molecules and their coupling is of utmost importance to support experimental progress.

Overall, the aim of this chapter is to develop approaches based on interferometric lithography for the formation of macroscopically extended arrays of gold nanostructures on solid surfaces. The plasmonic properties of these arrays will be studied as a function of array morphology. In addition, the coupling of LSPR, associated with such arrays to rhodamine B dye will be studied to determine whether strong coupling occurs for gold nanostructure arrays functionalised with films of this dye.

3.2 Experimental Details

3.2.1 Formation of Self-Assembled Monolayers

Glass microscope slides used as control surfaces were cleaned with piranha solution, a mixture of concentrated H_2SO_4 and H_2O_2 in a ratio of 7:3. **Warning:** this mixture is highly reactive and may explode upon contact with organic solvents, so it should be handled with extreme caution. After piranha processing, the glass slides were rinsed thoroughly with deionised water and then dried in a drying oven at 90 °C for 24 h.

Gold films were prepared on glass microscope slides by thermal vacuum evaporation using an Edwards Auto 306 system. First, a thin layer of chromium was deposited on the glass slides to act as an adhesion layer. Afterwards, the gold film was deposited on the chromium layer as an overlayer. Chromium /gold (Cr/Au) evaporations were carried out at a pressure of 10^{-6} mbar at room temperature. The Cr/Au bilayer films with nominal thicknesses of 3 nm and 25 nm were obtained at deposition rates of 0.1 nm s^{-1} and 0.2 nm s^{-1}, respectively. The bilayer thickness values were obtained from the QCM of the evaporator. Therefore, they may differ by up to 8% from the actual thickness value, which were subsequently determined by SE.

Following the evaporation process, the Au substrates (Au / Cr /glass) were immersed in 1 mM ethanolic solution of 1-Octadecanethiol (ODT) within 30 min after they were removed from the vacuum system. Gold substrates were left in ODT solution for at least 24 h to form closely packed SAMs. Prior to utilisation, the substrates were sonicated in ethanol for 3 min to remove any physiosorbed species, and then dried with nitrogen. For the purpose of photopatterning, the substrates were cut into small sizes (0.5 × 1 cm) to fit the exposure stage.

3.2.2 Fabrication of Gold Nanostructures

Figure 3.1 shows schematically the fabrication process used to make Au nanostructures. While all of the parameters can in principle be changed in order to control the lithography process, UV doses were maintained at constant values for the work described in this chapter, with being the annealing temperature, Cr thickness and Au thickness varied. ODT SAMs on Au surfaces were photopatterned by IL using a Lloyd's mirror two-beam interferometer. Details of the Lloyd's interferometer for the IL are described in section 2.5. Briefly, a frequency-doubled argon ion laser with a wavelength of 244 nm was operated at 70 mW. The laser beam passed through a lens-pinhole system before falling onto the Lloyd's mirror interferometer. Part of the coherent beam was focused directly onto the sample surface, while the other part of the beam was focused onto the mirror, from which it was reflected onto the sample surface and interfered

with the other part of the beam to yield sinusoidal patterns. A single exposure was employed to pattern ODT SAMs, and to create a 1D pattern of parallel lines. Double exposures, with rotation in between, were employed to create a 2D pattern of dot structures. The first exposure was carried out at a dose of 38.4 J cm^{-2} after placing the sample on the stage near the reflecting mirror, while the second exposure was carried out at a dose of 27.3 J cm^{-2} after rotating the sample on the stage to a certain angle (see Figure 3.2). After photopatterning, the laser beam was blocked by the beam shutter, and the photopatterned sample was immersed in etching solution for 13 min. This consisted of an ethanolic solution of 2 mM cysteamine and 8% ammonia. Following this, the sample was rinsed with ethanol, and dried with nitrogen. The photopatterned, etched sample was annealed in a chamber furnace (Carbolite). The annealing temperature used for all samples was between 450 °C and 600 °C, and the annealing time was 2 h at a heating rate of 7 °C min^{-1}. The annealed sample was left to cool in air. After annealing, the sample was then imaged under the AFM for further analysis. The same procedures were repeated for preparing each nanostructure sample, unless otherwise noted.

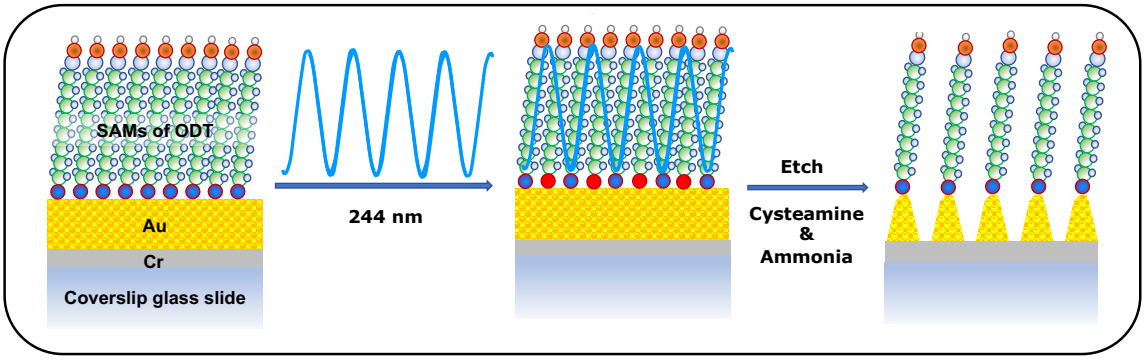

Figure 3.1. Schematic diagram showing the use of ODT SAMs as a resist layer to fabricate Au nanostructures.

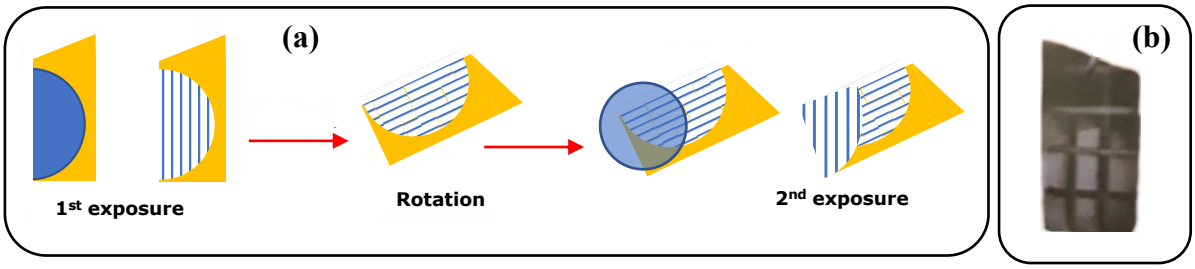

Figure 3.2. Schematic diagram illustrating (a) the fabrication of Au nanostructures using two exposures, with sample rotation in between, and (b) actual sample.

3.2.3 Refractive Index Studies

The bulk refractive index (RI) sensitivity of the Au nanostructures was evaluated by measuring the extinction spectra of annealed samples immersed in different liquids with refractive indices in the range from 1.33 RIU (deionised water) to 1.49 RIU (toluene). The absorption spectrum was measured while the sample was placed in a cuvette filled with a liquid of a given refractive index. Prior to inserting the sample, the solution in the cuvette was measured as a baseline. The measurement was performed after using the stabilisation procedure (i.e. rinsing the sample several times with ethanol and drying with nitrogen until no change in the extinction spectrum was observed).The stability of the optical response was evaluated by performing measurements sequentially in liquids with ascending and descending RI values. The plasmon shift was plotted as a function of the RI, and the RI sensitivity was determined by linear fitting.

3.2.4 Surface Functionalisation

Gold nanostructures were functionalised with Rhodamine B azidopropyl ester ($RBON_3$), which was synthesised by Dr Benjamin Bower, Department of Chemistry, University of Sheffield. In a typical process, the annealed samples were immersed in 1 mM $RBON_3$ solution for more than 24 h. Following this, the samples were sequentially rinsed with dimethylformamide (DMF), 0.5 mM hydrochloric acid (HCl), and then dried under nitrogen.

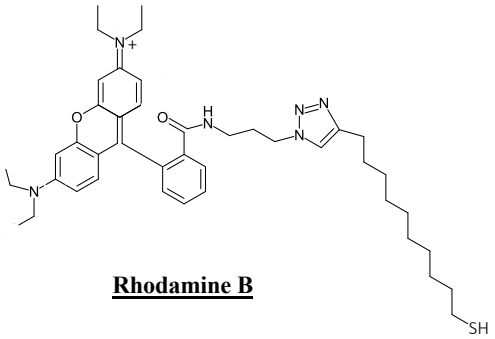

Rhodamine B

3.2.5 Surface Characterisation

Contact angle measurements were performed to verify the hydrophilic/ hydrophobic nature of the surface before and after formation of ODT SAMs on Au surface by the sessile drop method. The morphology of the resulting nanostructure was imaged by atomic force microscope (AFM) operating in tapping mode. The optical properties of the Au nanostructures were characterised by a Cary 50 spectrophotometer. The thicknesses of the Cr and Au layers, as well as the ODT SAMs, were determined by an Alpha-SE ellipsometer; X-ray photoelectron spectroscopy was used to reveal the molecular bonding within the film. More details are discussed in section 2.6.

3.3 Results and Discussion

3.3.1 Characterisation of Self-Assembled Monolayers on Gold Surfaces

To investigate the formation of ODT SAMs on Au substrates, different techniques were used, including CA, SE, AFM, and XPS. The typical time allowed for the formation of ODT SAMs was 24 h, and the substrates were used for measurements within 1 h after they were removed from the solution. The wettability of different surfaces was evaluated using CA measurements, and deionised water was utilised as the test liquid. The change in the CA values reveals the hydrophilic/ hydrophobic nature of the surface, which subsequently could be related to the formation of ODT SAMs. Figure 3.3 below shows the water CA of clean glass substrates, Au-coated substrates, and Au substrates with ODT SAMs. Each value is an arithmetic mean of a minimum five readings taken from at least three different substrates.

As a result, the cleaned substrates were hydrophilic (CA= 9°), and this is due to the presence of native oxide layer and hydroxyl groups on the surfaces as a result of piranha cleaning, as reported previously. [215] Even though the CA of the clean Au substrate was reported as 0°, it is a theoretical value measured only for perfectly clean Au surfaces. Correspondingly, there has always been an ongoing debate in the literature regarding the ease of contamination of Au surfaces. [216, 217] Our results also confirmed that this theoretical value is difficult to achieve, as the water CA of clean Au substrates very quickly reached 68 $\pm$ 2° within a few minutes. Furthermore, the resulting value confirmed that the Au-coated substrate had good wettability; therefore, droplets could spread over it. A significant increase in the water CA was observed after immersing the Au-coated substrates in the ODT solution for 24 h, where the water CA reached 100 $\pm$ 2°. [218]

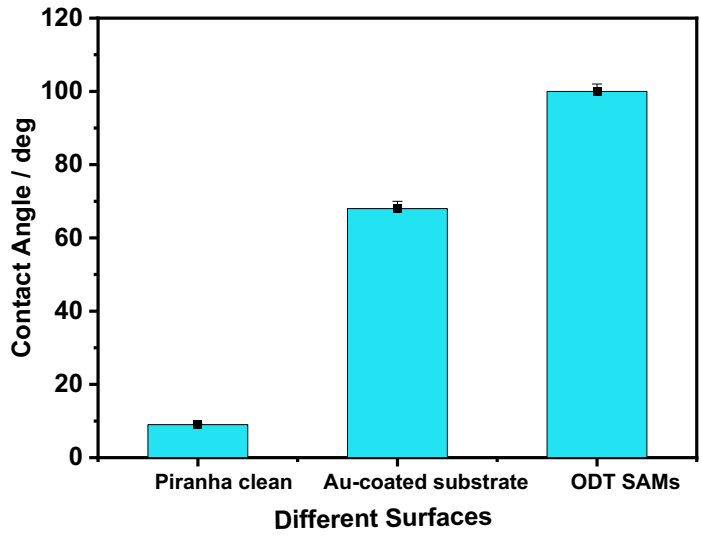

Figure 3.3. A schematic diagram showing the results of CA measurements for different surfaces.

This result indicates that the ODT molecules were successfully absorbed onto the Au-coated substrate, producing hydrophobic surfaces. [218] Comparatively, the SE results showed that the thickness of ODT SAMs was 1.8 $\pm$ 0.1 nm, which is in good agreement with the reported value. [219] Thus, the 'wettability' and thickness measurements of ODT SAMs are consistent with those of well-packed SAMs on Au surfaces. To further determine the formation of ODT SAMs, AFM imaging was performed. The topography of Au-coated substrate and Au-coated substrate with ODT SAMs was investigated by the tapping mode. The results are shown in Figure 3.4 below, and as shown, the Au film formed large crystallites on the substrate surface (see Figure 3.4a), and its roughness value (R_a) was calculated to be approximately 1.97 $\pm$ 0.1 nm. The formation of ODT SAMs reduced this value to 0.87 $\pm$ 0.1 nm, and thus, the mean diameter of the Au crystallites decreased (see Figure. 3.4b).

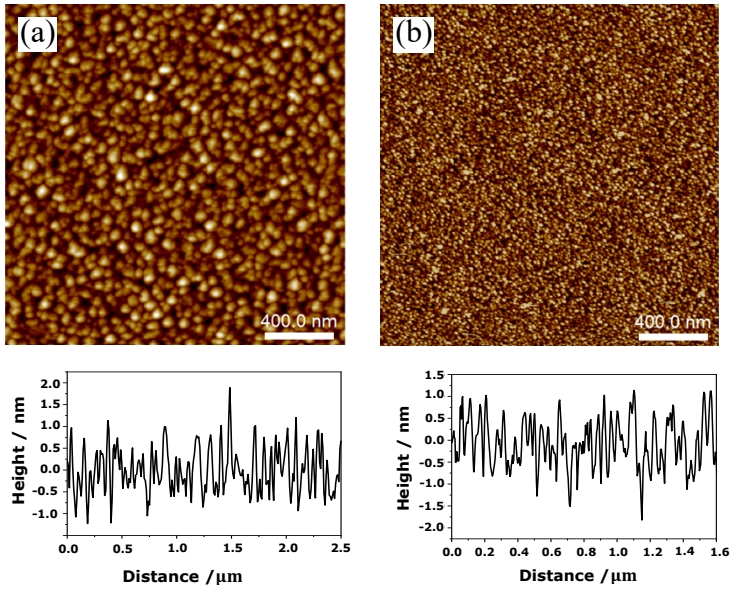

Figure 3.4. AFM height images (2 $\mu m \times 2\ \mu m$) of (a) Au-coated substrate and (b) Au-coated substrate with ODT SAMs.

Further evidence regarding the formation of ODT SAMs on the Au substrate was obtained via XPS analysis. The studies were performed using an Alpha-SE ellipsometer equipped with a He-Ne laser (λ = 633 nm) operating at 150 W with an emission current of 8 mA and under a vacuum of 10^{-9} mbar. Data analyses were performed with CasaXPS; two spots from each type of sample were analysed. The high resolution and survey spectra were collected at fixed analyser pass energies of 20 and 160 eV, respectively. The carbon 1s (C 1s) peak at 285.0 eV was used as a reference to calibrate all binding energies. Figure 3.5 shows XPS wide scan spectra of Au substrates, which have confirmed that the peaks are associated with the elements

of carbon (C), oxygen (O), sulfur (S), and gold (Au). It was also observed that the intensity of the C1s peak increased after the Au substrates were immersed in 1 mM ODT solution (see Figure 3.5a and b). Meanwhile, Figure 3.6 demonstrates the XPS spectra in the C1s region, in which peaks at the binding energy of 285.0 eV were attributed to the alkyl chain or methyl species (i.e. $C-C$ species). For the Au-coated substrates, the C1s peak showed a shoulder at higher binding energy (see Figure 3.6a), which might be due to the presence of surface contaminants containing $C-O$ or $C=O$ bonds. [220] The intensity of the higher binding energy shoulder, however, was reduced after the immersion of Au substrates in ODT solution, and the spectrum was dominated by the main feature at 285.0 eV (see Figure 3.6b). Figure 3.7 shows the XPS spectra in the S 2p region; for the Au-coated substrates, there was no evidence of attributable sulfur. Nevertheless, after the formation of ODT SAMs, a clear peak attributed to the sulfur species was observed. Moreover, the S 2p spectra highlight a single doublet with a binding energy of ≈162.0 eV, corresponding to the thiol sulfur atom, S $2p_{1/2}$ and S $2p_{3/2}$. The doublet results from spin-orbit coupling. Figure 3.8 shows the XPS spectra of the Au 4f region, in which no obvious change was observed.

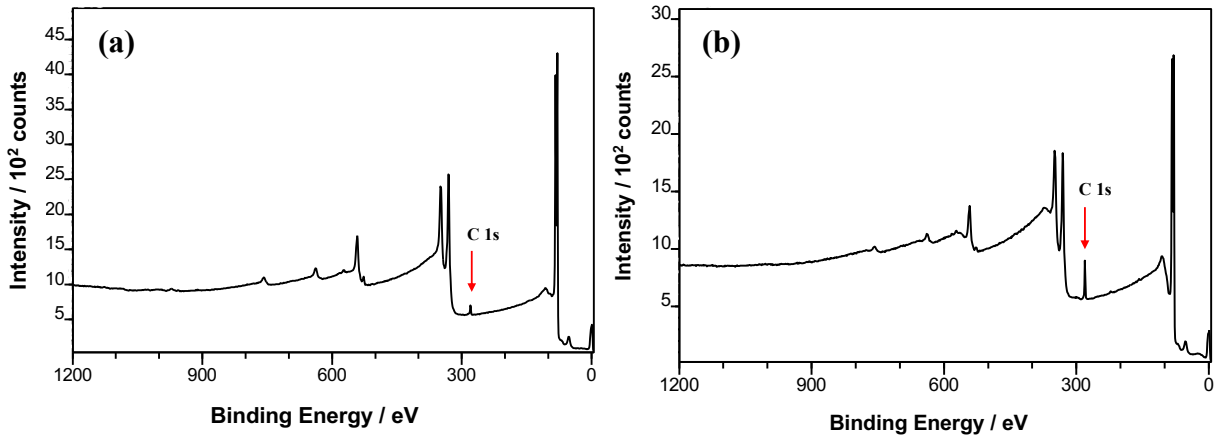

Figure 3.5. Survey-XPS spectra (wide scan) of the Au surface: (a) as-deposited Au and (b) after immersion in 1mM of ODT solution for 24 h.

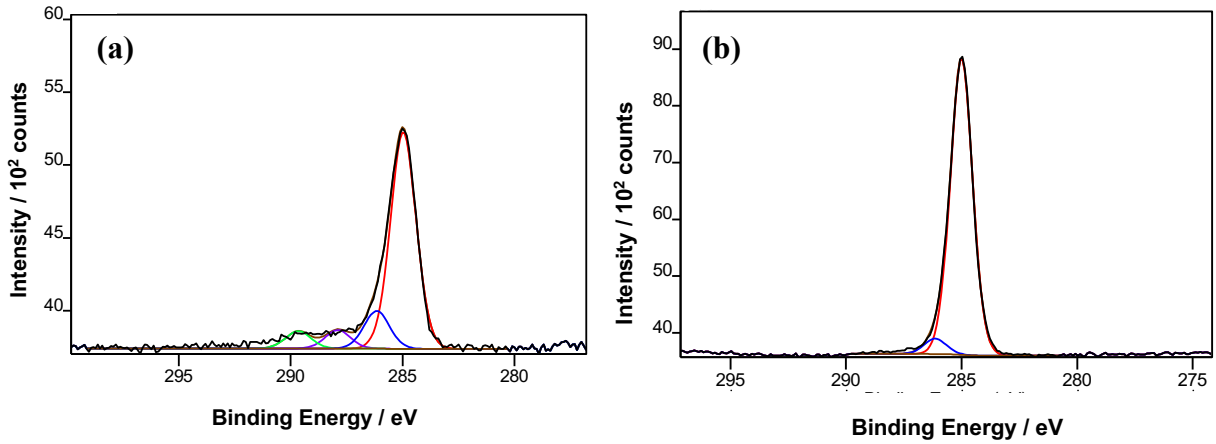

Figure 3.6. High-resolution spectra in C 1s region: (a) as-deposited Au and (b) after ODT SAM formation.

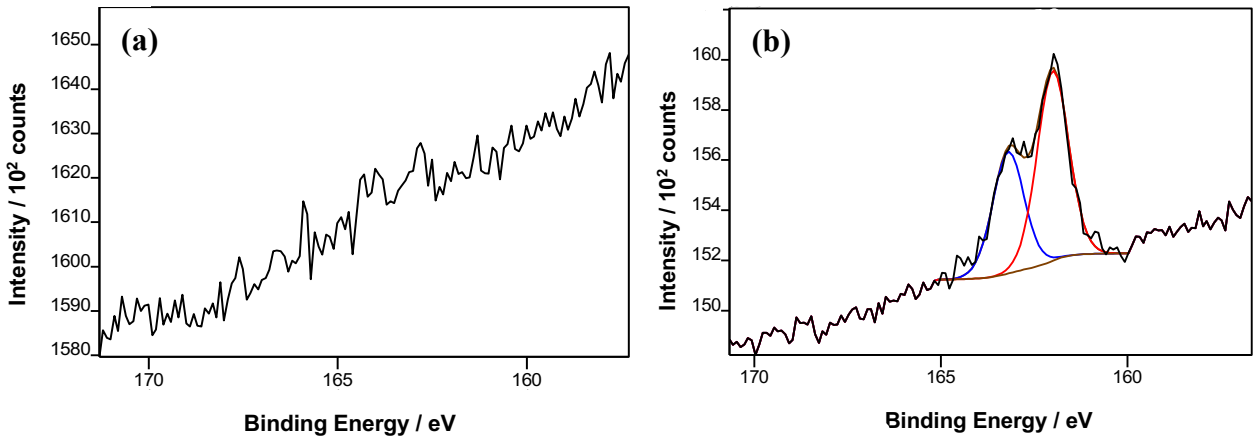

Figure 3.7. High-resolution spectra in S 2p region: (a) as-deposited Au and (b) after ODT SAM formation.

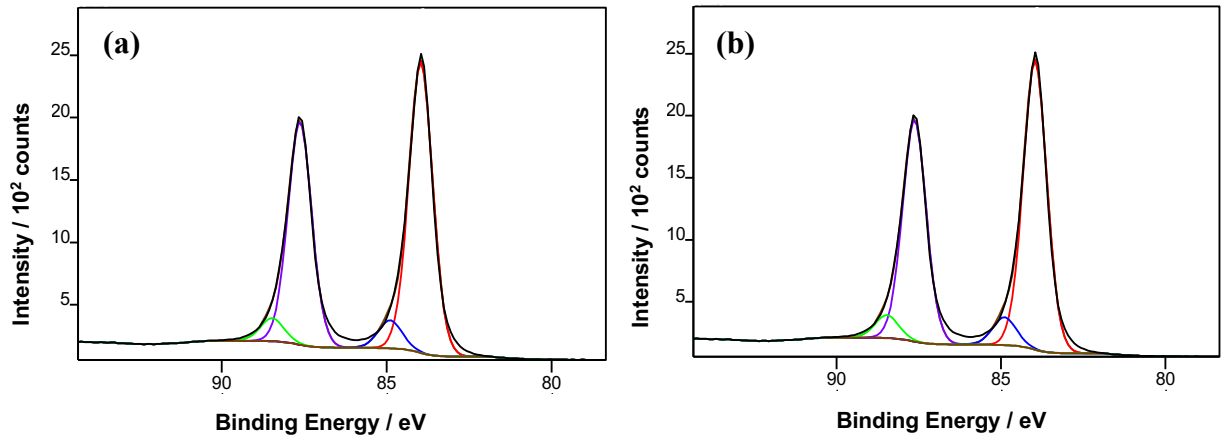

Figure 3.8. High-resolution spectra in Au 4f region: (a) as-deposited Au and (b) after ODT SAM formation.

3.3.2 Lithographic Fabrication of Plasmonic Gold Nanostructures

To enable programmable fabrication of macroscopically expanded arrays of Au nanostructures, the relationship between arrays morphology and the processing conditions was investigated systematically. IL was used to pattern the Au surface, as described previously in section 3.2.2, using ODT SAMs as the resist layer. The wavelength of the laser source used was 244 nm and it passed through the Lloyd's mirror two-beam interferometer system. A single exposure to the interferogram yielded patterns consisting of lines, with photooxidation occurring where the sample was exposed to maxima in the interferogram; rotation of the sample, followed by a second exposure, yielded arrays of dots. The photooxidation of ODT SAMs allowed for easy removal of exposed regions upon etching, which is due to the conversion of alkylthiolates into weakly bound alkylsulfonates. It was reported elsewhere that SAMs of thiolates on Au surfaces can be oxidised to weakly bound sulfonates by exposing the surfaces to deep UV light. [221] Figure 3.9 shows AFM height images of arrays of Au nanostructures, where the morphology of the structures is directly related to the exposure time. Accordingly, as can be noted, single exposure of the two-beam IL system resulted in a 1D line pattern, and double exposure resulted in a 2D dot pattern. The result supports the efficiency of IL to achieve nanoscale patterns. Overall, the three images provide evidence of the presence of well-defined periodic arrays of Au nanostructures with the complete removal of the oxidised SAMs. The resulting structures represent nanostructures with a pitch defined by the angle of incidence (θ), which is the angle between the mirror and the sample during UV exposure. The pitch of the line pattern below is about 314 ± 10 nm, which can be adjusted by rotating the sample stage. The line width is about 145 ± 12 nm, which is related to the exposure dose and the etching time. Figure 3.9c shows a large-scale AFM height image (4 μm × 4 μm) of dot arrays, in which the overall structure is highly uniform throughout the surface.

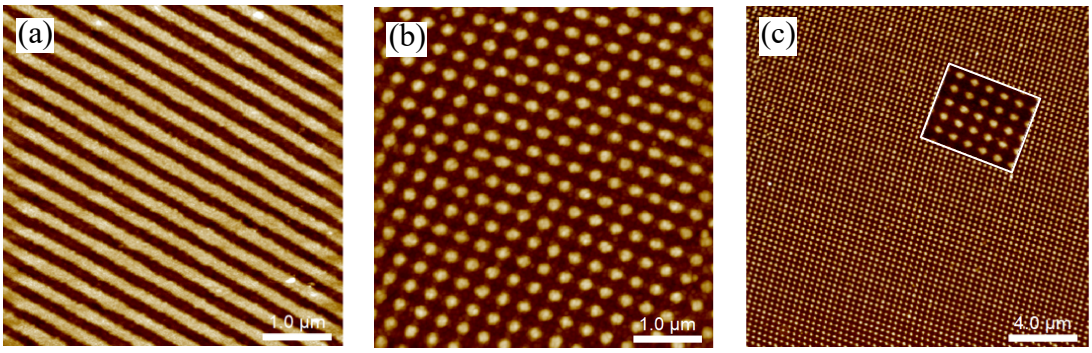

Figure 3.9. AFM height images of Au nanostructures fabricated by IL with: (a) single exposure; (b) double exposure with 90° between exposures; and (c) showing uniformity of structures on a large scale and the inset shows a region of the pattern at higher resolution.

3.3.2.1 Variations in Angle of Incidence

To investigate the fundamental properties of plasmonic Au nanostructures and the correlations between different parameters, nanostructures with different feature dimensions were produced by exposing ODT SAMs on Au surfaces to five different angles of incidence of the laser beam, namely 15±5°, 25±5°, 30±5°, 35±5°, and 40±5°. The feature dimensions were determined by calculating the pitch of the interference patterns, which is a measure of the centre-to-centre distance between neighbouring nanostructure arrays in a row or column. Indeed, the pitch of the interference patterns can be calculated theoretically using equation 1.56. According to this equation, the pitch of Au nanostructures is inversely proportional to the incidence angle. Figure 3.10 shows the AFM height image and cross-sectional surface profiling of Au nanostructures. The pitch, height, spacing and full width at half maximum (FWHM) of the nanostructure arrays were measured using the cross-section shown below each image in this thesis. As can be seen from Figure 3.10b, the height is calculated by measuring the height of each nanostructure from its base to its peak. While the spacing is calculated by measuring the distance between adjacent nanostructures within the array, and the FWHM is obtained by measuring the distance between the two points on either side of the peak. [89]

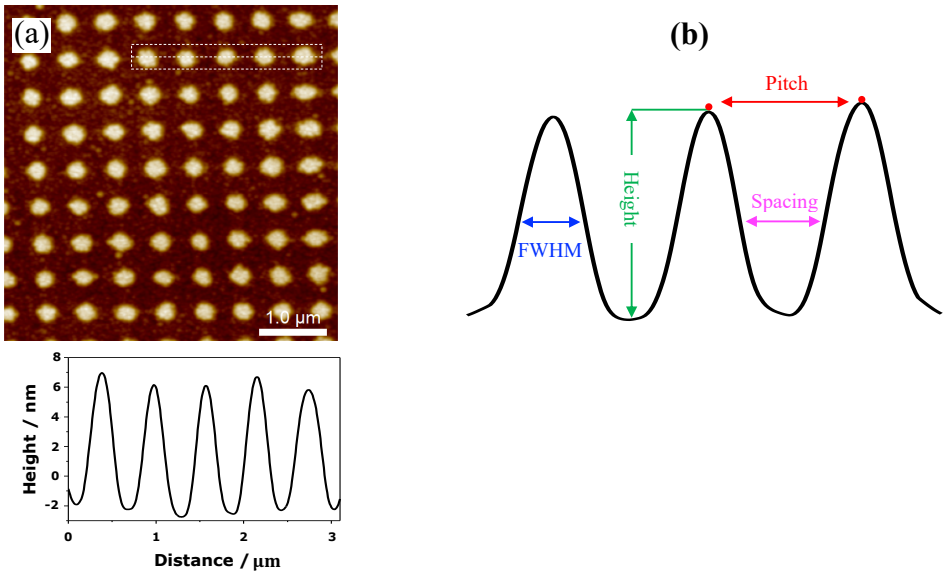

Figure 3.10. (a) AFM height image and (b) cross-sectional surface profiling of the Au nanostructures.

Figure 3.11 shows AFM height images of Au nanostructures fabricated by IL at different angles of incidence with a fixed rotation angle of 90°, in which they were subjected to double exposure using similar doses and etching times (1st dose = 38.4 J cm^{-2}, 2nd dose = 27.3 J cm^{-2}, etching time =13 min). Figure 3.11a shows the square arrays with a pitch of 503 ± 17 nm, a height of 11 ± 0.5 nm and a FWHM of 259 ±11, created with an incidence angle of 15±5°. As the angle of incidence was increased to 25±5° and then 30±5°, the pitch decreased from 315 ± 18 nm to 260 ± 14 nm, respectively (see Figures 3.11b and 3.11c). Consequently, each increase in the angle of incidence led to a decrease in the pitch of the nanostructures, which is consistent with the reported study. [204] With our IL setup, as the pitch decreased, the FWHM also decreased. For example, the FWHM decreased from 123 ± 5 nm to 112 ± 6 nm, when the pitch decreased from 260 ± 14 nm to 225 ± 13 nm, respectively (see Figures 3.11c and 3.11d). From the AFM images, it can also be noted that the largest dimension (or the largest nanostructure size) was obtained using the smallest incidence angle of 15±5° (see Figure 3.11a), and the smallest dimension (or the smallest nanostructure size) was obtained using the largest incidence angle of 40±5° (see Figure 3.11e). Accordingly, these results confirmed that the square arrays of the Au nanostructures vary in their dimensions in response to the angles of incidence. [89, 204]
In addition, AFM height images from three different samples for each angle of incidence were utilised to calculate the mean pitch, height, spacing, and FWHM of the Au nanostructures, with eight random readings taken from each sample. The results are summarised in Table 3.1 and Figure 3.12, respectively. It should be noted that the errors quotes are the standard errors in each case. Moreover, the theoretical values were calculated using equation 1.56, with air as the medium. For irradiation at 244 nm and an angle of incidence of 35±5°, the predicted pitch was calculated to be 213 nm. Chua et al. [222] reported the observation of patterns that are in good agreement with the theoretically calculated values. Comparing the measured value with the theoretical value, it was found that the pitches of the Au nanostructures (measured at 222 ± 10 nm and theoretically calculated at 213 nm) were very close, indicating that the high-resolution structures were fabricated by the Lloyd's mirror interferometer method. The small difference between the measured and theoretical values is probably due to the small uncertainty on the angle of incidence, which was set manually. The difference is expected to be approximately ±5° (see Table 3.1).

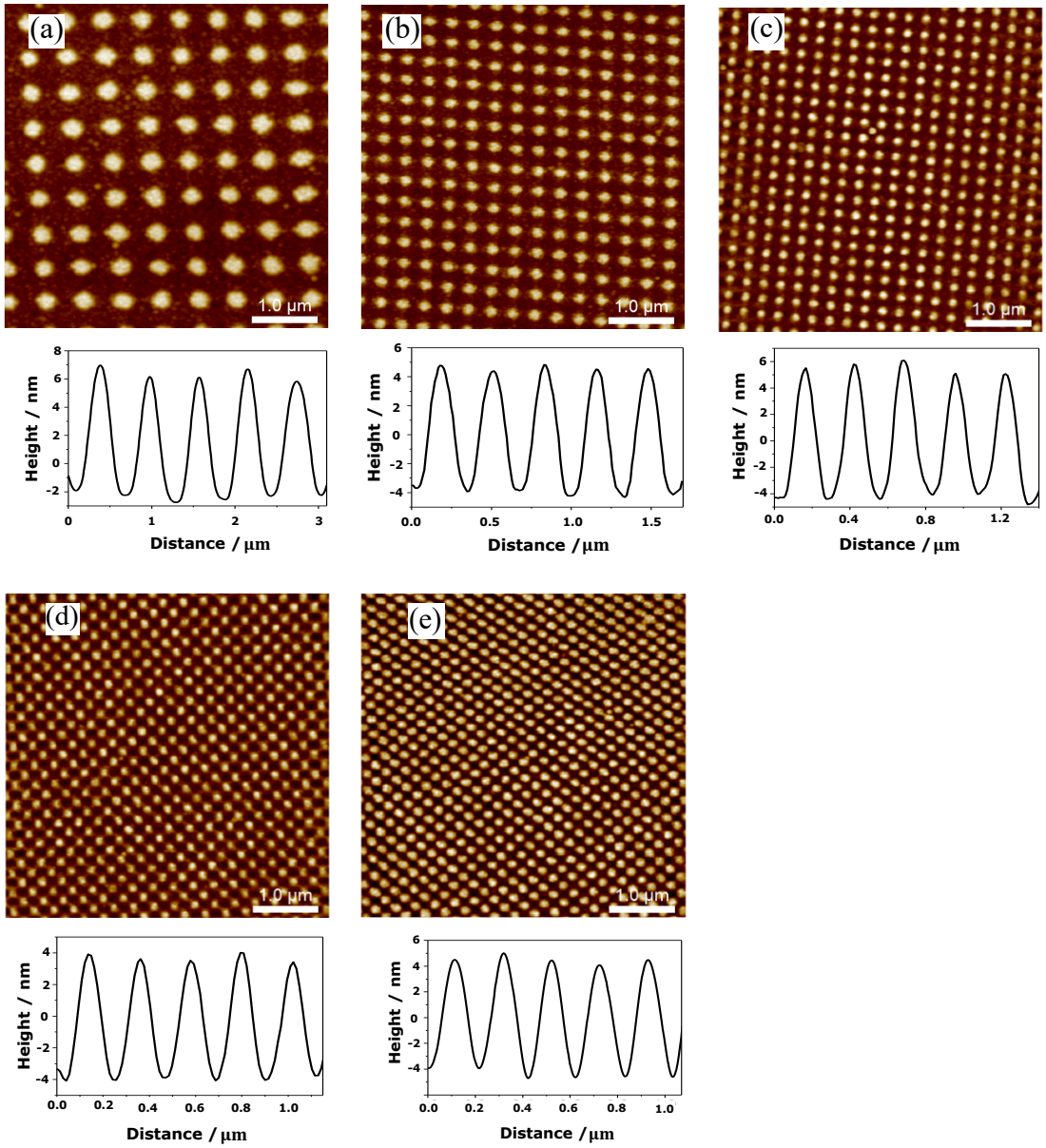

Figure 3.11. AFM height images of Au nanostructures fabricated using double exposure with different angles of incidence during IL (a): θ =15±5°, (b): θ = 25±5°, (c): θ = 30±5°, (d): θ = 35±5° (e): θ = 40±5°, and with a fixed angle rotation (ϕ = 90°).

Table 3.1. Effects of variations in the angle of incidence on the properties of Au nanostructures.

Angle of Incidence (θ)	Theoretical Pitch (nm)	Measured Pitch (nm)	Measured Height (nm)	Measured FWHM (nm)	Measured Spacing (nm)
15±5°	472	502 ± 15	10 ± 0.8	262 ± 10	333 ± 13
25±5°	289	311 ± 13	8 ± 0.5	147 ± 10	162 ± 13
30±5°	244	256 ± 13	6.3 ± 0.6	121 ± 7	137 ± 9
35±5°	213	222 ± 10	6 ± 0.1	109 ± 8	115 ± 7
40±5°	190	201 ± 15	5.5 ± 0.6	100 ± 11	102 ± 8

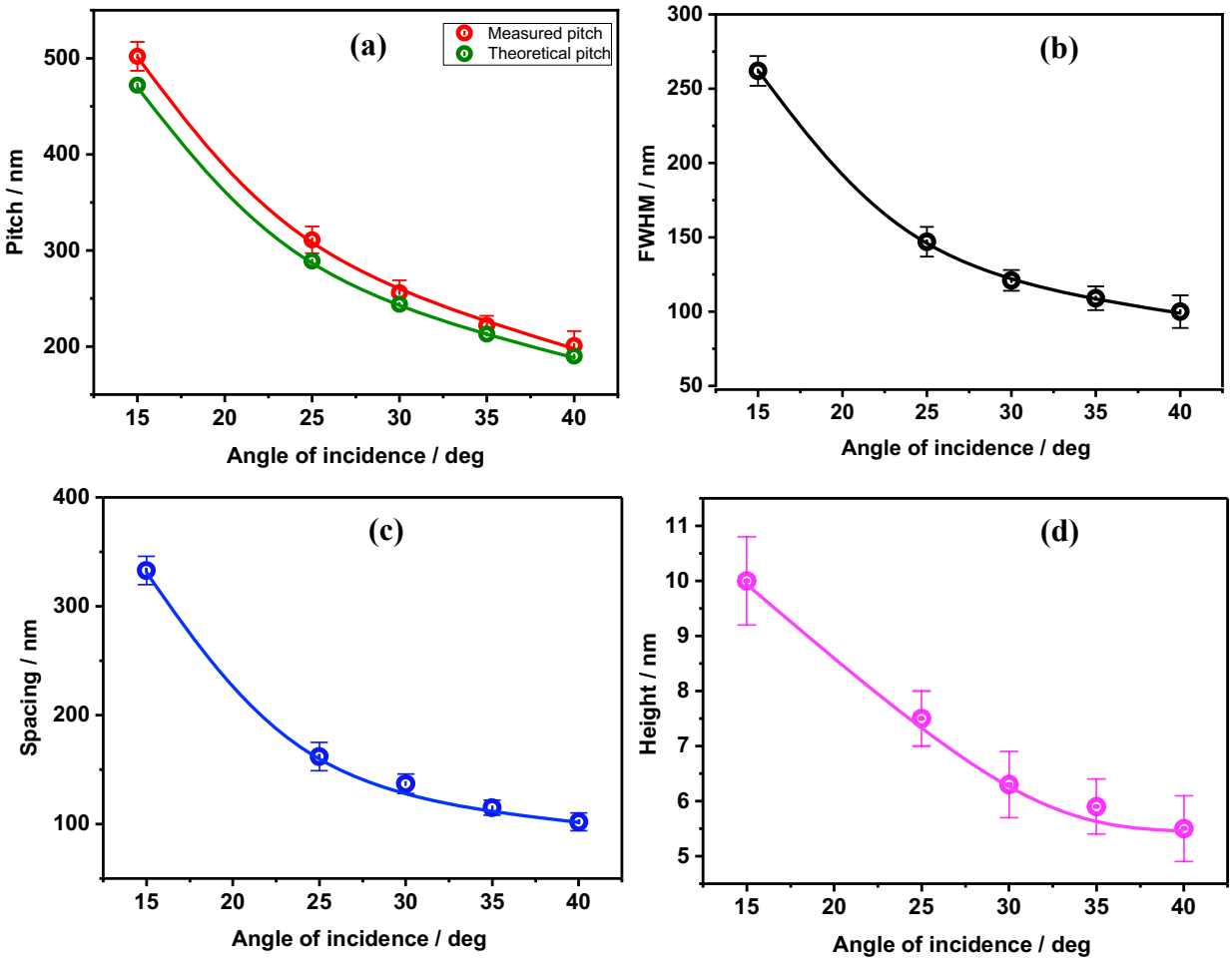

Figure 3.12. Graphs showing the dependence of nanostructure dimensions on the angles of incidence, where (a) represents pitch, (b) FWHM, (c) spacing, and (d) height of nanoarrays against different angles of incidence.

3.3.2.2 Variations in Angle of Rotation

Au nanostructures exhibit unique plasmonic properties, characterised by LSPRs that are highly sensitive to the size and shape of the nanostructures. [223] The angle of rotation (ϕ) plays a significant role in shaping the overall geometry of the nanostructure arrays. By controlling the angle of rotation, it is possible to create a variety of structures with a periodicity and geometry that are able to be controlled, which in turn tune their optical properties and behaviour, enabling custom-designed nanostructures for specific applications. In addition, IL, using Lloyd's mirror interferometer, enables rapid fabrication of samples with a variety of structures, enabling their suitability for sensing applications to be evaluated systematically. To demonstrate the value of this potential, a library of samples was fabricated using a fixed incidence angle between the sample and the mirror, while varying the angle of rotation. Figure 3.13 shows the AFM height images of Au nanostructures created by IL using Lloyd's interference setup with an incidence

angle of 25°, giving a pitch of about 319 ± 10 nm. Figure 3.13a presents a square array of dots with a FWHM of 149 ± 9 nm, obtained after rotating the sample to 90°. Moreover, when the sample was rotated 60° from normal incidence as shown in Figure 3.13b, a hexagonal array of dots was produced. Figures 3.13c, d, and e present the Au nanostructure arrays generated by rotating the samples to 30°, 20° and 15°, respectively. Hence, as the angle of rotation decreased, the arrays became elongated until ϕ =15°, rows of needles were formed. Figure 3.13f shows parallel lines of arrays formed by single exposure at a dose of 38.4 J cm^{-2} and with ϕ = 0°. It should also be noted that there are small aggregates of Au residues between the nanostructure arrays, as shown in Figure 3.13e, which suggests incomplete etching.

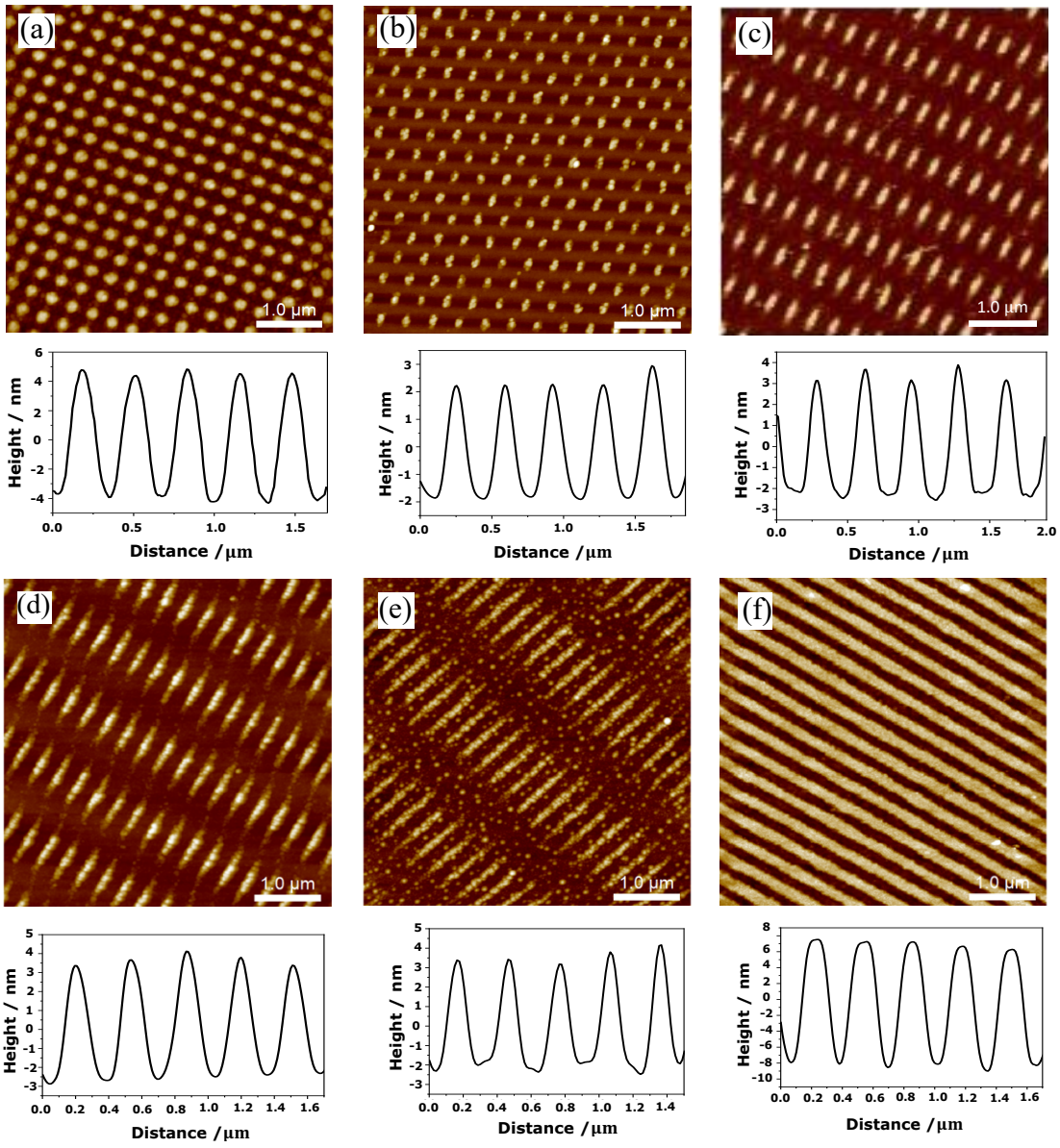

Figure 3.13. AFM height images of Au nanostructures fabricated by IL using double exposures with a fixed angle of incidence (θ = 25±5°) and six different rotation angles: (a) ϕ = 90°, (b) ϕ = 60°, (c) ϕ = 30°, (d) ϕ = 20°, (e) ϕ = 15°, and (f) ϕ = 0°.

3.3.3 Influence of Thermal Annealing on Gold Nanostructures

Annealing is a thermal treatment process utilised to modify the properties of materials through controlled heating and cooling cycles. [224] In the field of nanotechnology, annealing plays a crucial role in tailoring the structure, composition, and performance of nanomaterials, such as nanoparticles, nanowires, and thin films. Accordingly, this process allows for the elimination of defects, the optimisation of crystallinity, and the creation of unique properties that are not attainable through other means. Several studies have been conducted to evaluate the effect of the annealing process on material properties. Specifically, Matsumae et al. [225] explored the bonding performance of Au−Au with different adhesion layers, including Cr and Ti/Pt after annealing at 200 °C, 250 °C, and 300 °C. They found that the adhesion layers showed variable behaviours at different annealing temperatures. Medina et al. [226] studied the morphological evolution of Au films on SiO_2/Si substrates that were annealed at 100 °C for different times. As a result, they proposed a model to describe a recrystallisation process that is controlled by the surface crystalline reorientation. Serrano et al. [227] demonstrated the evolution of surface plasmons in Au films as a function of annealing temperature from ambient temperature to 500 °C. This evolution is attributed to the formation of agglomerated islands in the glass substrate by annealing.

In the current study, Au nanostructures fabricated by IL exhibit weak LSPR extinction spectra, which cannot be exploited for practical applications. Hence, thermal annealing was applied as a simple technique to produce nanostructures with strong LSPRs. The samples were first made by IL, etched with cysteamine solution, and then annealed. Figure 3.14 shows an example of a sample prepared with an incidence angle of 25°, and a rotation angle of 90°. The morphology of the sample and its structure after being annealed to 525 °C are presented in Figures 3.14a and b, respectively. Further, the extinction spectra of the sample before and after annealing are shown in Figure 3.14c. From the comparison of their AFM images and spectra, it can be seen that the annealed sample has a qualitatively different shape and stronger LSPR band. The morphology of the structure changed from being nearly flat-topped to almost pyramidal. Both phenomena arise from structural changes due to the annealing process. [89] The pitches of both structures, annealed and non-annealed, were measured to be approximately 319 ±14 nm; while the dimensions of annealed structures were much higher compared to the non-annealed structures. Furthermore, the spacing between the arrays was slightly reduced, possibly due to the incorporation of small crystals present between the nanostructure arrays with larger square arrays during the thermal annealing process.

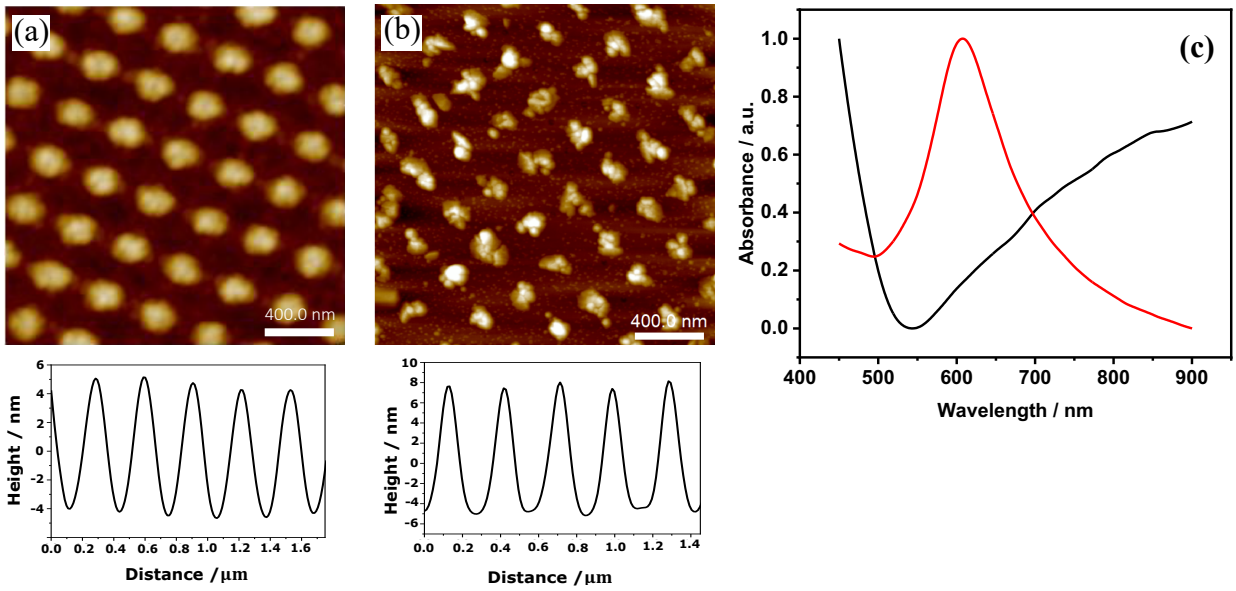

Figure 3.14. (a) and (b) Show the AFM height images (2 µm × 2 µm) of Au nanostructures before and after annealing, respectively. (c) Shows the UV-Vis spectra of annealed (red peak) and non-annealed (black peak) samples.

Figure 3.15 shows the extinction spectra of Au nanostructures before and after annealing. The samples were fabricated with different angles of incidence: 15±5°, 25±5°, 35±5°, and 40±5°; while the annealing temperature was set at 525 °C for 2 h. As can be noted in Figures 3.15a, b, c, and d, there are no obvious plasmon bands for the Au nanostructures before annealing at all angles of incidence, while after annealing, all the structures yielded strong plasmon bands. In general, the annealed samples showed strong plasmon bands in the range of 580−720 nm; however, there is no clear dependence of the LSPR bands on the variation of incidence angles. The data in Table 3.2 depict the extent of changes in dimensions and optical properties of Au nanostructures after annealing under different fabrication conditions. For samples fabricated with $\theta = 15\pm5°$, the pitch remained constant at approximately 514 nm following annealing, although the structures significantly increased in height (by a factor of ca. 3). For $\theta = 25\pm5°$, the pitch also remained the same at around 317 nm; however, a slight decrease was observed for others (i.e. spacing and FWHM), in addition to an increase in the height. For $\theta = 35\pm5°$, and $40\pm5°$, the results are consistent with the above, although there is a slight increase in heights, rather than large increases at other angles. Based on what we discussed earlier, each increase in the angles of incidence leads to a decrease in the dimensions of the nanostructures. It seems that for smaller angles (e.g. $\theta = 15\pm5°$), the Au nanostructures tend to undergo significant grain growth after annealing. This could be because larger nanostructures have more atoms available for diffusion and rearrangement, allowing for greater recrystallisation when energy is applied during annealing. For larger incidence angles (e.g. $\theta = 40\pm5°$), the diffusion

of atoms might be more limited due to the reduced number of atoms in each nanostructure. This can result in less noticeable grain growth after annealing, and thus, results in almost no change in height.

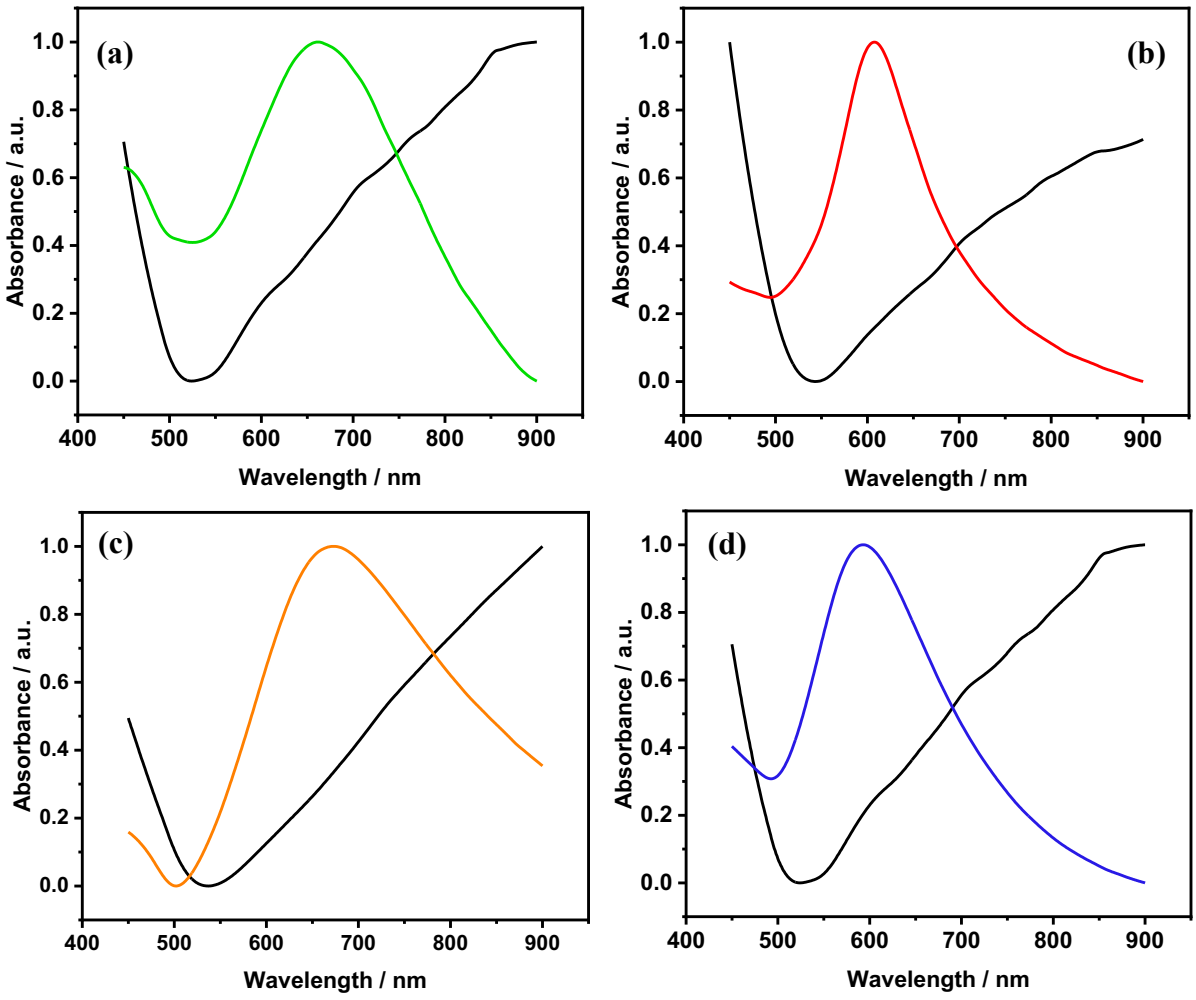

Figure 3.15. UV-vis spectra of Au nanostructures before annealing (black spectra) and after annealing (coloured spectra) at different angles of incidence: (a) $\theta = 15\pm5°$ (b) $\theta = 25\pm5°$, (c) $\theta = 35\pm5°$, and (d) $\theta = 40\pm5°$.

Table 3.2. Effect of Annealing on the dimensions and optical properties of Au nanostructures.

θ /deg	Annealing		Period (nm)	Height (nm)	Spacing (nm)	FWHM (nm)	λ_{max} (nm)
	Temp /°C	Time /h					
15°	as prepared	-	514 ± 13	10 ± 0.2	336 ± 16	263 ± 10	absent
15°	525°	2	514 ±18	29 ± 2	338 ± 13	228 ± 6	661
25°	as prepared	-	317 ± 9	7 ± 0.4	170 ± 11	140 ± 10	absent
25°	525°	2	317 ± 6	22 ± 2	148 ± 6	125 ± 5	608
35°	as prepared	-	219 ±11	6 ± 0.2	114 ± 2	103 ± 4	absent
35°	525°	2	219 ± 8	9 ± 1	106 ± 5	95 ± 11	673
40°	as prepared	-	196 ± 6	6 ± 0.6	97 ± 9	93 ± 7	absent
40°	525°	2	196 ± 4	7 ± 0.7	94 ± 6	89 ± 7	593

3.3.4 Effect of the Thickness of Adhesive Chromium Layer and Annealing Temperature on Morphologies and Optical Properties of Plasmonic Arrays of Gold Nanostructures

It is well known that the LSPR properties of Au nanostructures are strongly influenced by the particle size, shape, and interparticle spacing. In the evaporation protocol, the Au substrates can be modified by controlling different experimental conditions, such as Cr/Au film thickness, Cr/Au deposition rate, and vacuum pressure. In this section, a systematic study was conducted to determine the optimal annealing method for fabricated samples. The following parameters were focused on: Cr thickness of the evaporated Au substrates, and annealing temperature of the Au nanostructures. Hence, the effects of the Cr thickness of Au substrates between 1 to 14 nm, as well as the annealing temperature from 400 ℃ to 600 ℃ on the surface morphology and optical properties of Au nanostructures were studied by annealing the samples in a chamber furnace. As an initial step, a collection of Au/Cr substrates were prepared. The substrates were subjected to the same evaporation conditions, except for the thickness of Cr, which differed between each substrate. The selected Cr thickness was chosen to cover the entire range of Au nanostructures fabricated by IL. Experimentally, the higher Cr thickness was used, the darker substrate colour was observed. The thicknesses of Cr and Au were determined by QCM, and SE, and the results are shown in Figure 3.16. The QCM thickness measurements were in good agreement with the SE measurements. In a small number of cases, the QCM measurements differed from the SE data. This is to be expected, as QCM measurements are subject to greater ratio errors, and the SE measurements are regarded as definitive.

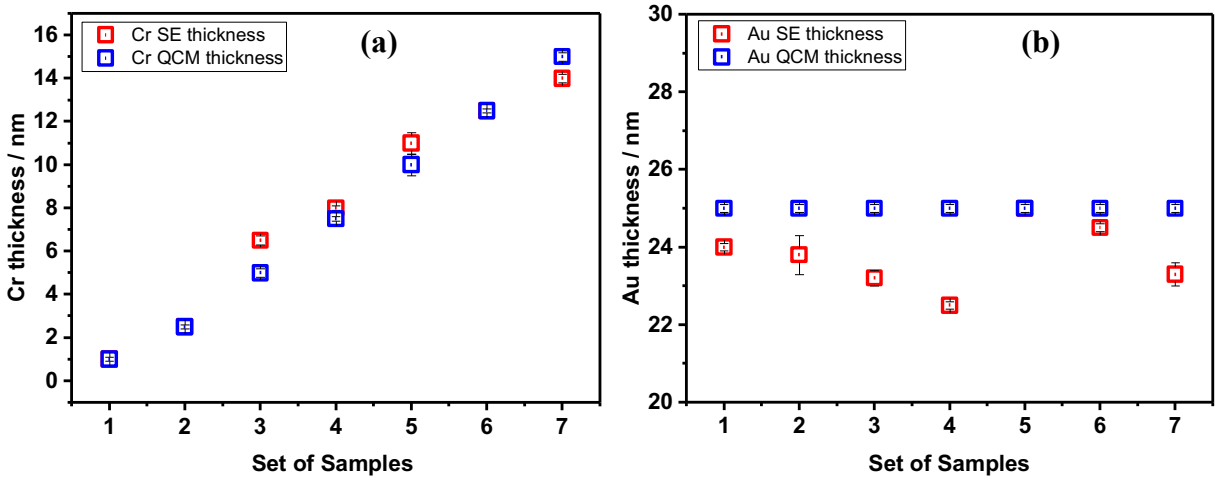

Figure 3.16. Thickness of gold substrates: (a) chromium thickness obtained by QCM ( ) and SE ( ) and (b) gold thickness obtained by QCM ( ) and SE ( ).

3.3.4.1 Surface Morphology

The surface morphology of Au nanostructures plays a crucial role in determining their final optical properties. Hence, optimising the performance of nanostructures often involves thermal annealing. A common method to enhance the adhesion of Au films to glass substrates is to use an adhesion layer. Correspondingly, as it is more chemically reactive than noble metals, Cr is the most commonly used adhesion layer material. Chromium is able to chemically bond to the glass substrates, thus improving adhesion and enhancing the thermal stability of the overlayer. During the deposition process, both the adhesion layer and overlayer undergo nucleation, grain growth, and continuous film formation. [224, 228, 229]

Special attention is given here to the changes in the surface morphology of Au nanostructures induced by annealing, as well as the variation in Cr thicknesses. Subsequently, for this purpose, seven different sets of samples were selected. The fabrication procedure was consistent for all samples, as they were fabricated by IL using the same exposure doses (1st dose = 38.4 J cm^{-2}, 2nd dose = 27.3 J cm^{-2}), and the same etching time (13 min). After IL fabrication, thermal annealing was carried out in air for 2 h (heating rate 7 °C min^{-1}). Each group contained eight samples and each sample was annealed at different temperatures. Moreover, the thickness of Cr varied from group to group, while the thickness of Au remained the same at approximately 24 ± 1 nm (see Table 3.3). The surface morphology of freshly-fabricated Au nanostructures and their corresponding resulted annealed samples were examined using AFM in tapping mode under ambient conditions. As a consequence, Figures 3.17a and 3.17b show photos of the actual sample obtained before and after thermal annealing, respectively. In general, freshly-fabricated samples appeared in faint colour, while all annealed samples appeared in bright golden colours, regardless of annealing temperatures. The changes in the surface colour indicate pronounced modifications in the Au nanostructures caused by the annealing. [230]

Table 3.3. Conditions of evaporated Cr/Au substrates and annealing of Au nanostructures.

Set	**Cr/Au Substrate**		**Au nanostructures fabricated by IL**							
	Cr/Au SE Thickness (nm)		**Annealing Temperatures (°C) / 2 h**							
	Cr	**Au**	**400**	**450**	**475**	**500**	**525**	**550**	**575**	**600**
1	1.5 ± 0.1	24 ± 1	✓	✓	✓	✓	✓	✓	✓	✓
2	2.5 ± 0.2									
3	6 ± 0.5									
4	8 ± 0.1									
5	11 ± 0.1									
6	12.5 ± 0.1									
7	14 ± 0.1									

Figure 3.17c displays a representative AFM height image of freshly-fabricated samples before annealing, revealing well-defined periodic arrays. Subsequent annealing resulted in significant changes in surface morphology, with variations observed at different annealing temperatures. Consequently, the evolution of surface morphology can be classified into three main categories. The first category represents Au nanostructures with regular patterns after annealing. This was observed in two sets of samples: (set 1) nanostructures fabricated on Au substrates with a Cr thickness of 1.5 ± 0.1 nm, and (set 2) nanostructures fabricated with a Cr thickness of 2.5 ± 0.2 nm. For clarity, Figure 3.18 demonstrates only a selection of annealed samples, with particular emphasis on the Au nanostructure morphology at the lowest, average, and highest levels of annealing temperatures.

Figures 3.18a, b, and c show AFM height images of the annealed samples obtained from set 1 after annealing at 475, 500, and 600 ℃, respectively. As can be noted, the annealing does not significantly affect the morphology of the nanostructures, as regular patterns were maintained at different annealing temperatures, although some surface damage to the Au nanostructures occurred. Similarly, the samples obtained from set 2 and annealed at different temperatures showed a consistent level of pattern regularity, (see Figures 3.18d, e, and f). We hypothesise that when Cr is deposited in thin layers (i.e. Cr $\leq$ 2.5 nm), the resulting Cr grains tend to be small. Meanwhile, Au tends to recrystallise during annealing, as mentioned previously. When the Cr grains are small, there is less surface area for the Au to nucleate onto, resulting in smaller and more uniform Au crystallites that do not spread or diffuse significantly during annealing. This can lead to regular patterns where the Au remains localised on the small Cr grains.

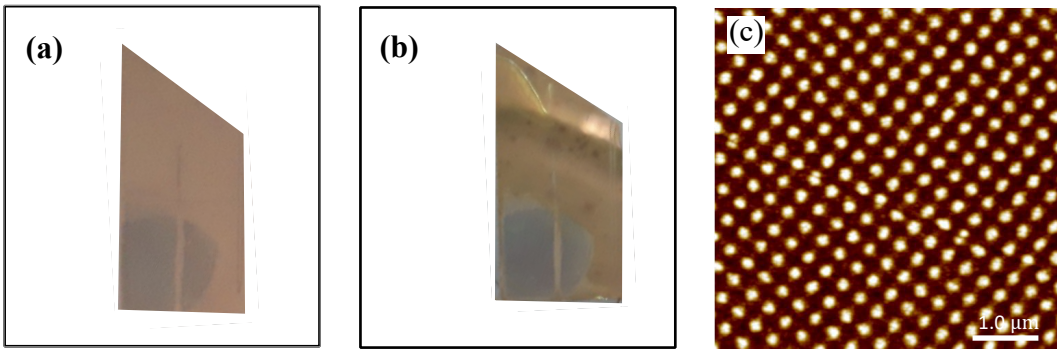

Figure 3.17. Photos of the actual sample (a) before and (b) after annealing. (c) AFM height image of the freshly-fabricated sample.

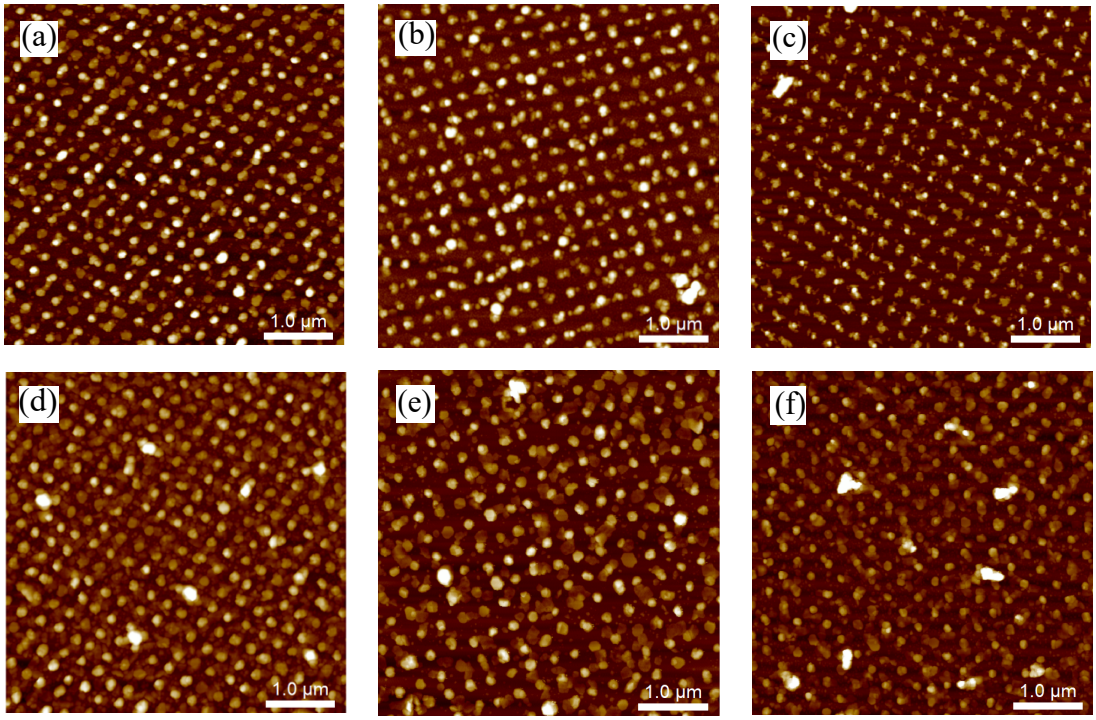

Figure 3.18. (a), (b), and (c) AFM height images of Au nanostructures with a Cr thickness of 1.5 ± 0.1 nm annealed at 475, 500, and 600 ℃, respectively. (d), (e), and (f) nanostructures with a Cr thickness of 2.5 ± 0.2 nm annealed at 475, 500, and 600 ℃, respectively.

The second category includes Au nanostructures with less-uniform patterns, particularly at high annealing temperatures. This was observed in four sets of samples: (set 3) nanostructures with a Cr thickness of 6 ± 0.5 nm, (set 4) 8 ± 0.1 nm, (set 5) 11 ± 0.1, and (set 6) 12.5 ± 0.1 nm. Figures 3.19a, b, c, and d show AFM images of Au nanostructures obtained from set 3, 4, 5, and 6 annealed at 500 ℃ for 2 h, respectively. As can be noted, the patterns remained regular despite changes in Cr thickness. Consequently, the uniform patterns indicate that there was no significant diffusion of Cr/Au during low-temperature annealing. These results also suggest that the chosen temperatures are suitable for preventing Cr/Au diffusion in this specific context, ensuring structural integrity. Figures 3.19e, f, and g depict the impact of annealing at 575 ℃ on the morphology of Au nanostructures for the same sets. Lishchuk et al. [89] reported that annealing at temperatures above 555 ℃ led to the complete destruction of the nanostructures. In the current case, patterns still appear at 575 °C with Cr thickness up to 8 ± 0.1 nm. However, above 2.5 ± 0.1 nm Cr, increasing annealing temperatures led to less regular patterns (see Figures 3.19e and f), except in the case of 11 ± 0.1 nm and 12.5 ± 0.1 nm, where the patterns were completely lost at 575 °C (see Figures 3.19g and h). This indicates that slight diffusion of Au occurred after increasing the annealing temperature in both sets 3 and 4, whereas more pronounced diffusion occurred in sets 5 and 6. Furthermore, when the annealing temperatures

increased to 600 ℃, as shown in Figure 3.19i, complete destruction of the nanostructures occurred. Thus, annealing temperatures significantly affected the pattern uniformity.

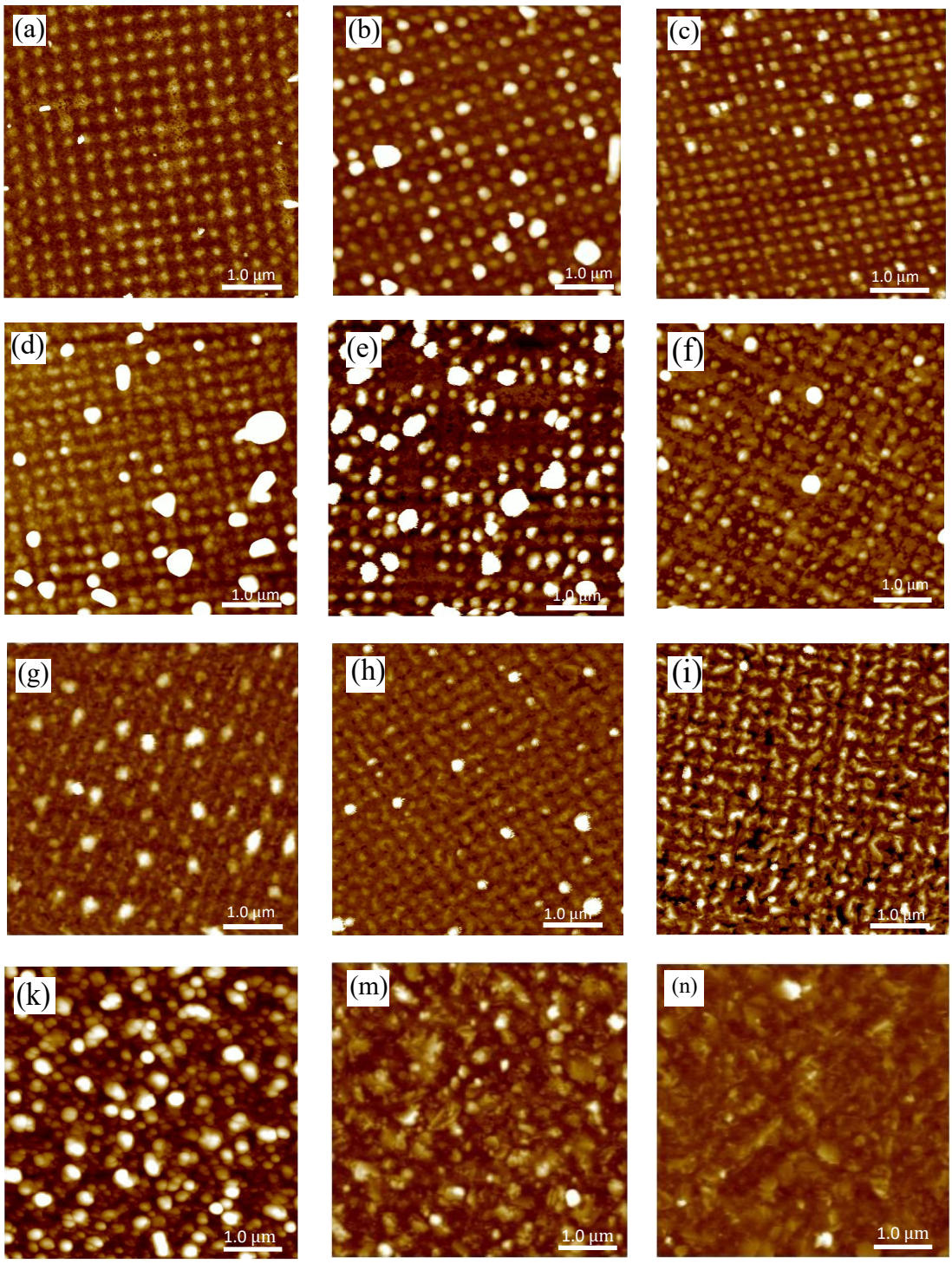

Figure 3.19. (a), (b), (c), and (d) AFM height images of Au nanostructures prepared with Cr thicknesses of 6 ± 0.5 nm, 8 ± 0.1 nm, 11 ± 0.1 nm, and 12.5 ± 0.1 nm annealed at 500 ℃ for 2 h, respectively. (e), (f), (g), and (h) Annealed at 575 ℃ obtained from set 3, 4, 5, and 6, respectively. (i) Represents AFM height images of samples annealed at 600 ℃. (k), (m), and (n) Au nanostructures prepared with a Cr thickness of 14 ± 0.1 nm and annealed at 500 , 575, and 600 ℃ for 2 h, respectively.

The third category refers to Au nanostructures that, following annealing, do not exhibit any recognisable patterns. This phenomenon was found in one set of samples: (set 7) nanostructures prepared with a Cr thickness of 14 ± 0.1 nm. Figures 3.19k, m, and n demonstrate AFM height images of Au nanostructures annealed at 500, 575, and 600 ℃, respectively. As can be observed from these images, the patterns are completely lost, even at low annealing temperatures. From Figure 3.19 one can see that the change in surface morphology has become more obvious with higher Cr thicknesses. It is assumed that when Cr is deposited in thick layers (i.e. Cr ≥ 2.5 nm), the resulting Cr grains tend to be large, which may reduce the barrier effect that restricts the movement of Au atoms and, thus, facilitate the diffusion of Au.

Separately, the effect of different annealing temperatures on the pitch of Au nanostructures was evaluated. Figure 3.20 shows AFM height images of samples with a Cr thickness of 1.5 ± 0.1 nm annealed at three different temperatures for 2 h. The samples appear to have facets at their edges, indicating that a certain level of crystallinity has been achieved at different annealing temperatures. Accordingly, Bosman et al. reported that the annealing increases the crystallinity of Au nanostructure. [231] As a consequence, the samples showed average pitches of 317 ± 11, 316 ± 9.01, and 321 ± 9.0 nm, when they annealed at 450, 550, and 600 °C, respectively. Thus, the variation in annealing temperatures did not significantly affect the pitches of the Au nanostructures, given that they exhibited almost the same values after thermal annealing. It is believed that the small variations in their pitch values are not due to annealing, as the same variations are observed for them before annealing. Most likely, this is due to the differences in the fabrication conditions.

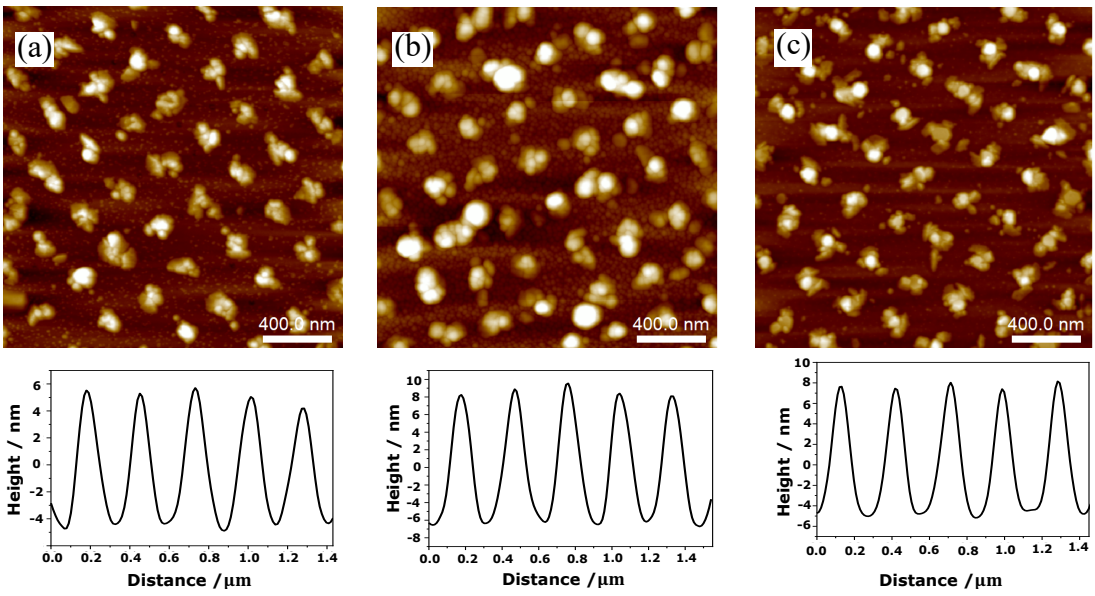

Figure 3.20. AFM height images (2 µm × 2 µm) of samples annealed at (a) 450 °C, (b) 550 °C, and (c) 600 °C.

3.3.4.2 Optical Properties

In this section, the focus is on the systematic study of the LSPR position as a function of the variation in Cr thickness and annealing temperature of Au nanostructures. The data listed in Table 3.3 provide the different chromium thicknesses as well as their corresponding annealing temperatures. From our previous experiments, which focused on annealing the as-fabricated samples at different times, it was found that annealing of Au nanostructures for less than 2 h did not exhibit plasmon bands, so all samples were annealed for 2 h. Figure 3.21a displays the LSPR peak position for five samples with a Cr thickness of 1.5 ± 0.1 nm annealed at 400, 450, 500, 550, and 600 °C. As can be noted, there are significant changes in the LSPR peak position with increasing temperatures. These changes vary from one sample to another depending on the annealing temperatures. One can observe that there is a weak plasmon band after annealing at 400 ℃, indicating that the nanostructures were not able to sufficiently recrystallise at this level of annealing. Regardless of the Cr thickness, this result was consistent for all annealed samples; instead, strong plasmon bands started to appear for samples annealed at 450 ℃ and became more intense for samples annealed at higher temperatures. The well-localised and significantly enhanced extinction bands of the annealed samples are attributed to the LSPR of the Au nanostructure. It is evident from the extinction spectra that the LSPR band is very broad at the annealing temperature of 450 °C, and becomes narrower and more pronounced with increasing temperature. Moreover, increasing the annealing temperature caused a blue shift in the position of the plasmon band by approximately 107 nm (from 662 nm at 450 °C 555 nm at 600 °C), shown in Figure 21b.

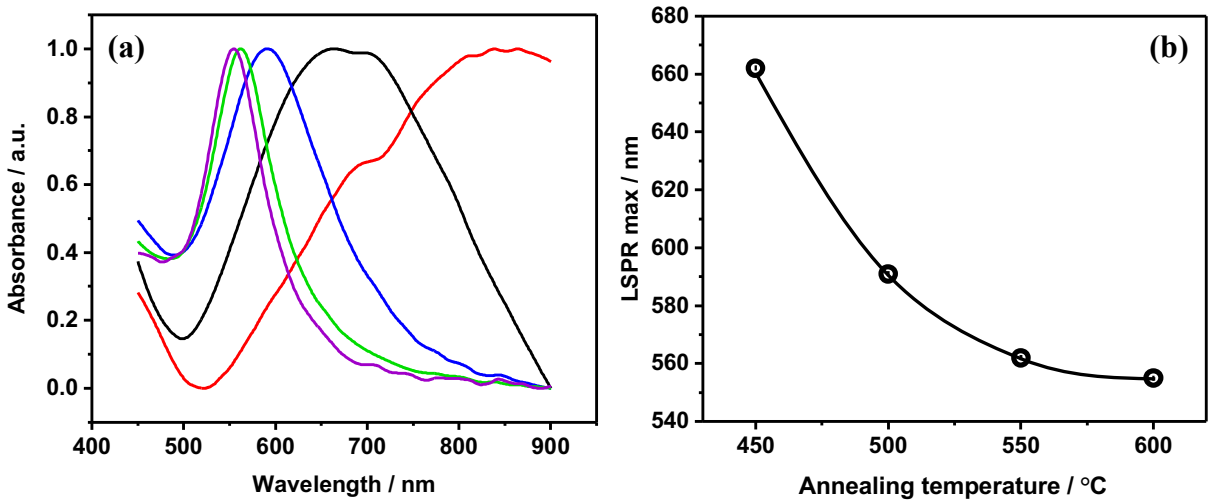

Figure 3.21. LSPR spectra of Au nanostructure samples with a thickness of Cr =1.5 ± 0.1 nm annealed at 400 °C (—), 450 °C (—), 500 °C (—), 550 °C (—), 600 °C (—), and (b) LSPR peak positions as a function of annealing temperatures.

It is believed that as the annealing temperature increases, the structural morphology properties of the annealed samples change, and consequently the total contact area of the sample with the environment changes in different ways, resulting in a different resonance spectrum. Figure 3.22a displays the LSPR spectra of samples with a Cr thickness of 2.5 ± 0.2 nm annealed at different temperatures; the position of the LSPR peak as a function of annealing temperature is shown in Figure 3.22b. At the lower annealing temperature (i.e. 450 °C), the extinction peak was broad, and as the annealing temperature increased to 600 °C, the extinction peak became narrower, which is consistent with the result displayed in Figure 3.20. However, no clear trend in the peak positions of these samples was observed with increasing annealing temperature. It is assumed that at lower Cr thicknesses (i.e. Cr = 1.5 ± 0.1 nm, and Cr = 2.5 ± 0.2 nm), the extinction spectra of Au nanostructures exhibit a reduction in spectral width or bandwidth with increasing annealing temperature. This means that as the annealing temperatures increase, the optical properties of Au nanostructures become more confined and focused within a narrower range of wavelengths, reflecting a potential enhancement in structural homogeneity or size uniformity among the nanostructures as they undergo annealing at higher temperatures. Thus, the spectral data are in agreement with the AFM results, as the patterns remained uniform with increasing annealing temperatures.

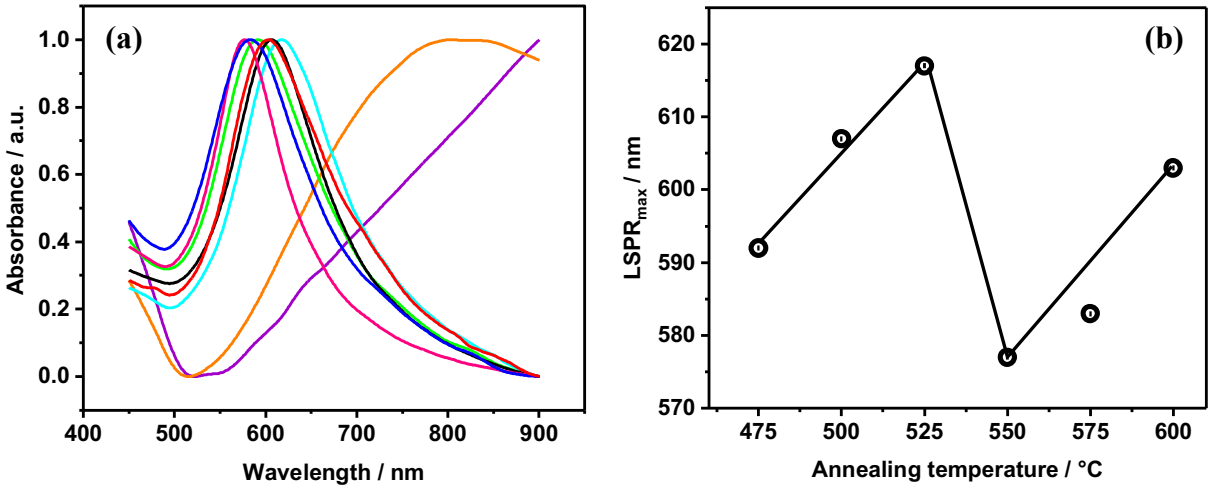

Figure 3.22. (a) LSPR spectra of Au nanostructure samples with a thickness of Cr =2.5 ± 0.1 nm annealed at 400 °C (—), 450 °C (—), 475 °C (—), 500 °C (—), 525 °C (—), 550 °C (—), 575 °C (—), 600 °C (—), and (b) the LSPR peak position of samples against annealing temperatures.

Figure 3.23 shows the LSPR spectra of annealed samples with a Cr thickness of 6 ± 0.5 nm. It should be noted that a different evaluation of the extinction peak was observed for this set of samples when compared to the samples with low Cr thicknesses described above, where broad spectra were obtained at different annealing temperatures instead of narrow spectra. The LSPR peak position showed a notable correlation with variations in the annealing temperature. More specifically, as the annealing temperature was gradually increased from 500 to 600 °C, with intermittent steps at 525, 550, and 575 °C, there was a consistent trend of the extinction peak shifting to shorter wavelengths, starting at 660 nm and decreased to 652 nm, then 649 nm, and finally reaching 610 nm. This observed shift in the extinction peak suggests a continuous modification of the Au nanostructure's morphology and optical properties throughout the annealing process, with the intermediate temperatures contributing to the incremental changes.

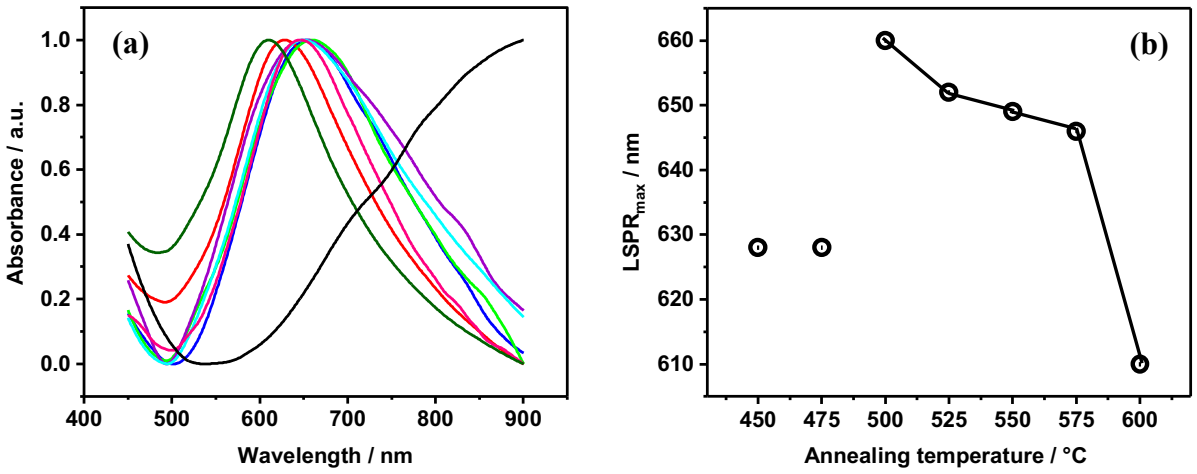

Figure 3.23. (a) LSPR spectra of Au nanostructure samples with a thickness of Cr = 6 ± 0.1 nm annealed at 400 °C (—), 450 °C (—), 475 °C (—), 500 °C (—), 525 °C (—), 550 °C (—), 575 °C (—), 600 °C (—), and (b) the LSPR peak position of samples against annealing temperatures.

Similar behaviour is also observed in the case of thicker Cr films, specifically with Cr = 8.0 ± 0.1 nm, 11.0 ± 0.1, and 12.5 ± 0.1. In these cases, the extinction peaks become broader, and the LSPR positions change, but in an irregular manner for each thickness. Figure 3.24a displays the change in LSPR peak position as a function of annealing temperature for Au nanostructures with a Cr thickness of 8.0 ± 0.1 nm. It clearly shows that the LSPR was initially centred at 724 nm upon annealing at 450 °C, subsequently exhibiting a blue shift with increasing annealing temperatures. At 475 °C, the peak position shifted to 701 nm, and as the annealing temperature increased to 500°C, it further blue-shifted to 678 nm. The trend of blue-shifting continued, resulting in a peak position of 624 nm at 525 °C and 608 nm at 600 °C (see Figure 3.24b). It

was also observed that the extinction band became narrower after annealing at 600 °C. This phenomenon can be seen after annealing at 600 °C for almost all nanostructures with different Cr thicknesses, where the plasmon band is typically observed between 585 nm and 612 nm. In Figure 3.25a, it is shown that all the extinction spectra of Au nanostructures with a Cr thickness of 11 ± 0.1 nm display the presence of a broad plasmon band between 720 nm and 631 nm. In addition, there is no clear trend in the LSPR peak positions of these samples, with the extinction peaks located at 720, 697 , 718, 694 , 723, and 631nm corresponding to annealing temperatures of 475 , 500 , 525, 550, 575, and 600 °C, respectively (see Figure 3.25b).

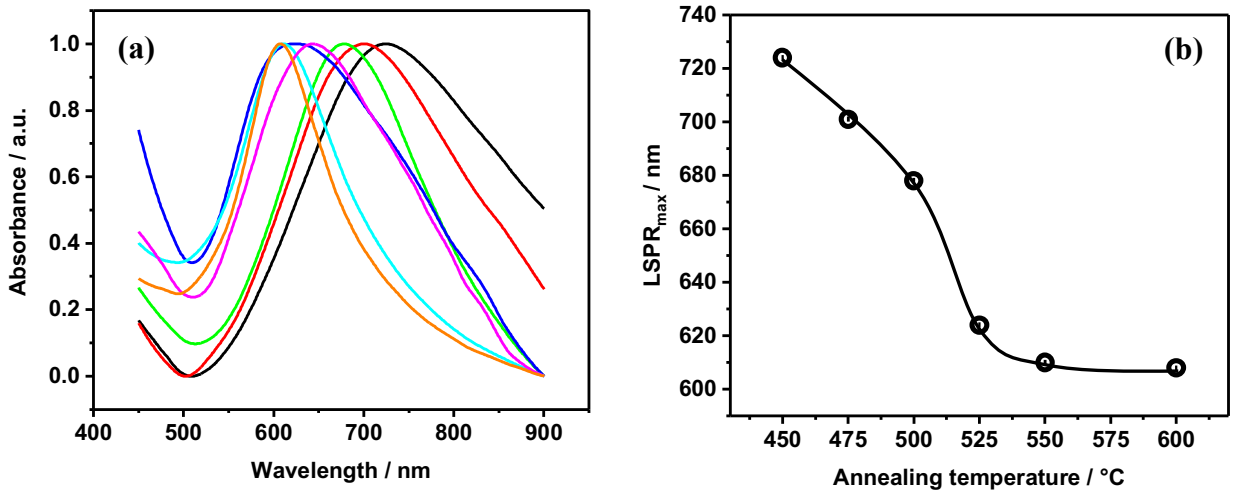

Figure 3.24. (a) LSPR spectra of Au nanostructure samples with a thickness of Cr = 8.0 ± 0.1 nm annealed at 450 °C (—), 475 °C (—), 500 °C (—), 525 °C (—), 550 °C (—), 575 °C (—), 600 °C (—), and (b) the peak position of samples against annealing temperatures.

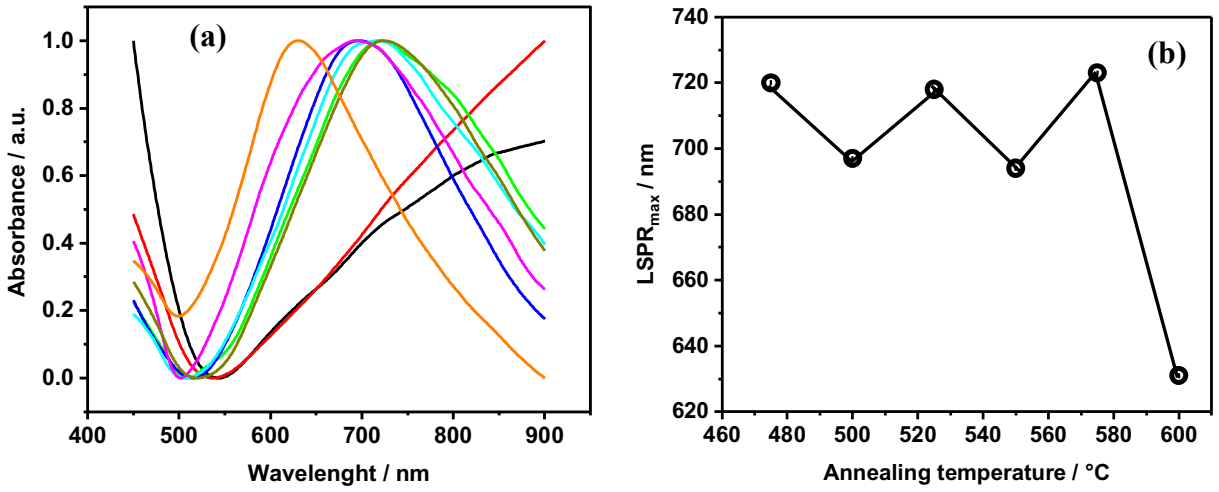

Figure 3.25. (a) LSPR spectra of Au nanostructure samples with a thickness of Cr = 11.0 ± 0.1 nm annealed at 400 °C (—), 450 °C (—), 475 °C (—), 500 °C (—), 525 °C (—), 550 °C (—), 575 °C (—), 600 °C (—), and (b) the peak position of samples against annealing temperatures.

Figure 3.26 displays the LSPR spectra of annealed samples with a Cr thickness of 12.5 ± 0.1 nm. As can be noted, there is a significant increase in the plasmon band width with increasing Cr thickness, which indicates that the presence of a thicker layer of Cr somehow influences the plasmonic properties of the Au nanostructures. This could be explained by the morphological characteristics of these samples, as the AFM images demonstrated that with increasing Cr thickness to higher thicknesses, the potential for Au diffusion increases, and therefore, pattern destruction occurs. Moreover, it is evident from Figure 3.26 that each thickness of Cr has different behaviours on the LSPR peak of Au nanostructures with annealing temperature. This difference is more pronounced for the higher Cr thickness. Furthermore, within the range of annealing temperatures tested, namely 475 °C and 500 °C, a strong dependence of the LSPR peak position on the Cr thickness was observed. In particular, with increasing Cr thickness, there was a clear and consistent trend of the plasmon peak toward longer wavelengths (see Figure 3.27).

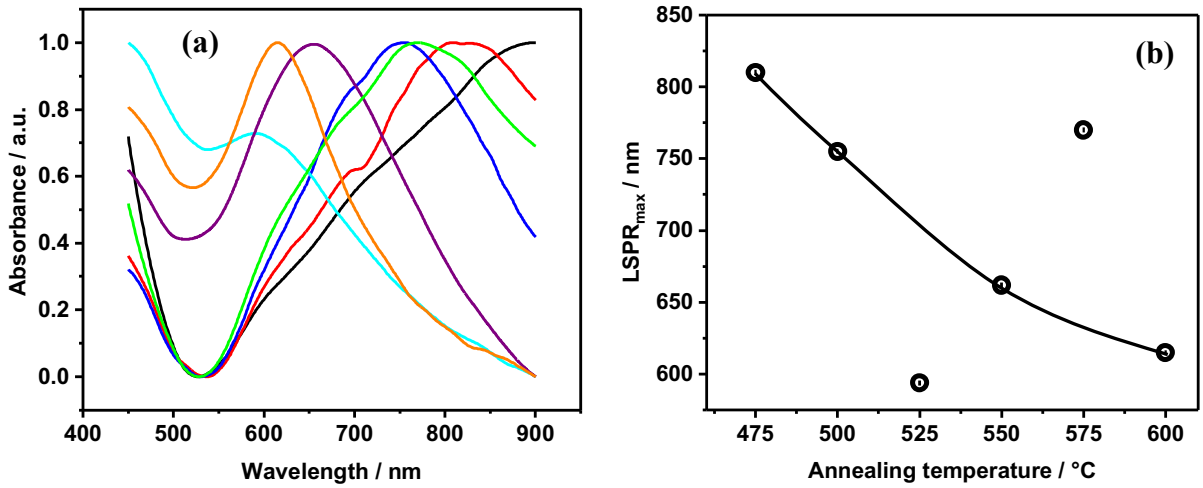

Figure 3.26. (a) LSPR spectra of Au nanostructure samples with a thickness of Cr = 12.5 ± 0.1 nm annealed at 400 °C (—), 475 °C (—), 500 °C (—), 525 °C (—), 550 °C (—), 575 °C (—) ,600 °C (—), and (b) the peak position of samples against annealing temperatures.

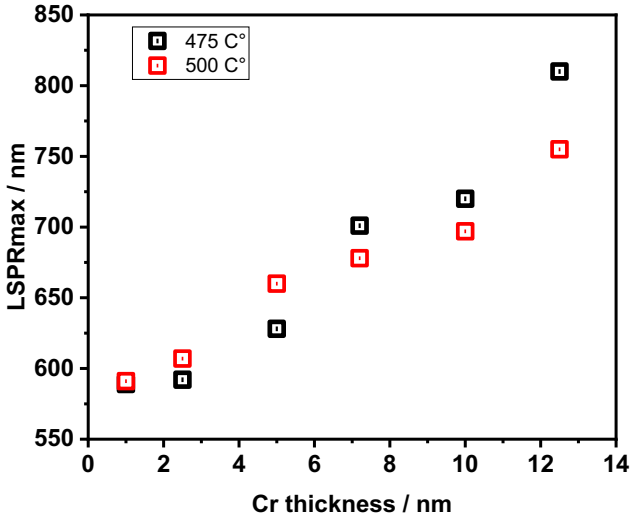

Figure 3.27. The position of the LSPR band at different Cr thicknesses annealed at 475 °C(■) and 500 °C (□).

To summarise, annealing the samples with varying Cr thicknesses and at different annealing temperatures for 2 h has a significant effect on the surface morphology of Au nanostructures, especially when higher thicknesses and temperatures are used. At lower Cr thicknesses, the resulting patterns exhibit a consistent and uniform appearance, and this characteristic remains unchanged even when the annealing temperature is increased. However, as the thickness of the Cr is increased, the uniformity of the patterns diminishes, and with further increases in the annealing temperature, the patterns lose their uniformity. Moreover, for thin Cr layers, the annealing process leads to sharp, well-defined plasmon bands, attributed to recrystallisation of the Au, but there is no clear systematic dependence of the LSPR band on the annealing temperature. However, as the thickness of the Cr increases, there is an increase in the width of the plasmon band and a tendency for the position of the plasmon band to become increasingly blue-shifted as the temperature is increased during annealing. These effects are possibly attributable in part to differences in Au crystal nucleation and mobility. For thin Cr layers, the Cr grains are small, and Au tends to nucleate forming smaller, more uniform crystallites that do not spread or diffuse during annealing. These yield plasmon energies at ~ 2 eV. For thicker Cr layers, Au nucleation is less well controlled, and yields smaller crystallites. Annealing at higher temperature is required to recrystallise Au into the optimal crystal morphologies formed thinner Cr layers. The data presented in Table 3.4 summarise the extent of changes in the surface morphology and optical properties of Au nanostructures as a result of variation in Cr thicknesses and annealing temperatures.

Table 3.4. Effects of thermal treatment at different annealing temperatures (AT) on the surface morphology and optical properties of Au nanostructures formed on different layers of Cr.

AT/ °C	Au nanostructures with different Cr thickness						
	1.5 ± 0.1nm	**2.5± 0.2 nm**	**6± 0.5 nm**	**8± 0.1 nm**	**11± 0.1 nm**	**12.5± 0.1 nm**	**14 ± 0.1 nm**
400	No plasmon resonance and regular IL pattern						
600	After annealing at 600 °C, narrow LSPR bands around 585 – 612 nm were observed for all evaporated thicknesses of the Cr prime layer						
450-575	1. Regular IL pattern 2. Narrow LSPR band 3. FWHM depends on annealing temperature 4. Wide λ LSPR range 5. λ $LSPR_{max}$ depends on annealing temperature 6. Difficult to control the thickness of Cr layer	1. Regular IL pattern 2. Narrow LSPR band 3. FWHM does not depend on annealing temperature 4. Narrow λ LSPR range 5. λ $LSPR_{max}$ does not depend on annealing temperature 6. Easy to control the thickness of Cr layer	1. Less regular IL pattern 2. Variable LSPR band 3. FWHM does not depend on annealing temperature 4. Narrow λ LSPR range 5. λ LSPR max does not depend on annealing temperature 6. Easy to control the thickness of Cr layer	1. Less regular IL pattern 2. Variable LSPR band 3. FWHM depends on annealing temperature 4. Wide λ LSPR range 5. λ LSPR max depends on annealing temperature 6. Easy to control the thickness of Cr layer	1. Less regular IL pattern 2. Broad LSPR bands 3. FWHM does not depends on T°C 4. narrow λ LSPR range (690-720 nm) 5. λ $LSPR_{max}$ does not depend on annealing temperature 6. Easy to control the thickness of Cr layer	1. Pseudo-pattern with defects 2. Broad LSPR band 3. FWHM depends on annealing temperature 4. wide λ LSPR range (ca. 600-800 nm) 5. λ LSPR max depends on annealing temperature 6. Easy to control the thickness of Cr layer	1. No IL pattern 2. No LSPR band

3.3.5 Evaluation of Refractive Index Sensitivity of Gold nanostructure

The main principle of LSPR sensing is the dependence of the position of the LSPR peak on the refractive index of the surrounding environment. From an analytical perspective, it is desirable for the refractive index sensitivity to be as higher as possible; thus, ensuring the largest possible shift in the position of the plasmon band following binding of an analyte to the Au surface. The refractive index sensitivity measurement offers a simple and reproducible method for detecting the sensitivity of Au nanostructures without causing any damage or destabilisation. It ensures that any shift noticed can be attributed to the variation in the refractive index of the surrounding medium. Consequently, this method is a highly valuable approach to estimate the performance efficiency of Au nanostructures as biosensors. Many experimental and theoretical studies have been performed to investigate the refractive index (RI) sensitivity of different shapes and sizes of metal nanostructures. For example, Chen et al. [232] conducted a study examining the RI sensitivity of different Au nanostructures, including nanospheres, nanorods, nanotubes, and nanobranches. His findings revealed that among these structures, Au nanospheres showed the lowest RI sensitivity of 44 nm/RIU, while Au nanobranches showed the highest RI sensitivity of 703 nm/RIU, where RIU stands for refractive index unit. Hegde et al. [233] reported that Au nanostars exhibited the highest RI sensitivity of 484 nm/RIU in solution and 318 nm/RIU when deposited on the substrate. Ryosuke et al. [201] successfully fabricated Au nanostructures on QCM devices using NIL; and subsequently explored the sensitivity of these structures to changes in refractive index, where they determined that their RI sensitivity was 233nm/RIU. Stella et al. [234] reported that when immobilised on a glass substrate, Au nanorods exhibited sensitivity of 252 nm/RIU. Further, according to Lischuk et al. [89], Au nanostructures fabricated by IL have a refractive index sensitivity of 145 nm/RIU.

The RI sensitivity of Au nanostructures was evaluated at this stage by measuring the extinction spectra of annealed samples immersed in various liquids, including deionised water ($n = 1.33$), ethanol ($n = 1.36$), glycerol ($n = 1.47$) and toluene ($n = 1.49$). Figure 3.28 shows the response of the LSPR peak position to refractive index changes. It can be seen that the increase in the refractive index of the surrounding medium results in a red shift of the LSPR band, which is in agreement with the Maxwell-Garnett effective medium theory. [235] For example, the plasmon peak was shifted from 632 nm to 678 nm, when the refractive index was increased from $n = 1.33$ to $n = 1.49$. The refractive index sensitivity was evaluated by plotting the LSPR peak position against the refractive index of liquids, as shown in Figure 3.28b. A linear regression was applied, and the sensitivity was calculated by the slope of the fitted line.

Therefore, the highest RI sensitivity of Au nanostructures was found to be around 231 nm/RIU, which is consistent with the reported value. [201]

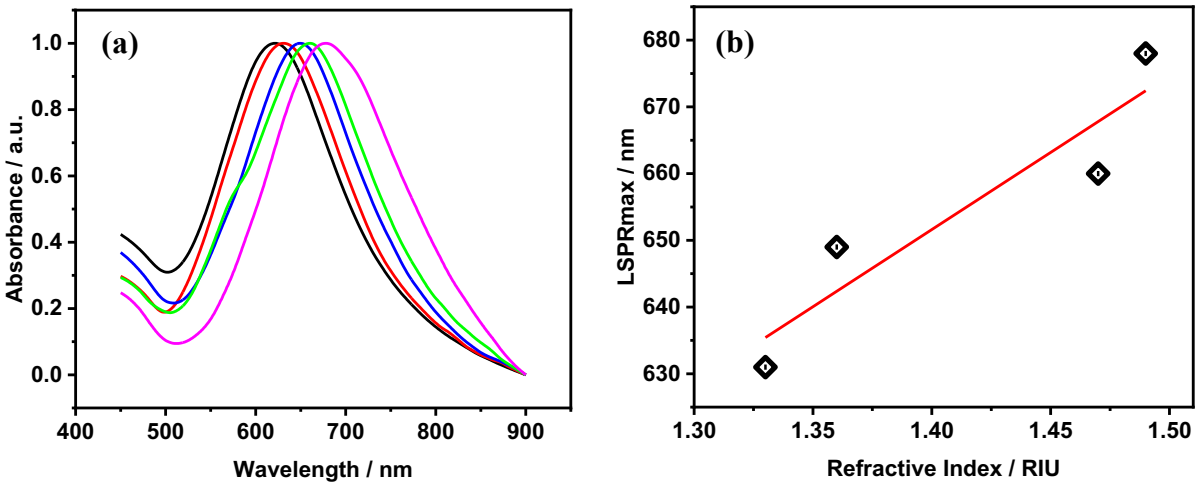

Figure 3.28. (a) UV-Vis spectra of Au nanostructures obtained in air (—), water (—), ethanol (—), glycerol (—), toluene (—) and (b) LSPR position against refractive index.

3.3.6 Gold Nanostructures Functionalised by Rhodamine B

Previous work has demonstrated that strong coupling is achieved between LSPRs and excitons in light-harvesting complexes. This has inspired the design of synthetic biomimetic materials inspired by biological light-harvesting systems, with the aim of developing a new approach to the fabrication of photonic materials. As a first step in this direction, films of a synthetic dye, Rhodamine B, were formed on Au nanostructure arrays and extinction spectra were acquired. The dye selected was Rhodamine B azidopropyl ester ($RBON_3$), which has an absorption maximum that is close in energy to the plasmon bands of arrays Au nanostructures fabricated using IL as described above. Moreover, Rhodamine B is cheap and readily available, and can be modified easily for conjugation to a surface. The $RBON_3$ used in this work was provided by Dr Benjamin Bower, Department of Chemistry, University of Sheffield. The absorption spectrum of $RBNO_3$ with a thiol linker are shown in Figure 3.29. The absorption displays a maximum at 558 nm. Arrays of Au nanostructures were functionalised with $RBON_3$ by immersing the annealed samples in a 1 mM solution of $RBNO_3$ in ethanol for 24 h. The optical properties of the nanoarrays interacting with $RBON_3$ were studied using UV-Vis spectroscopy.

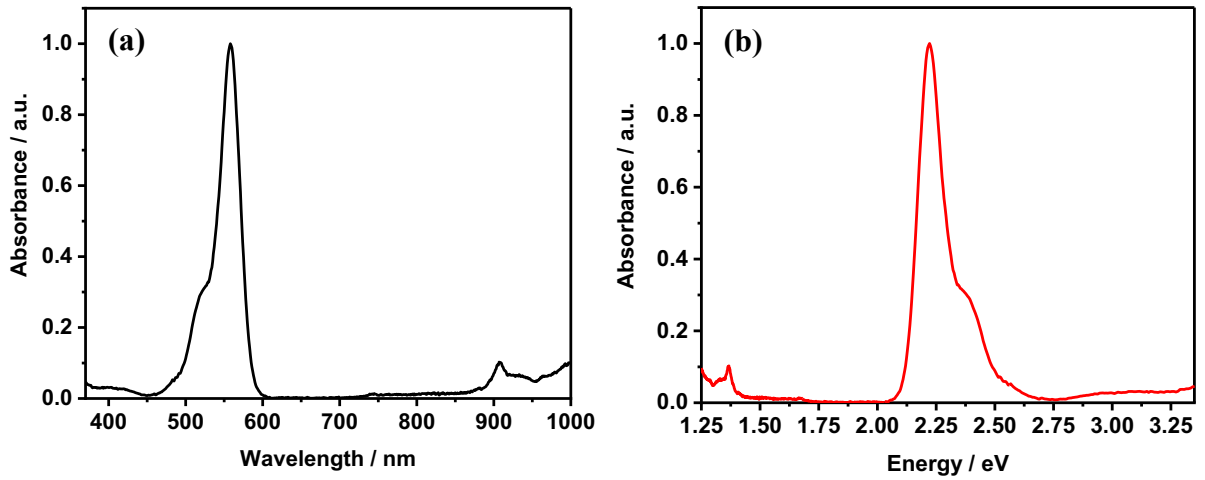

Figure 3.29. (a) Absorption spectrum of $RBON_3$ in the wavelength (nm), and (b) in energy (eV).

Figure 3.30a shows an AFM image of the Au nanostructure sample functionalised with $RBON_3$ for 48 h. The sample was fabricated by IL using double exposures with $\theta = 25°, \phi = 90°$ and annealed at 500 °C. The extinction spectrum of the Au nanostructure array was observed at $\lambda_{max} = 591$ nm (2.09 eV). After formation of a Rhodamine B terminated self-assembled monolayer on the annealed array, extinction spectra were measured at different angles of

incidence. If there is plasmon-exciton coupling, the energies of the coupling states should vary as a function of the wavevector of the incident light. The wavevector is conveniently varied by changing the angle of incidence of the excitation beam. Extinction spectra for Rhodamine B terminated SAMs on Au nanostructure arrays are shown in Figure 3.30b. For light at normal incidence on the array (red spectrum in Figure 3.30b), the extinction spectrum exhibits a main peak at ~ 2.2 eV, together with a shoulder at lower binding energy (~ 2.0 eV). This represents a significant change from the spectrum acquired for the clean Au array. It is suggestive of a splitting of the plasmon band to yield two new overlapping features. As the angle of incidence is increased to 7.5° (light blue spectrum), the shoulder becomes more pronounced, and clearly begins to resemble a second peak. As the angle of incidence is increased increments to 15°, the separation between the two components in the extinction spectrum increases. However, as the angle of incidence is increased still further, the peaks move closer together, until at 20° the spectrum resembles that recorded at normal incidence.

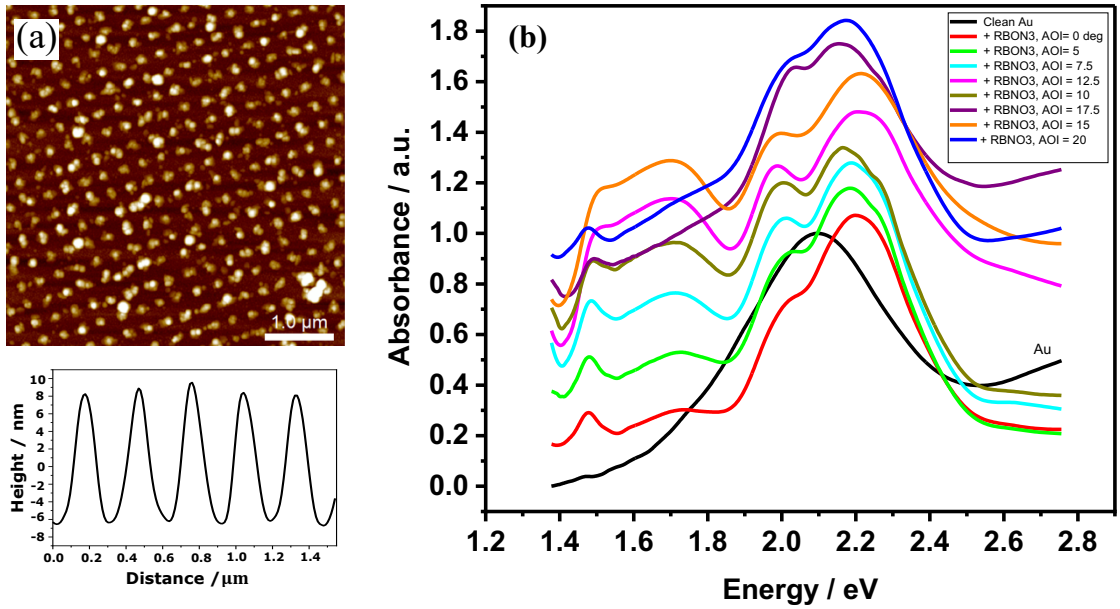

Figure 3.30. (a) An AFM height image of Au nanostructure arrays functionalised with $RBON_3$, (b) the extinction spectra of Au nanostructures in the presence of $RBON_3$-thiol at different angles of incidence.

In plasmonic, we study the interactions between light and metal/dielectric interfaces. Light has electric and magnetic fields at right-angles to the propagation direction. Electrons in a metal can interact with the electric field. For bulk metal, the electrons will be randomly organised. However, for a metal nanoparticle, the oscillating electric field associated with the light beam causes oscillation of the electrons leading to the formation of an oscillating dipole. Resonance occurs where the frequency of the light is matched to the frequency of a strong absorption in the nanoparticle. This resonance frequency is shape-dependent. For small particles, the response will be angle-independent. However, for nanoparticles supported on a substrate, an image dipole will form, giving rise to angle-dependence. At a metal-dielectric interface, the dielectric constant ε is related to the refractive index n:

$$\varepsilon = n^2 \tag{3.2}$$

The wavevector for the photon is:

$$k_{photon} = \frac{2\pi}{\lambda} \tag{3.3}$$

and the dispersion relation for a wave propagating at the metal surface (the surface plasmon polariton, SPP) is:

$$k_x = \frac{\omega}{c}\left(\frac{\varepsilon_1 \varepsilon_2}{\varepsilon_1 + \varepsilon_2}\right) \tag{3.4}$$

where ω is the angular frequency and c is the speed of light.

In the dielectric, $\omega = ck_x$.

At low frequency, the SPP behaves like a photon, but as the wavevector increases, the dispersion bends over, approaching an asymptotic limit of

$$\omega_{spp} = \omega_p\sqrt{1 - \varepsilon_2} \tag{3.5}$$

$$= \omega_p\sqrt{2} \text{ in air} \tag{3.6}$$

where ω_p is the plasma frequency. Thus, in a simple system, k is always $< k_{SPP}$.

A number of methods exist that enable measurement of the dispersion. Two are of particular interest: (a) coupling to a prism (using an oil immersion lens); and (b) coupling to a grating. Diffraction at the grating creates orders with an additional momentum term. These additional orders lie above the light line ($\omega = ck_x$); thus allows us to access the plasmon curve.

To test whether these changes in the spectrum resulted from strong plasmon-exciton coupling, the system was modelled as coupled harmonic oscillators using the methodology reported previously by Lishchuk et al. [236] Figure 3.31 shows the measured spectrum for angles of incidence of 0, 10 and 15°, together with fits to the spectra. For a splitting in the normal modes to be visible, it is necessary for the difference in the energies of the real modes at resonance:

$$\sqrt{E_C^2 - \frac{1}{4}(\gamma_1 - \gamma_2)^2} \qquad 3.7$$

to remain real. Here, E_C is the scaled coupling energy (approximately equal to the Rabi energy) and γ_1 and γ_2 are the linewidths of the uncoupled plasmon and exciton modes. Thus, one criterion for strong coupling is that

$$E_C \geq \frac{1}{2}(\gamma_1 - \gamma_2) \qquad 3.8$$

Here, $\gamma_{\mathrm{LSPR}} \sim 0.4$ eV and $\gamma_{\mathrm{mol}} \sim 0.1$ eV, hence the splitting should be ~ 0.15 eV, a condition that is not satisfied for these systems not satisfied for these systems. Spectra were acquired for five different arrays over a range of angles of incidence. The spectra were fitted using the coupling oscillator model, and the coupling were determined and plotted in Figure 3.29. It can be seen that the largest coupling energies, of 0.25 ± 0.1 eV, where observed at angles of incidence of $\sim 12°$.

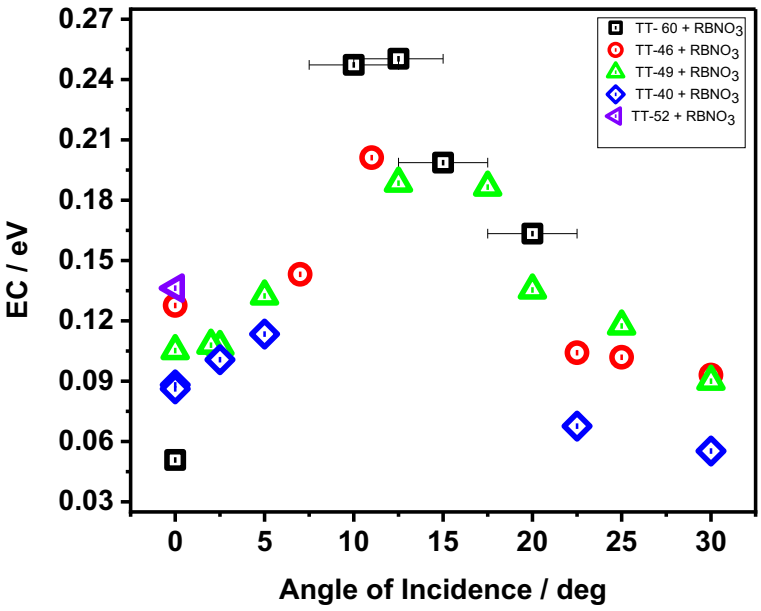

Figure 3.31. Variation in the coupling energies of different nanostructures arrays after adsorption of $RBON_3$-thiol.

3.4 Conclusion

In the current study, the formation of ODT SAMs on Au surfaces was confirmed using different techniques. The first evidence came from CA evaluation, where CA increased from $68 \pm 2°$ to $100 \pm 2°$ after immersing the Au substrates in a 1 mM ODT solution for 24 h. This increase indicated that the thiol groups were successfully attached to the Au surface, thus creating hydrophobic surfaces. The thickness of ODT SAMs estimated by SE was 1.8 ± 0.1 nm, which is consistent with the values expected when forming fully packed SAMs. Furthermore, from the XPS measurements, it was found that the S 2p component, which has a main peak with a binding energy of 162.0 eV, was observed only after the Au substrates were immersed in the ODT solution. By analysing AFM images, it was also observed that the Au surface roughness decreased from 1.97 to 0.87 nm after immersing the Au substrates in ODT solution, indicating an increase in surface smoothness.

IL is a powerful method for fabricating nanostructures with high resolution and large area. In comparison with EBL and FIB, IL is straightforward, flexible, and inexpensive. In this study, IL was used to generate a variety of nanostructures by exposing ODT SAMs on the Au surface to UV light at a wavelength of 244 nm in a Lloyd's mirror interferometer, using a dose of 38.4 J cm^{-2} for single exposure, and 38.4 J cm^{-2} followed by 27.3 J cm^{-2} for double exposures. It was demonstrated that the Au nanostructures can be controlled by changing the exposure and etching conditions. The pitch of the interference patterns generated by the interferometer can be controlled by adjusting the angle at which the mirror is set with respect to the incoming laser beam (θ). The symmetry and geometry of the nanoarrays can be controlled by changing the rotation angles (ϕ) between exposures. At $\phi = 90°$, square arrays of dots were produced, while at $\phi = 60°$, hexagonal arrays were produced. As ϕ was decreased, the arrays became elongated until $\phi = 15°$, parallel rows of needles were produced. The LSPR of these arrays are a function of the shape, size, spacing and pitch of the structures. Measurements performed in liquids with different refractive indices showed that the higher refractive index of the medium resulted in a red shift of the plasmon band. The highest refractive index sensitivity of the Au nanostructures was measured at 231 nm/RIU, which it is relatively high and competitive with, if not superior to, the sensitivity typically achieved for Au nanostructures fabricated with other techniques. Comparatively, SPR is a widely used biosensing technique that relies on the changes in the refractive index near a metal surface to detect molecular binding events. Conventional SPR typically achieves sensitivities in the range of 1000−4000 nm/RIU. [237] Therefore, the 231 nm/RIU sensitivity of Au nanostructures appears lower at first glance. IL, though, enables the

precise fabrication of metal nanostructures with tailored properties, including size, shape, and spacing. These structures can be optimised for specific applications, offering advantages such as enhanced LSPR effects, which can greatly enhance sensitivity. While conventional SPR offers high sensitivity, it is typically limited to planar surfaces and requires the use of expensive prisms or gratings. In contrast, IL can create complex 3D nanostructures that can be integrated into microfluidic devices, enabling more versatile and miniaturised sensing platforms.

The influence of different Cr evaporated thicknesses (1.5 ± 0.1 nm, 2.5 ± 0.1 nm, 6 ± 0.5 nm, 8 ± 0.1 nm, 11 ± 0.1 nm, 12.5 ± 0.1 nm and 14 ± 0.1 nm) and annealing temperatures (400 °C, 450 °C, 475 °C, 500 °C, 525 °C, 550 °C, 575 °C and 600 °C) on the morphology and LSPR spectra of Au nanostructures were investigated. Therefore, thermal annealing resulted in well-defined plasmonic bands, which were attributed to the recrystallisation of the gold. It has been observed that the Cr thickness of evaporated Au substrates and the annealing temperatures of Au nanostructures were found to play an important role on the LSPR properties and evolutions of nanostructure morphology. For samples with lower Cr thickness (i.e. 1.5 ± 0.1 nm and 2.5 ± 0.1 nm), uniform IL patterns were maintained at different annealing temperatures from 400 to 600 °C. Less uniform IL patterns, however, were observed for samples with thicker Cr layers (6.0 ± 0.5 nm, 8 ± 0.1 nm, 11 ± 0.1 nm, and 12.5 ± 0.1 nm), and the patterns were completely lost at higher Cr thickness (14 ± 0.1 nm). This can be explained by the fact that a thin Cr layer may prevent the diffusion of gold due to its small grains, while a thicker Cr layer may facilitate the diffusion of Au due to its large grains and, potentially, a reduced barrier effect. The LSPR band did not show a clear systematic dependence on the annealing temperatures. Nevertheless, for samples with Cr thicknesses of 1.5 ± 0.1 nm and 8 ± 0.1 nm, clear trends were observed with increasing annealing temperature. It was also observed that the increase in the thickness of the Cr led to an increase in the width of the plasmon band, which subsequently suggests that the Au may aggregate during annealing. Comparatively, the LSPRs of Au nanostructures was monitored in the presence of $RBON_3$. The results demonstrate that the presence of $RBON_3$ led to the splitting of the LSPR band; it can be assumed that this splitting results from plasmon-exciton coupling. Accordingly, the system was modelled as coupled harmonic oscillators to confirm whether changes in the spectrum are due to the strong plasmon-exciton coupling. The coupling energy was observed to be 0.25 ± 0.1 eV when the incidence angle was at 12°.

Chapter 4

4 Towards Plexcitonic Circuits

4.1 Introduction

The nanoscale confinement and coupling of electromagnetic radiation in plexcitonic modes has attracted great interest due to the innovative possibilities of their applications in light harvesting and light emitting devices. Plexcitons, short for plasmon-exciton polaritons, are quasiparticles that arise from the strong coupling between plasmons and excitons in certain materials. [238] This strong coupling results in unique optical properties that can have a significant impact on the behaviour of the material. Plexcitons can be achieved in various mediums; typically those that support plasmonic and excitonic properties, such as metallic nanoparticles (e.g. gold and silver), or nanostructured thin films. Correspondingly, biosensors based on gold nanoparticles in solution have demonstrated their ability to provide a direct colorimetric sensing response to bacteria. [239] Nevertheless, when it comes to consumer applications, gold nanoparticle-based biosensors need to be immobilised onto surfaces to reduce potential health risk associated with exposure to nanomaterials. In this chapter, a new strategy for controlling gold nanoparticles on solid surfaces is explored. Initially, polymer brushes were grown from surface-linked initiator sites using atom transfer radical polymerisation. Interference lithography (IL) was then used to pattern the brush surfaces via the Lloyd's mirror two-beam interferometer system. Following this, the plasmonic properties of the immobilised gold nanoparticles were compared to those in solution. In addition, we explored the possibility of coupling LSPR associated with this system to dye molecules.

The use of selectively activated surfaces to create brush systems has attracted great interest, as these structures can be exploited to combine topographical properties with the possibility of selecting the appropriate chemical function for applications in electronic and biological fields. [240, 241] Specifically, polymer brushes consist of polymer chains tethered at one end to a surface. They enable the design of stimuli-responsive smart surfaces that respond to ambient environmental changes, such as pH and temperature, and which also prevent non-specific adsorption. [242, 243] Polymer brushes can be produced by "grafting-to" and "grafting-from" methods. [244] In the "grafting-to" method, the chains are first polymerised and subsequently anchored to the surface, while in the "grafting-from" method, the polymerisation is performed at the surface with chains growing from an immobilised initiator monolayer. The conformation

and structure of the brush is controlled by the number of chains attached per surface unit area- the grafting density. The brush is considered to be in a ‘ mushroom regime’, when the adjacent chains are sufficiently separated that they do not interact with each other. Comparatively, at high grafting densities, the polymer chains are close enough that they are subject to steric and /or electrostatic repulsions, causing them to stretch away from the surface in a “brush-like” conformation. [244] Furthermore, the “grafting-from” approach is often preferred to synthesise brushes attached to substrate surfaces or particles using different polymerisation techniques, such as conventional radical, controlled radical and group transfer. [245]

The development of controlled/living polymerisation systems leads to the synthesis of defined-polymer brushes that are covalently bonded to the surface. In particular, surface-initiated atom transfer radical polymerisation (SI-ATRP) allows the growth of well-defined brushes on the surface under mild conditions. Therefore, the SI-ATRP has been widely used to create various functional surfaces, such as non-biofouling and anti-bacterial properties. [246, 247] However, the main drawback of SI-ATRP is the use of relatively large amounts of transition metal catalysts, as an excessive amount of catalyst (e.g. copper) may prevent the application of the normal SI-ATRP method to biomaterials, such as cells. [248] In addition, the SI-ATRP reaction should be undertaken in an airtight reaction flask to prevent oxidation of the catalytic species. To overcome these drawbacks, an activator regenerated by electron transfer (ARGET) ATRP was introduced. ARGET ATRP requires a smaller concentration of Cu(II) species (<300 ppm), along with a relatively large amount of reducing agent. Subsequently, this is an important in reducing Cu(II) to Cu(I), even in the presence of air. [249] Moreover, SI-ARGET ATRP has been tested with a variety of monomers, including: 2-(dimethylamino) ethyl methacrylate [250], methyl methacrylate [251] and *n*-butyl acrylate. [252] The ARGET ATRP mechanism is illustrated schematically in Figure 4.1 below.

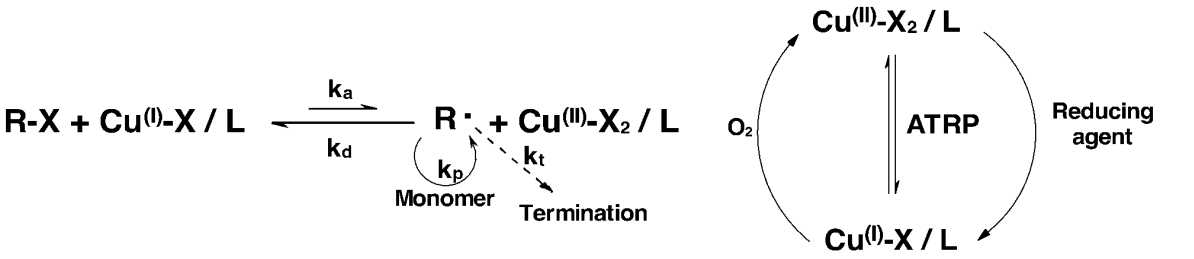

Figure 4.1. Schematic illustration of the ARGET ATRP mechanism. [253]

Gold nanoparticles (AuNPs) have unique optical and electronic properties that make them a promising platform for studies in optoelectronics, therapeutic, and sensing applications. [254−256] They exhibit LSPR, owing to their nanoscale sizes, a phenomenon that can be controlled by manipulating factors, such as particle size, shape, and interparticle interactions, as well as the surrounding environment. [254] In particular, incorporating AuNPs onto solid substrates is important in creating more flexible and reusable devices, leading to improved repeatability and costs compared to solution-based applications. Several strategies have been used to immobilise AuNPs, including covalent interactions using thiol or amine-terminated moieties, electrostatic interactions, and weaker physical interactions such as van der Waals forces. [257] However, the most common method to precisely control particle spacing and clustering is through nano- and microfabrication techniques. [258−260]

The ability to pattern polymer brushes at the micro and nanometre scale has received significant attention for their applications, ranging from the creation of integrated circuits and information storage devices to the fabrication of semiconductor microelectronics. [261−263] Furthermore, the capability to tune the thickness and grafting density of brushes has provided a particularly useful platform for taking advantage of the unique properties of nanoparticles (NPs) available in precisely defined sizes and shapes and in large quantities through wet chemistry approaches. [264]. Thus, by controlling the interaction of NPs with polymer brushes through the properties of polymer brushes, including the length of the polymer chains [265] and external stimuli, such as pH [266], it becomes possible to assemble particles into specific architectures that can be easily tuned. The assembly of NPs into ordered structures is crucial for plasmonic NPs, as their collective properties are enhanced when they are separated by small gaps. [243, 267] Patterned polymer brushes are traditionally obtained through two main approaches. One method involves immobilising the initiators on surfaces that have been pre-patterned using optical lithography techniques. The other method entails patterning the initiator on the surface, followed by surface initiated polymerisation of a suitable monomer from the initiator site. [268] Several techniques have been used to pattern initiator monolayers, such as micro-contact printing [269], scanning probe microscope [270], and nanoimprint lithography. [271] These techniques, however, are complex and require multiple steps, resulting in surface contamination. In addition, growing brushes in this manner may result in lower resolution features when the brush height is similar in length to the pattern width, due to chain relaxation into the voided spaces. [272] Therefore, the aim of the current study is to pattern poly(cysteine methacrylate) brushes in a single step using IL, before exploiting the resulting structures to organise AuNPs.

4.2 Experimental Details

4.2.1 Self-Assembled Monolayers of BIBB-APTES on Glass Slides

Glass microscope coverslips were cleaned with piranha solution followed by a thorough rinse with deionised water (>15.0 MΩ cm) and then placed in the oven to dry (see Section 2.2). Prior to use, a 2% solution of APTES in ethanol was prepared. The glass microscope coverslips were submerged in the APTES solution for 30 min, then rinsed with ethanol and dried with nitrogen. During the initial process, the APTES must be deposited onto the glass slide by surface binding to the oxygen atoms of the APTES molecules; the amine group that terminates APTES is used as a functional group for subsequent reactions. In the following step, the glass coverslips were annealed for 30 min at 120 °C. The BIBB solution was prepared by mixing 0.37 mL of 3 mmol BIBB and 0.41mL of 3 mmol triethylamine with 60 mL of DCM. The APTES-functionalised glass coverslips were then submerged in the solution for 30 min. The functionalised coverslips were rinsed with ethanol and DCM and dried with nitrogen. Consequently, the amine group of the APTES molecules binds to the carbonyl carbon, which displaces the bromine and leaves the other bromine atom for further functionalisation as a leaving group (see Figure 4.2).

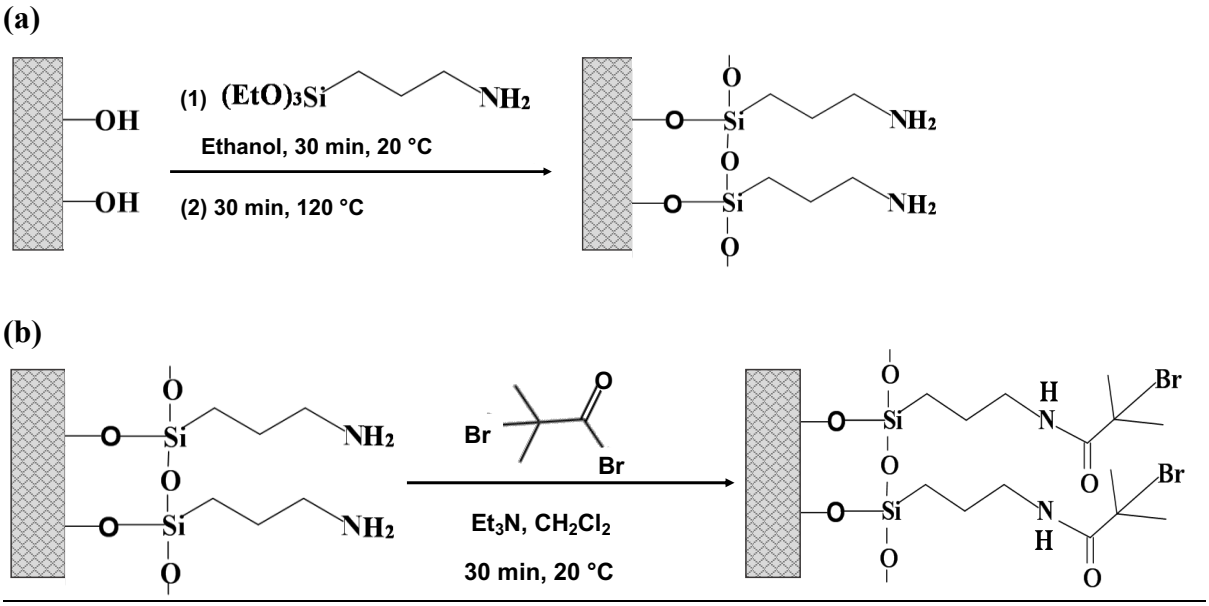

Figure 4.2. (a) A schematic diagram showing the deposition of APTES on glass slides and (b) a schematic diagram representing the interaction of BIBB with APTES on glass slides.

4.2.2 Immobilisation of Polymer Brushes on BIBB−APTES Slides

The synthesis of cysteine methacrylate monomer is described in more detail in section 2.4.2. For the brush attachment, the CysMA monomer (750 mg, 2.231 mmol) was dissolved in 4 mL deionised water. After the complete dissolution of the monomer, 1-ascorbic acid (0.18 mL, 1.02 x10^{-5} mol) was added initially to the monomer, followed by a solution of Cu (bipy)$_2$ Cl_2 (0.18 mL, 1.02 x10^{-5} mol). The solution was shaken to ensure complete mixing and then left for approximately 25 min. During this time, the solution turned into a brown colour, indicating the formation of active Cu(I) complexes. The PCysMA solution was then transferred into tubes containing the initiator-coated samples. After the polymerisation was complete, the samples were washed with deionised water, ethanol and dried under nitrogen gas (see Figure 4.3).

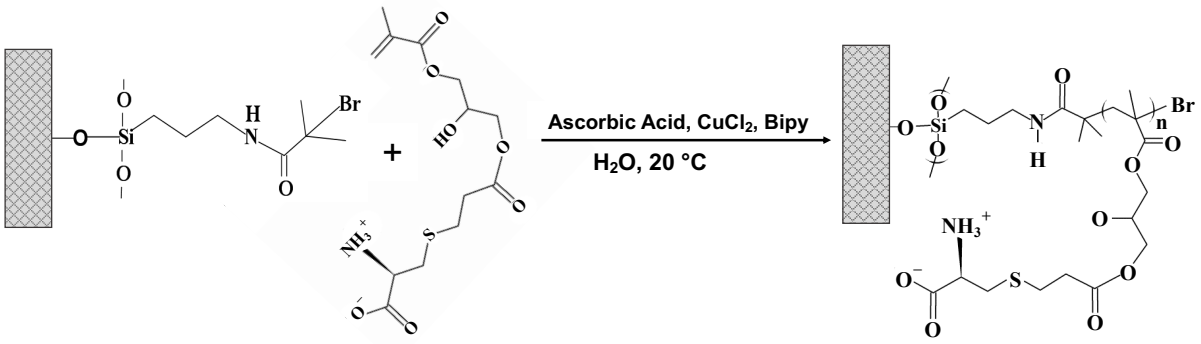

Figure 4.3. Schematic illustration of ARGET ATRP of PCysMA from BIBB-APTES -initiator- coated glass surfaces at room temperature.

4.2.3 Synthesis of Gold Nanoparticles

Gold nanoparticles (AuNPs) were synthesised by a previously published protocol using the chemical reduction of Au salts with sodium citrate ($Na_3C_6H_5O_7$). [273] In an Erlenmeyer flask, 100 mL of 1mmol dm^{-3} tetrachloroauric acid ($HAuCl_4$) was heated (T = 220 °C) under stirring at 300 rpm. After heating to boiling point, 50 mL of 38.8 mmol dm^{-3} $Na_3C_6H_5O_7$ was quickly added to the flask with vigorous stirring. The mixture ($HAuCl_4$ / $Na_3C_6H_5O_7$) was continuously heated for a period of time (ca., 10 min). The resulting yellow solution turned ruby red within minutes, indicating the formation of AuNPs. Following this, the stirrer-hot plate was turned off and the solution was allowed to cool to room temperature. The AuNPs solution was stored in a bottle wrapped in aluminium foil and kept at 5 °C until use.

4.2.4 Immobilisation of Gold Nanoparticles on Patterned Brush Surfaces

Figure 4.4 shows a schematic description of the immobilisation process of AuNPs on patterned PCysMA brushes. Briefly, the process started by cleaning glass microscope slides with piranha solution, before being functionalised with APTES. The BIBB initiator molecules were then coupled to the APTES-functionalised surface. Afterwards, the PCysMA brushes were grafted onto the initiator-coated surfaces through SI-ARGET-ATRP. IL with a two-beam interference system at a wavelength of 244 nm was used to pattern the grafted polymer brush surfaces; the samples were exposed to doses ranging from 1 and 100 J cm^{-2} to produce patterns of different widths. Moreover, two exposure modes were employed in the present work: a single exposure involved exposure of the sample once to the interferogram; in double exposure, the sample was rotated through an angle(ϕ) and exposed a second time, yielding in overlapping patterns of surface modification. Following this, a small amount (ca. 1 mL) of AuNPs solution was poured onto the patterned polymer brush sample to cover the entire surface and left covered overnight at ambient conditions. Finally, the samples were rinsed with deionised water to remove the unbound nanoparticles and dried under nitrogen flow.

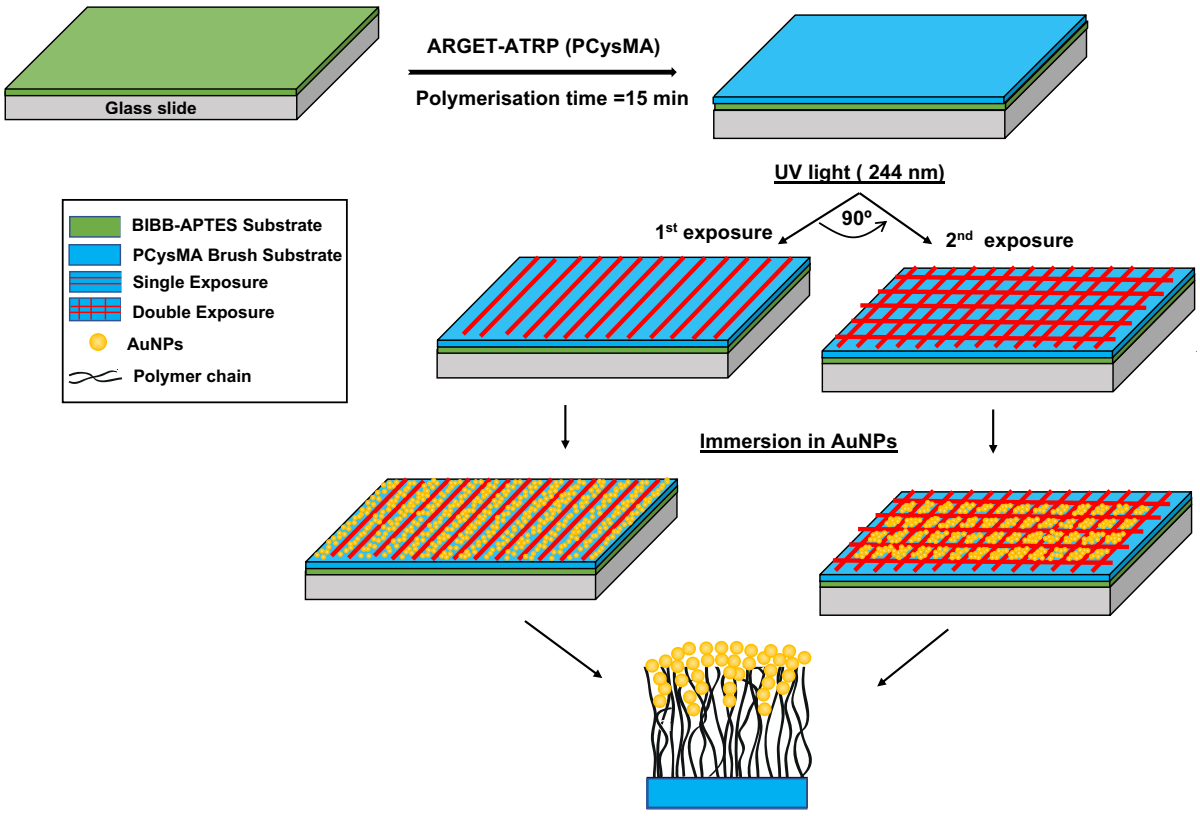

Figure 4.4. Schematic illustration of the process used to fabricate arrays of plasmonic AuNPs on top of the patterns of polymer brushes prepared by the IL approach.

4.2.5 Surface Functionalisation and Attachment

Firstly, AuNPs immobilised on the polymer nanostructures were functionalised with 11-amino-1-undecanthiol (AUT); samples were immersed in a 2 mM solution of AUT in ethanol for 20 h, then rinsed with ethanol and dried with nitrogen. Secondly, the samples were submerged in glutaraldehyde (GA) (12.5% in deionised water) for 30 min, rinsed sequentially with deionised water and ethanol, and dried under nitrogen flow. Afterwards, the samples were immersed in a 10 mM aqueous solution of AB-NTA [N-(5-Amino-1-carboxypentyl) iminodiacetic Acid], pH 5 overnight. Next, the samples were washed with deionised water and dried under nitrogen. This was followed by immersing the samples in a 10 mM aqueous solution of nickel sulfate for 5−7 min. Subsequently, the samples were rinsed with deionised water, dried with nitrogen, and then immersed in His-tagged BT6 Maquette in 20 mM HEPES buffer (0.03% BDDM, pH = 7.5) overnight in a humid chamber in a refrigerator. Finally, the samples were sequentially rinsed with HEPES buffer and deionised water, and dried with nitrogen.

4.2.6 Characterisation and Refractive Index Measurements

The process of grafting PCysMA brushes onto BIBB-APTES glass substrates was investigated using XPS and SE. The surface morphologies of the patterned polymer brushes as well as the immobilised nanoparticles were imaged using AFM. Samples were dried under nitrogen flow before imaging. A silicon nitride probe was used to scan the samples in tapping mode. Imaging processing and particle count analysis was undertaken using Nanoscope analysis software. The UV−vis spectra of the immobilised AuNPs were measured using a Cary 50 spectrophotometer in the spectral range from 450 nm to 900 nm. Analysis of peak positions and corresponding intensities was conducted using Originlab software. In addition, dynamic light scattering was used to determine the size of the synthesised AuNPs, and X-ray diffraction was used to confirm the crystalline nature of the nanoparticles. Nuclear magnetic resonance spectroscopy was used to confirm the formation of cysteine methacrylate monomer and the results were as follows: *^{1}H NMR (400.1MHz, D_2O) δ (ppm) =1.89 (s, 3H), 2.60−3.16 (m, 6H), 3.79 (m, 1H), 3.84 (m, 1H), 4.20−4.20 (m, 4H) 5.67 (s, 1H), 6.10 (1H).^{13}C NMR (400.13 MHz, D_2O) δ (ppm) =17.33, 26.28, 32.04, 33.95, 53.47, 65.27, 65.26, 66.81, 127.18, 135.57, 168.72, 172.75, 174.07.*

To measure the bulk RI sensitivity of AuNPs immobilised on polymer nanostructures, different concentrations of aqueous solution of NaCl [0−4 %] were used. The bulk RI sensitivity was obtained by plotting the peak position of LSPR against the RI of the surrounding medium.

4.3 Results and Discussion

4.3.1 Characterisation of the BIBB−APTES Initiator on Glass Substrates

The initiator film was prepared according to the previous study [160], in which APTES SAMs deposited on glass substrates were reacted with BIBB in the presence of triethylamine to form the BIBB-APTES initiator. The formation of the initiator was confirmed by CA, SE, AFM, and XPS analysis. Figure 4.5a illustrates the water CA of clean glass substrates, APTES substrates, and BIBB-APTES substrates. The values shown are the averages of five readings taken from three different substrates. As a consequence, the CA was observed to be 9 ± 1° for the clean glass substrates due to the presence of Si-OH groups, while it increased to 46 ± 2° for APTES SAMs. The surface of the SAMs was hydrophilic due to its amino-terminal group ($-NH_2$). The CA increased to 64 ± 2° with BIBB deposition indicating successful modification on the surface. The CA is increased because the surface termination has reduced polarity compared to APTES. This result is in agreement with previous studies. [274, 275] The SE thickness of the resulting BIBB-APTES film was approximately 1.27 ± 0.2 nm. Figure 4.5b shows the AFM height image of the BIBB-APTES initiator. The surface roughness was calculated from a (2 µm × 2 µm) area, which showed smooth surfaces (Ra = 0.51 nm), which is consistent with the formation of high quality films.

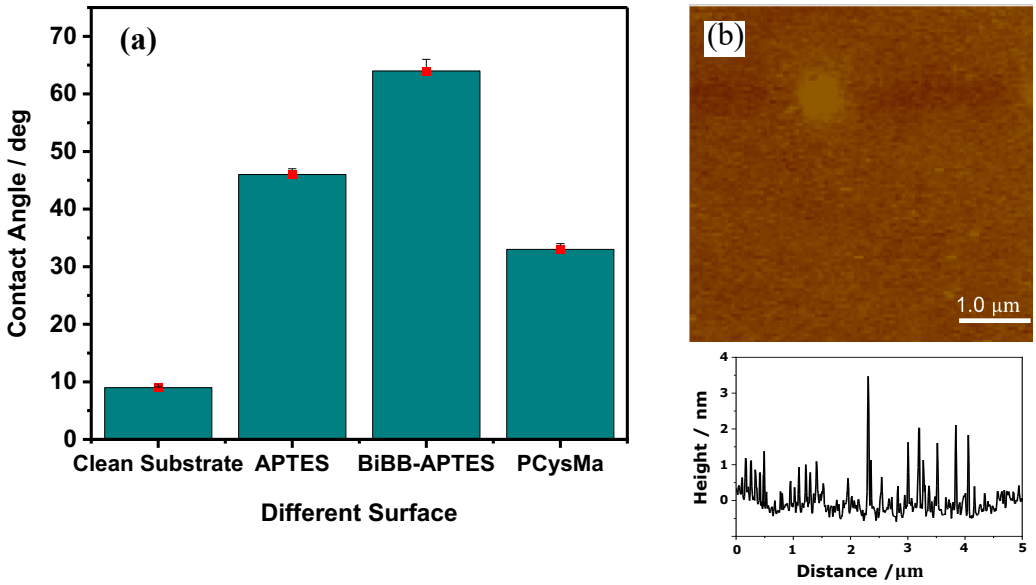

Figure 4.5. (a) Schematic illustration of the contact angle results for different surfaces and (b) An AFM height image of the BIBB-APTES substrates.

Figure 4.6 below displays typical results from XPS measurements conducted on BIBB-APTES substrates. The XPS wide scans confirmed the presence of carbon, oxygen, nitrogen, bromine, and others. In the spectral region of the C 1s core level (see Figure 4.6a), the XPS spectrum was fitted with three components with binding energies of 285.0 eV, 286.4 eV, and 288.1 eV, corresponding to $C-C$, $C-O$ / $C-N$ and $C=O$, respectively. In the N 1s spectral region (see Figure 4.6b), the XPS spectrum was fitted with two components with binding energies of 399.4 eV and 401.4 eV, which were attributed to $C-NH_2$ and $C-NH_3^+$, respectively. In the Br 3d core level spectral region (see Figure 4.6c), the XPS was also fitted with two components with binding energies of 70.2 eV and 71.4 eV, which were attributed to Br $3d_{5/2}$ and Br $3d_{3/2}$ and resulted from the spin-orbit coupling. [276]

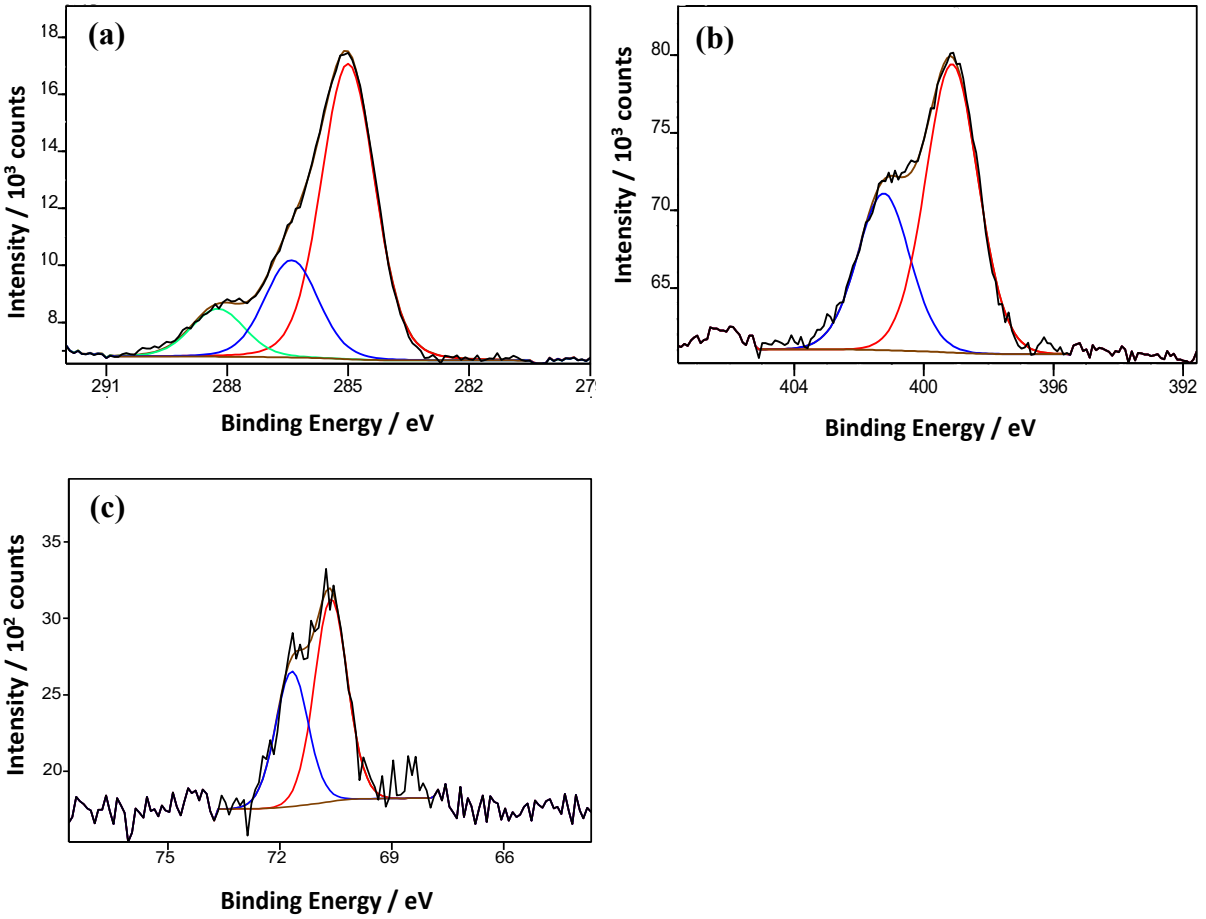

Figure 4.6. XPS spectra of the BIBB-APTES modified glass substrates: (a) the C 1s core-level spectrum comprised three peaks, (b) the N 1s core-level spectrum comprised two peaks, and (c) the Br 3d core-level spectrum comprised two peaks.

4.3.2 Growth of PCysMA Brushes from BIBB−APTES Substrates

Polymer brushes were prepared via controlled ARGET-ATRP based on the procedure provided by Alswieleh et al. [277] After polymerisation, the CA was measured to be 33 ± 2°. XPS data were obtained after the formation of PCysMA brushes on BIBB-APTES substrates to confirm their chemical structures. Figure 4.7a shows the high-resolution XPS spectra of C 1s, N 1s, and S 2p (see Figure 4.7a). The XPS C 1s spectrum was fitted with three components; the main peak observed at 285.0 eV was attributed to $C-C$, the second peak at 286.3 eV was attributed to $C-O$ / $C-N$ and the third peak at 288.7 eV was attributed to $C=O$ (see Figure 4.7b). The $C-C$, $C-O$ / $C-N$ and $C=O$ atomic ratios derived from the fitted C 1s spectrum were 2 : 1.5 : 1, which are close to the theoretical ratio of 2 : 1.3 : 1. The high-resolution N 1s spectrum was fitted using two components with binding energies of 399.1 eV and 401.5 eV, which were attributed to $C-NH_2$ and $C-NH_3^+$ species, respectively (see Figure 4.7c). It is anticipated that approximately 80 % of the primary amine groups are protonated. In the spectral region of the S 2p core level (see Figure 4.7d), the XPS spectrum was fitted with two components. The main peak was centred at a binding energy of 163.5 eV, while the other peak was located at 164.5 eV corresponding to S $2p_{3/2}$ and S $2p_{1/2}$ caused by the spin–orbit interaction. [276, 278]

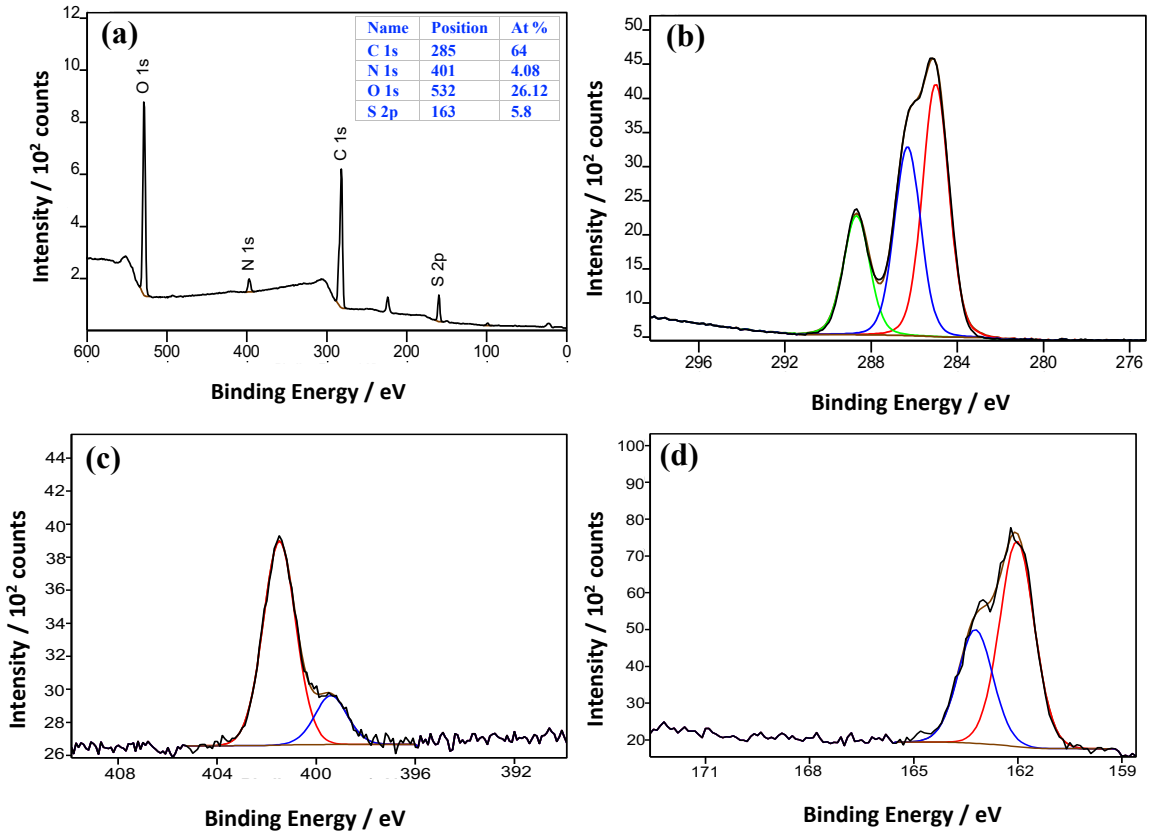

Figure 4.7. XPS analysis of PCysMA grafted onto BIBB-APTES: (a) wide scan spectrum; (b) C 1s spectrum; (c) N 1s spectrum; and (d) S 2p spectrum.

The thickness of the polymer brushes can be controlled by varying the polymerisation time or the activator/deactivator ratio. [279] In the current study, the brush thickness was modified by varying the polymerisation time. Using this approach, samples can be polymerised within the same polymerisation solution and the result can be directly compared, leading to a systematic study. PCysMA brushes were grown from BIBB-APTES film functionalised glass substrates via SI-ARGET-ATRP, which is known as an efficient and convenient technique for producing dense uniform polymer brushes. The dry brush thickness was measured using SE. Figure 4.8 below shows the variation in the thickness of PCysMA brushes with the polymerisation time at 20 °C. During the first 60 min, the brush thickness and polymerisation time showed an approximate linear relationship. Subsequently, as the polymerisation time increased, the brush thickness increased at a lower rate. Some of the chains undergo terminations; over time the number of terminations grows, and the polymerisation rate declines. A fixed polymerisation time of 15 min was selected for the rest of the work described, providing a brush thickness of 20 nm. Up to this thickness, the brush growth was consistent and uniform, and films could be prepared repeatedly. This result is consistent with the reported study. [277]

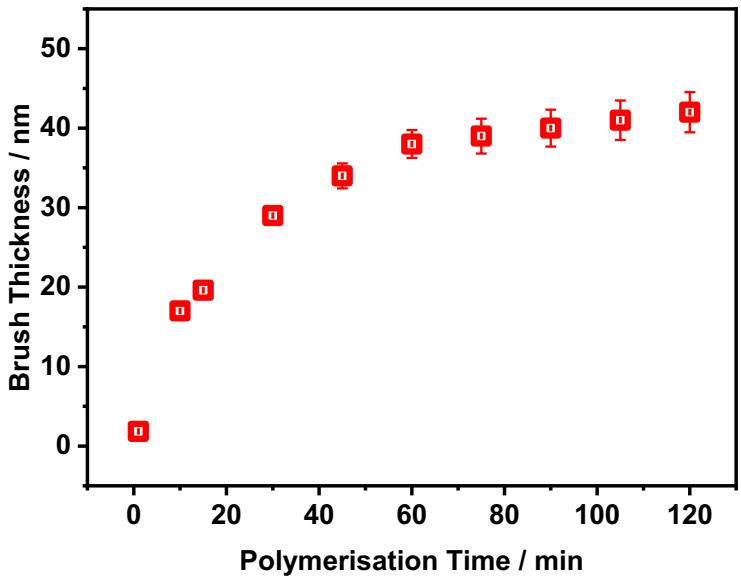

Figure 4.8. Variation in PCysMA brush thickness with polymerisation time using SE.

4.3.3 Patterning of Polymer Brushes Using Interferometric Lithography

The fabrication process used to generate patterned polymer brushes is shown schematically in Figure 4.4. A Lloyd's mirror two-beam interferometer system was utilised to pattern PCysMA brushes deposited on BIBB-APTES substrates. The interferogram consists of alternating bands of constructive and destructive interference with a pitch of $\lambda/2 \sin\theta$, where λ is the wavelength of the laser, and θ is the angle of the incident beam. Therefore, the polymer brushes were removed from the regions exposed to the maxima in the interferogram. The dimensions of the polymer nanostructures were adjusted by varying the UV exposure dose, as well as the angle between interfering beams and the polymerisation time. In this study, PCysMA brushes were successfully patterned in a single step upon exposure to a 244 nm UV laser beam; with doses ranging from 5 J cm^{-2} to 100 J cm^{-2} applied. Figure 4.9 below shows AFM height images of polymer nanostructures created by IL using single exposures and incidence angles of $20 \pm 5°$. Figure 4.9a displays the surface morphology of the sample exposed to a dose of 5 J cm^{-2}. The AFM image reveals alternating bands of contrast with a pitch of 485 $\pm$12 nm, equal to that of interferogram. The height difference between the bright maxima and dark minima in the height image in Figure 4.9a is 0.6 ± 0.1 nm. If the dose is increased to 10 J cm^{-2}, the image contrast becomes more pronounced at the cross section at the bottom of Figure 4.9b, revealing that the height difference is increased to 1.1 ± 0.1 nm. The height difference increases further to 2.3 ± 0.1 nm after a dose of 30 J cm^{-2} (see Figure 4.9c).

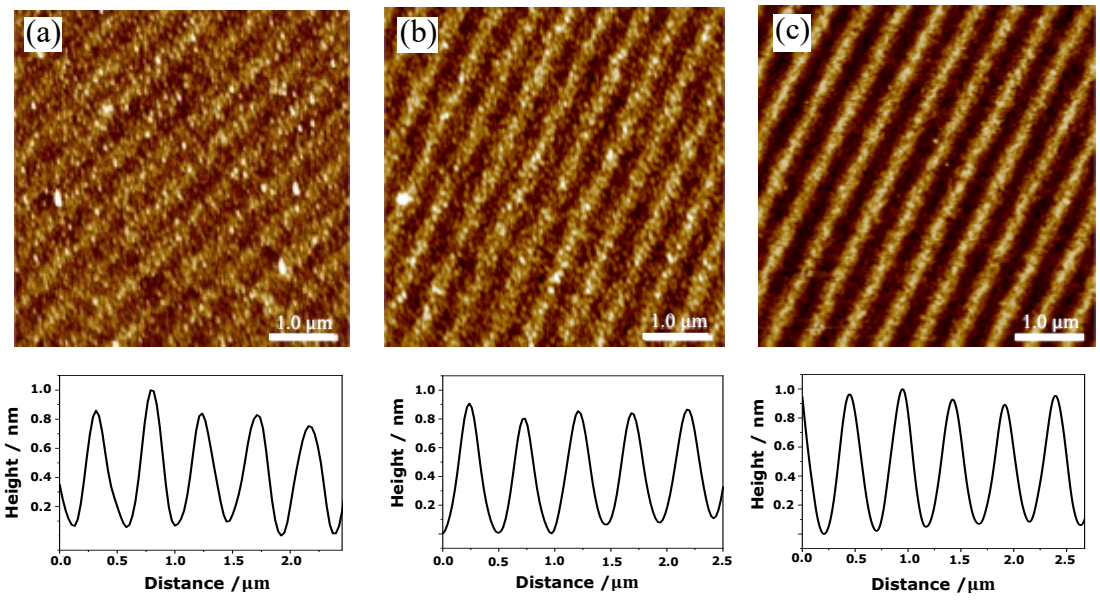

Figure 4.9. AFM height images of PCysMA nanostructures patterned by IL using single exposures at fixed incidence angles ($\theta = 20 \pm 5°$), and different doses: (a) dose = 5 J cm^{-2}, (b) 10 J cm^{-2} , and (c) 30 J cm^{-2}.

Thus, the observations suggest that the regions of the sample that are exposed to maxima in the interferogram are etched. As the dose increases, the amount of material removed from regions exposed to maxima in the interferogram increases until eventually all polymeric material is removed. Figure 4.10a illustrates the FWHM of the polymer nanostructures as a function of exposure dose. Indeed, it can be observed that there is an increase corresponding to the increase in doses. Meanwhile, the height of the polymer brushes (obtained from cross-section via AFM topographical images) also increases as a function of exposure dose (see Figure 4.10b). These results indicate that polymer brushes are able to be controlled in these nanostructures, which is consistent with the reported studies. [274, 277]

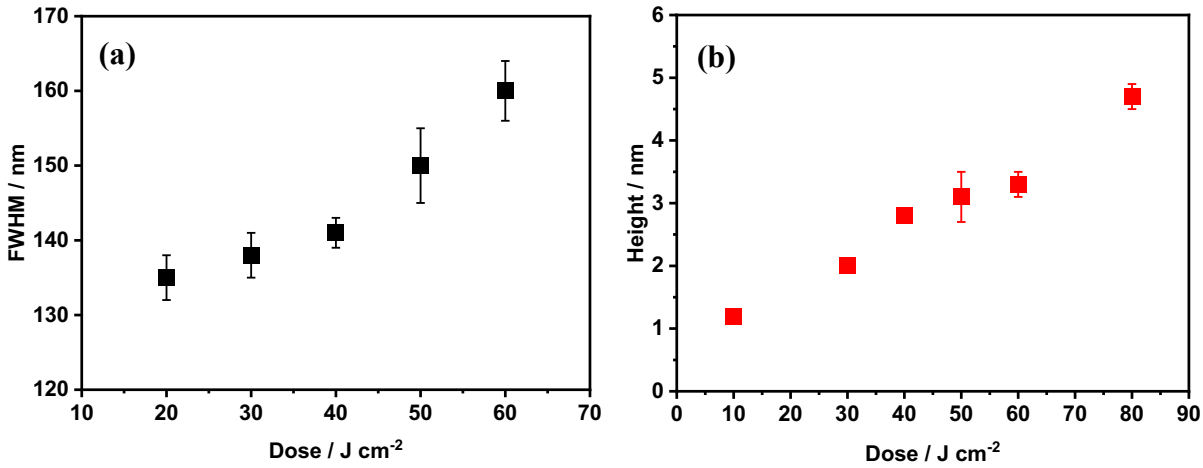

Figure 4.10. (a) and (b) Variation in the brush nanostructure FWHM and height difference between exposed and unexposed regions, respectively, as a function of UV dose during patterning.

In Figures 4.11a−d, AFM height images of linear polymer nanostructures are presented. These nanostructures were created through single exposures, each using a dose of 30 J cm^{-2}. The key variable here was the angle at which the exposure occurred (θ): 20±5°, 25±5°, 30±5°, and 40±5°. These angles resulted in different pitches between the nanostructures as follows: 485 ± 12 nm, 324 ± 9 nm, 267 ± 10 nm, and 206 ± 13 nm, respectively. Thus, as the incidence angle increased, the pitch between the nanostructures decreased. In addition to the single exposure procedure, a double exposure strategy was also utilised. After the first exposure, the samples were rotated through an angle of 90°. In Figures 4.11e and 4.11f, AFM height images of the square polymer nanostructures are displayed. These nanostructures were created using incidence angles of 25° and 20°, respectively. The first exposures to both samples were carried out at doses of 35 and 65 J cm^{-2} after placing the samples close to the reflecting mirror, while

the second exposures were then carried out at doses of 30 and 60 J cm^{-2} after rotating the samples to 90°, respectively.

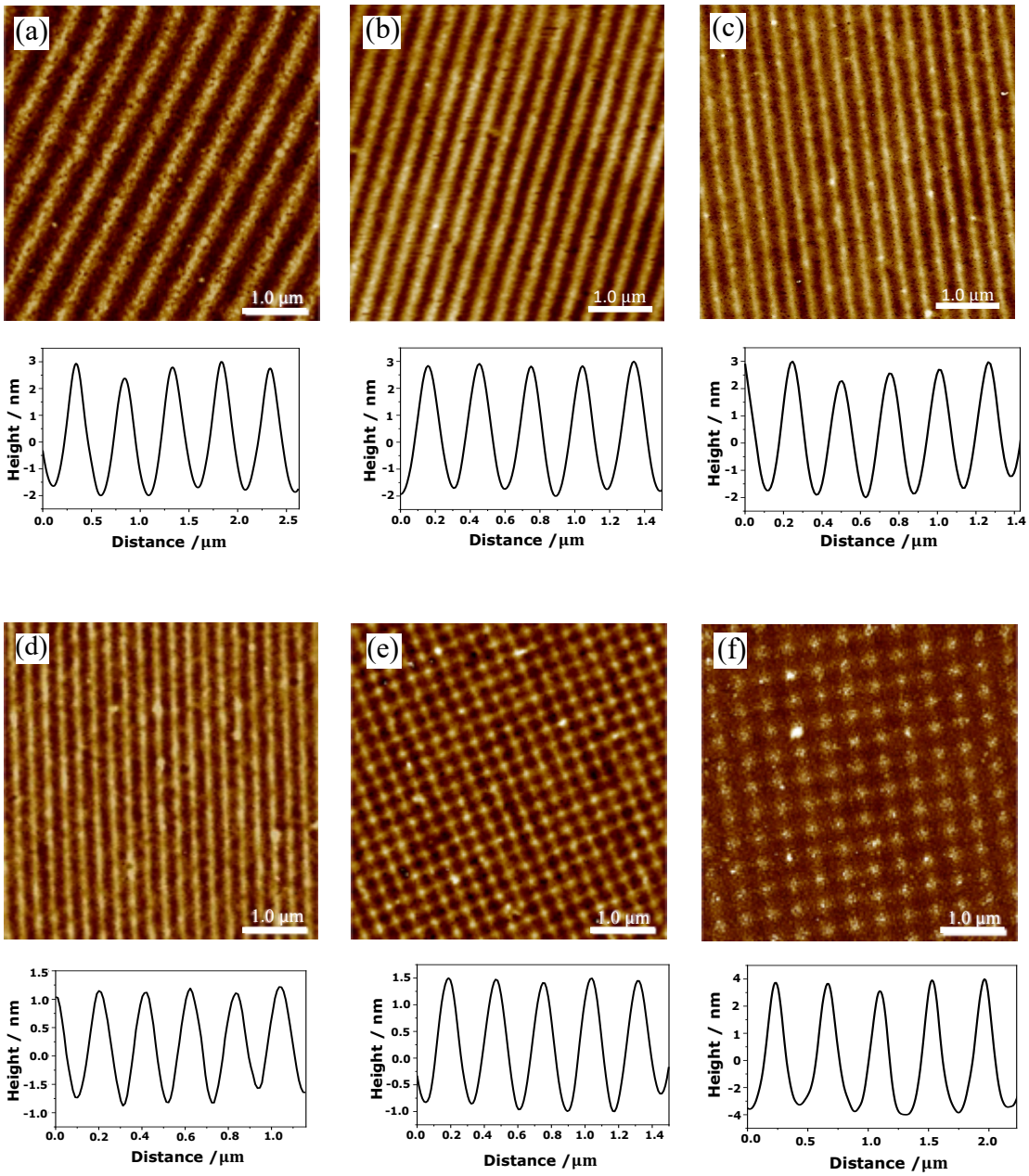

Figure 4.11. AFM height images of the patterned brush surfaces. (a, b, c, and d) Linear nanostructures obtained by exposing samples to a single dose of 30 J cm^{-2} with varying angles of incidence: (a) $\theta = 20\pm5°$, (b) $\theta = 25\pm5°$, (c) $\theta = 30\pm5°$, and (d) $\theta = 40\pm5°$. (e and f) Square polymeric nanostructures obtained by subjecting samples to double exposure: (e) 1st dose = 35 J cm^{-2}, 2nd dose = 30 J cm^{-2}, $\theta = 20\pm5°$, $\phi = 90°$, and (f) 1st dose = 65 J cm^{-2}, 2nd dose = 60 J cm^{-2}, $\theta = 25\pm5°$, $\phi = 90°$.

4.3.4 Characterisation of Gold Nanoparticles

Gold nanoparticles were synthesised by citrate reduction of gold salts according to the classical Turkevich method, where $HAuCl_4$ was boiled in deionised water and reduced with $Na_3C_6H_5O_7$, which stabilises the final nanoparticles by electrostatic repulsion. Figure 4.12a demonstrates the characteristic absorption spectrum of AuNPs with an extinction peak wavelength of 520 nm. The size of AuNPs in solution was determined by dynamic light scattering (DLS), and therefore, the particle size was 11.5 ± 0.5 nm. AFM imaging of PCysMA brush surfaces coated with AuNPs was utilised to characterise the coating in terms of particle shape, size, and organisation on the brush surfaces. Figure 4.12b demonstrates the AFM height image of AuNPs immobilised on the brush surface obtained after 6 h of immersion in the colloidal suspension. As can be noted, the AuNPs have a spherical shape, and it is evident that the close packing of the nanoparticles required only a few hours to occur in agreement with the literature [280]. The cross-section of the AFM image enabled the possibility to estimate the diameter of the particles via measuring the height of the spherical particle embedded on the brush surfaces (see Figure 4.12c). Using this strategy, an average diameter of 10.8 ± 1.9 nm was obtained, which is in agreement with that obtained by DLS.

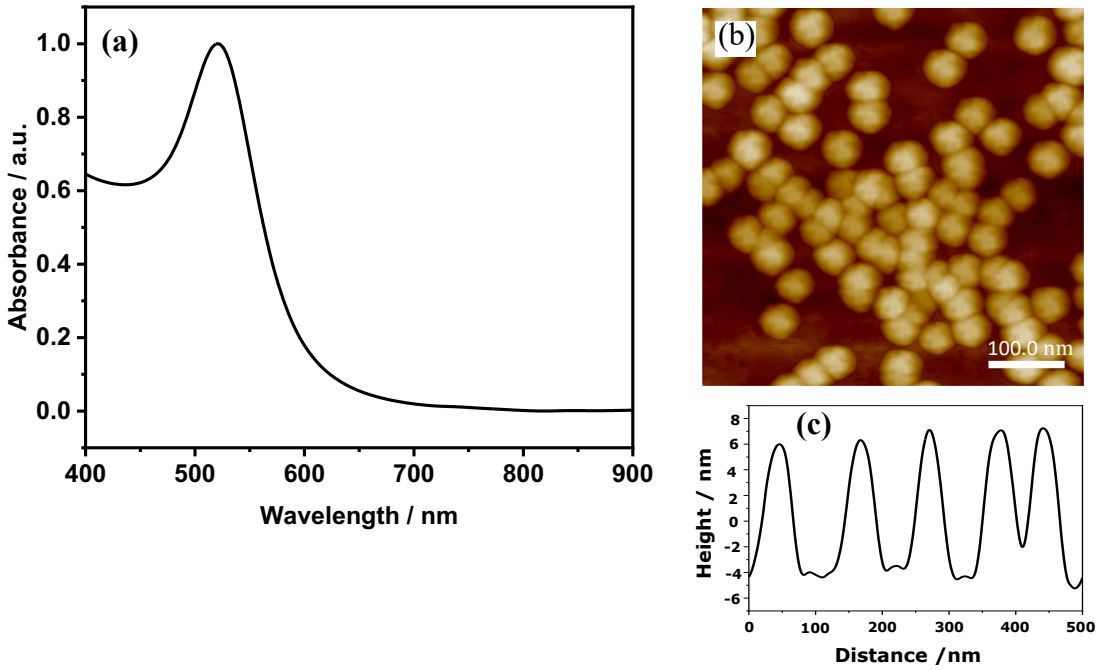

Figure 4.12. (a) UV−vis spectrum of the Au colloidal solution and (b) AFM height image of AuNPs deposited on the BIBB-APTES glass substrate.

4.3.5 Immobilisation of Nanoparticles on Patterned Brush surfaces

The spherical Au nanoparticles were immobilised on patterned polymer brushes as described previously in Section 4.2.4. Figure 4.13 shows AFM height images of polymer nanostructures before and after the immobilisation of AuNPs. In Figures 4.13a, b, and c, the polymer brush samples were patterned via IL using single exposures at doses of 25 J cm^{-2}, 35 J cm^{-2}, and 50 J cm^{-2}, along with their incidence angles of 20°, 20° and 25°, respectively. Following this, the patterned samples were immersed in the AuNPs solution overnight. In Figures 4.13d, e and f, AFM height images of nanospheres immobilised onto patterned samples, corresponding to the samples in Figures 4.13a−c, respectively. It can be observed that colloidal AuNPs go into the patterned polymer brushes with a high level of selectively. This high level of selectivity can be attributed to two main factors: (i) the patterning process allows complete removal of the brush from the exposed regions; (ii) citrate-coated AuNPs exhibit a strong binding affinity towards PCysMA brushes, which enables repeated washing of samples under sonication after the

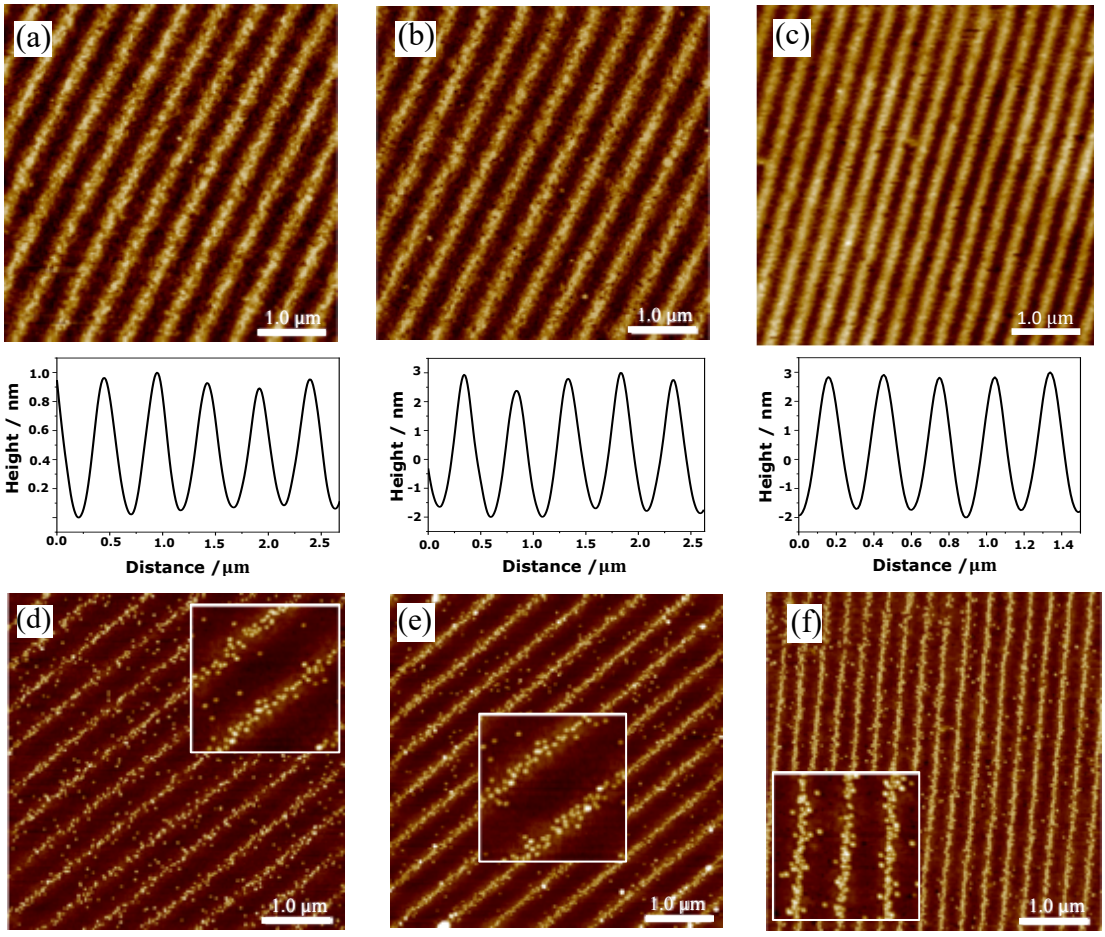

Figure 4.13. AFM height images of polymer nanostructures patterned by single exposures at doses of (a) 25 J cm^{-2}, (b) 35 J cm^{-2}, and (c) 50 J cm^{-2}. (d), (e) and (f) the same samples after immersion in AuNP solution for 24 h, respectively. The inset shows a region of the pattern at higher resolution.

immobilisation of AuNPs without damaging or affecting the uniformity of the nanostructures. Figure 4.14 displays AFM height images of square arrays of polymer nanostructures fabricated by IL using a double exposure strategy. In Figures 4.14a, b and c, the exposure doses (1^{st} /2^{nd} dose) were (7/5 J cm^{-2}), (10/7 J cm^{-2}), and (65/60 J cm^{-2}), with incidence angles of 15°, 20° and 25°, respectively. It can be observed that uniform arrays of nanoparticles can be assembled on the surfaces of the polymer nanostructures defined by the exposure conditions (see Figures 4.14d, e, and f) In addition, hole arrays of polymer nanostructures containing Au nanoparticles with an average diameter of approximately 13 $\pm$ 2 nm were formed when the samples were subjected to double exposure at higher doses (see Figure 4.14f). Consequently, it can be said that when double exposure is performed at lower doses (i.e. below 30/25 J cm^{-2}), the resulting polymer nanostructures are well suited to produce dots in a square lattice. Conversely, at higher exposure doses (i.e. above 30/25 J cm^{-2}), polymer nanostructures are more suitable for creating holes within a square lattice when subsequently immobilised with AuNPs.

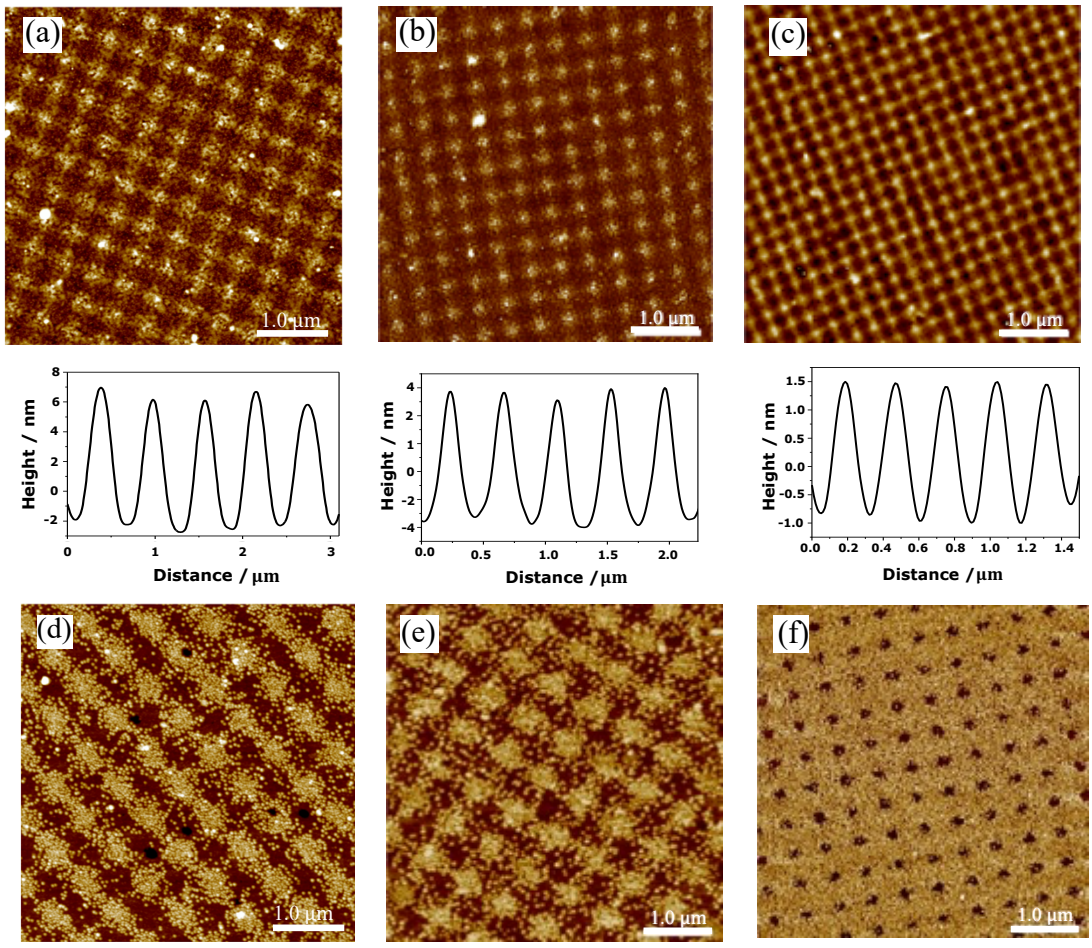

Figure 4.14. (a), (b) and (c) AFM height images showing polymer nanostructures fabricated by IL using double exposure at doses of (7/5 J cm^{-2}), (10/7 J cm^{-2}), and (65/60 J cm^{-2}), respectively. (d, e, and f) Images showing polymer nanostructures after immersion in AuNPs for 24 h.

This result may indicate that exposing the samples to double exposure with high doses resulted in the complete removal of both brush and initiator from the exposed regions; thus, creating a charged surface enabling nanoparticle immobilisation. Figure 4.15a shows a scanning electron microscopy (SEM) image of polymer nanostructures containing AuNPs. Thus, the SEM image showed the morphology and uniformity of the AuNPs attached to the polymer nanostructures, which is consistent with the AFM images. Moreover, microscale patterning was conducted by exposing the polymer brush functionalised BIBB-APTES substrates through a mask. AFM in the tapping mode was used to image the resulting patterns. Figure 4.15b demonstrates polymer microstructures following exposure through 2000 mesh grid to 5 J cm^{-2}. There is a clear contrast between the masked (bars) and the exposed regions (squares), with the exposed regions demonstrating the dark colour. Figure 4.15c shows the AFM height image of Au nanoparticles immobilised on the polymer microstructures; the results confirm that citrate-coated AuNPs exhibit strong binding affinity for PCysMA, leading to direct attachment of the particles to the brushes.

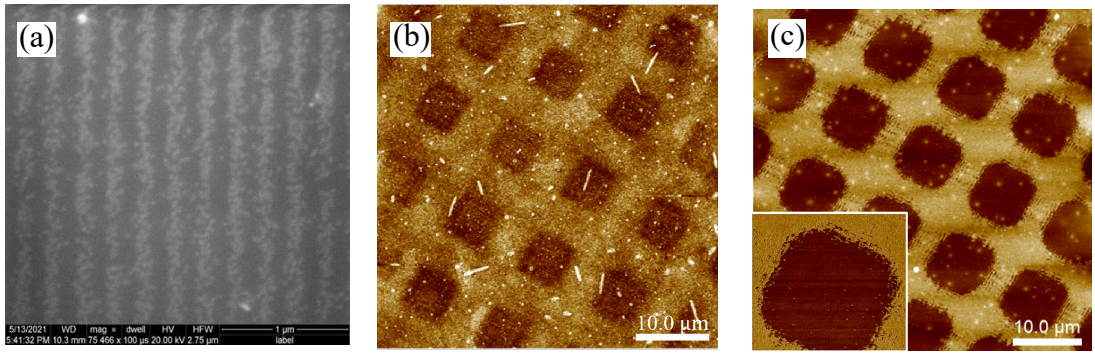

Figure 4.15. (a) SEM image of polymer nanostructures containing AuNPs. (b) and (c) AFM height images of polymer nanostructures before and after addition of AuNPs, respectively. The inset shows a region of the pattern at higher resolution.

Even though the AuNPs appeared red in the solution, the resulting nanoparticles immobilised on the surface of the polymer brushes appeared violet (see Figures 4.16a and b). This change in colours may indicate the aggregation or clustering of nanoparticles on flat surfaces. [281] To evaluate the properties of AuNPs immobilised on substrates, it is important to understand how the LSPR properties of immobilised AuNPs may differ from those in solution. Therefore, the extinction spectra of AuNPs upon the deposition on various polymer nanostructures were studied. Figures 4.16c and d show the AFM height image and LSPR spectrum of linear polymer nanostructures containing AuNPs fabricated using a single exposure at dose of 35 J cm^{-2} with $\theta = 20°$. It can be also observed that the extinction peak of the nanoparticles shifted from 520

nm (in solution) to 563 nm after being immobilised on the brush surface. The redshift of the plasmon peak from its initial position in the solution can be attributed to the change in the surrounding environment, together with the rather dense nanoparticle packing. [282] When the Au nanoparticles move from the water-air interface to the substrate surface as a monolayer, the distance between the nanoparticles becomes shorter and the influence of near-field interparticle coupling on the particle plasmon resonance increases. Therefore, this leads to a significant shift of the extinction peak to higher wavelengths [283].

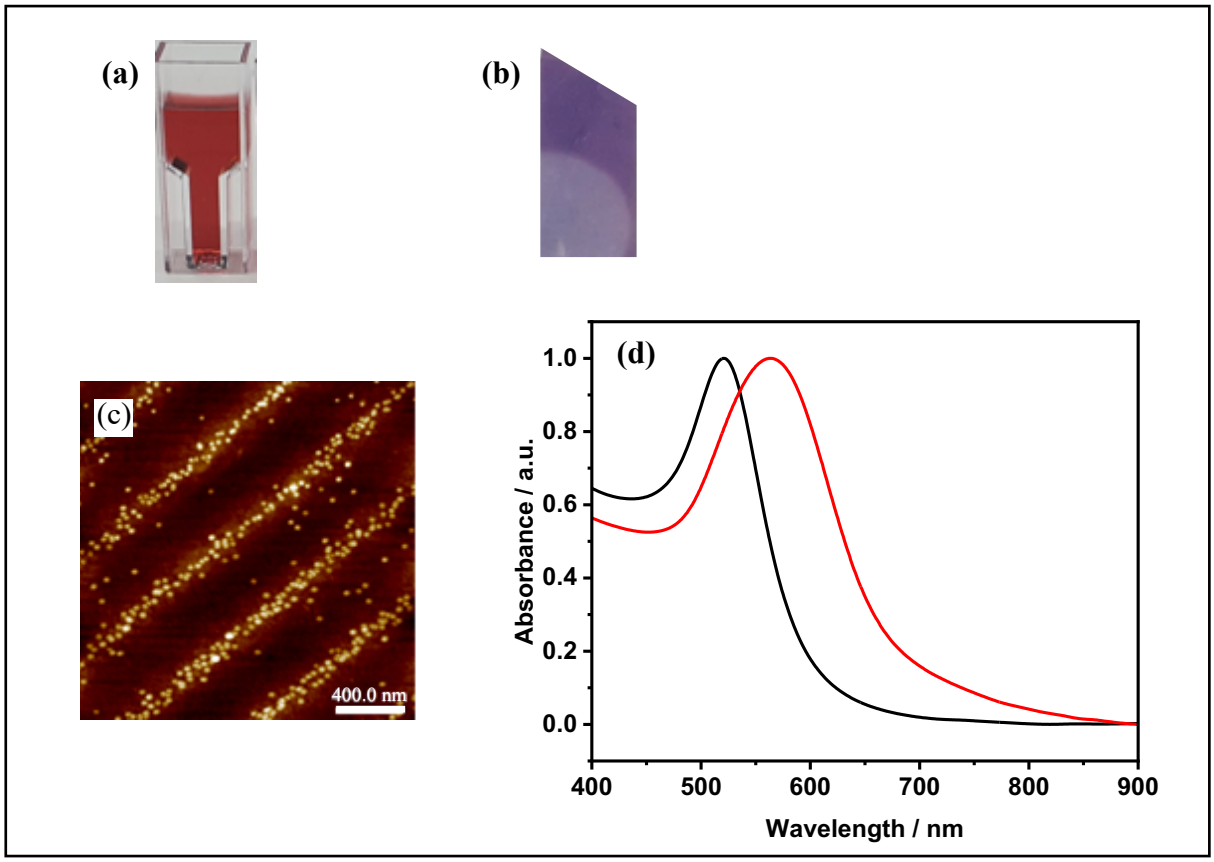

Figure 4.16. (a) and (b) Photographs of AuNPs in solution and immobilised onto patterned PCysMA brush surface, respectively. (c) AFM height image of immobilised AuNPs on linear polymer nanostructures. (d) Extinction peaks of the immobilised AuNPs (—) and those in solution (—).

Figures 4.17a and 4.17b show the extinction spectrum and AFM image of AuNPs immobilised on square arrays of polymer nanostructures formed by double exposure at doses of 10 and 7 J cm^{-2} with $\theta = 15°$, respectively. It can be observed that the extinction peak of AuNPs shifted towards longer wavelengths after immobilisation on the patterned PCysMA brushes (i.e., from 520 nm in solution to 572 nm on the brush surfaces). A similar result was also observed when examining AuNPs immobilised on hole polymer nanostructures formed through the double exposure process at higher doses of 100 and 95 J cm^{-2}. In this case, the extinction peak shifted from 520 nm to 548 nm, as illustrated in Figure 4.17d and e. Accordingly, these results confirm

that the Au nanoparticles came closer together on the surface, resulting in aggregation, which is in contrast to the behaviour of AuNPs dispersed in a water solution. Moreover, the difference in the level of spectral shift between the square nanostructure (i.e. redshift of 50 nm) and the hole nanostructure samples (i.e. redshift of 28 nm) can be explained by various factors related to the specific properties and geometry of the nanostructures. In square nanostructures, Au nanoparticles are immobilised in specific regions. This precise arrangement forces the Au nanoparticles to assemble in very close proximity to one another, causing them to interact strongly and, therefore, influence the way they interact with light. In contrast, when referring to hole nanostructures, it means that the nanoparticles are assembled over larger areas. In this case, nanoparticles have more freedom to move and interact with incident light, resulting in a less pronounced redshift.

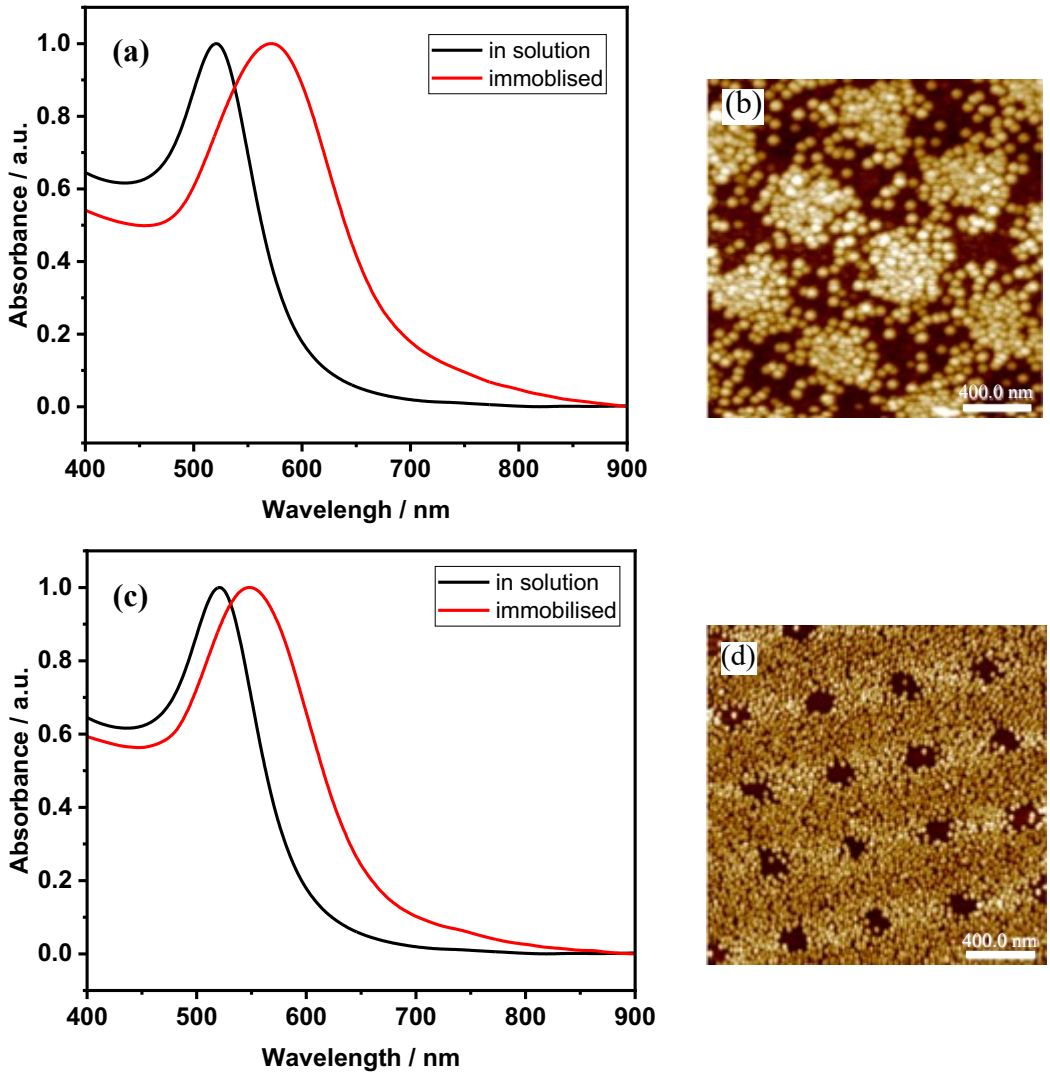

Figure 4.17. (a) and (b) Absorption spectra and AFM height image of AuNPs immobilised on square polymeric nanostructures. (c) and (d) Absorption spectra and AFM height image of AuNPs immobilised on hole polymeric nanostructures, respectively.

4.3.6 Annealing of AuNPs Immobilised on Polymer Nanostructures

Figures 4.18a and 4.18b display photographs of AuNPs immobilised on the polymer brushes before and after annealing, respectively. The annealing process was carried out at a temperature of 600 °C for 2 h. Before thermal annealing, the sample exhibited a dark violet colour, but after annealing, it exhibited a bright colour, indicating a potential modification in the electronic structure or crystalline arrangement of the nanoparticles. Figures 4.18c and 4.18d show AFM height images of AuNPs immobilised on polymer nanostructures before and after annealing at 600 °C for 2 h. The morphology of the surfaces shows that the assembled AuNPs are distributed on the surface in a random way before annealing; however, after 2 h of annealing, the AuNPs show a higher packing ratio, suggesting that they are aggregated, upon annealing, compared to the unannealed sample. This result is consistent with the reported study. [284] Furthermore, cross-section analysis showed that the height difference between the bright maxima and dark minima was about 10.7 ± 0.2 nm, while the FWHM was about 48 ± 1.1 nm. When the sample was annealed, the height difference decreased to 8 ± 0.1 nm, and the FWHM increased to 64 ± 0.3 nm. Moreover, the extinction spectra reveal a significant change in the annealed surface. Specifically, there is a noticeable shift in the peak position towards longer wavelengths (i.e. from 567 to 631 nm), whilst the absorption band also becomes broader (see Figure 4.19a). This change may be attributed to the plasmon near-field coupling effect, suggesting that the spacing between nanoparticle assembles was reduced during annealing.

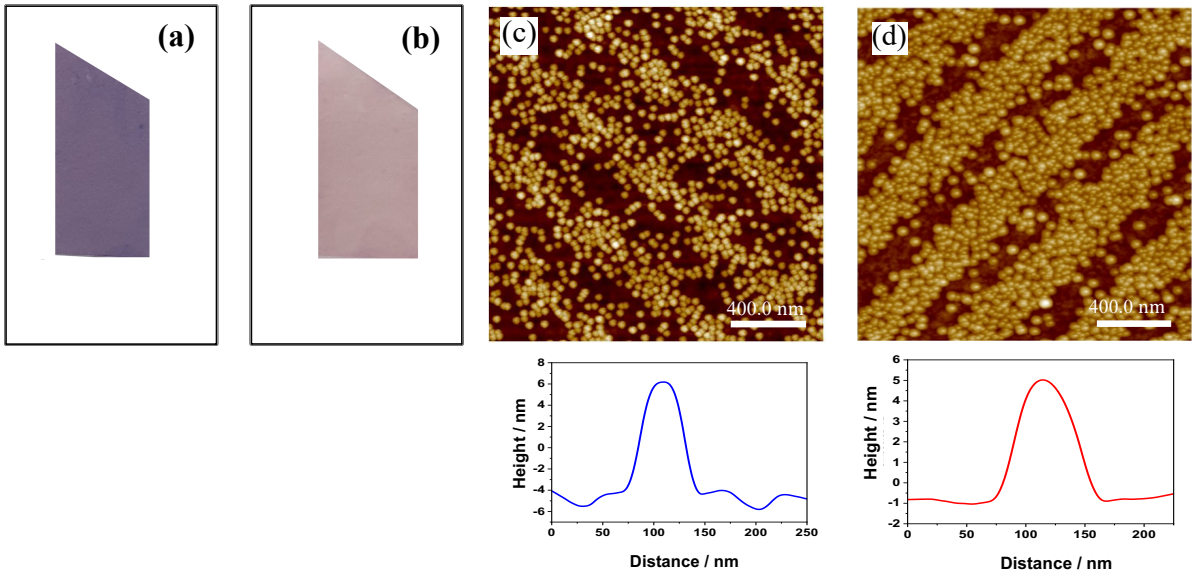

Figure 4.18. (a) and (b) Photos of AuNPs immobilised on polymer brushes before and after annealing at 600 °C for 2 h, respectively. (c) and (d) AFM height images of AuNPs immobilised on linear polymer nanostructures before and after annealing at 600 °C for 2 h, respectively.

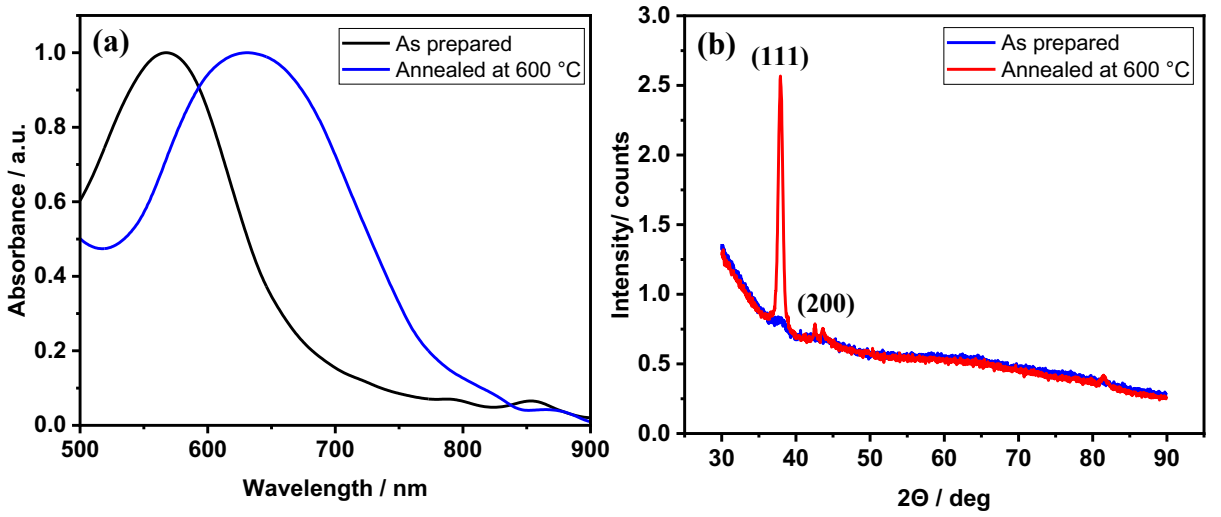

Figure 4.19. (a) Extinction spectra of AuNPs immobilised on the linear polymer nanostructure sample before and after annealing at 600 °C for 2 h. (b) XRD patterns of AuNPs before and after annealing at 600 °C for 2 h.

The X-ray diffraction (XRD) patterns of AuNPs immobilised on the polymer brush surfaces were obtained before and after thermal annealing, and the results are presented above in Figure 4.19b. For the nanoparticles before annealing, the diffraction peak (111) of gold is weak and very broad, indicating that the AuNPs immobilised on the polymer brush surfaces are not well crystallised. Interestingly, the XRD patterns changed significantly after annealing at 600 °C for 2 h. The annealed sample shows pronounced diffraction peaks for gold, (111) and (200) planes at $2\theta = 38.2°$ and 44.4°, respectively (Joint Committee on Power Diffraction Standards-JCPDS no. 04-0784, USA). These results are in agreement with the reported study. [285] Hence, the XPD pattern suggests that AuNPs are crystalline.

4.3.7 Refractive Index Sensitivity of Immobilised AuNPs

To evaluate the sensing response of AuNPs immobilised on polymer nanostructures to a change in the refractive index, different concentrations of NaCl solution were used. The samples were immersed in 0−4 % sodium chloride solutions, which were measured to have refractive indices of 1.0−1.38 RIU. Figure 4.20a shows the response of the plasmon band of immobilised AuNPs to the changing NaCl concentration. As in the case of Au nanostructures, LSPR band maxima were determined for all the immobilised nanoparticles. The results indicate that each increase in the refractive index of the surrounding medium resulted in a redshift in the LSPR bands. The red line in the scatterplot represents the linear regression model fitted to the data (see Figure 4.20b). The R-squared value, which measures the goodness of fit, is 0.90. This means that 90% of the variance in the dependent variable is explained by the independent variable, indicating

a strong fit of the regression model to the data. The sample given in Figure 4.20 showed a refractive index sensitivity of 96 nm/RIU; this value is much lower than that obtained for the Au nanostructures. It is believed that some of the AuNPs penetrate between the brush chains at the initial moment of immobilisation. Moreover, when samples are immersed in an aqueous solution, the polymer brushes tend to stretch farther from the surface, causing the nanoparticles on top of the brushes to penetrate deeper into the brush areas; thus, reducing their sensitivity (see Figure 4.20d).

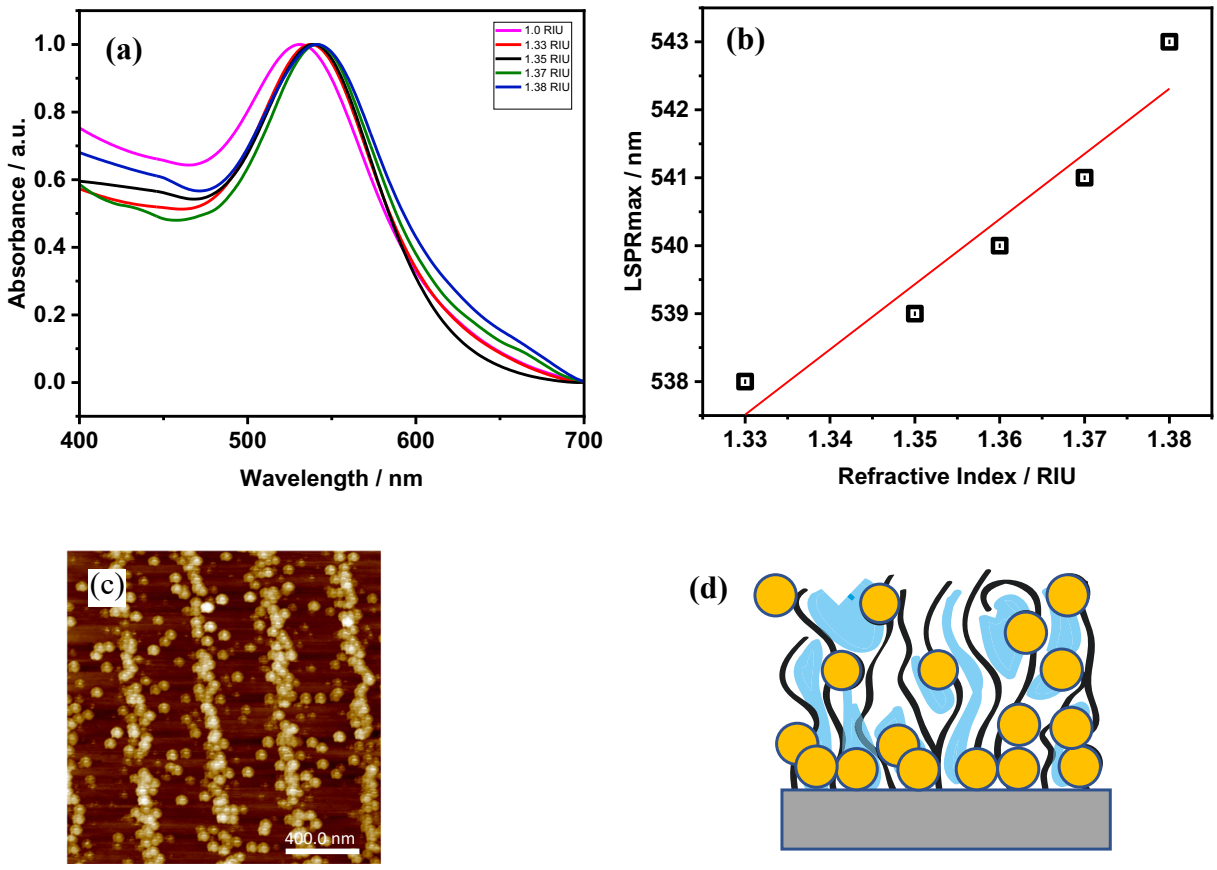

Figure 4.20. (a) UV−vis absorption spectra of immobilised AuNPs recorded with each solution. (b) and (c) Refractive index and AFM height image of the sample. (d) Representative scheme of brush stretching and penetration of nanoparticles upon immersion in an aqueous solution.

4.3.8 Functionalisation of Immobilised AuNPs with Maquettes

The procedure for immobilising AuNPs on patterned films was previously described in section 4.2. The procedure used to functionalise His_6-tagged BT6 maquettes on the surfaces of AuNPs embedded in patterned polymer films was consistent with that previously reported. [275] The aldehyde-terminated surface was first formed by the adsorption of AUT and then reacted with GA. This was followed by coupling the gold surface with an *N*-(5-amino-1-carboxypentyl) iminodiacetic acid to produce a NTA functionalised film. It was then complexed with Ni^{2+} to enable sit-specific binding of His_6-tagged BT6 maquettes. Figure 4.21a−c shows the extinction spectra and AFM images of the functionalised sample with a particle height of 11 ± 2 nm and a diameter of 23 ± 4 nm at a nanostructure pitch of 480 ± 15 nm. A strong feature attributed to the LSPR was observed at 2.13 eV (581 nm, in blue). For light at normal incidence on the array (in black), the extinction spectrum was observed to change dramatically. The LSPR peak is split to yield a small, broad feature at 2.3 eV (539 nm) and larger, narrower feature at 1.9 eV (635 nm). We hypothesise that the splitting results from plasmon-exciton coupling, with hybridisation of the plasmon mode associated with the nanoparticles and the Q_y band associated with the maquettes leading to the formation of new plasmon-exciton polaritons (plexcitons) correspond to the new features in the extinction spectrum of the coupled system.

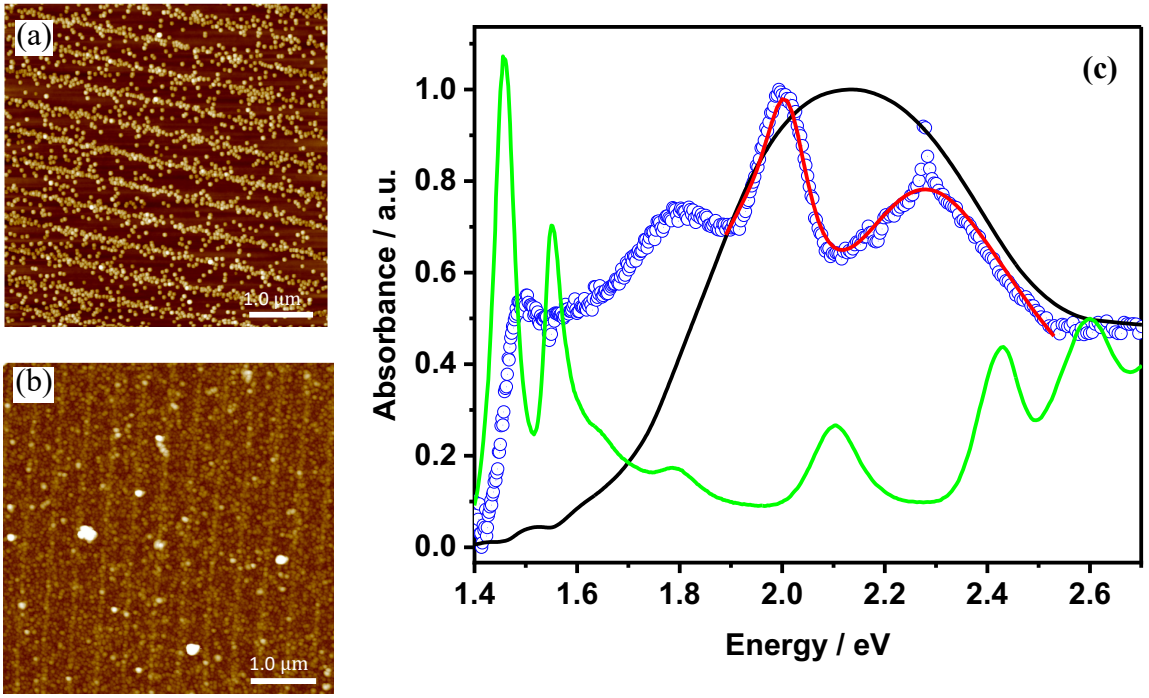

Figure 4.21. (a) and (b) AFM height images of the AuNPs immobilised on patterned surfaces before and after functionalisation with His_6-tagged BT6 maquettes (green spectrum), and (c) Extinction spectra of the sample before and after the attachment of maquettes, respectively.

In the strong coupling regime, the dispersion of the coupled modes (the plexcitons) varies as a function of the wavevector (which depends on the angle of incidence of the light with the sample surface). Thus, the extinction spectrum of the functionalised sample was measured at different angles of incidence (0−25°). For light at normal incidence on the array (red spectrum in Figure 4.22), the extinction spectrum demonstrates a main peak at ~ 1.9 eV, along with a shoulder at higher binding energy (~ 3.2 eV). As the angle of incidence is increased to 5° (light green spectrum), the shoulder becomes more pronounced. As the angle of incidence is increased to 25°, the separation between the two components in the extinction spectrum increases. To test whether these changes in the spectrum are due to strong-exciton coupling, the system was modelled as coupled harmonic oscillators using a method reported previously by Lishchuk et al. [236] Figure 4.21c above displays a measured spectrum (black symbols), together with a calculated spectrum (red line). A good fit was achieved. The mean coupling energy determined from the fitting was 0.16 ± 0.03 eV.

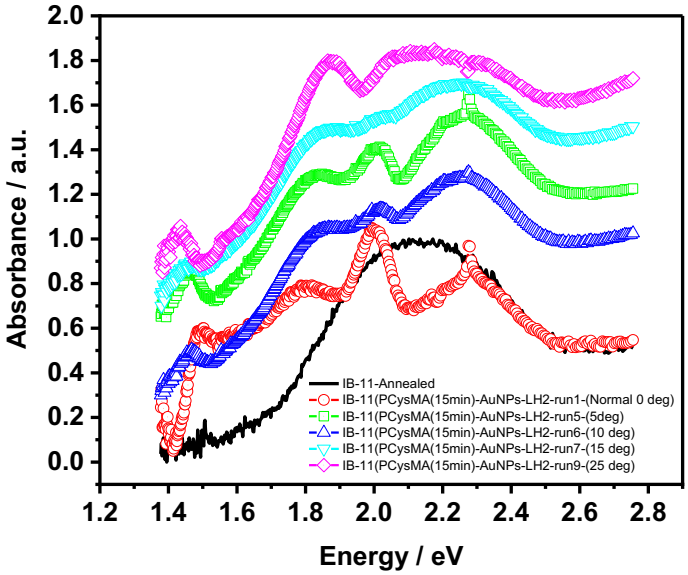

Figure 4.22. The extinction spectra of AuNPs embedded on patterned surfaces in the presence of maquettes at different angles of incidence.

4.4 Conclusion

In this chapter, cysteine methacrylate monomer (CysMA) has been successfully synthesised. This monomer was utilised to prepare PCysMA brushes via SI-ARGET-ATRP with an average brush thickness of 3−40 nm. The chemical structures of the BIBB-APTES films and PCysMA brushes were confirmed by XPS, and the physical properties were characterised by SE and CA measurements. This work has demonstrated that a one-step process is possible for creating patterned polymer brushes by interferometric lithography, and the polymer brushes can be photo-patterned through the use of a Lloyd's mirror interferometer or a mask. What is more, AFM confirmed the successful nano- and micropatterning of the polymer brushes. It has also been demonstrated that patterned PCysMA brushes are able to provide a platform for the highly tunable assembly of AuNPs into ordered arrays on surfaces. Moreover, the nanoparticles that were immobilised on the patterned surfaces exhibited different behaviour from those dispersed in the water solution, as it was observed that the extinction peak of AuNPs shifted to longer wavelengths and became broader when immobilised on the polymer brush surface.

This change in their behaviour is mostly due to the aggregation of nanoparticles on the polymer surfaces. In addition, the effect of the annealing process on the morphology and plasmon band of AuNPs deposited on polymer nanostructures was also evaluated. It was revealed that the peak position of the plasmon band was red-shifted from 567 to 631 nm, when the sample was annealed at 600 °C. The XRD spectra demonstrated no clear peak prior to the annealing process, although it showed a sharp and narrow peak after annealing. Moreover, cross-section analysis of the AFM images showed that the particle height and FWHM increased from 10.7 $\pm$ 0.2 to 12 $\pm$ 0.3 nm, and from 48 $\pm$ 1.1 to 79 $\pm$ 0.3 nm following annealing, respectively. These results suggest that the annealing process led to the recrystallisation of the nanoparticles. Furthermore, the sensing response of nanoparticles immobilised on polymer nanostructures in the presence of different concentrations of NaCl was evaluated. As a consequence, each increase in NaCl concentration resulted in a red shift in the peak position of the plasmon band, and the highest refractive index sensitivity was measured at 96 nm/RIU. Additionally, the sensing response of the nanoparticles in the presence of His_6-tagged BT6 maquettes was also investigated. It was observed that the LSPR peak was split into two new features, indicating the possibility of plasmon-exciton coupling. The system was modelled as coupled harmonic oscillators to test whether changes in the spectrum are associated with plasmon-exciton coupling; the coupling energy was calculated to be 0.16 $\pm$ 0.03 eV.

Chapter 5

5 Fabrication of Aluminium Nanostructures

5.1 Introduction

Over the past few decades, plasmonics has been extensively studied using nanostructures made of silver or gold, which exhibit plasmonic properties from the infrared to the visible spectral region. These metals, however, come with inherent limitations that hinder the development of plasmonic devices toward the blue and UV parts of the electromagnetic spectrum. For example, gold nanostructures do not exhibit plasmonic resonance below 520 nm, owing to the presence of interband transitions. Conversely, silver nanostructures exhibit plasmonic resonances down to 350 nm, but they suffer from strong oxidation, and thus, lose their plasmatic properties over time. [286] In addition, existing or new applications may require the extension of plasmonics towards higher energies, specifically in the UV regions. Therefore, aluminium has emerged as an alternative plasmonic material, due to its ability to support plasmon resonance in the UV region while maintaining low losses. Nowadays, aluminium is considered to be one of the most promising materials capable of pushing the plasmon spectral boundaries towards energies as high as 6.0 eV. Compared to other metals, aluminium is cheap, widely available and non-toxic. In general, aluminium plasmonics is very attractive for many applications including SERS in ultraviolet [287], label-free biosensing application [288], photocatalysis [289], metal enhanced fluorescence [290], and light harvesting devices. [291] However, only a few studies focusing on LSPR in the UV region have been reported, suggesting that aluminium is still in its infancy. The most important aspect in developing plasmonic applications for aluminium is the ability to fabricate well-defined aluminium nanostructures, enabling the control of their plasmonic properties.

Zorić et al. [292] were able to fabricate aluminium nanodiscs using EBL, as they drew specific shapes on resistive layers, resulting in two-dimensional patterns of nanodiscs with well-defined size and shape, as well as tunable interparticle spacing. In that particular study, extinction spectroscopy and theoretical calculations were used to investigate the mechanisms of radiative and non-radiative damping of dipole plasmonic resonance carried by aluminium nanodiscs and related the results to their electronic band structures. The same research group fabricated aluminium nanodiscs by colloidal lithography [293], where the plasmonic properties of these nanodiscs were thoroughly investigated. Aluminium nanostructures have also been fabricated

using nanoimprint lithography (NIL). In one study, aluminium nanovoid-type substrates were fabricated for ultraviolet-SERS detection purposes. The nanoarrays covered large areas of the substrate surface (1 cm^2), and each nanovoid had a diameter of 180 nm and a depth of 20 nm. The result showed that the UV Raman signal of adenine was enhanced by more than three orders of magnitude when using nanovoids compared to planar aluminium substrates. [294] Comparatively, Ekinici et al [295] used extreme ultraviolet interference lithograph (EUVIL) to fabricate well-defined aluminium nanodot arrays on quartz substrates. A 30-nm-thick layer of hydrogen silsesquioxane (HSQ) was deposited on an 80-nm polymethylmethacrylate (PMMA) film, and then exposed to a 13.4 nm UV light source. Subsequently, following exposure, a tetramethylammonium hydroxide solution was used to develop the HSQ photoresist. The resulting patterns were transferred onto the PMMA layer through reactive ion etching, and finally the aluminium was evaporated through the remaining PMMA, leaving an ordered array of dots.

There is an argument that aluminium is not suitable for plasmonics, as it oxidises rapidly, leading to a deterioration in its optical properties. It is true that a native layer of alumina (Al_2O_3) forms on the surfaces of aluminium particles or aluminium films within a few minutes of exposure to air. Correspondingly, Langhammer et al. [293] studied the oxidation of a 20-nm-thick aluminium film using angle-resolved XPS. The results showed that the native oxide layer with a thickness of 2.5−3 nm was formed within a few hours of exposure to air. The oxide layer with the same thickness remained stable for more than 30 days, suggesting that the native oxide acted as a passivation layer to prevent further oxidation. Thus, the underlying aluminium retains its metallic character. The oxidation of aluminium nanoparticles has also been studied by Knight et al. [296] They used EBL to fabricate 100 nm diameter aluminium nanodiscs with various oxidation fractions. The oxidation rate of the aluminium nanoparticles was controlled by introducing a predetermined amount of oxygen into the deposition chamber during metal deposition. The absorption spectra of the aluminium nanoparticles were then determined. The measurements showed that in pure aluminium nanoparticles (0% oxide), the plasmon peak appeared at 400 nm, while as the oxide fraction increased, the scattering efficiency decreased, and the extinction peak shifted to longer wavelengths ($\lambda = 550$ nm at 40% oxide). Upon reaching 50% oxide, the plasmon peak disappeared. It was also noted that the LSPR linewidth did not increase significantly during this process; therefore, the oxide fraction can be used as a parameter to adjust the LSPR position of the aluminium nanoparticles.

A number of studies have also been performed to investigate the formation of alkylphosphonic acid SAMs on aluminium oxide surfaces. [297] It has been shown that upon exposure to UV

light, the C-P bond is cleaved, making the alkyl chain more susceptible to dissolution. This differs from thiols, which are converted to sulfonates upon exposure to UV light. SAMs have a number of advantages when compared to conventional polymeric photoresists, such as being easily assembled onto the surface, simply by immersing clean substrates in a suitable solution for several hours; therefore, eliminating more complicated coating methods. Correspondingly, the focus of this chapter is to demonstrate the feasibility of using interferometric lithography to fabricate aluminium nanostructures via direct, double exposure of SAMs and wet etching.

5.2 Experimental Details

5.2.1 Preparation of Aluminium Substrates

Glass microscope slides with dimensions of 22× 60 mm were used for the present experiments. Prior to aluminium deposition, the glass slides were cleaned with piranha solution as described previously in Section 2.2. **Note:** *extreme precautions should be taken when handling piranha solution at all time*s. Thermal evaporation was performed using an Edwards Auto 306 system. The aluminium deposition was accomplished at room temperature (25℃) and at a base pressure of 10^{-6} mbar with a deposition rate of 0.1 nm s^{-1}. The thickness of the deposited aluminium was determined by QCM and SE and was approximately 27 ± 2 nm. After aluminium deposition, the substrates were exposed to the atmosphere for 40 min to allow the formation of the native alumina layer. [279] Following this, a 2 mM solution of 16-phosphonohexadecanioc (PHDA) in ethanol was prepared. The aluminium substrates were then immersed in this solution for 24 h, allowing for the formation of closely packed PHDA SAMs. After the formation of SAMs, the aluminium substrates were rinsed with ethanol and dried under nitrogen flow. Finally, the substrates were cut into small samples (0.5 × 1 cm) prior to lithographic experiments.

5.2.2 Fabrication of Aluminium Nanostructures

The procedures that were used to make the aluminium nanostructures were almost identical to those used to make the gold nanostructures (i.e., using the same Lloyd's mirror system and UV beam source, 244 nm). Briefly, aluminium films were initially prepared on glass substrates to allow the optical properties of the samples to be studied. PHDA SAMs were formed on the aluminium substrates to act as the photoresist layer. Afterwards, UV light at 244 nm with power of 15 mW was applied to draw the desired pattern on the PHDA SAMs of the sample surface. The angle of incidence was set to 25±5°, while the angle of rotation was set to 90°. A single exposure at a dose of 51 J cm^{-2} was applied to create a 1D pattern of lines; double exposure, with rotation in between, was applied to create a 2D pattern of dots: the first exposure was performed at a dose of 51 J cm^{-2}, and the second dose was performed at a dose of 43.4 J cm^{-2}. It is worth mentioning that in order to avoid over-exposing the sample in one direction, the second exposure is usually reduced from the first. Moreover, the patterned samples were etched by immersion in a 0.5 mM sodium hydroxide (NaOH) solution for 4 min. A schematic illustration of the fabrication procedure, unless otherwise stated, is shown in Figure 5.1 below.

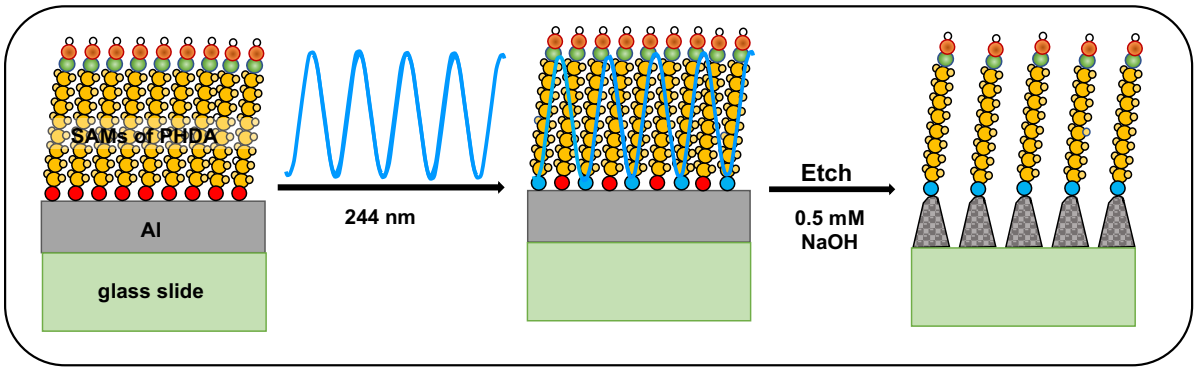

Figure 5.1. Schematic showing the use of PHDA SAMs as a resist for the fabrication of aluminium nanostructures.

5.2.3 Encapsulation and Stability of Aluminium Nanostructure Arrays

Following IL fabrication, arrays of aluminium nanostructures were coated with a 5 to 10-nm-thick titanium layer by thermal evaporation using an Edwards Auto 306 system. The thickness of the titanium covering the aluminium nanostructures was measured by QCM. To test the stability of aluminium nanostructures, the samples were rinsed thoroughly for approximately 1 min sequentially with deionised water and ethanol. This step was repeated at least six times, and between each step, the samples were dried under a steam of nitrogen, and then the peak shifts were determined in air using UV-Vis spectroscopy. Furthermore, the stability was also tested by immersing the samples in deionised water or ethanol for a period of time. The surface morphology of aluminium nanostructures before and after encapsulation were examined using AFM in the tapping mode under ambient conditions.

5.3 Results and Discussion

5.3.1 Lithographic Fabrication of Aluminium Nanostructures

The feasibility of patterning PHDA SAMs formed on aluminium oxide surfaces was examined. UV exposure was carried out by IL using the Lloyd's mirror two-beam interferometer system. In accordance with previous results in Chapters 3 and 4, this technique allows the fabrication of periodic nanostructure arrays over large areas with high resolution. Furthermore, it has been confirmed that the pitch can be easily adjusted by changing the incidence angle, and the feature size can be modified by adjusting the incidence angle, as well as exposure doses. In this work, the monolayer was exposed to 244 nm at 51 J cm^{-2}, which caused cleavage of the P−C bond at the base of the PHDA SAMs, as well as thickening of the native aluminium oxide. The exposed area (~ 0.8 cm^2) was etched by immersing the samples in 0.5 mM NaOH solution. Figure 5.2 shows AFM height images of aluminium nanostructures, where the nanoarrays appear with a high level of uniformity over the fabricated area. In Figure 5.2a, a periodic array of line patterns was created through exposing the sample to a single exposure at a dose of 51 J cm^{-2}, with an incidence angle of 25±5°, and etched with 0.5 mM NaOH for 4 min. Accordingly, exposing the sample twice with a 90° rotation between the exposures resulted in a square array of dot (see Figure 5.2b), where the sample was exposed to 51 J cm^{-2} and then to 43.4 J cm^{-2}. The average pitch associated with these structures was calculated to be 335 ± 16 nm and a FWHM of 173 ± 15 nm.

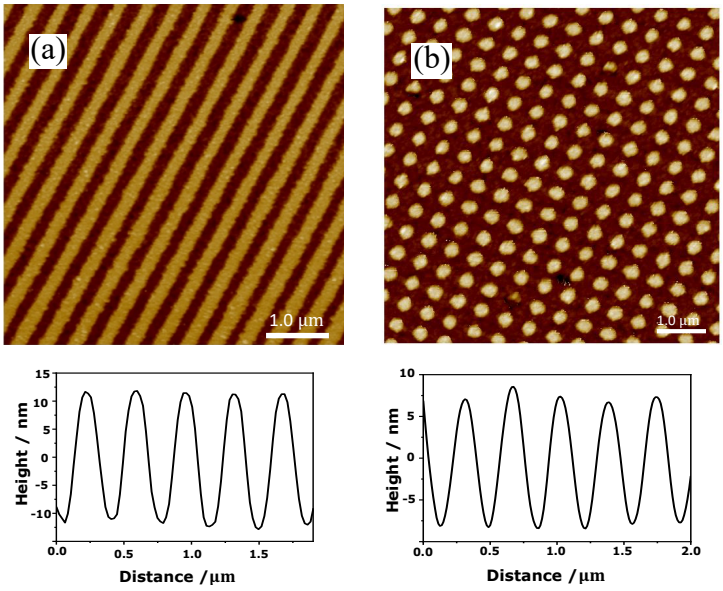

Figure 5.2. AFM height images of aluminium nanostructures fabricated by IL with an incidence angle of 25±5°: (a) line structures created using single exposure of 51 J cm^{-2}, and (b) dot structures created using double exposures of 51and 43.4 J cm^{-2}.

Figures 5.3a and 5.3b show the AFM height image and extinction spectrum of the aluminium nanostructures, respectively. The resulting structures were arrays of dots. The cross-sectional AFM analysis revealed that the height difference between the bright maxima and dark minima was about 15 ± 0.9 nm, the FWHM was 168 ± 11 nm, and the space between nanostructures was about 192 ± 9 nm. It can be observed that the spectrum exhibits a strong broad peak located at 715 nm. In general, the extinction peaks arising from aluminium nanostructures tend to be broader and exhibit lower energies when compared to those of gold nanostructures. Therefore, the choice of metal has a significant impact on the optical properties of particles. Temple et al [298] demonstrated that gold and aluminium nanoparticles with identical shapes and sizes can exhibit different behaviours. According to their findings, aluminium nanoparticles exhibit broader and weaker extinction peaks in comparison to gold nanoparticles, except when the gold nanoparticles exhibit extinction peaks near the gold interband threshold. Moreover, aluminium exhibits higher radiation efficiency in the ultraviolet and visible, while gold exhibits higher radiation efficiency in the near infrared. [298]

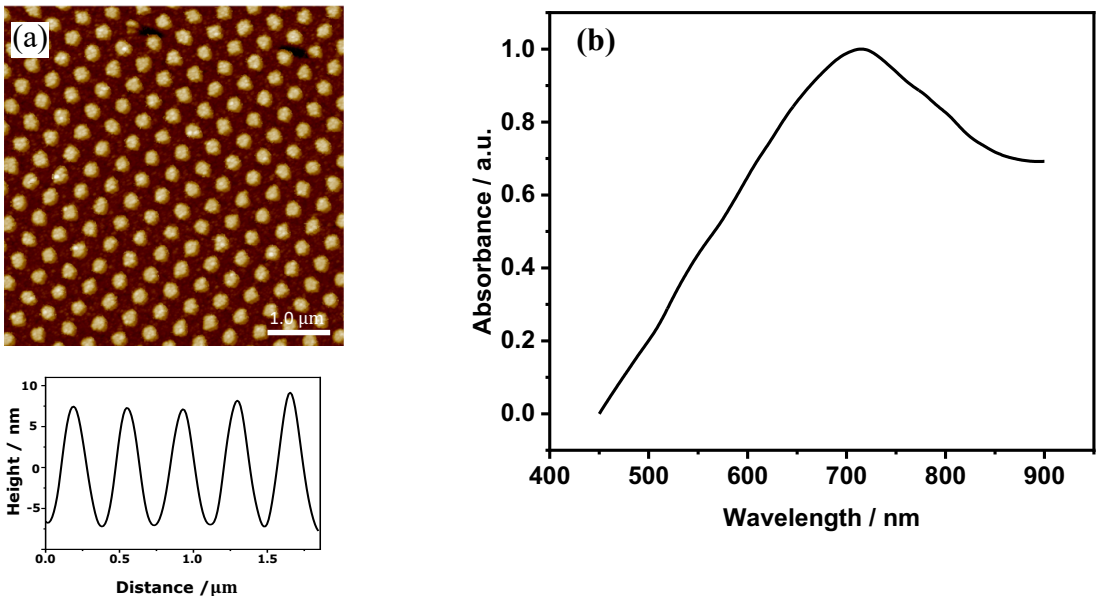

Figure 5.3. (a) AFM height image of aluminium nanostructures fabricated by IL using Lloyd's mirror two-beam interferometer with $\theta = 25 \pm 5°$.

Research conducted by Rassekh et al. [299] studied the impact of different shapes of aluminium nanoparticles, including sphere, cylinder, hemisphere, and pyramid on absorption enhancement in silicon thin-film solar cells. The results demonstrated that the use of aluminium nanoparticles can achieve more than 30% conversion efficiency for plasmonic solar cells compared to cells without particles. It was also observed that spherical nanoparticles had the highest absorption peak, while hemispheres had the lowest. Nevertheless, optimisation of parameters such as the height of cylinder or disk-shaped particles and their distance from the substrates can further enhance absorption. Ekinci et al. [300] showed that the variation in the diameter of aluminium nanoparticles and nanorods affects their optical properties. As the diameter increased, the plasmon resonance peak of the nanoparticles shifted to longer wavelengths and became broader due to increased retardation effects. In particular, the extinction peak of aluminium was centred at 455 nm when the particle diameter was 125 nm. Subsequently, as the diameter increased to 150 nm, and then to 162 nm, the peak position shifted to 480 nm and then 500 nm, respectively. In addition, it was found that with a particle diameter of 40 nm, the extinction peak appeared to be 280 nm. For the aluminium nanorods, the plasmon resonance peak associated with the short axis shifted to longer wavelengths with increasing length, while the resonance associated with the long axis shifted to shorter wavelengths.

Knight et al [296] investigated the dark field scattering behaviour of aluminium nanodiscs with varying the nanoparticle size. These nanodiscs were fabricated on UV-grade fused silica substrates by electron beam lithography, and characterised using a custom-built hyperspectral UV−visible microscope. It was observed that for small nanodisks (i.e. diameter =70 nm), the scattering peak was sharp and centred at 300 nm. However, as the diameter size increased, the peak in the scattering spectrum became broader and shifted toward longer wavelengths. Knight et al. hypothesised that the shift in the position of the scattering maximum was attributable to changes in the fraction of oxidised aluminium in the nanostructures. They acquired SE data for the nanostructures, and modelled them to determine the dielectric function, which was resolved into contributions from the metal and the oxide. They used the resulting dielectric functions to perform finite-difference time-domain (FDTD) of the spectra and obtained a very good match to experimental data.

For the largest particles studied (diameter 180 nm) Knight et al. observed a scattering intensity maximum at ~ 600 nm. Based on their hypothesis, it is possible that the additional red shift in the extinction maximum observed in Figure 5.3 is attributable to an increased ratio of oxide to metallic aluminium. This could arise from two sources. First, because of the sinusoidal intensity distribution in the interferogram, the nanostructures in Figure 5.3 could perhaps be

better described as domes rather than discs, thus containing relatively more oxide for a given diameter. Second, it is possible that the sodium hydroxide etch used here yields slightly less well controlled removal of aluminium, perhaps with enhanced thickening of the oxide layer. Therefore, these possibilities should be explored in future work.

5.3.2 Encapsulation of Aluminium Nanoarrays

The native oxide layer plays an important role in the structural and chemical properties of the material, and while this layer serves to stabilise bulk aluminium from external influences, the high surface area to volume ratio of aluminium nanostructures makes it more vulnerable. The thickness of Al_2O_3 depends on several factors related to the surrounding environment, such as temperature, humidity, and the percentage of oxygen. Under dry conditions, the alumina will thicken rapidly to a limit of around 3 nm at 20 °C; however, when water vapour is present in the atmosphere, the growth of the oxide layer becomes infinite. [301] Similarly, temperature has a significant impact; increasing the temperature not only accelerates the growth rate of alumina, but also increases the maximum thickness that the film will reach. [302] Aluminium is unstable in acidic and basic environments, and the nanostructures are also susceptible to degradation in salt solutions. This causes a problem for the long-term stability of aluminium nanostructures. Even a slight increase of a few nanometres in the thickness of the alumina would lead to a significant change in nanoparticle morphology, accounting for the existence of a large fraction of particles of 20 nm in height, and even a small reduction in size can have a significant impact on its optical properties. Subsequently, the ideal solution, is to encapsulate the aluminium nanostructure arrays with a material that prevents further oxidation, and creates a surface that is more resilient against harsh environments. [303]

In the present study, after completing the optical measurements, the fabricated samples were coated with a 5 nm titanium layer using a thermal evaporator. The choice of titanium was based on its chemical stability and ease of deposition on surfaces. Figure 5.4 displays tapping mode AFM height images of nanostructure arrays before and after encapsulation with 5 nm titanium. It can be observed that there is no obvious change in the morphology of the nanostructures, as the cross section analysis showed that the pitch of the nanostructures was retained at 335 ± 16 nm, although the height increased slightly from 15 ± 0.9 nm to 17 ± 0.5 nm after encapsulation. Further, the extinction spectra of as-fabricated and encapsulated sample are presented in Figure 5.5; where it can be seen that the extinction peak is slightly enhanced in the present of titanium. Considering the peak at 713 nm in as-fabricated, it is slightly blue-shifted by 13 nm after

encapsulation. These findings suggest that the introduction of the titanium layer had a relatively minor effect on the optical properties of the nanostructures. The height retention indicates that the titanium layer did not significantly change the overall structure of the nanoarrays.

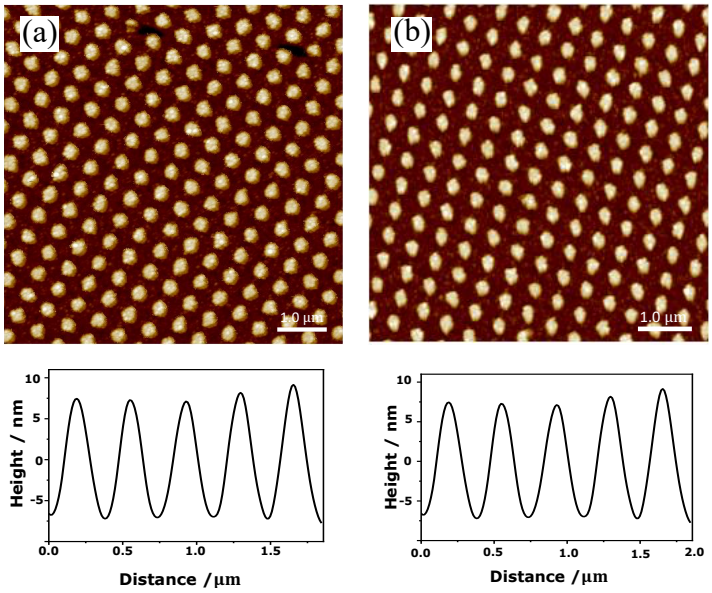

Figure 5.4. AFM height images of aluminium nanostructures: (a) before and (b) after coating with a 5 nm titanium layer.

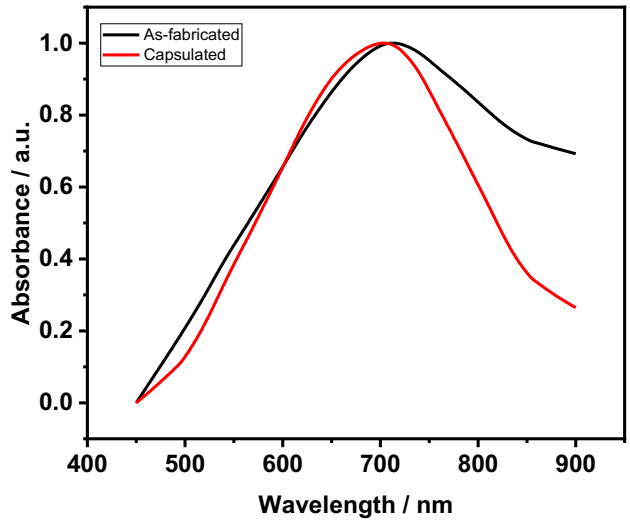

Figure 5.5. Extinction spectra of aluminium nanostructures before and after encapsulation with a 5 nm titanium layer.

The optical properties of aluminium nanostructures are essential for their potential applications, including biosensing. Consequently, it was necessary to evaluate the optical stability of these nanostructures. To achieve this, a series of rinses were performed on the sample surfaces using deionised water and ethanol. Figure 5.6 displays a comparison between the stability of freshly-fabricated and encapsulated nanostructures, in which the samples were sequentially rinsed 6 times with deionised water and ethanol. In general, aluminium nanostructures fabricated by IL showed relatively good stability under ambient conditions; however, when subjected to rinsing with deionised water and ethanol, significant differences were observed between the uncoated and 5-nm titanium-coated samples. In particular, the uncoated sample experienced a substantial blue shift of 35 nm after the sixth rinse (see Figure 5.7a). Conversely, the coated nanostructures showed a much smaller blue shift of only 3 nm following the sixth rinse (see Figure 5.7c). This suggests that the presence of titanium layers enhances the optical stability of aluminium nanostructures. Figures 5.7b and 5.7d show AFM height images of aluminium nanostructures before and after encapsulation, respectively. It should be noted that no noticeable changes in the morphology of the nanostructures were detected following the rinsing procedure in both cases, where the cross-section analysis showed almost the same values before and after rinsing (see Table 5.1). Due to the interaction between water and aluminium, rinsing the sample with water is likely to accelerate the oxidation process; thus, the blue shift in the plasmonic band may be due to the change in the structure of the native oxide layer.

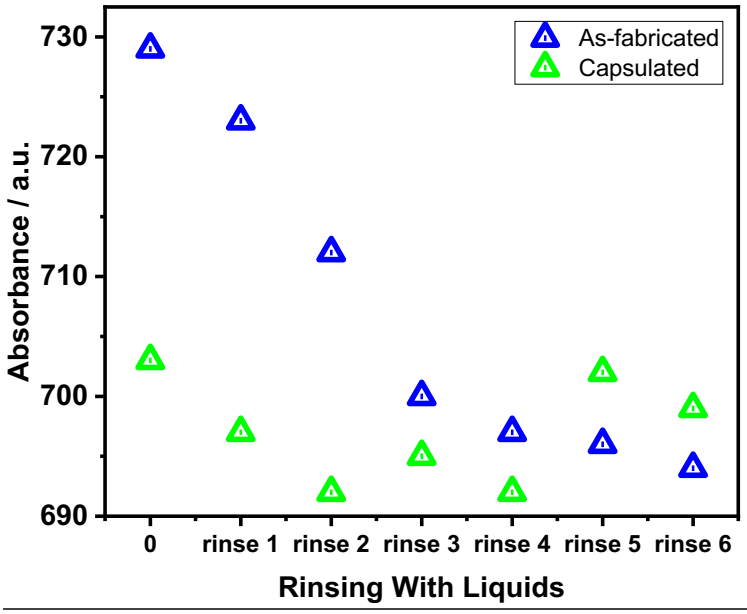

Figure 5.6. Peak position of aluminium nanostructures against rinsing with water and ethanol: (△) freshly-fabricated sample and (△) after coating with a 5 nm titanium layer.

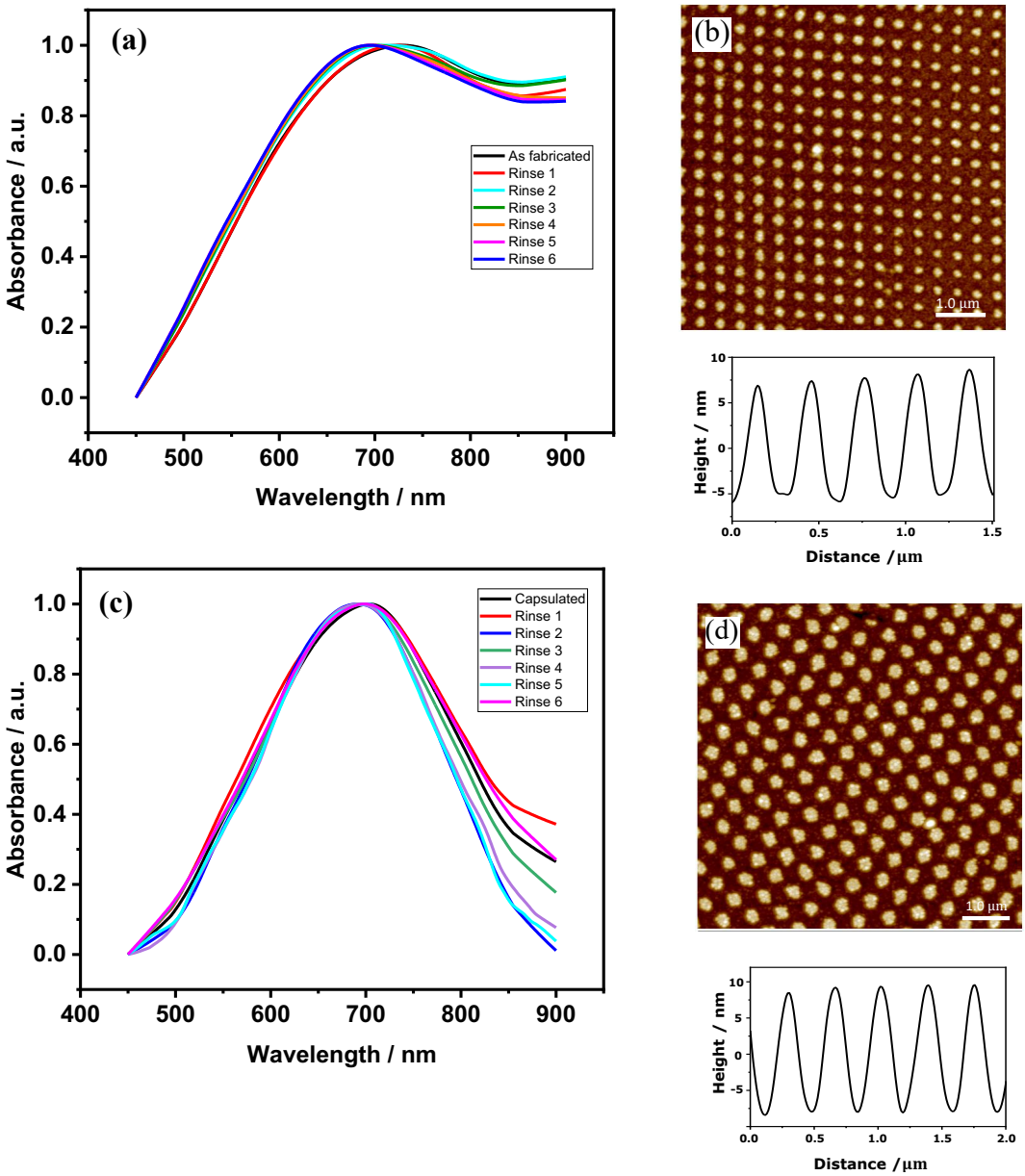

Figure 5.7. (a) and (b) Extinction spectra and AFM image of the freshly-fabricated sample, (c) and (d) Extinction spectra and AFM height image of the encapsulated sample after rinsing with deionised water and ethanol for 6 times, respectively.

Table 5.1. Results of cross-section analysis of uncoated and coated nanostructure arrays before and after rinsing with deionised water and ethanol for 6 times.

Sample	Period (nm)	Height (nm)	Spacing (nm)	FWHM (nm)
Uncoated arrays	302 ± 16	13 ± 0.8	153 ± 10	137 ± 11
Uncoated after rinsing	302 ± 16	13 ± 0.2	151 ± 12	137 ± 7
Coated arrays	335 ± 18	17 ± 0.5	193 ± 9	167 ± 11
Coated after rinsing	335 ± 18	17 ± 0.4	192 ± 10	167 ± 9

The encapsulated aluminium nanostructures were also stored in ethanol to test their resistance over time. The measured extinction spectra obtained from this experiment are plotted in Figure 5.8. Notably, after being immersed in ethanol for the initial 24 h, a significant change in the peak position was observed, resulting in a red-shift of 16 nm. Hence, the peak shifted from 703 nm (in air) to 719 nm. This shift can be attributed to the refractive index of ethanol, which is higher ($n = 1.36$ RIU) than that of air ($n = 1.00$ RIU). [304] When the nanostructures were immersed in ethanol, the change in the surrounding medium caused the incident light to interact differently with the nanostructure surface. This change led to a shift in the plasmon resonance frequency, resulting in the observed red-shift. However, the encapsulated arrays demonstrated a remarkable recovery and stabilisation after a period of 72 h. As a result, the extinction peak gradually returned to its original position. This phenomenon suggested that the encapsulated nanostructures were flexible and able to adapt to changes in their environment.

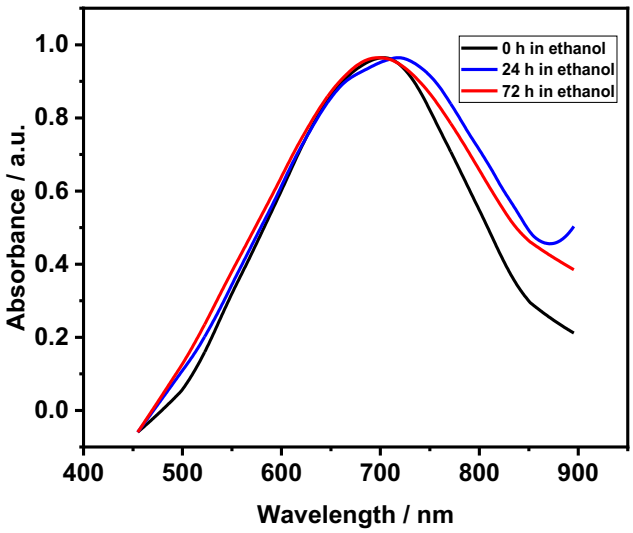

Figure 5.8. Extinction spectra of encapsulated sample before and after being stored in ethanol for 72 h.

5.3.3 Conclusion

In conclusion, ordered arrays of aluminium nanostructures were fabricated using IL through a two-beam interference. A PHDA monolayer, acting as the photoresist layer, was exposed to 51 J cm^{-2} to create a periodic array of line patterns. To create a square array of dots, it was exposed to 51 J cm^{-2} first and then 43.4 J cm^{-2} with a 90° rotation between the exposures. The exposed area was etched in a 0.5 mM NaOH solution. The feasibility of using titanium as a stabilising material for nanostructure arrays to prevent structural changes of particles in aggressive media was tested. A 5 nm titanium layer was found to be sufficient to prevent significant changes to the plasmon band under vigorous rinsing and for at least 72 h after immersion, demonstrating that this method is effective in protecting the arrays for long periods of time.

Chapter 6

6 Conclusion and Future Work

In conclusion, interferometric lithography is a simple, flexible, and inexpensive technique for making a variety of nanostructure arrays over macroscopic areas. Using equation (1.56), the experimental parameters can be selected to obtain the desired patterns on the photoresist layer. Changing the angles of incidence of the laser beam results in nanostructures of different pitches ranging from 600 nm to 100 nm; while changing the angles of rotation results in nanostructures with a variety of shapes, such as dot, hexagonal, elongated and line arrays. Both EBL and FIB provide the freedom to produce more arbitrary structures with finer features; however, the tools themselves are quite expensive and require considerable experience to obtain good results. Furthermore, creating nanostructures with large areas, as in the current study, by EBL and FIB is also impractical in terms of the time required for the fabrication process.

This investigation demonstrated an efficient method for fabricating arrays of nanostructures on different solid surfaces by interference lithography using a Lloyd's mirror interferometer. The fabrication process developed in Chapter Three is based on the exposure of ODT SAMs on gold surfaces to 244 nm UV light, resulting in the formation of macroscopically extended arrays of gold nanostructures. The plasmonic properties of these nanostructure arrays were thoroughly investigated, and their plasmonic behaviour was determined based on their size and shape, which can be easily controlled by lithographic conditions. Understanding this behaviour has led to the creation of reusable sensors and the potential application of nanostructures as inexpensive platforms. Meanwhile, other parameters, such as chromium thickness and annealing temperature, have been demonstrated to play an important role in the morphology and optical properties of gold nanostructures. The sensing response of the reusable system was tested in the presence of rhodamine B dye, where splitting of the plasmon band was observed upon attaching of the rhodamine B dye to the surface of the gold nanostructures. This splitting indicated that strong plasmon-exciton coupling was obtained, which was later confirmed by modelling the system as coupled harmonic oscillators.

In chapter Four, it was successfully demonstrated that there is the ability to directly pattern polymer brushes using interferometric lithography. This ability to pattern polymer brushes in a single step provides the advantage of simplicity and reduced risk of surface contamination. Moreover, it has been shown that this direct patterning method can uniquely create patterned

brushes of different shapes. By exploiting the fact that the polymer chains are tethered to the surface in the unexposed regions, gold nanoparticles were successfully assembled into specific architectural arrangements; thus, enhancing their unique properties. This, in turn, allowed for the creation of an inexpensive and tuneable sensitive platform. The effect of thermal annealing on the optical properties of gold nanoparticles deposited on polymer nanostructures was also investigated. Finally, in Chapter Five, an exploration was undertaken into the feasibility of patterning PHDA SAMs on aluminium substrates and using NaOH as an etching solution. The optical properties of aluminium nanostructures developed with this process were evaluated, in order to provide a methodology for creating structures with controllable plasmon band. Both Bare and titanium coated aluminium nanostructures were also subjected to different conditions to test the efficacy of using titanium layer as stabilising material to prevent the dissolution of aluminium.

Based on the results presented in the current work, there are a lot of interesting topics that could be considered in future work. For example, in Chapter Three, the effects of chromium thickness and annealing temperature on the morphology and optical properties of the gold nanostructures were studied, as both parameters demonstrated a significant influence on the nanostructures. Accordingly, it is assumed that the difference in gold thickness leads to different behaviours of the nanostructures; thus, in future work, the effect of gold thickness, annealing temperature and rotation angles on the optical properties can be investigated. In addition, it will be interesting to test the structures developed in Chapters Three and Four in a real bio-sensing environment, where it is expected that their advantages will become more evident. In Chapter Four, it was found that the extinction spectra of gold nanoparticles were redshifted and become broader when immobilised on polymeric surfaces. Subsequently, any future work to provide a better understanding of the behaviour of nanoparticles attached to polymeric nanostructures and this can be explored through the following aspects. For instance, an attempt can be made to control the density of gold nanoparticles deposited on the polymer brushes, which can be achieved by varying the thickness of the polymer brushes by altering the growth time, as well as controlling the deposition rate of the nanoparticles by varying the immersion time. Moreover, the effect of annealing process on particle size, shape, and optical properties can be evaluated extensively via controlling the annealing temperature and annealing time. In Chapter Five, the possibility of fabricating of aluminium nanostructures was confirmed. Subsequently, it will be interesting to see if strong coupling can be observed in this regime.

7 References

1. Noguez C. Surface plasmons on metal nanoparticles: the influence of shape and physical environment. The Journal of Physical Chemistry C. 2007 Mar 15;111(10):3806-19.

2. Barnes WL, Dereux A, Ebbesen TW. Surface plasmon subwavelength optics. nature. 2003 Aug;424(6950):824-30.

3. Thompson D. Michael Faraday's recognition of ruby gold: the birth of modern nanotechnology. Gold Bulletin. 2007 Dec;40(4):267-9.

4. Hergert W, Wriedt T, editors. The Mie theory: basics and applications. Springer; 2012 Jun 30.

5. Anker JN, Hall WP, Lyandres O, Shah NC, Zhao J, Van Duyne RP. Biosensing with plasmonic nanosensors. Nature materials. 2008 Jun;7(6):442-53.

6. Li W, Zhao X, Yi Z, Glushenkov AM, Kong L. Plasmonic substrates for surface enhanced Raman scattering. Analytica chimica acta. 2017 Sep 1;984:19-41.

7. Liu Z, Boltasseva A, Pedersen RH, Bakker R, Kildishev AV, Drachev VP, Shalaev VM. Plasmonic nanoantenna arrays for the visible. Metamaterials. 2008 May1;2(1):45-51.

8. Vo-Dinh T, Fales AM, Griffin GD, Khoury CG, Liu Y, Ngo H, Norton SJ, Register JK, Wang HN, Yuan H. Plasmonic nanoprobes: from chemical sensing to medical diagnostics and therapy. Nanoscale. 2013 Mar 2;5(21):10127-40.

9. Murray WA, Barnes WL. Plasmonic materials. Advanced materials. 2007 Nov 19;19(22): 3771-82.

10. Raether H. Surface plasmons. Springer tracts in modern physics. 1989;111:1.
11. Hessel A, Oliner AA. A new theory of Wood's anomalies on optical gratings. Applied optics. 1965 Oct 1;4(10):1275-97.

12. Fano U. Zur theorie der intensitätsanomalien der beugung. Annalen der Physik. 1938; 424(5):393-443.

13. Couture M, Zhao SS, Masson JF. Modern surface plasmon resonance for bioanalytics and biophysics. Physical Chemistry Chemical Physics. 2013;15(27):11190-216.

14. Kravets VG, Kabashin AV, Barnes WL, Grigorenko AN. Plasmonic surface lattice resonances: a review of properties and applications. Chemical reviews. 2018 Jun 4;118(12) :5912-51.

15. Cosgrove T, editor. Colloid science: principles, methods and applications. John Wiley & Sons; 2010 Feb 16.

16. Haynes CL, Van Duyne RP. Nanosphere lithography: a versatile nanofabrication tool for studies of size-dependent nanoparticle optics. The Journal of Physical Chemistry B. 2001 Jun 21;105(24):5599-611.

17. Grigorenko AN, Geim AK, Gleeson HF, Zhang Y, Firsov AA, Khrushchev IY, Petrovic J. Nanofabricated media with negative permeability at visible frequencies. Nature. 2005 Nov;438(7066):335-8.

18. Kawata S, Inouye Y, Verma P. Plasmonics for near-field nano-imaging and superlensing. Nature photonics. 2009 Jul;3(7):388-94.

19. Atwater HA, Polman A. Plasmonics for improved photovoltaic devices. Nature materials. 2010 Mar;9(3):205-13.

20. Jackson DJ. Classical Electrodynamics, John Wiley & Sons, Inc., 1998.

21. Ashcroft NW, Mermin ND. Solid state physics (saunders college, philadelphia). Google Scholar. 1976;404.

22. Maier SA. Plasmonics: fundamentals and applications. New York: springer; 2007 May 16.

23. Frenkel J. On the transformation of light into heat in solids. I. Physical Review. 1931 Jan 1;37(1):17.

24. Yablonovitch E. Inhibited spontaneous emission in solid-state physics and electronics. Physical review letters. 1987 May 18;58(20):2059.

25. Liu GB, Xiao D, Yao Y, Xu X, Yao W. Electronic structures and theoretical modelling of two-dimensional group-VIB transition metal dichalcogenides. Chemical Society Reviews. 2015;44(9):2643-63.

26. Sugawara Y, Kelf TA, Baumberg JJ, Abdelsalam ME, Bartlett PN. Strong coupling between localized plasmons and organic excitons in metal nanovoids. Physical review letters. 2006 Dec 29;97(26):266808.

27. Hakala TK, Toppari JJ, Kuzyk A, Pettersson M, Tikkanen H, Kunttu H, Törmä P. Vacuum Rabi splitting and strong-coupling dynamics for surface-plasmon polaritons and rhodamine 6G molecules. Physical Review Letters. 2009 Jul 31;103(5):053602.

28. Liu X, Galfsky T, Sun Z, Xia F, Lin EC, Lee YH, Kéna-Cohen S, Menon VM. Strong light–matter coupling in two-dimensional atomic crystals. Nature Photonics. 2015 Jan;9(1):30-4.

29. Feng M. Quantum-information processing in strong-excitation regime with trapped ions in microcavity. The European Physical Journal D-Atomic, Molecular, Optical and Plasma Physics. 2004 May;29:189-93.

30. Lambright S, Butaeva E, Razgoniaeva N, Hopkins T, Smith B, Perera D, Corbin J, Khon E, Thomas R, Moroz P, Mereshchenko A. Enhanced lifetime of excitons in nonepitaxial Au/CdS core/shell nanocrystals. ACS nano. 2014 Jan 28;8(1):352-61.

31. Wang H, Liu T, Huang Y, Fang Y, Liu R, Wang S, Wen W, Sun M. Plasmon-driven surface catalysis in hybridized plasmonic gap modes. Scientific reports. 2014 Nov 18;4(1):1-7.

32. Zhang W, Govorov AO, Bryant GW. Semiconductor-metal nanoparticle molecules: Hybrid excitons and the nonlinear Fano effect. Physical review letters. 2006 Oct 4;97(14):146804.

33. Tischler JR, Bradley MS, Zhang Q, Atay T, Nurmikko A, Bulović V. Solid state cavity QED: Strong coupling in organic thin films. Organic Electronics. 2007 Apr 1;8(2-3):94-113.

34. Sagle LB, Ruvuna LK, Ruemmele JA, Van Duyne RP. Advances in localized surface plasmon resonance spectroscopy biosensing. Nanomedicine. 2011 Oct;6(8):1447-62.

35. Zhang Y, Huang R, Zhu X, Wang L, Wu C. Synthesis, properties, and optical applications of noble metal nanoparticle-biomolecule conjugates. Chinese Science Bulletin. 2012 Jan;57(2):238-46.

36. Kim DK, Kerman K, Saito M, Sathuluri RR, Endo T, Yamamura S, Kwon YS, Tamiya E. Label-free DNA biosensor based on localized surface plasmon resonance coupled with interferometry. Analytical Chemistry. 2007 Mar 1;79(5):1855-64.

37. Park TJ, Lee SJ, Kim DK, Heo NS, Park JY, Lee SY. Development of label-free optical diagnosis for sensitive detection of influenza virus with genetically engineered fusion protein. Talanta. 2012 Jan 30;89:246-52.

38. Lee JH, Kim BC, Oh BK, Choi JW. Highly sensitive localized surface plasmon resonance immunosensor for label-free detection of HIV-1. Nanomedicine: Nanotechnology, Biology and Medicine. 2013 Oct 1;9(7):1018-26.

39. Goodall BL, Robinson AM, Brosseau CL. Electrochemical-surface enhanced Raman spectroscopy (E-SERS) of uric acid: a potential rapid diagnostic method for early preeclampsia detection. Physical Chemistry Chemical Physics. 2013;15(5):1382-8.

40. Hiep HM, Nakayama T, Saito M, Yamamura S, Takamura Y, Tamiya E. A microfluidic chip based on localized surface plasmon resonance for real-time monitoring of antigen–antibody reactions. Japanese Journal of Applied Physics. 2008 Feb 15;47(2S):1337.

41. Zhu H, Wei L, Niu P. The novel coronavirus outbreak in Wuhan, China. Global health research and policy. 2020 Dec;5(1):1-3.

42. Funari R, Chu KY, Shen AQ. Detection of antibodies against SARS-CoV-2 spike protein by gold nanospikes in an opto-microfluidic chip. Biosensors and Bioelectronics. 2020 Dec 1;169:112578.

43. Huang L, Ding L, Zhou J, Chen S, Chen F, Zhao C, Xu J, Hu W, Ji J, Xu H, Liu GL. One-step rapid quantification of SARS-CoV-2 virus particles via low-cost nanoplasmonic sensors in generic microplate reader and point-of-care device. Biosensors and Bioelectronics. 2021 Jan 1;171:112685.

44. Qiu G, Gai Z, Tao Y, Schmitt J, Kullak-Ublick GA, Wang J. Dual-functional plasmonic photothermal biosensors for highly accurate severe acute respiratory syndrome coronavirus 2 detection. ACS nano. 2020 Apr 13;14(5):5268-77.

45. Lin JC, Liatsis P, Alexandridis P. Flexible and Stretchable Electrically Conductive Polymer Materials for Physical Sensing Applications. Polymer Reviews. 2022 Mar 30:1-60.

46. Yang HU, D'Archangel J, Sundheimer ML, Tucker E, Boreman GD, Raschke MB. Optical dielectric function of silver. Physical Review B. 2015 Jun 22;91(23):235137.

47. Le Ru E, Etchegoin P. Principles of Surface-Enhanced Raman Spectroscopy: and related plasmonic effects. Elsevier; 2008 Nov 17.

48. Fu Q, Stein M, Li W, Zheng J, Kruis FE. Conductive films prepared from inks based on copper nanoparticles synthesized by transferred arc discharge. Nanotechnology. 2019 Oct 10;31(2):025302.

49. Zareei A, Gopalakrishnan S, Mutlu Z, He Z, Peana S, Wang H, Rahimi R. Highly Conductive Copper–Silver Bimodal Paste for Low-Cost Printed Electronics. ACS Applied Electronic Materials. 2021 Aug 13;3(8):3352-64.

50. Rajasekharan Unnithan R, Sun M, He X, Balaur E, Minovich A, Neshev DN, Skafidas E, Roberts A. Plasmonic colour filters based on coaxial holes in aluminium. Materials. 2017 Apr 4;10(4):383.

51. Gérard D, Gray SK. Aluminium plasmonics. Journal of Physics D: Applied Physics. 2014 Dec 15;48(18):184001.

52. West PR, Ishii S, Naik GV, Emani NK, Shalaev VM, Boltasseva A. Searching for better plasmonic materials. Laser & photonics reviews. 2010 Nov 2;4(6):795-808.

53. Ashigwuike EC, Ushie OJ, Mackay R, Balachandran W. A study of the transduction mechanisms of electromagnetic acoustic transducers (EMATs) on pipe steel materials. Sensors and Actuators A: Physical. 2015 Jun 15;229:154-65.

54. Moskovits M. Surface-enhanced spectroscopy. Reviews of modern physics. 1985 Jul 1;57(3):783.

55. Richards R, Bönnemann H. Synthetic approaches to metallic nanomaterials. Nanofabrication towards biomedical applications: techniques, tools, applications, and impact. 2005 Jan 20:1-32.

56. Amina SJ, Guo B. A review on the synthesis and functionalization of gold nanoparticles as a drug delivery vehicle. International journal of nanomedicine. 2020;15:9823.

57. Trasobares J, Vaurette F, François M, Romijn H, Codron JL, Vuillaume D, Théron D, Clément N. High speed e-beam lithography for gold nanoarray fabrication and use in nanotechnology. Beilstein journal of nanotechnology. 2014 Oct 30;5(1):1918-25.

58. Shah M, Badwaik V, Kherde Y, Waghwani HK, Modi T, Aguilar ZP, Rodgers H, Hamilton W, Marutharaj T, Webb C, Lawrenz MB. Gold nanoparticles: various methods of synthesis and antibacterial applications. Frontiers in Bioscience-Landmark. 2014 Jun 1;19(8):1320-44.

59. Wouters D, Schubert US. Nanolithography and nanochemistry: probe-related patterning techniques and chemical modification for nanometer-sized devices. Angewandte Chemie International Edition. 2004 May 3;43(19):2480-95.

60. Sharma E, Rathi R, Misharwal J, Sinhmar B, Kumari S, Dalal J, Kumar A. Evolution in Lithography Techniques: Microlithography to Nanolithography. Nanomaterials. 2022 Aug 11;12(16):2754.

61. Barcelo S, Li Z. Nanoimprint lithography for nanodevice fabrication. Nano Convergence. 2016 Dec;3(1):1-9.

62. Qin D, Xia Y, Whitesides GM. Soft lithography for micro-and nanoscale patterning. Nature protocols. 2010 Mar;5(3):491.

63. Wu MH, Whitesides GM. Fabrication of two-dimensional arrays of microlenses and their applications in photolithography. Journal of micromechanics and microengineering. 2002 Sep 5;12(6):747.

64. Cabrini S, Carpentiero A, Kumar R, Businaro L, Candeloro P, Prasciolu M, Gosparini A, Andreani C, De Vittorio M, Stomeo T, Di Fabrizio E. Focused ion beam lithography for two dimensional array structures for photonic applications. Microelectronic Engineering. 2005 Mar 1;78:11-5.

65. Tseng AA, Chen K, Chen CD, Ma KJ. Electron beam lithography in nanoscale fabrication: recent development. IEEE Transactions on electronics packaging manufacturing. 2003 Oct 14;26(2):141-9.

66. Liu GY, Xu S, Qian Y. Nanofabrication of self-assembled monolayers using scanning probe lithography. Accounts of Chemical Research. 2000 Jul 18;33(7):457-66.

67. Kasani S, Curtin K, Wu N. A review of 2D and 3D plasmonic nanostructure array patterns: fabrication, light management and sensing applications. Nanophotonics. 2019 Dec 1;8(12):2065-89.

68. Mohammad MA, Muhammad M, Dew SK, Stepanova M. Fundamentals of electron beam exposure and development. InNanofabrication 2012 (pp. 11-41). Springer, Vienna.

69. Altissimo M. E-beam lithography for micro-/nanofabrication. Biomicrofluidics. 2010 Jun 15;4(2):026503.

70. Baldacchini T, editor. Three-dimensional microfabrication using two-photon polymerization: fundamentals, technology, and applications. William Andrew; 2015 Sep 29.

71. Broers AN. Fabrication limits of electron beam lithography and of UV, X-ray and ion-beam lithographies. Philosophical Transactions of the Royal Society of London. Series A: Physical and Engineering Sciences. 1995 Dec 15;353(1703):291-311.

72. Manoccio M, Esposito M, Passaseo A, Cuscunà M, Tasco V. Focused ion beam processing for 3D chiral photonics nanostructures. Micromachines. 2020 Dec 23;12(1):6.

73. Utke I, Moshkalev S, Russell P, editors. Nanofabrication using focused ion and electron beams: principles and applications. Oxford University Press; 2012 May 1.

74. Zhang L, Thomas JP, Guan X, Heinig NF, Leung KT. High-energy ion (He+, Si++, Ga+, Au++) interactions with PMMA in ion beam lithography. Nanotechnology. 2020 May 28;31(32):325301.

75. Arshak K, Mihov M. State-of-the-art of focused ion beam nanolithography. J Optoelectron Adv Mater. 2005 Feb 1;7:193-8.

76. Hulteen JC, Van Duyne RP. Nanosphere lithography: A materials general fabrication process for periodic particle array surfaces. Journal of Vacuum Science & Technology A: Vacuum, Surfaces, and Films. 1995 May;13(3):1553-8.

77. Dimitrov AS, Nagayama K. Continuous convective assembling of fine particles into two-dimensional arrays on solid surfaces. Langmuir. 1996 Mar 6;12(5):1303-11.

78. Zhang C, Cvetanovic S, Pearce JM. Fabricating ordered 2-D nano-structured arrays using nanosphere lithography. MethodsX. 2017 Jan 1;4:229-42.

79. Tabatabaei M, Sangar A, Kazemi-Zanjani N, Torchio P, Merlen A, Lagugné-Labarthet F. Optical properties of silver and gold tetrahedral nanopyramid arrays prepared by nanosphere lithography. The Journal of Physical Chemistry C. 2013 Jul 18;117(28):14778-86.

80. Hulteen JC, Treichel DA, Smith MT, Duval ML, Jensen TR, Van Duyne RP. Nanosphere lithography: size-tunable silver nanoparticle and surface cluster arrays. The Journal of Physical Chemistry B. 1999 May 13;103(19):3854-63.

81. Dill FH. Optical lithography. IEEE transactions on electron devices. 1975 Jul;22(7):440-4.
82. Luo C, Xu C, Lv L, Li H, Huang X, Liu W. Review of recent advances in inorganic photoresists. RSC advances. 2020;10(14):8385-95.

83. Bhansali S, Vasudev A, editors. MEMS for biomedical applications. Elsevier; 2012 Jul 18.

84. Kamitani A, Morishita S, Kotaki H, Arscott S. Microfabricated microfluidic fuel cells. Sensors and Actuators B: Chemical. 2011 Jun 20;154(2):174-80.

85. Wolferen H, Abelmann L. Laser interference lithography. Lithography: Principles, processes and materials. 2011 Jan:133-48.

86. Griffiths D. Introduction to electrodynamics fourth edition. 2021

87. Fowles GR. Introduction to modern optics. Courier Corporation; 1989.

88. Byun I, Kim J. Cost-effective laser interference lithography using a 405 nm AlInGaN semiconductor laser. Journal of Micromechanics and Microengineering. 2010 Apr 23;20(5):055024.

89. Tsargorodska A, El Zubir O, Darroch B, Cartron ML, Basova T, Hunter CN, Nabok AV, Leggett GJ. Fast, simple, combinatorial routes to the fabrication of reusable, plasmonically active gold nanostructures by interferometric lithography of self-assembled monolayers. ACS nano. 2014 Aug 26;8(8):7858-69.

90. Tilli M, Paulasto-Krockel M, Petzold M, Theuss H, Motooka T, Lindroos V, editors. Handbook of silicon based MEMS materials and technologies. Elsevier; 2020 Apr 17.

91. Kimura A, Gao W, Kim W, Hosono K, Shimizu Y, Shi L, Zeng L. A sub-nanometric three-axis surface encoder with short-period planar gratings for stage motion measurement. Precision engineering. 2012 Oct 1;36(4):576-85.

92. Kodate K, Kamiya T, Takenaka H, Yanai H. Analysis of two-dimensional etching effect on the profiles of fine holographic grating made of positive photoresist AZ2400. Japanese Journal of Applied Physics. 1978;17(S1):121.

93. Titchmarsh PF. Lloyd's single-mirror interference fringes. Proceedings of the Physical Society (1926-1948). 1941 Jul 1;53(4):391.

94. Xie Q, Hong MH, Tan HL, Chen GX, Shi LP, Chong TC. Fabrication of nanostructures with laser interference lithography. Journal of alloys and compounds. 2008 Jan 31;449(1-2):261-4.

95. Shi L, Zeng L, Li L. Fabrication of optical mosaic gratings with phase and attitude adjustments employing latent fringes and a red-wavelength dual-beam interferometer. Optics express. 2009 Nov 23;17(24):21530-43.

96. Shimizu Y, Aihara R, Ren Z, Chen YL, Ito S, Gao W. Influences of misalignment errors of optical components in an orthogonal two-axis Lloyd's mirror interferometer. Optics Express. 2016 Nov 28;24(24):27521-35.

97. Shimizu Y. Laser interference lithography for fabrication of planar scale gratings for optical metrology. Nanomanufacturing and Metrology. 2021 Mar;4(1):3-27.

98. Li X, Shimizu Y, Ito S, Gao W. Fabrication of scale gratings for surface encoders by using laser interference lithography with 405 nm laser diodes. International Journal of Precision Engineering and Manufacturing. 2013 Nov;14(11):1979-88.

99. Lasagni AF, Beyer E. Fabrication of periodic submicrometer and micrometer arrays using laser interference-based methods. In Laser Surface Engineering 2015 Jan 1 (pp. 423-439). Woodhead Publishing.

100. Stankevičius E, Daugnoraitė E, Račiukaitis G. Mechanism of pillars formation using four-beam interference lithography. Optics and Lasers in Engineering. 2019 May 1;116:41-6.

101. Zhou H, Zeng L. Method to fabricate orthogonal crossed gratings based on a dual Lloyd's mirror interferometer. Optics Communications. 2016 Feb 1;360:68-72.

102. Shah M, Badwaik V, Kherde Y, Waghwani HK, Modi T, Aguilar ZP, Rodgers H, Hamilton W, Marutharaj T, Webb C, Lawrenz MB. Gold nanoparticles: various methods of synthesis and antibacterial applications. Frontiers in Bioscience-Landmark. 2014 Jun 1;19(8):1320-44

103. Kumar S, Gandhi KS, Kumar R. Modeling of formation of gold nanoparticles by citrate method. Industrial & Engineering Chemistry Research. 2007 May 9;46(10):3128-36.

104. Wangoo N, Bhasin KK, Mehta SK, Suri CR. Synthesis and capping of water-dispersed gold nanoparticles by an amino acid: bioconjugation and binding studies. Journal of colloid and interface science. 2008 Jul 15;323(2):247-54.

105. Niidome Y, Nishioka K, Kawasaki H, Yamada S. Rapid synthesis of gold nanorods by the combination of chemical reduction and photoirradiation processes; morphological changes depending on the growing processes. Chemical Communications. 2003(18):2376-7.

106. Frens G. Controlled nucleation for the regulation of the particle size in monodisperse gold suspensions. Nature physical science. 1973 Jan;241(105):20-2.

107. Chow MK, Zukoski CF. Gold sol formation mechanisms: role of colloidal stability. Journal of colloid and interface science. 1994 Jun 1;165(1):97-109.

108. Ji X, Song X, Li J, Bai Y, Yang W, Peng X. Size control of gold nanocrystals in citrate reduction: the third role of citrate. Journal of the American Chemical Society. 2007 Nov 14;129(45):13939-48.

109. Yang S, Wang Y, Wang Q, Zhang R, Ding B. UV irradiation induced formation of Au nanoparticles at room temperature: the case of pH values. Colloids and Surfaces A: Physicochemical and Engineering Aspects. 2007 Jul 5;301(1-3):174-83.

110. Brust M, Walker M, Bethell D, Schiffrin DJ, Whyman R. Synthesis of thiol-derivatised gold nanoparticles in a two-phase liquid–liquid system. Journal of the Chemical Society, Chemical Communications. 1994 Jan 1(7):801-2.

111. Giersig M, Mulvaney P. Preparation of ordered colloid monolayers by electrophoretic deposition. Langmuir. 1993 Dec;9(12):3408-13.

112. Gole A, Murphy CJ. Seed-mediated synthesis of gold nanorods: role of the size and nature of the seed. Chemistry of Materials. 2004 Sep 21;16(19):3633-40.

113. Chen Y, Gu X, Nie CG, Jiang ZY, Xie ZX, Lin CJ. Shape controlled growth of gold nanoparticles by a solution synthesis. Chemical Communications. 2005 Aug 12(33):4181-3.

114. Bridges CR, DiCarmine PM, Fokina A, Huesmann D, Seferos DS. Synthesis of gold nanotubes with variable wall thicknesses. Journal of Materials Chemistry A. 2013;1(4):1127-33.

115. Xu ZC, Shen CM, Xiao CW, Yang TZ, Zhang HR, Li JQ, Li HL, Gao HJ. Wet chemical synthesis of gold nanoparticles using silver seeds: a shape control from nanorods to hollow spherical nanoparticles. Nanotechnology. 2007 Feb 7;18(11):115608.

116. Ulman A. An Introduction to Ultrathin Organic Films: From Langmuir--Blodgett to Self-Assembly. Academic press; 2013 Oct 22.

117. Yamada R, Uosaki K. In situ scanning tunneling microscopy observation of the self-assembly process of alkanethiols on gold (111) in solution. Langmuir. 1998 Feb 17;14(4):855-61.

118. Xu S, Cruchon-Dupeyrat SJ, Garno JC, Liu GY, Kane Jennings G, Yong TH, Laibinis PE. In situ studies of thiol self-assembly on gold from solution using atomic force microscopy. The Journal of chemical physics. 1998 Mar 22;108(12):5002-12.

119. Ulman A. Formation and structure of self-assembled monolayers. Chemical reviews. 1996 Jun 20;96(4):1533-54.

120. Dubois LH, Zegarski BR, Nuzzo RG. Fundamental studies of microscopic wetting on organic surfaces. 2. Interaction of secondary adsorbates with chemically textured organic monolayers. Journal of the American chemical Society. 1990 Jan;112(2):570-9.

121. Sagiv J. Organized monolayers by adsorption. 1. Formation and structure of oleophobic mixed monolayers on solid surfaces. Journal of the American Chemical Society. 1980 Jan;102(1):92-8.

122. Tripp CP, Hair ML. An infrared study of the reaction of octadecyltrichlorosilane with silica. Langmuir. 1992 Apr;8(4):1120-6.

123. Wasserman SR, Tao YT, Whitesides GM. Structure and reactivity of alkylsiloxane monolayers formed by reaction of alkyltrichlorosilanes on silicon substrates. Langmuir. 1989 Jul;5(4):1074-87.

124. Ulman A. Ultrathin organic films: from langmuir-blodgett to self-assembly. J. Mat. Ed. 1989;11:207.

125. Bain CD, Evall J, Whitesides GM. Formation of monolayers by the coadsorption of thiols on gold: variation in the head group, tail group, and solvent. Journal of the American Chemical Society. 1989 Aug;111(18):7155-64.

126. Shaporenko A, Ulman A, Terfort A, Zharnikov M. Self-assembled monolayers of alkaneselenolates on (111) gold and silver. The Journal of Physical Chemistry B. 2005 Mar 10;109(9):3898-906.

127. Shaporenko A, Cyganik P, Buck M, Terfort A, Zharnikov M. Self-assembled monolayers of aromatic selenolates on noble metal substrates. The Journal of Physical Chemistry B. 2005 Jul 21;109(28):13630-8.

128. Watcharinyanon S. Structure of Self-Assembled Monolayers on Gold Studied by NEXAFS and Photoelectron Spectroscopy (Doctoral dissertation, Karlstads universitet).

129. Dubey M, Weidner T, Gamble LJ, Castner DG. Structure and order of phosphonic acid-based self-assembled monolayers on Si (100). Langmuir. 2010 Sep 21;26(18):14747-54.

130. Siqueira Petri DF, Wenz G, Schunk P, Schimmel T. An improved method for the assembly of amino-terminated monolayers on SiO2 and the vapor deposition of gold layers. Langmuir. 1999 Jun 22;15(13):4520-3.

131. Zhang Z, Hu R, Liu Z. Formation of a porphyrin monolayer film by axial ligation of protoporphyrin IX zinc to an amino-terminated silanized glass surface. Langmuir. 2000 Feb 8;16(3):1158-62.

132. Heid S, Effenberger F, Bierbaum K, Grunze M. Self-assembled mono-and multilayers of terminally functionalized organosilyl compounds on silicon substrates. Langmuir. 1996 Apr 17;12(8):2118-20.

133. Ritsema van Eck GC, Chiappisi L, de Beer S. Fundamentals and applications of polymer brushes in air. ACS Applied Polymer Materials. 2022 Jan 14;4(5):3062-87.

134. Sorkin R, Kampf N, Dror Y, Shimoni E, Klein J. Origins of extreme boundary lubrication by phosphatidylcholine liposomes. Biomaterials. 2013 Jul 1;34(22):5465-75.

135. Mitra D, Kang ET, Neoh KG. Polymer-based coatings with integrated antifouling and bactericidal properties for targeted biomedical applications. ACS Applied Polymer Materials. 2021 Apr 20;3(5):2233-63.

136. Keating IV JJ, Imbrogno J, Belfort G. Polymer brushes for membrane separations: a review. ACS applied materials & interfaces. 2016 Oct 26;8(42):28383-99.

137. Durmaz EN, Sahin S, Virga E, De Beer S, De Smet LC, De Vos WM. Polyelectrolytes as building blocks for next-generation membranes with advanced functionalities. ACS Applied Polymer Materials. 2021 Aug 26;3(9):4347-74.

138. Wei M, Gao Y, Li X, Serpe MJ. Stimuli-responsive polymers and their applications. Polymer Chemistry. 2017;8(1):127-43.

139. Moghaddam SZ, Thormann E. Surface forces and friction tuned by thermo-responsive polymer films. Current Opinion in Colloid & Interface Science. 2020 Jun 1;47:27-45.

140. Yu Y, Pérez MB, Cao C, de Beer S. Switching (bio-) adhesion and friction in liquid by stimulus responsive polymer coatings. European polymer journal. 2021 Mar 15;147: 110298.

141. Li D, Xu L, Wang J, Gautrot JE. Responsive polymer brush design and emerging applications for nanotheranostics. Advanced Healthcare Materials. 2021 Mar;10(5): 2000953.

142. Wu T, Efimenko K, Genzer J. Combinatorial study of the mushroom-to-brush crossover in surface anchored polyacrylamide. Journal of the american chemical society. 2002 Aug 14;124(32):9394-5.

143. Brittain WJ, Minko S. A structural definition of polymer brushes. Journal of Polymer Science Part A: Polymer Chemistry. 2007 Aug 15;45(16):3505-12.

144. Williams DR. Grafted polymers in bad solvents: octopus surface micelles. Journal de Physique II. 1993 Sep 1;3(9):1313-8.

145. Minko S. Grafting on solid surfaces: “grafting to” and “grafting from” methods. In Polymer surfaces and interfaces 2008 (pp. 215-234). Springer, Berlin, Heidelberg.

146. Zdyrko B, Luzinov I. Polymer brushes by the “grafting to” method. Macromolecular rapid communications. 2011 Jun 16;32(12):859-69.

147. Halperin A, Tirrell M, Lodge TP. Tethered chains in polymer microstructures. Macromolecules: Synthesis, Order and Advanced Properties. 1992:31-71.

148. Yang X, Shi J, Johnson S, Swanson B. Growth of ultrathin covalently attached polymer films: Uniform thin films for chemical microsensors. Langmuir. 1998 Mar 31;14(7):1505-7.

149. Mansky P, Liu Y, Huang E, Russell TP, Hawker C. Controlling polymer-surface interactions with random copolymer brushes. Science. 1997 Mar 7;275(5305):1458-60.

150. Ulman A. Formation and structure of self-assembled monolayers. Chemical reviews. 1996 Jun 20;96(4):1533-54.

151. Zhang F, Fan JB, Wang S. Interfacial polymerization: From chemistry to functional materials. Angewandte Chemie International Edition. 2020 Dec 1;59(49):21840-56.

152. Colombani D. Chain-growth control in free radical polymerization. Progress in polymer science. 1997 Jan 1;22(8):1649-720.

153. Hyun J, Chilkoti A. Surface-initiated free radical polymerization of polystyrene micropatterns on a self-assembled monolayer on gold. Macromolecules. 2001 Jul 31;34(16):5644-52.

154. Yuan M, Cui X, Zhu W, Tang H. Development of environmentally friendly atom transfer radical polymerization. Polymers. 2020 Aug 31;12(9):1987.

155. Matyjaszewski K, Xia J. Atom transfer radical polymerization. Chemical reviews. 2001 Sep 12;101(9):2921-90.

156. Patten TE, Xia J, Abernathy T, Matyjaszewski K. Polymers with very low polydispersities from atom transfer radical polymerization. Science. 1996 May 10;272(5263):866-8.

157. Matyjaszewski K, Patten TE, Xia J. Controlled/"living" radical polymerization. Kinetics of the homogeneous atom transfer radical polymerization of styrene. Journal of the American Chemical Society. 1997 Jan 29;119(4):674-80.

158. Jones DM, Brown AA, Huck WT. Surface-initiated polymerizations in aqueous media: effect of initiator density. Langmuir. 2002 Feb 19;18(4):1265-9.

159. Kim JB, Huang W, Miller MD, Baker GL, Bruening ML. Kinetics of surface-initiated atom transfer radical polymerization. Journal of Polymer Science Part A: Polymer Chemistry. 2003 Feb 1;41(3):386-94.

160. Alswieleh AM, Cheng N, Canton I, Ustbas B, Xue X, Ladmiral V, Xia S, Ducker RE, El Zubir O, Cartron ML, Hunter CN. Zwitterionic Poly (amino acid methacrylate) Brushes. Journal of the American Chemical Society. 2014 Jul 2;136(26):9404-13.

161. Krishnakumar P. Wetting and spreading phenomena. Physics. 2010 May 13;563:1-2.

162. Quetzeri-Santiago MA, Castrejón-Pita JR, Castrejón-Pita AA. On the analysis of the contact angle for impacting droplets using a polynomial fitting approach. Experiments in Fluids. 2020 Jun;61(6):1-3.

163. Nilavarasi K, Madhurima V. Novel method for determination of contact angle of highly volatile liquids. arXiv preprint arXiv:1908.00246. 2019 Aug 1.

164. Da Cunha AP, Mogaji TS, Cardoso EM. A Method for Measuring Contact Angle and for Analysing the Surface Wettability. In9th World Conference on Experimental Heat Transfer, Fluid Mechanics and Thermodynamics–ExHFT 2017.

165. Law KY. Definitions for hydrophilicity, hydrophobicity, and superhydrophobicity: getting the basics right. The Journal of Physical Chemistry Letters. 2014 Feb 20;5(4):686-8.

166. Lafuma A, Quéré D. Superhydrophobic states. Nature materials. 2003 Jul;2(7):457-60.

167. Celia E, Darmanin T, de Givenchy ET, Amigoni S, Guittard F. Recent advances in designing superhydrophobic surfaces. Journal of colloid and interface science. 2013 Jul 15;402:1-8.

168. Aldobiani M, Al-mahaqeri HM, Mareai AS, Osamah Algeredi PB, Kanna AR. Determination of contact angle of various fluids in oil industry. Int. Ref. J. Eng. Sci. 2018;7:61-3.

169. Bateni A, Laughton S, Tavana H, Susnar SS, Amirfazli A, Neumann AW. Effect of electric fields on contact angle and surface tension of drops. Journal of colloid and interface science. 2005 Mar 1;283(1):215-22.

170. Drelich JW, Boinovich L, Chibowski E, Della Volpe C, Hołysz L, Marmur A, Siboni S. Contact angles: History of over 200 years of open questions. Surface Innovations. 2019 Apr 8;8(1–2):3-27.

171. Bain CD, Troughton EB, Tao YT, Evall J, Whitesides GM, Nuzzo RG. Formation of monolayer films by the spontaneous assembly of organic thiols from solution onto gold. Journal of the American Chemical Society. 1989 Jan;111(1):321-35.

172. Binnig G, Quate CF, Gerber C. Atomic force microscope. Physical review letters. 1986 Mar 3;56(9):930.

173. Korayem MH, Kavousi A, Ebrahimi N. Dynamic analysis of tapping-mode AFM considering capillary force interactions. Scientia Iranica. 2011 Feb 1;18(1):121-9.

174. Wang X, Ramírez-Hinestrosa S, Dobnikar J, Frenkel D. The Lennard-Jones potential: when (not) to use it. Physical Chemistry Chemical Physics. 2020 Jan 12;22(19):10624-33.

175. Guriyanova S, Golovko DS, Bonaccurso E. Cantilever contribution to the total electrostatic force measured with the atomic force microscope. Measurement Science and Technology. 2009 Dec 22;21(2):025502.

176. Tortonese M. Cantilevers and tips for atomic force microscopy. IEEE engineering in medicine and biology magazine. 1997 Mar;16(2):28-33.

177. Trache A, Meininger GA. Atomic force microscopy (AFM). Current protocols in microbiology. 2008 Feb;8(1):2C-.

178. Boussu K, Van der Bruggen B, Volodin A, Snauwaert J, Van Haesendonck C, Vandecasteele C. Roughness and hydrophobicity studies of nanofiltration membranes using different modes of AFM. Journal of colloid and interface science. 2005 Jun 15;286(2):632-8.

179. Yang CW, Hwang S, Chen YF, Chang CS, Tsai DP. Imaging of soft matter with tapping-mode atomic force microscopy and non-contact-mode atomic force microscopy. Nanotechnology. 2007 Jan 18;18(8):084009.

180. Watanabe K, Yamazui H, Inoue R. New application fields developed by Hard X-ray Photoelectron Spectroscopy: “PHI Quantes”. Technical Journal. 2017 Apr:34.

181. Stevie FA, Donley CL. Introduction to x-ray photoelectron spectroscopy. Journal of Vacuum Science & Technology A: Vacuum, Surfaces, and Films. 2020 Dec 24;38(6): 063204.

182. Kumar N, Kumbhat S. Essentials in nanoscience and nanotechnology. John Wiley & Sons; 2016 Apr 11.

183. Wei QF, Gao WD, Hou DY, Wang XQ. Surface modification of polymer nanofibres by plasma treatment. Applied Surface Science. 2005 May 30;245(1-4):16-20.

184. Rocha FS, Gomes AJ, Lunardi CN, Kaliaguine S, Patience GS. Experimental methods in chemical engineering: Ultraviolet visible spectroscopy—UV-Vis. The Canadian Journal of Chemical Engineering. 2018 Dec;96(12):2512-7.

185. Mayerhöfer TG, Pahlow S, Popp J. The Bouguer-Beer-Lambert law: Shining light on the obscure. ChemPhysChem. 2020 Sep 15;21(18):2029-46.

186. Gonçalves D, Irene EA. Fundamentals and applications of spectroscopic ellipsometry. Química Nova. 2002;25:794-800.

187. Langereis E, Heil SB, Van De Sanden MC, Kessels WM. In situ spectroscopic ellipsometry study on the growth of ultrathin TiN films by plasma-assisted atomic layer deposition. Journal of applied Physics. 2006 Jul 15;100(2):023534.

188. Garcia-Caurel E, De Martino A, Gaston JP, Yan L. Application of spectroscopic ellipsometry and Mueller ellipsometry to optical characterization. Applied spectroscopy. 2013 Jan 1;67(1):1-21

189. Cody D, Babeva T, Madjarova V, Kharchenko A, Mintova S, Barrett CJ, Naydenova I. In-situ ellipsometric study of the optical properties of LTL-doped thin film sensors for copper (II) ion detection. Coatings. 2020 Apr;10(4):423.

190. Rzodkiewicz W, Panas A. Application of spectroscopic ellipsometry for investigations of compaction and decompaction state in Si-SiO_2 systems. InJournal of Physics: Conference Series 2009 Aug 1 (Vol. 181, No. 1, p. 012035). IOP Publishing.

191. Lin KT, Lin H, Jia B. Plasmonic nanostructures in photodetection, energy conversion and beyond. Nanophotonics. 2020 Sep 2;9(10):3135-63.

192. Park W. Optical interactions in plasmonic nanostructures. Nano Convergence. 2014 Dec;1(1):1-27.

193. Najiminaini M, Vasefi F, Kaminska B, Carson JJ. A three-dimensional plasmonic nanostructure with extraordinary optical transmission. Plasmonics. 2013 Jun;8(2):217-24.

194. Liu CH, Hong MH, Cheung HW, Zhang F, Huang ZQ, Tan LS, Hor TS. Bimetallic structure fabricated by laser interference lithography for tuning surface plasmon resonance. Optics express. 2008 Jul 7;16(14):10701-9.

195. Rafsanjani SH, Cheng T, Mittler S, Rangan C. Theoretical proposal for a biosensing approach based on a linear array of immobilized gold nanoparticles. Journal of applied physics. 2010 May 1;107(9):094303.

196. Jiang H, Li T, Ertorer E, Yang J, Sabarinathan J, Mittler S. A biosensor based on periodic arrays of gold nanodisks under normal transmission. Sensors and Actuators A: Physical. 2013 Jan 15;189:474-80.

197. Jiang H, Sabarinathan J, Manifar T, Mittler S. 3-D FDTD analysis of gold-nanoparticle-based photonic crystal on slab waveguide. Journal of Lightwave Technology. 2009 Jul 1;27(13):2264-70.

198. Najiminaini M, Vasefi F, Kaminska B, Carson JJ. Optical resonance transmission properties of nano-hole arrays in a gold film: effect of adhesion layer. Optics express. 2011 Dec 19;19(27):26186-97.

199. Vasefi F, Najiminaini M, Kaminska B, Carson JJ. Effect of surface plasmon cross-talk on optical properties of closely packed nano-hole arrays. Optics Express. 2011 Dec 5;19(25):25773-9.

200. Yue W, Wang Z, Yang Y, Chen L, Syed A, Wong K, Wang X. Electron-beam lithography of gold nanostructures for surface-enhanced Raman scattering. Journal of Micromechanics and Microengineering. 2012 Oct 26;22(12):125007.

201. Nishitsuji R, Sueyoshi K, Hisamoto H, Endo T. Fabrication of Gold Nanostructures on Quartz Crystal Microbalance Surface Using Nanoimprint Lithography for Sensing Applications. Micromachines. 2022 Aug 29;13(9):1430.

202. Shao L, Zheng J. Fabrication of plasmonic nanostructures by hole-mask colloidal lithography: Recent development. Applied Materials Today. 2019 Jun 1;15:6-17.

203. Chen Y, Bi K, Wang Q, Zheng M, Liu Q, Han Y, Yang J, Chang S, Zhang G, Duan H. Rapid focused ion beam milling based fabrication of plasmonic nanoparticles and assemblies via “sketch and peel” strategy. ACS nano. 2016 Dec 27;10(12):11228-36.

204. Hedberg-Dirk EL, Martinez UA. Large-scale protein arrays generated with interferometric lithography for spatial control of cell-material interactions. Journal of Nanomaterials. 2010 May;2010.

205. Dishner MH, Hemminger JC, Feher FJ. Formation of a self-assembled monolayer by adsorption of thiophene on Au (111) and its photooxidation. Langmuir. 1996 Dec 25 ;12 (26):6176-8.

206. Guo Q, Li F. Self-assembled alkanethiol monolayers on gold surfaces: resolving the complex structure at the interface by STM. Physical Chemistry Chemical Physics. 2014;16(36):19074-90.

207. Ulman A. Formation and structure of self-assembled monolayers. Chemical reviews. 1996 Jun 20;96(4):1533-54.

208. Garg N, Carrasquillo-Molina E, Lee TR. Self-assembled monolayers composed of aromatic thiols on gold: Structural characterization and thermal stability in solution. Langmuir. 2002 Apr 2;18(7):2717-26.

209. Love JC, Estroff LA, Kriebel JK, Nuzzo RG, Whitesides GM. Self-assembled monolayers of thiolates on metals as a form of nanotechnology. Chemical reviews. 2005 Apr 13;105(4):1103-70.

210. Chaudhury MK. Adhesion and friction of self-assembled organic monolayers. Current opinion in colloid & interface science. 1997 Feb 1;2(1):65-9.

211. Lewis M, Tarlov M, Carron K. Study of the photooxidation process of self-assembled alkanethiol monolayers. Journal of the American Chemical Society. 1995 Sep; 117(37): 9574-5.

212. Lim DK, Jeon KS, Kim HM, Nam JM, Suh YD. Nanogap-engineerable Raman-active nanodumbbells for single-molecule detection. Nature materials. 2010 Jan;9(1):60-7.

213. Kinkhabwala A, Yu Z, Fan S, Avlasevich Y, Müllen K, Moerner WE. Large single-molecule fluorescence enhancements produced by a bowtie nanoantenna. Nature photonics. 2009 Nov;3(11):654-7.

214. Stellacci F, Bauer CA, Meyer-Friedrichsen T, Wenseleers W, Marder SR, Perry JW. Ultrabright supramolecular beacons based on the self-assembly of two-photon chromophores on metal nanoparticles. Journal of the American Chemical Society. 2003 Jan 15;125(2):328-9.

215. Wright DS, Flavel BS, Quinton JS. Streaming zeta potential measurements of surface-bound organosilane molecular species. In2006 International Conference on Nanoscience and Nanotechnology 2006 Jul 3. IEEE.

216. Adamson AW, Gast AP. Physical chemistry of surfaces. New York: Interscience publishers; 1967.

217. Smith T. The hydrophilic nature of a clean gold surface. Journal of Colloid and Interface Science. 1980 May 1;75(1):51-5.

218. Yang J, Zhou M, Liu J, Wang H, Weng C. Fabrication and tribological properties of self-assembled monolayers of alkanethiols on nickel substrates. Applied Surface Science. 2021 Sep 1;559:149963.

219. Jakubowicz A, Jia H, Wallace RM, Gnade BE. Adsorption kinetics of p-nitrobenzenethiol self-assembled monolayers on a gold surface. Langmuir. 2005 Feb 1;21(3):950-5.

220. Ishida T, Hara M, Kojima I, Tsuneda S, Nishida N, Sasabe H, Knoll W. High resolution X-ray photoelectron spectroscopy measurements of octadecanethiol self-assembled monolayers on Au (111). Langmuir. 1998 Apr 14;14(8):2092-6.

221. Sun S, Chong KS, Leggett GJ. Photopatterning of self-assembled monolayers at 244 nm and applications to the fabrication of functional microstructures and nanostructures. Nanotechnology. 2005 Jul 18;16(9):1798.

222. Chua JK, Murukeshan VM. Patterning of two-dimensional nanoscale features using grating-based multiple beams interference lithography. Physica Scripta. 2009 Jul 1;80(1):015401.

223. Karakouz T, Tesler AB, Bendikov TA, Vaskevich A, Rubinstein I. Highly stable localized plasmon transducers obtained by thermal embedding of gold island films on glass. Advanced Materials. 2008 Oct 17;20(20):3893-9.

224. Chu J, Liu X, Zhang X, Zhang J, Xiao J, Chen X, Xu J. Annealing temperature dependence of mechanical and structural properties of chromium-gold films on the silica glass substrate. Thin Solid Films. 2023 Jun 1;774:139849.

225. Matsumae T, Kurashima Y, Higurashi E, Takagi H. Surface activated bonding of Au/Cr, Au/Ta and Au/Pt/Ti films after degas annealing for Si/sapphire gas cell. Microelectronic Engineering. 2019 Jun 1;214:68-73.

226. Alonzo-Medina GM, González-González A, Sacedón JL, Oliva AI, Vasco E. Local slope evolution during thermal annealing of polycrystalline Au films. Journal of Physics D: Applied Physics. 2012 Oct 6;45(43):435301.

227. Serrano A, Rodriguez De La Fuente O, García MA. Extended and localized surface plasmons in annealed Au films on glass substrates. Journal of Applied Physics. 2010 Oct 1;108(7).

228. Majni G, Ottaviani G, Prudenziati M. Interdiffusion of thin Cr and Au films deposited on silicon. Thin Solid Films. 1976 Oct 1;38(1):15-9.

229. Birleanu C, Pustan M, Merie V, Müller R, Voicu R, Baracu A, Craciun S. Temperature effect on the mechanical properties of gold nano films with different thickness. InIOP Conference Series: Materials Science and Engineering 2016 Aug 1 (Vol. 147, No. 1, p. 012021). IOP Publishing.

230. Siegel J, Kvítek O, Kolská Z, Slepicka P, Švorčík V. Gold nanostructures prepared on solid surface. Metallurgy–advances in materials and processes. InTech. 2012 Sep 19:43-70.

231. Bosman M, Zhang L, Duan H, Tan SF, Nijhuis CA, Qiu CW, Yang JK. Encapsulated annealing: enhancing the plasmon quality factor in lithographically–defined nanostructures. Scientific reports. 2014 Jul 2;4(1):1-6.

232. Chen H, Kou X, Yang Z, Ni W, Wang J. Shape-and size-dependent refractive index sensitivity of gold nanoparticles. Langmuir. 2008 May 20;24(10):5233-7.

233. Hegde HR, Chidangil S, Sinha RK. Refractive index sensitivity of Au nanostructures in solution and on the substrate. Journal of Materials Science: Materials in Electronics. 2022 Mar;33(7):4011-24.

234. Marinakos SM, Chen S, Chilkoti A. Plasmonic detection of a model analyte in serum by a gold nanorod sensor. Analytical chemistry. 2007 Jul 15;79(14):5278-83.

235. Janicki V, Sancho-Parramon J, Zorc H. Refractive index profile modelling of dielectric inhomogeneous coatings using effective medium theories. Thin solid films. 2008 Mar 31;516(10):3368-73.

236. Lishchuk A, Csányi E, Darroch B, Wilson C, Nabok A, Leggett GJ. Active control of strong plasmon−exciton coupling in biomimetic pigment−polymer antenna complexes grown by surface−initiated polymerisation from gold nanostructures. Chemical science. 2022;13(8):2405-17.

237. Kabashin AV, Kravets VG, Grigorenko AN. Label-free optical biosensing: going beyond the limits. Chemical Society Reviews. 2023.

238. Manuel AP, Kirkey A, Mahdi N, Shankar K. Plexcitonics–fundamental principles and optoelectronic applications. Journal of Materials Chemistry C. 2019;7(7):1821-53.

239. Liu G, Lu M, Huang X, Li T, Xu D. Application of gold-nanoparticle colorimetric sensing to rapid food safety screening. Sensors. 2018 Nov 27;18(12):4166.

240. Bailey RC, Hupp JT. Micropatterned polymeric gratings as chemoresponsive volatile organic compound sensors: implications for analyte detection and identification via diffraction-based sensor arrays. Analytical chemistry. 2003 May 15;75(10):2392-8.

241. Nath N, Chilkoti A. Creating “smart” surfaces using stimuli responsive polymers. Advanced materials. 2002 Sep 3;14(17):1243-7.

242. Panzarasa G, Soliveri G, Sparnacci K, Ardizzone S. Patterning of polymer brushes made easy using titanium dioxide: direct and remote photocatalytic lithography. Chemical Communications. 2015;51(34):7313-6.

243. Siegel RA, Firestone BA. pH-dependent equilibrium swelling properties of hydrophobic polyelectrolyte copolymer gels. Macromolecules. 1988 Nov;21(11):3254-9.

244. Welch ME, Xu Y, Chen H, Smith N, Tague ME, Abruna HD, Baird B, Ober CK. Polymer brushes as functional, patterned surfaces for nanobiotechnology. Journal of Photopolymer Science and Technology. 2012 Jun 26;25(1):53-6.

245. Becer CR, Haensch C, Hoeppener S, Schubert US. Patterned Polymer Brushes Grafted from Bromine-Functionalized, Chemically Active Surface Templates. Small. 2007 Feb 5;3(2):220-5.

246. Yang W, Zhou F. Polymer brushes for antibiofouling and lubrication. Biosurface and Biotribology. 2017 Sep 1;3(3):97-114.

247. Cheng Z, Zhu X, Shi ZL, Neoh KG, Kang ET. Polymer microspheres with permanent antibacterial surface from surface-initiated atom transfer radical polymerization. Industrial & engineering chemistry research. 2005 Aug 31;44(18):7098-104.

248. (Kim JY, Lee BS, Choi J, Kim BJ, Choi JY, Kang SM, Yang SH, Choi IS. Cytocompatible polymer grafting from individual living cells by atom-transfer radical polymerization. Angewandte Chemie International Edition. 2016 Dec 5;55(49):15306-9.

249. Matyjaszewski K, Dong H, Jakubowski W, Pietrasik J, Kusumo A. Grafting from surfaces for "everyone": ARGET ATRP in the presence of air. Langmuir. 2007 Apr 10;23(8):4528-31.

250. Diaz IL, Sierra CA, Jérôme V, Freitag R, Perez LD. Target grafting of poly (2-(dimethylamino) ethyl methacrylate) to biodegradable block copolymers. Journal of Polymer Science. 2020 Aug 15;58(16):2168-80.

251. Kwak Y, Matyjaszewski K. ARGET ATRP of methyl methacrylate in the presence of nitrogen-based ligands as reducing agents. Polymer International. 2009 Mar;58(3):242-7.

252. Tanaka K, Matyjaszewski K. Controlled copolymerization of n-butyl acrylate with nonpolar 1-alkenes using activators regenerated by electron transfer for atom-transfer radical polymerization. Macromolecules. 2007 Jul 24;40(15):5255-60.

253. Jakubowski W, Min K, Matyjaszewski K. Activators regenerated by electron transfer for atom transfer radical polymerization of styrene. Macromolecules. 2006 Jan 10;39(1):39-45.

254. Willets KA, Van Duyne RP. Localized surface plasmon resonance spectroscopy and sensing. Annu. Rev. Phys. Chem.. 2007 May 5;58:267-97.

255. Verma MS, Rogowski JL, Jones L, Gu FX. Colorimetric biosensing of pathogens using gold nanoparticles. Biotechnology advances. 2015 Nov 1;33(6):666-80.

256. Huang X, Jain PK, El-Sayed IH, El-Sayed MA. Plasmonic photothermal therapy (PPTT) using gold nanoparticles. Lasers in medical science. 2008 Jul;23:217-28.

257. Pena-Pereira F, Duarte RM, Duarte AC. Immobilization strategies and analytical applications for metallic and metal-oxide nanomaterials on surfaces. TrAC Trends in Analytical Chemistry. 2012 Nov 1;40:90-105.

258. Fan M, Andrade GF, Brolo AG. A review on the fabrication of substrates for surface enhanced Raman spectroscopy and their applications in analytical chemistry. Analytica chimica acta. 2011 May 5;693(1-2):7-25.

259. Shiohara A, Wang Y, Liz-Marzán LM. Recent approaches toward creation of hot spots for SERS detection. Colloidal Synthesis of Plasmonic Nanometals. 2020 Apr 23:563-622.

260. Fang L, Li Y, Chen Z, Liu W, Zhang J, Xiang S, Shen H, Li Z, Yang B. Tunable polymer brush/au nps hybrid plasmonic arrays based on host–guest interaction. ACS applied materials & interfaces. 2014 Nov 26;6(22):19951-7.

261. Geissler M, Xia Y. Patterning: Principles and some new developments. Advanced Materials. 2004 Aug 4;16(15):1249-69.

262. Nie Z, Kumacheva E. Patterning surfaces with functional polymers. Nature materials. 2008 Apr;7(4):277-90.

263. Senaratne W, Andruzzi L, Ober CK. Self-assembled monolayers and polymer brushes in biotechnology: current applications and future perspectives. Biomacromolecules. 2005 Sep 12;6(5):2427-48.

264. Lu X, Rycenga M, Skrabalak SE, Wiley B, Xia Y. Chemical synthesis of novel plasmonic nanoparticles. Annual review of physical chemistry. 2009 May 5;60:167-92.

265. Onses MS, Nealey PF. Tunable assembly of gold nanoparticles on nanopatterned poly (ethylene glycol) brushes. Small. 2013 Dec 20;9(24):4168-74.

266. Tokareva I, Minko S, Fendler JH, Hutter E. Nanosensors based on responsive polymer brushes and gold nanoparticle enhanced transmission surface plasmon resonance spectroscopy. Journal of the American Chemical Society. 2004 Dec 15;126(49):15950-1.

267. Romo-Herrera JM, Alvarez-Puebla RA, Liz-Marzán LM. Controlled assembly of plasmonic colloidal nanoparticle.

268. Rastogi A, Paik MY, Tanaka M, Ober CK. Direct patterning of intrinsically electron beam sensitive polymer brushes. ACS nano. 2010 Feb 23;4(2):771-80.

269. Jones DM, Smith JR, Huck WT, Alexander C. Variable adhesion of micropatterned thermoresponsive polymer brushes: AFM investigations of poly (N-isopropylacrylamide) brushes prepared by surface-initiated polymerizations. Advanced Materials. 2002 Aug 16;14(16):1130-4.

270. Kaholek M, Lee WK, LaMattina B, Caster KC, Zauscher S. Fabrication of stimulus-responsive nanopatterned polymer brushes by scanning-probe lithography. Nano Letters. 2004 Feb 11;4(2):373-6.

271. Liu Y, Klep V, Luzinov I. To patterned binary polymer brushes via capillary force lithography and surface-initiated polymerization. Journal of the American Chemical Society. 2006 Jun 28;128(25):8106-7.

272. Paik MY, Xu Y, Rastogi A, Tanaka M, Yi Y, Ober CK. Patterning of polymer brushes. A direct approach to complex, sub-surface structures. Nano letters. 2010 Oct 13;10(10): 3873-9.

273. Dong J, Carpinone PL, Pyrgiotakis G, Demokritou P, Moudgil BM. Synthesis of precision gold nanoparticles using Turkevich method. KONA Powder and Particle Journal. 2020 Jan 10;37:224-32.

274. Clarkson CG, Johnson A, Leggett GJ, Geoghegan M. Slow polymer diffusion on brush-patterned surfaces in aqueous solution. Nanoscale. 2019;11(13):6052-61.

275. Zhang T, Du Y, Kalbacova J, Schubel R, Rodriguez RD, Chen T, Zahn DR, Jordan R. Wafer-scale synthesis of defined polymer brushes under ambient conditions. Polymer Chemistry. 2015;6(47):8176-83.

276. Ahmad SA, Leggett GJ, Hucknall A, Chilkoti A. Micro-and nanostructured poly [oligo (ethylene glycol) methacrylate] brushes grown from photopatterned halogen initiators by atom transfer radical polymerization. Biointerphases. 2011 Mar 28;6(1):8

277. Al-Jaf O, Alswieleh A, Armes SP, Leggett GJ. Nanotribological properties of nanostructured poly (cysteine methacrylate) brushes. Soft Matter. 2017;13(10):2075-84.

278. Cavalleri O, Gonella G, Terreni S, Vignolo M, Floreano L, Morgante A, Canepa M, Rolandi R. High resolution X-ray photoelectron spectroscopy of L-cysteine self-assembled films. Physical chemistry chemical physics. 2004;6(15):4042-6.

279. Christau S, Thurandt S, Yenice Z, Von Klitzing R. Stimuli-responsive polyelectrolyte brushes as a matrix for the attachment of gold nanoparticles: The effect of brush thickness on particle distribution. Polymers. 2014 Jun 27;6(7):1877-96.

280. Seitz O, Chehimi MM, Cabet-Deliry E, Truong S, Felidj N, Perruchot C, Greaves SJ, Watts JF. Preparation and characterisation of gold nanoparticle assemblies on silanised glass plates. Colloids and Surfaces A: Physicochemical and Engineering Aspects. 2003 May 29;218(1-3):225-39.

281. Kim JY, Lee JS. Synthesis and thermally reversible assembly of DNA−gold nanoparticle cluster conjugates. Nano letters. 2009 Dec 9;9(12):4564-9.

282. Swami A, Kumar A, Sastry M. Lamellar multilayer hexadecylaniline-modified gold nanoparticle films deposited by the Langmuir-Blodgett technique. Journal of Chemical Sciences. 2003 Jun;115:185-93.

283. Su KH, Wei QH, Zhang X, Mock JJ, Smith DR, Schultz S. Interparticle coupling effects on plasmon resonances of nanogold particles. Nano letters. 2003 Aug 13;3(8):1087-90.

284. Abbas RR, Richardson TH, Hobson A, Hassan A, Abbas TR. Effect of annealing on the surface plasmon resonance of dodecanethiol encapsulated gold nanoparticles

Langmuir–Schafer thin films. Colloids and Surfaces A: Physicochemical and Engineering Aspects. 2014 Mar 5;444:95-103.

285. Cheng L, Li X, Dong J. Size-controlled preparation of gold nanoparticles with novel pH responsive gemini amphiphiles. Journal of Materials Chemistry C. 2015;3(24):6334-40.

286. Martin J, Plain J. Fabrication of aluminium nanostructures for plasmonics. Journal of Physics D: Applied Physics. 2014 Dec 15;48(18):184002.

287. Jha SK, Ahmed Z, Agio M, Ekinci Y, Löffler JF. Deep-UV surface-enhanced resonance Raman scattering of adenine on aluminum nanoparticle arrays. Journal of the American Chemical Society. 2012 Feb 1;134(4):1966-9.

288. Canalejas-Tejero V, Herranz S, Bellingham A, Moreno-Bondi MC, Barrios CA. Passivated aluminum nanohole arrays for label-free biosensing applications. ACS applied materials & interfaces. 2014 Jan 22;6(2):1005-10.

289. Honda M, Kumamoto Y, Taguchi A, Saito Y, Kawata S. Plasmon-enhanced UV photocatalysis. Applied Physics Letters. 2014 Feb 10;104(6):061108.

290. Chowdhury MH, Ray K, Gray SK, Pond J, Lakowicz JR. Aluminum nanoparticles as substrates for metal-enhanced fluorescence in the ultraviolet for the label-free detection of biomolecules. Analytical chemistry. 2009 Feb 15;81(4):1397-403.

291. Akimov YA, Koh WS. Resonant and nonresonant plasmonic nanoparticle enhancement for thin-film silicon solar cells. Nanotechnology. 2010 May 13;21(23):235201.

292. Zoric I, Zach M, Kasemo B, Langhammer C. Gold, platinum, and aluminum nanodisk plasmons: material independence, subradiance, and damping mechanisms. ACS nano. 2011 Apr 26;5(4):2535-46

293. Langhammer C, Schwind M, Kasemo B, Zoric I. Localized surface plasmon resonances in aluminum nanodisks. Nano letters. 2008 May 14;8(5):1461-71.

294. Ding T, Sigle DO, Herrmann LO, Wolverson D, Baumberg JJ. Nanoimprint lithography of Al nanovoids for deep-UV SERS. ACS applied materials & interfaces. 2014 Oct 22;6(20):17358-63.

295. Ekinci Y, Solak HH, Löffler JF. Plasmon resonances of aluminium nanoparticles and nanorods. Journal of Applied Physics. 2008 Oct 15;104(8):083107.

296. Knight MW, King NS, Liu L, Everitt HO, Nordlander P, Halas NJ. Aluminum for plasmonics. ACS nano. 2014 Jan 28;8(1):834-40.

297. Pellerite MJ, Dunbar TD, Boardman LD, Wood EJ. Effects of fluorination on self-assembled monolayer formation from alkanephosphonic acids on aluminum: Kinetics and structure. The Journal of Physical Chemistry B. 2003 Oct 23;107(42):11726-36.

298. Temple TL, Bagnall DM. Optical properties of gold and aluminium nanoparticles for silicon solar cell applications. Journal of applied physics. 2011 Apr 15;109(8).

299. Rassekh M, Shirmohammadi R, Ghasempour R, Astaraei FR, Shayesteh SF. Effect of plasmonic Aluminum nanoparticles shapes on optical absorption enhancement in silicon thin-film solar cells. Physics Letters A. 2021 Aug 27;408:127509.

300. Ekinci Y, Solak HH, Löffler JF. Plasmon resonances of aluminum nanoparticles and nanorods. Journal of Applied Physics. 2008 Oct 15;104(8).

301. Hart RK. The oxidation of aluminium in dry and humid oxygen atmospheres. Proceedings of the Royal Society of London. Series A. Mathematical and Physical Sciences. 1956 Jul 10;236(1204):68-88.

302. Hayden BE, Wyrobisch W, Oppermann W, Hachicha S, Hofmann P, Bradshaw AM. The interaction of oxygen with aluminium: Mainly ellipsometric aspects. Surface Science. 1981 Aug 1;109(1):207-20.

303. Richardson JA, Wood GC. The interpretation of impedance changes on oxide-coated aluminum produced by immersion in inhibitive and corrosive aqueous media. Journal of the Electrochemical Society. 1973 Feb 1;120(2):193.

304. Lin FC, See KM, Ouyang L, Huang YX, Chen YJ, Popp J, Huang JS. Designable spectrometer-free index sensing using plasmonic Doppler gratings. Analytical chemistry. 2019 Jul 22;91(15):9382-7.

8 Appendix

8.1 Fabrication of Gold Nanostructures by Interferometric Lithography

8.1.1 Additional AFM images

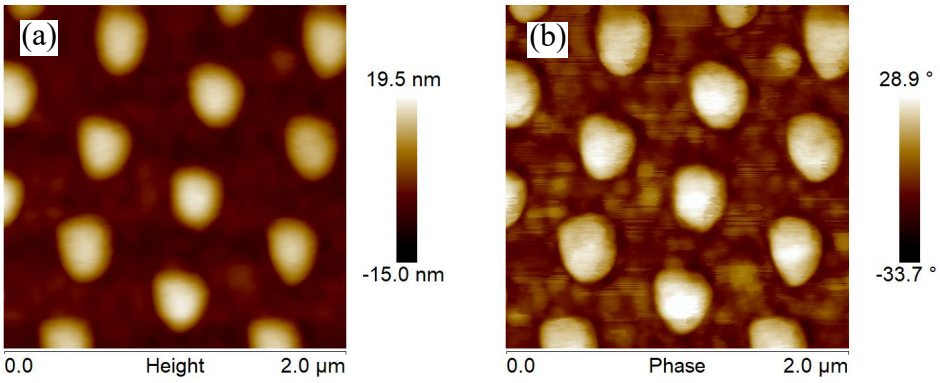

Figure 8.1. AFM images of gold nanostructures: (a) height and (b) phase.

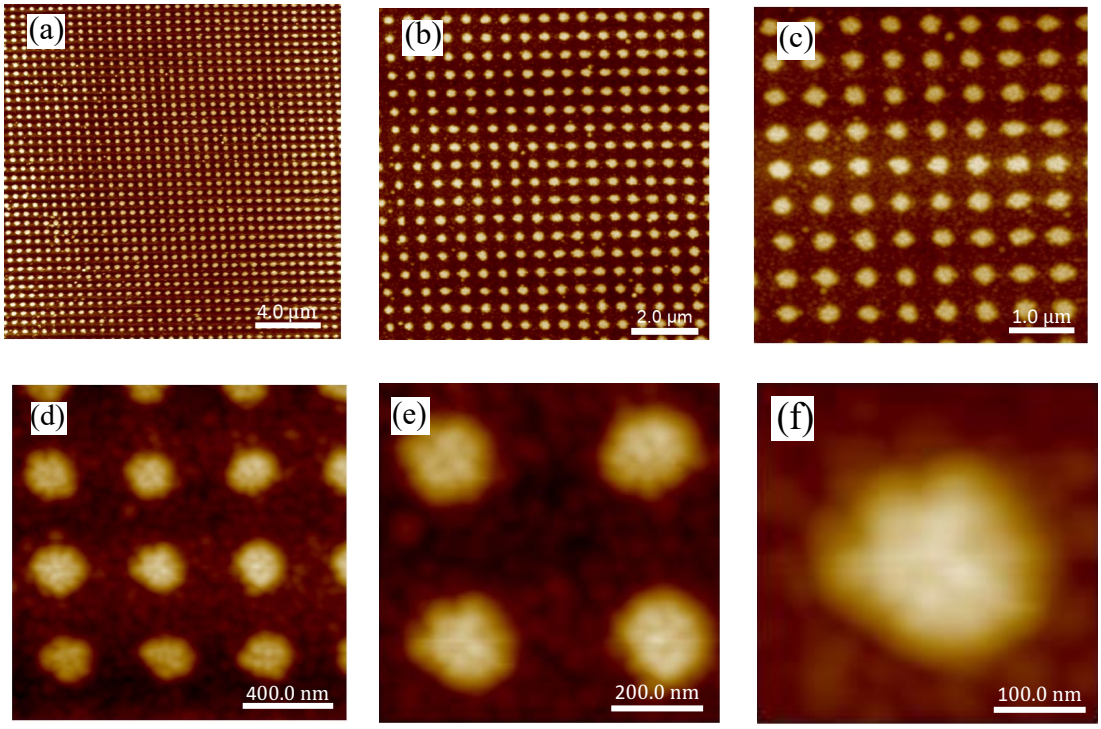

Figure 8.2. AFM height images of Au nanostructures with different scan size: (a) 20.0 µm, (b) 10.0 µm, (c) 5.0 µm, (d) 2.0 µm, (e) 1.0 µm, and (f) 500.0 nm.

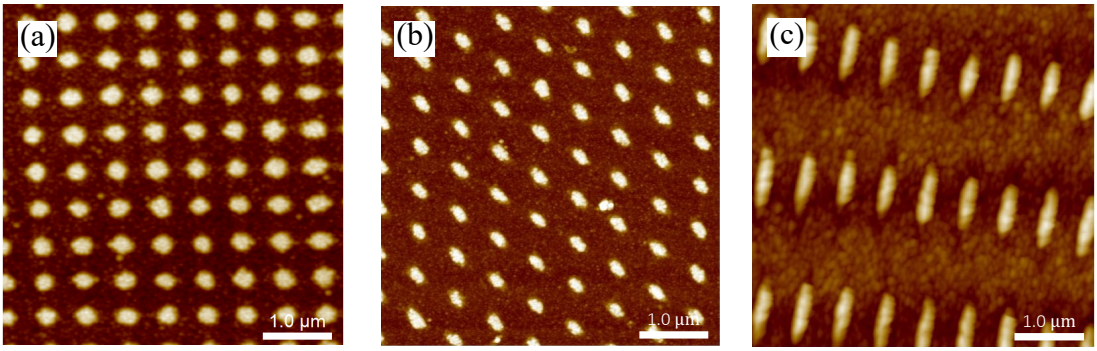

Figure 8.3. AFM height images of Au nanostructures fabricated using a 244 nm light source with an incidence angle of 15°: (a) square arrays, (b) hexagonal arrays, and (c) rows of needles.

8.1.2 Ellipsometry Thickness Measurements

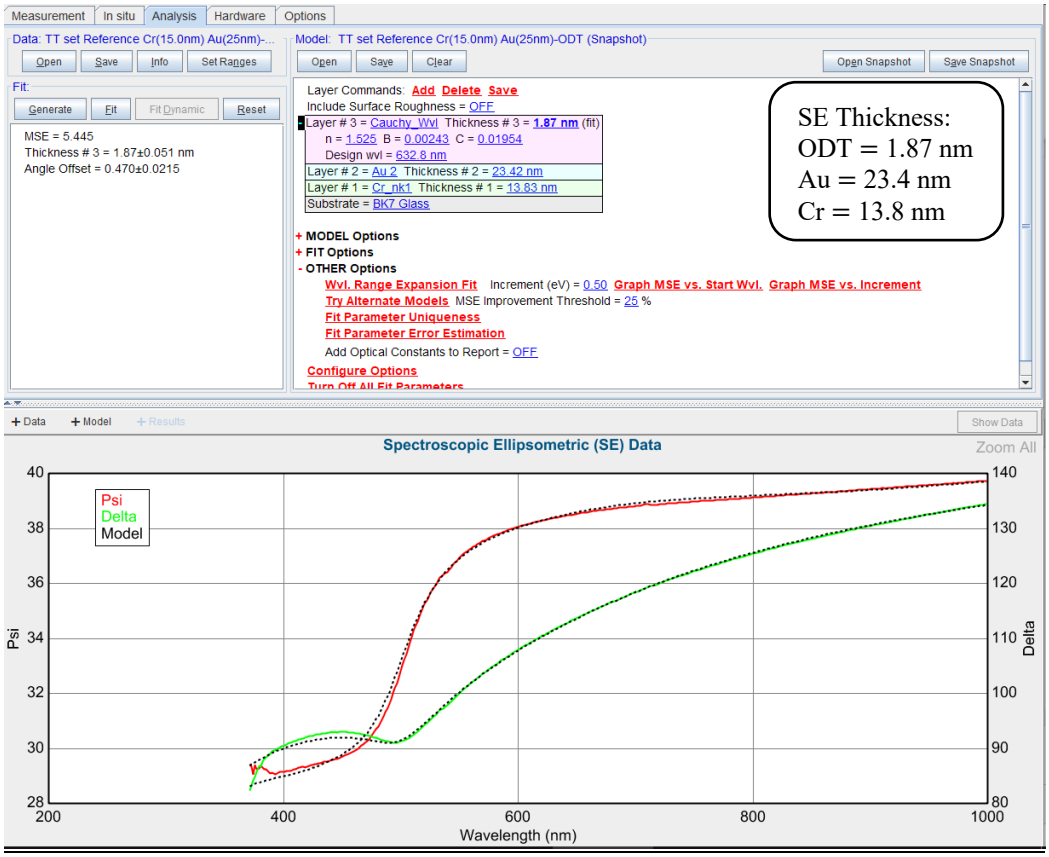

Figure 8.4. Ellipsometry thickness of ODT SAMs on gold/chromium surface.

8.1.3 Harmonic Oscillators Model

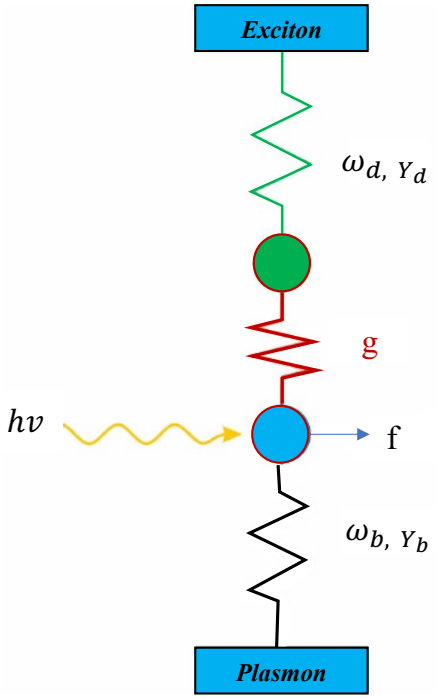

Figure 8.5. Schematic illustration of the harmonic oscillators model.